NMR Studies of the Electronic Structure, Lithium-Ion Dynamics, and Prelithiation of Lithium-Ion Battery Anode Materials

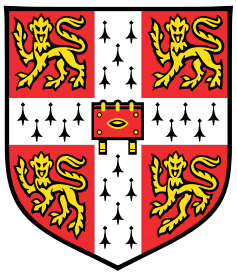

Dylan Charles Maxwell

Department of Chemistry
University of Cambridge

This thesis is submitted for the degree of
Doctor of Philosophy

Girton College December 2021

Declaration

This thesis is the result of my own work and includes nothing which is the outcome of work done in collaboration except as declared in the Preface and specified in the text. I further state that no substantial part of my thesis has already been submitted, or, is being concurrently submitted for any such degree, diploma or other qualification at the University of Cambridge or any other University or similar institution except as declared in the Preface and specified in the text. It does not exceed the prescribed word limit for the relevant Degree Committee.

Dylan Charles Maxwell
December 2021

Abstract

NMR Studies of the Electronic Structure, Lithium-Ion Dynamics, and Prelithiation of Lithium-Ion Battery Anode Materials

Dylan Charles Maxwell

The development of high energy density Li-ion batteries is essential if we are to succeed in the electrification of the transport system. Central to this is the need for electrodes with increased specific capacity (mAh/g and mAh/cm^3) which can run for 100s to 1000s cycles. The manufacturing of these electrodes must also be cheap and scalable in order to meet the demands of future electric vehicles. A Li-ion battery has two types of electrodes, anodes, and cathodes. This work focuses on anodes, specifically graphite and Si anodes. Si anodes have a high theoretical capacity (3579 mAh/g), nearly 10 times more than graphite) and a low (0.1 - 0.4 V vs Li/Li+) operating voltage. However, Si undergoes up to 300% volume expansion upon reaching the fully lithiated $Li_{3.75}Si$ phase. This causes both particle and electrode fracture, leading to continuous electrolyte decomposition at the electrode surface, forming an SEI. This results in irreversible consumption of Li, impedance increase, and capacity fading. Carbon coatings and additives can enhance cyclability, as well as the electrical conductivity of Si electrodes. Carbon coatings can also help manage the stress and strain of the electrode when Si is lithiated, reducing pulverisation. These approaches are costly and not compatible with commercial manufacturing techniques.

In this work silicon-graphene composite anodes are produced through a highly scalable, one-step mixing process. Utilising microfluidic technology, graphite is exfoliated into graphene and mixed thoroughly to produce a homogeneous composite anode. The project aims to explore prelithiation of these anodes as a technique to further improve cyclability and then use solid-state NMR (ssNMR) to understand the differences in the lithiation mechanism during two different prelithiation techniques, electrochemical and chemical.

Although much progress has been made on Si and Li metal anodes, graphite remains the major active component in Li-ion battery anodes. This is owing to its good specific capacity, 372 mAh/g, low cost, non-toxicity, low voltage hysteresis which is important for high energy

efficiency and good cyclability. Graphite also has a low average lithiation voltage, $\sim$ 100 mV, which along with its flat voltage profile, results in a high operating voltage in full cells. Graphite is known to lithiate via a staged mechanism following either the Daumas-Hérold or the Rüdorff-Hofmann model. The stages are defined by the number, n, of graphene layers between adjacent Li layers. Some discrepancies exist in the literature as to the exact voltages and capacities the different stages form, especially the earlier stages. This could be due to differences in cycling rates as faster charging could lead to non-equilibrium states and the existence of multiple stages coexisting at once. In addition, what is still not fully understood is how the intercalation occurs when transitioning from the dilute stages to the dense stages. Also what is not known is whether lithium diffuses only in a 2D plane or whether any 3D diffusion occurs.

In-situ and *ex-situ* ^{7}Li ssNMR was used to probe the local chemical environment of Li and its dynamics in electrochemically lithiated graphite. Electrochemical GITT measurements, variable temperature XRD and ^{7}Li ssNMR, including relaxometry techniques (T_1, T_2 and $T_{1\rho}$), were used to study the intercalation of lithium into graphite and Li dynamics at different states of charge. Notably, through $T_{1\rho}$ measurements, it was shown that the lithium dynamics in the dilute stages is much faster than in the dense stages. These techniques will enable a deeper understanding of Li-ion dynamics in graphite could help further the understanding of ion dynamics in graphite and other layered intercalation compounds.

The ^{13}C NMR peak positions for the lithiated graphite stages 3L - 1 were assigned using *ex-situ* ^{13}C NMR and XRD measurements. The dense stage LiC_{12} and LiC_6 compounds were shown via ^{13}C and ^{7}Li to be metallic in nature, with both T_1 times following the Korringa relation. The ^{7}Li NMR shifts in graphite can be described by a direct Fermi-contact Knight shift while the ^{13}C NMR shifts can be described in part by the combination of an anisotropic spin-dipolar Knight shift and an Isotropic Knight Shift.

Acknowledgements

Foremost, I would like to thank Professor Clare for her support and guidance throughout this project. It has been a pleasure to work within the Grey group and the great working atmosphere in the group I believe stems from Clare. Not only does Clare challenge us to produce great science, but her care for each member of the group fosters an enjoyable and collaborative environment. I have enjoyed being challenged by Clare each time I have presented my work to her and truly believe this has pushed the outcome of my work far beyond the expectations I had for myself at the beginning of the project.

I would like to thank Professor Andrea Ferrari for initially accepting me to study at Cambridge through the doctoral training program as well as his guidance on my projects, particularly on the silicon-graphene project. I would also like to thank Andrea for challenging me through the work with the Graphene Flagship. I have enjoyed learning from our many collaborators within the Energy Storage work package as well as the challenging projects that I have worked on.

Thanks to Dr Abdul-Rahman Raji for initially inspiring me to work on Li ion batteries. I learned much with you in just a short year.

I have enjoyed learning many new techniques during the PhD most notably solid-state NMR. For this, I would like to thank Dr Gunwoo Kim and Dr Josh Stratford, who initially taught me how to perform the experiments. I would particularly like to thank Dr Chris O'Keefe who has taught me much of what I know in terms of NMR. His day-to-day support and friendship have been invaluable, and I have always been able to count on him even while running VT NMR experiments well into the night. I would also like to thank him for proofreading the thesis.

Thank you to Dr Chao Xu for his guidance in all things electrochemistry as well helping me with his magic touch when assembling graphite half-cells. Dr Svetlana Menkin is also thanked for her enthusiasm, guidance, and help in finishing the silicon-graphene project. Svetlana is also thanked for her help in proofreading the thesis. Jeremiah Marcellino is thanked for his collaboration on the silicon-graphene project in helping to develop the co-

microfluidization technique. It has truly been enjoyable to work on the project with such a great friend.

I would also like to thank Dr Chris Truscott, Dr Quentin Jacquet and Mike Jones for their help in performing some of the XRD measurements.

I am grateful for all the friends I have made along the way in both the Grey lab and the Cambridge Graphene Centre. Particularly those in the evening shift in the Grey labs this last year that have made it possible to continue working during these uncertain times. Liam Bird is also thanked for his help in running the Energy Storage lab and I enjoyed our collaboration in designing the electrochemical pressure cell. I wish both Liam and Jeremiah good luck in finishing their PhDs.

The EPSRC is thanked for funding my studies.

I would like to thank my parents for giving me a great start to life and laying the foundations that have allowed me to get this far. As well as my wife's parents and family for their continued support and encouragement. I feel lucky to have them all in my life.

Finally, and most importantly, I would like to thank my wife, Alison for her unwavering support and sacrifice these last 4 years whilst I have pursued my studies. I am so incredibly grateful that you chose to move your life to Cambridge so we could be together, my life is so much richer when we are together. Your love, loyalty and encouragement have kept me going. You are my rock and this PhD would have not come to completion without you. I would also like to thank Alison for giving me our beautiful daughter, Sage. This last year has been amazing and trying all in one and you and Sage have been what has kept me going.

I would like to dedicate this thesis to Alison, Sage, and Walker.

Table of contents

List of figures

List of tables

Nomenclature

Acronyms / Abbreviations

AM Alkali metal

BET Brunauer–Emmett–Teller

BMS Bulk magnetic susceptibility

CE Coulombic efficiency

CI Coulombic inefficiency

DFT Density functional theory

EFG Electric field gradient

FID Free induction decay

FWHM Full-width-half-maximum

GIC Graphite intercalation compound

HOPG Highly orientated pyrolytic graphite

ICE Initial coulombic efficiency

LIB Lithium ion battery

NG Natural graphite

OCV Open circuit voltage

PAS Principal axis system

REDOR Rotational-echo double-resonance

RF Radio frequency

SEI Solid electrolyte interphase

SG Synthetic graphite

Chapter 1

Introduction

1.1 Lithium ion batteries

More than half of the global greenhouse gas emissions are caused by the burning of fossil fuels.[1] Climate change is caused largely by our consumption of fossil fuels.[1] The outcomes of the most recent Conference of the Parties summit, COP26, have highlighted that an accelerated transition towards renewable energy production is vital if the climate crisis is to be solved.[2] Transportation is the cause of around a quarter of all global greenhouse gases.[1] Electric vehicles (EVs), which release no emissions (provided they are powered by renewable electricity), are one of the main technological solutions to reducing these emissions, with many governments pushing to phase out petrol and diesel cars in the next decade.[2]

Renewable energy sources often provide intermittent energy. A method for storing excess energy, which can be used when energy demand is high, is therefore essential. EVs also need to store electrical energy. The key technology that is in common with both of these issues is of course batteries. A battery is a device that stores energy in the form of chemical energy and then releases this as electrical energy; this occurs via redox reactions. In secondary cell batteries, unlike primary cell batteries, these redox reactions are reversible, meaning that the battery can be charged and discharged many times over.[3] A typical battery has three major components: an anode, a cathode and an electrolyte, as shown in Figure 1.1. The electrolyte should be ionically conducting but electronically insulating to allow ions to travel between the two electrodes, which are electronically isolated by a separator. During discharge of the battery, ions move from the anode to the cathode. At the same time, electrons travel from the anode through an external circuit and then enter the cathode, enabling a device to be powered. When the battery is being charged, the process is reversed.

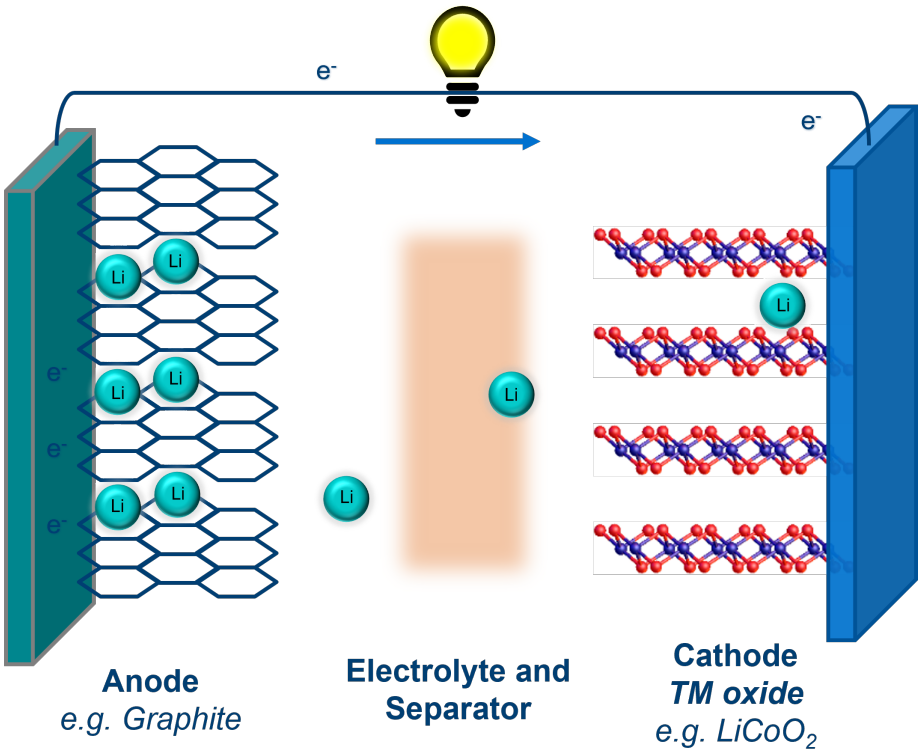

Figure. 1.1 A schematic showing the composition of a typical lithium-ion battery consisting of a layered transition metal oxide cathode and a graphite anode. The electrolyte, also shown, allows Li ions to reversibly shuttle between the anode and cathode during the dis/charging of a device. The battery in the figure is discharging.

Lithium-ion batteries (LIBs), the first commercialised secondary cells (Sony, 1991) are the current battery of choice for much of modern technology such as EVs.[4] This is because Li has the third lowest atomic mass and also one of the lowest redox potentials of any element (-3.04 V vs standard hydrogen electrode). These factors mean that LIBs have high energy and power densities compared to other battery technologies.[5]

The uptake of EVs by consumers has been slow due in part because LIBs are expensive and have low energy densities with respect to combustion engine vehicles. The large and heavy LIBs used in EVs limit the distance they can drive on a single charge which creates range anxiety.[6] The other major obstacles preventing the large-scale uptake of EVs is the time taken to charge the batteries. Combustion engine vehicles can conveniently be refilled in minutes and can go many hundreds of miles between refueling, whereas EVs typically can take up to an hour to charge.[7]

It is therefore important to improve the energy densities of current LIBs in order to increase the range that EVs can travel, as well as to improve renewable energy storage

capabilities. In addition, future LIBs would benefit from fast dis/charge rates to reduce charging times for EVs as well to provide the high power needed for fast acceleration. These batteries will also need to last for many 100s if not 1000s of dis/charge cycles as these batteries are expensive and will need to be used for many years in order to become more commercially viable.[6]

To meet the demands of future applications, batteries must deliver higher gravimetric and volumetric energy densities, long life time, high power density, whilst still being cheap and easy to manufacture on a large scale.[6] High energy densities would greatly improve the mileage of electric vehicles, with current energy densities reaching around 240 Wh/kg and mileage ranges now exceeding 600 km for some premium EVs.[6] The batteries also come at a very high cost; more affordable cars have ranges limited to around 200 km. This is compared to combustion engine vehicles which can have ranges that exceed 1000 km.

The energy density of a LIB depends on the specific capacity of the anode and cathode materials as well as the potential difference between them. The specific capacity is a measure of how many Li ions can be dis/charged into an electrode relative to its mass. The potential difference between the anode and cathode is determined by the difference in their chemical potentials, which is an intrinsic property of the materials. Therefore, one of the main ways to increase the energy density of a battery is to increase the specific capacity of either of the electrodes. One of the most important parameters that determines the cycle life of an anode or cathode material is the Coulombic efficiency (CE). The CE is a measure of the amount of lithium that is reversibly stored in an electrode during a particular cycle. In an anode half-cell configuration, it is the amount of lithium that is delithiated from the working electrode during charging, divided by the amount of lithium that was stored in the working electrode during the previous discharge.[8] The coulombic efficiency should be maximized to ensure the battery has a long life time and can continue to provide enough energy for many charge-discharge cycles.

LIBs can also be improved by increasing the rate at which Li ions can be inserted and removed from the anode and cathode, so that they can be dis/charged faster. Materials are often characterised by their C-rates, which is the rate of time it takes to charge or discharge them. A C-rate of 1C, means that a battery can be dis/charged in 1 hour, while for 2C it is 30 minutes and for 0.5C it is 2 hours.

When a new battery electrode material is being, tested the material is often initially tested in a half-cell configuration. A half-cell uses the electrode of interest as the working electrode, which is cycled against a Li metal counter electrode. There is a large excess of Li in the counter electrode, which means the potential does not change significantly during cycling.

This means the Li metal acts as both a source of Li and also as a pseudo-reference electrode and the potentials of the working electrode can be referenced against Li/Li^+, as they will be throughout this thesis. This allows the redox potentials of the working electrode to be determined as well as the capacity and any degradation mechanisms. In a LIB full-cell, an anode is cycled against a Li containing cathode such as $LiCoO_2$ or $LiNi_{0.6}Mn_{0.2}Co_{0.2}O_2$ (NMC622). The operating voltage is given by the potential difference between the cathode and the anode and therefore, it can be challenging to isolate which electrode is causing capacity degradation.[9] The areal capacity of the electrodes must be well balanced to prevent Li metal plating at the anode and to maximise the energy density of the battery.[10,11] This makes full-cell testing more challenging but these measurements are important as they show the true performance of a LIB material. Degradation mechanisms can also be different in full-cell and half-cell configurations due to the large excess of Li in the counter electrode in a half-cell configuration.[12–14]

1.2 Anodes

In this work, we will focus on gaining insight into improvements that can be made to anode materials. The ideal anode material in a LIB would be able to reversibly de/lithiate Li ions at a high rate, without loss of capacity, possess a low electrode potential (voltage), and offer a high specific capacity.[15] This would give the material the high energy density and fast dis/charge times needed for modern battery applications. One contender is the Li metal anode as it has the highest energy density and lowest redox potential. However, during cycling, dendrites (i.e., protruding Li filaments) can form at the surface of the Li metal anode, especially at high charging rates. Dendrite formation can lead to short-circuiting of the battery which can cause fires and are a major safety concern.[16]

Two other types of anode materials are intercalation materials, which are layered materials where Li ions occupy the spacing between the layers, and alloying materials that form alloys with Li ions. Each type stores Li ions at a slightly higher electrode potential than that at which Li metal or Li dendrites form. The lithiation in both types of materials proceeds via the formation of Li containing phases with increasing Li content. Alloying anodes typically have higher specific capacities than intercalating materials.[15]

The low lithiation potentials of most anodes fall out of the stable potential window of commonly used electrolytes, such as those based on organic solvents.[17] This means that the chemical potential of the anode is above the lowest unoccupied molecular orbital (LUMO) of the electrolyte. As a result, the electrolyte is reduced and the insoluble decomposition

products form a layer known as the solid electrolyte interphase (SEI) on the anode surface. This layer is ionically conducting and electronically insulating and the SEI acts to passivate the anode from further electrolyte breakdown.[18] The formation of a stable SEI is important for the long term cyclability of the LIB. Important also is the ionic conductivity of the SEI which needs to be high enough for fast dis/charging rates.[17]

Testing of an anode material is typically done in a half-cell configuration, so that the impact on the cyclability of the battery from one electrode can be isolated. In LIB half-cells the Li metal electrode is always the anode as it will always have the lowest redox potential of the electrodes in the cell, this means typical anode materials will then become the cathode in half-cells and therefore lithiation occurs during discharge rather than charge, as it would do in a full-cell.

1.3 Graphite Anodes

The first commercial LIBs combined a $LiCoO_2$ (LCO) cathode with a graphitic anode.[19] 30 years later, graphite is still the material of choice for the anode in commercial LIBs.[20] This is because graphite has a low discharge potential that is only slightly higher than that of Li metal ($\sim$ 100 mV vs Li/Li^+), which is important for achieving a high energy density battery as the overall battery voltage is the potential difference between the cathode (high potential electrode) and anode (low potential electrode). Graphite also has very low voltage hysteresis (Fig. 2), such that the energy input into the battery can be extracted with high efficiency. Other chemistries, such as alloying anodes, have higher discharge capacities but have lower full-cell operating voltages which limit energy density.[15] Graphite's layered structure allows Li ions to reversibly de/intercalate between the graphene layers, which leads to a long cycle life. Through selecting an appropriate electrolyte, such as 1 M $LiPF_6$ in EC:DMC, the intercalation reaction can occur with more than 99.9% efficiency, which means LIBs with graphite anodes have long cycle lives.[21]

The reaction between graphite and lithium proceeds via a staged intercalation process, as proposed by Daumas and Herold, where the stage number, n, denotes the number of graphene sheets between each lithium layer.[22] The stoichiometry of the lithiation reaction can be represented by Li_xC_6, with $0 \leq x \leq 1$, where the fully lithiated LiC_6 phase has a theoretical capacity of 372 mAh/g.[23] The stages are also differentiated into dilute and dense phases, where dilute stages are so named because the layers are not fully filled, as shown by the mismatch between x and the expected stoichiometry based on the stage number, where $x = 1/n$.[24] In the dense phases, the layers are fully filled. In the dilute stages, the lithium

is disordered and "liquid-like", whilst in the dense stages the Li layers become ordered and "solid-like".[24] It is for this reason the dilute phases are often denoted with an L to differentiate them from dense phases.

When cycled in a half-cell against Li metal, the voltage profile of graphite (Figure 1.2) shows characteristic voltage plateaus during first-order phase transitions. These indicate two-phase regions, where two stages co-exist; the plateaus occur because the chemical potential of these phases must be equal. Sloped regions in the voltage profile are indicative of solid-solution phase transitions.[25]

The intercalation of lithium into graphite has been extensively studied by X-ray diffraction (XRD) and neutron diffraction.[22–27] The Bragg peaks that correspond to the average spacing between the graphene layers and the 00n peak (for stage n) during *ex-situ*, *in-situ* and *operando* measurements have been used to determine the staged intercalation mechanism.[22,25–27] The results of these studies are the basis for the intercalation models discussed in the literature.[22]

During the first discharge (in a half-cell), a plateau can be seen at ~ 0.8 V in Figure 1.2. The capacity that occurs at $x < 0$ is due the reduction of the electrolyte, which forms a protective SEI layer on the graphite surface during the first discharge.[17] Between $0 < x < 0.04$, during both charge and discharge, Li has been found to de/intercalate randomly throughout the graphite structure, and this phase has been termed stage 1L.[25,26]

At 0.2 V, the next plateau that occurs is due to the first-order phase transition between stage 1L and 4L.[25] The phase transition, which occurs between $0.04 < x < 0.08$, is confirmed to be a first first-order phase transition by the distinct change in the Bragg peak during *in-situ* XRD measurements.[25,26] Further lithiation results in the formation of the stage 3L phase which coincides with the sloped region between $0.13 - 0.2$ V.[24] The exact mechanism for the phase transition between stages 4L and 3L is still not fully understood.[25,26] XRD measurements show that the average layer spacing smoothly increases as more Li is added during this phase transition. This suggests that the material is composed of both the 4L and 3L phases, with the concentration of the 3L phase increasing as more Li is added.[25] Operando neutron diffraction measurements showed that the maximum amount of the stage 4L phase occurs at $x = 0.07$ which corresponds to LiC_{86}, while the maximum amount of stage 3L phase occurs at $x = 0.15$ corresponding to LiC_{40}.[26] Other reports give stoichiometries of LiC_{27-40} for stage 3L and LiC_{37-86} for stage 4L.[24,28,29] The next phase transition is between 3L and 2L, which occurs between $0.11 - 0.13$ V. The stoichiometry of stage 2L is typically reported as LiC_{18} but it has also been reported up to stoichiometries of LiC_{27}.[23,24,28] The next two phase transitions are from stage 2L to 2 and stage 2 to 1. These two-phase first-order

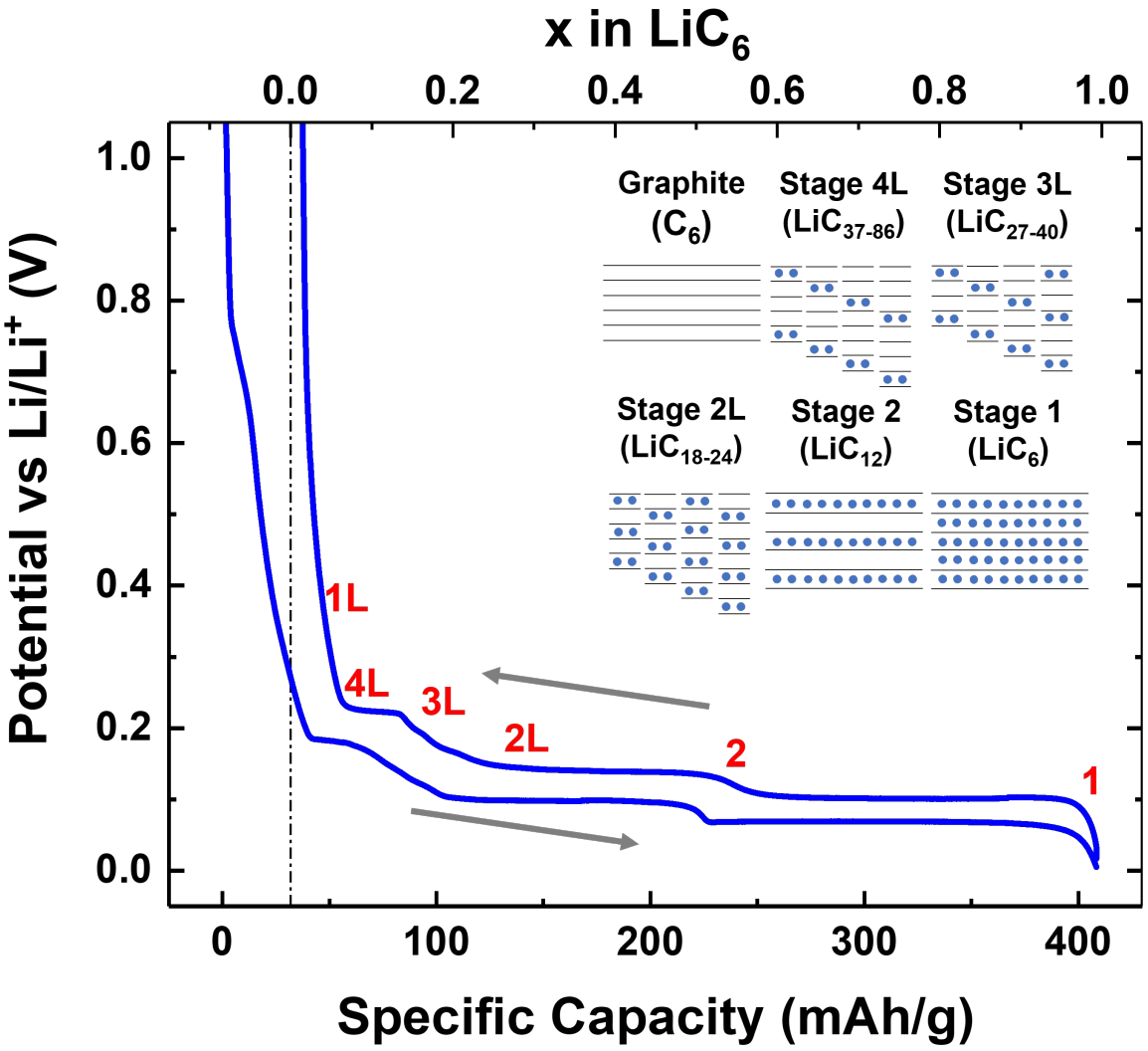

Figure. 1.2 Potential profile of a graphite half-cell during discharging (intercalation) and charging (deintercalation) at C/50 in the first cycle. The arrows indicate the direction of charge. The potential is shown as a function of specific capacity, as well as x in Li_xC_6. The x values have been corrected so that the capacity is only due to lithium intercalated into graphite and any capacity due to SEI formation is accounted for. Labels along the voltage profile, indicate the dominant stage that is formed at the indicated potential and capacity. The inset shows diagrams for each stage with their proposed stoichiometery also shown. Blue circles represent Li ions and black lines represent graphene sheets.

phase transitions are characterised by long plateaus at 0.11 V for stage 2L to 1 and 0.07 V for stage 2 to 1. The slopped regions after each of these two plateaus occurs when the stage 2 and 1 are fully formed. The stoichiometries of these phases are LiC_{12} and LiC_6 with $x = 0.5$ and 1, respectively. Unlike the dilute stages, the composition of the dense stages is

less controversial due to the longer range ordering of the dense stages, which makes them easier to prepare and characterise.[24,26]

Graphite has two crystallographic forms, hexagonal and rhombohedral, which have ABAB and ABCABC stacked structures, respectively. Typically, graphite contains $< 30\%$ of the rhombohedral phase as it is less thermodynamically stable than the hexagonal phase.[20] When Li intercalates into graphite, it causes shearing of the two graphene sheets either side of the Li layers such that the graphite becomes /A/A/ stacked when fully lithiated.[22] Here, the slash denotes a Li layer. The stage 4L, 3L, 2L and 2 compounds have been reported to have /ABAB/BABA/, /ABA/ACA/, /AB/BA/ and /AA/AA/ stacked structures, respectively.[26] The interlayer spacing increases from 3.35 Å to 3.70 Å when the graphite is fully lithiated, leading to a small overall volume expansion of 10.4%.[20,25]

The exact voltage and x value at which the stages are formed depend on the type of graphite used (natural or synthetic), the temperature, as well as the current rate and direction.[24–27,30] The plateau that occurs during the transition between stage 3L and stage 2L was shown by Dahn to be more prominent at higher temperatures, while below 10 °C, the transition is directly from stage 3L to stage 2.[25] This is due to the very small difference in potentials, 5 mV at room temperature, between the stage 3L and 2L phases.[25,26] Higher current densities can also lead to the same effect, suggesting that this phase transition is sensitive to the kinetics of the reaction.[31] The amount of turbostratic disorder in the graphite is also important, with more disordered graphites not showing a clear presence of the higher stage compounds ($n > 2$).[24] These dependencies, which are possibly due to the kinetics of the reaction, lead to ambiguity in defining the stages, particularly with dilute stages. What is also not well known is exactly how the transition between stages occurs, particularly when transitioning between even and odd stages where some layers would have to completely empty or fill.

Based on the final stoichiometry of stage I, LiC_6, the overall reversible reaction for Li insertion into graphite is follows as such

$$Li^+ + e^- + 6C \rightleftharpoons LiC_6 \tag{1.1}$$

When the LiC_6 stage is reached, the theoretical specific capacity of graphite, $Q_{graphite}$, is $372\,\mathrm{mAh/g}$, a value determined from the stoichiometry in the reaction above in Equation 1.1 and using Faraday's first law of electrolysis such that

$$Q_{graphite} = \frac{nF}{M_w} \tag{1.2}$$

where n is the number of electrons involved in the reaction, in this case for Li, $n = 1$. F is Faraday's constant and M_w is the molecular weight of electrode material (C_6).

1.3.1 Natural vs synthetic graphite

There are two main types of graphite used in commercial LIB anodes, natural (NG) and synthetic (SG) graphite.[20] NG is directly mined and often has to be treated to increase the purity, while SG is produced via heat treatment of carbon precursors (typically derived from petroleum) above 2500 °C.[20,24] NG typically has a flake type morphology, with larger well orientated crystalline domains. SG is typically spherical or 'potato' shaped, with smaller crystalline domains that are fairly isotropic in their orientations.[20] SG usually has better rate performance than NG, but NG typically has higher specific capacities and lower first cycle losses.[32,33] NG commonly shows worse cycle performance than SG, which has been attributed to swelling and cracking of the graphite particles.[32] Coatings and electrolyte additives can be used to improve the cycle performance of NG.[32,34] NG, at $\sim$ \$8 per kg, is cheaper than SG at $\sim$ \$13 per kg.[35] The cheaper price means NG is more frequently used in LIBs for portable electronics where cycle life is more important. SG is used in LIBs for EV applications, where performance is more important. Improving the cycle life of NG anodes could help to reduce the cost of LIBs.

Another type of graphite that has been widely studied is highly orientated pyrolitic graphite (HOPG).[22,27,36] These graphites are well ordered with large (few μm) crystallite size. This makes it a particularly interesting material to study (via Raman spectroscopy and XRD) the changes in the crystallographic structure of graphite during Li intercalation.[22,27,37,38] However, in some studies, the potential profile of HOPG shows small differences when compared to the microcrystalline graphite typically used in LIB.[20,27] This could be because the larger crystallite sizes affect the kinetics of the reaction. Understanding the lithiation mechanisms of the different graphite types, could help us to understand why they have different cycle performance.

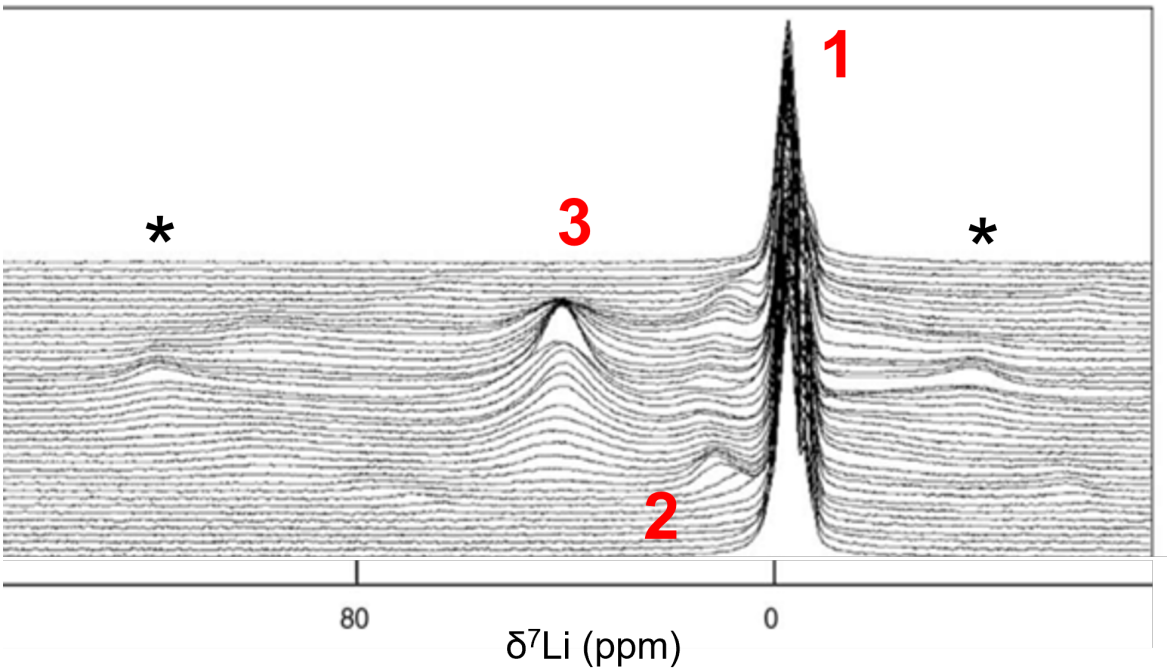

Figure. 1.3 *In-situ* ^{7}Li NMR spectra of graphite lithiation during the first dis/charge cycle. Peaks $1-3$ correspond to the different chemical environments in lithiated graphite. Peak 1 corresponds to diamagnetic Li species in the electrolyte and SEI. Peaks 2 and 3 correspond, respectively, to the dilute and dense stage lithiated graphite phases. The peaks denoted by * correspond to the satellite transitions which occur because ^{7}Li has a spin $I = 3/2$. Figure adapted with permission from reference.[29] Copyright 2006, Elsevier Ltd.

1.3.2 ^{7}Li NMR of graphite lithiation

Nuclear magnetic resonance (NMR) is a useful, non-destructive tool that can be used to understand Li intercalation into graphite.[29,39,40] Letallier *et al.* reported on *in-situ* ^{7}Li NMR measurements during the first dis/charge cycle of a graphite half-cell.[29] The spectra, shown in Figure 1.3 exhibit three characteristic peaks. The first peak at around 0 ppm corresponds to diamagnetic Li species in the electrolyte and SEI. The second and third peaks correspond, respectively, to the dilute and dense stage lithiated graphite phases. The peaks denoted by * correspond to the satellite transitions which occur because ^{7}Li has a spin $I = 3/2$. During intercalation of Li into of graphite, peak 2 shifts from $2-12$ ppm for stage 4L to 2L. When the dense stage 2 phase is formed, peak 3 appears at 45 ppm and grows in intensity upon further lithiation. This peak decreases in frequency to 42 ppm during the formation of the dense stage 1 phase.[29] Peaks 2 and 3 are subject to the Knight shift interaction.[29] The quadrupolar and Knight shift interactions will be described in Chapter 2.

More recent studies have looked at the lithiation of graphite cycled in a full-cells, using *operando* and *in-situ* magic angle spinning (MAS) NMR.[41,42] Märker *et al.* reported on *operando* ^{7}Li NMR measurements of NMC811/graphite full-cells using industry-standard electrodes.[41] The full-cells were cycled at realistic dis/charge rates over multiple cycles at different temperatures. The rate and temperature dependence of Li metal plating on the graphite anode were probed and the results offered insight into how Li metal deposition could be avoided during cycling of realistic LIBs.[41] Freytag *et al.* reported on the first *in-situ* MAS measurements of a full-cell LIB with a $LiCoO_2$ cathode and a graphite anode.[42] ^{7}Li NMR measurements were performed under 10 kHz MAS, which enabled the acquisition of high resolution spectra throughout the first charge/discharge cycle of a full-cell. The technique was used to track the state of charge of the full-cell as well as monitor Li metal deposition on the graphite anode.[42]

1.4 Silicon anodes

Silicon, an alloying anode, is one of the most promising materials for future LIBs due to its high specific capacity. In its fully lithiated state, $Li_{3.75}Si$, silicon has a specific capacity of 3579 mAh/g which is nearly 10 times higher than that of graphite.[43] Additionally, the majority of delithiation occurs between 350 mV and 480 mV; this low discharge potential makes silicon a good material for high energy density batteries.[44] Silicon is also the second most abundant element in the earth's crust making it is both cheap and abundant, an important factor when the potential for commercialisation of a material is considered.[45]

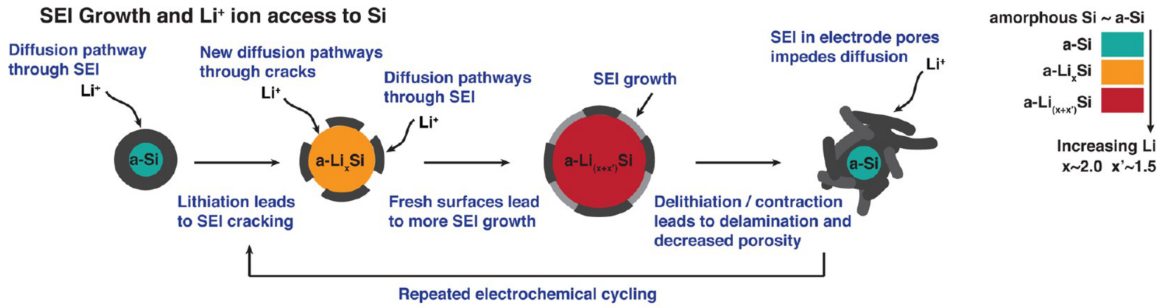

Figure. 1.4 Mechanism of continuous SEI formation on Si nanoparticles during electrochemical cycling. The volume expansion of Si that occurs during lithiation leads to cracking of the SEI which exposes fresh Si surfaces on which further SEI is formed. The continuous formation of the SEI impedes the lithiation of the Si as the Li must diffuse through the SEI layer. This increased impedance results in capacity degradation. Figure adapted with permission from reference.[46] Copyright 2016, American Chemical Society

The low lithiation potential of silicon falls outside the electrochemical stability window of typical electrolytes resulting in electrolyte reduction at the surface of the silicon, thereby forming an SEI. The high specific capacity leads to a large volume expansion of up to 300% during lithiation which leads to cracking of not only of the silicon, but also the SEI that has formed.[47] Cracking of the SEI exposes fresh silicon surfaces which leads to more breakdown of the electrolyte. This process continues during subsequent cycles and leads to the consumption of Li and the electrolyte, resulting in capacity fading and higher impedance.[48] This process is depicted in Figure 1.4. The volume expansion and contraction during cycling also leads to pulverisation of the electrode, meaning contact between silicon particles is hindered; therefore, the electronic conductivity of silicon, already low due to its semiconducting properties, is further decreased. Pulverization of the electrode can also lead to silicon particles completely losing electrical contact meaning it cannot be reversibly lithiated and this leads to loss of capacity.[49,50]

Figure 1.5 shows a typical voltage profile of a silicon anode during the first two dis/charge cycles. Each unique de/lithiation step has been labelled 1 - 7. During the first lithiation of crystalline silicon (c-Si), a two-phase reaction occurs, c-Si undergoes a phase transition to amorphous lithium silicide (a-Si).[51,52] This phase transformation shows a characteristic plateau at ~ 100 mV and is labelled as step 1 in Figure 1.5. The lithiation process begins at the surface of the Si particles and the addition of Li, as well as the increased electron density, leads to Si-Si bond breaking with small Si clusters and Si dumbbells forming.[53] Further lithiation results in the formation of the crystalline phase, c-$Li_{3.75}Si$. This process, labelled as step 2 in Figure 1.5, leads to further break up of Si-Si bonds which results in the formation of isolated Si atoms.[53] Eventually, below ~ 50 mV, the overlithiated c-$Li_{3.75+\delta}Si$ forms. This phase can accommodate extra Li without significant structural changes compared to the c-$Li_{3.75}Si$ phase. The c-$Li_{3.75+\delta}Si$ phase is metastable and has been shown to self-discharge.[54] Delithiation of the c-$Li_{3.75}Si$ is characterised by a distinct plateau at ~ 420 mV, labelled as step 3 in Figure 1.5. During this process, the small number of Si clusters that remain in the Si structure act as nucleation sites and grow in size and form an amorphous Si matrix.[53]

The second lithiation of the now amorphous Si is characterised by two pseudo-plateaus labelled as 4 and 5 in Figure 1.5. The first reaction (4) forms a-Li_xSi with $x = 0 - 2.33$ and occurs between $300 - 200$ mV. During this process, the a-Si structure is broken into small clusters and dumbbells. The more open structure of the a-Si compared to the initial c-Si structure allows this initial process to occur at a higher voltage.[53] The second reaction (5) results in the formation of a-Li_xSi with $x = 2.33 - 3.5$ and occurs between $300 - 200$

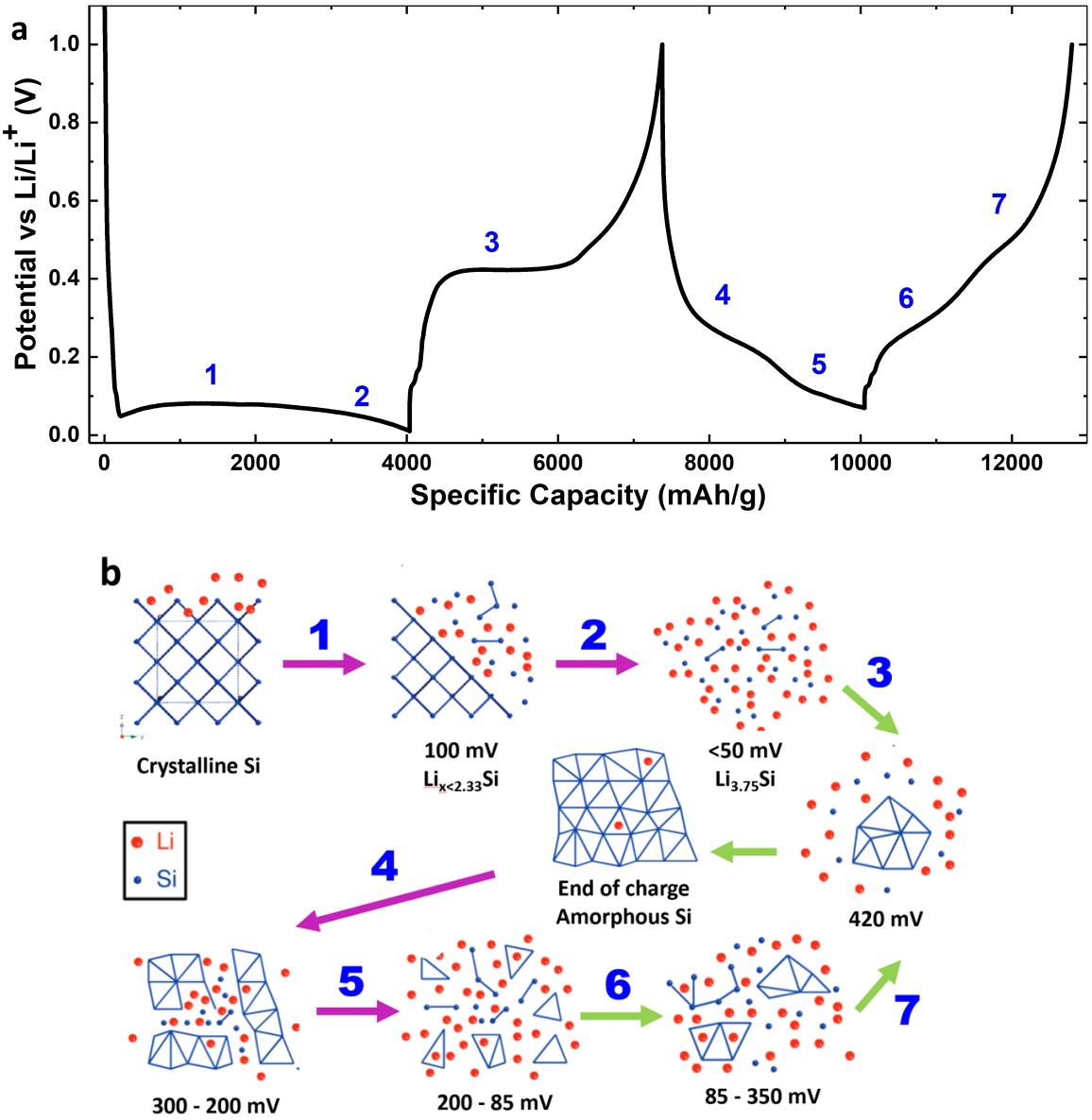

Figure. 1.5 a) Potential profile of a typical silicon-graphene anode during the first and second dis/charge. The first discharge is a deep discharge to 0 mV while the second discharge is to 85 mV and therefore the c-$Li_{3.75}Si$ phase does not form. b) Illustration of the processes involved in the lithiation of crystalline Si during the first cycle and amorphous Si during the second cycle. Li atoms are red and Si atoms are blue. Purple arrows indicate a discharge (lithiation) process and green arrows indicate a charge (delithiation) process. Figure adapted with permission from reference.[53] Copyright 2011, American Chemical Society.

mV. During this process, the Si clusters are further broken up. Further lithiation would again result in the c-$Li_{3.75}Si$ and c-$Li_{3.75+\delta}Si$ phases. If an incomplete lithiation occurs, as

is depicted during the second discharge in Figure 1.5, the delithiation reaction pathway is different to that which occurs after complete lithiation. The difference occurs due to the increased presence of Si clusters, each of which grows during delithiation. These clusters eventually fuse together to form the a-Si matrix. These processes are shown as steps 6 and 7 in Figure 1.5. The growth of the Si cluster is characterised by the lower voltage process (6) and occurs between $85 - 350$ mV. The higher voltage process (7) is due to the fusing of the Si cluster and occurs between $350 - 550$ mV.[53]

1.4.1 Nanostructured Silicon

The cyclability of silicon anodes can be improved by using nanostructured silicon such as nanoparticles and nanowires.[55,56] The high surface area to volume ratio of such materials reduces the stress induced by volumetric change as compared to bulk silicon.[57] In addition, the spacing between the silicon nanoparticles can also act to buffer the volume expansion. Once formed, the SEI does not crack as much as in larger silicon particles, less Li and electrolyte is irreversibly consumed and hence the cyclability is improved. Although the increased surface area results in a lower first cycle CE.[57] One of the main factors that influence charging rates is the ionic conductivity.[58] Ionic conductivity is limited by the diffusion of Li ions through the electrolyte, SEI and electrodes.[59] The structure of the electrode, both at the micro and macro level, plays an important role in determining the rate capabilities of the battery.[60] Nanostructured silicon has improved ionic conductivity as the length of the solid-state diffusion path-ways through the silicon are decreased, leading to lower charge transfer resistance. However, nanostructured electrodes can also have higher tortuosity which leads to a decreased ionic conductivity.[61,62] Nanoparticles also have lower electronic conductivity since the number of overlapping orbitals decreases which leads to a larger band gap. Electronic conductivity is also lower because the number of grain boundaries is increased compared to bulk silicon and electrons must hop between nanoparticles.[63]

Amorphous silicon has also been shown to have good cyclability and capacity retention over many cycles, which has been attributed to the fact that the Li insertion is homogeneous and therefore causes less pulverization of the silicon.[64–66] On the other hand, for c-Si, the lithiation occurs faster along the (110) crystallographic plane which leads to inhomogeneous volume expansion and increased stress.[67]

1.5 Electrolytes

Electrolytes are the medium through which Li ions are transported between the anode and cathode. They typically consist of a Li salt and an organic solvent, though ionic liquids and solid electrolytes are also being researched for their use in LIBs.[68,69] The ideal electrolyte should have high ionic conductivity, good thermal stability and a wide electrochemical stability window.[70] The most common electrolyte in LIBs uses lithium hexafluorophosphate ($LiPF_6$) as the salt, dissolved in ethylene carbonate (EC) and dimethyl carbonate (DMC).[71] The popularity of this electrolyte is because it offers a reasonable balance between all the desirable properties.[72] It has good ionic conductivity and can form a stable SEI on graphite.[17]

The SEI formed on silicon anodes when using standard electrolytes, such as 1.2 M $LiPF_6$ in EC:DEC, consists of mostly lithium alkyl carbonates, lithium carbonate and low concentrations of LiF.[73] As well as this, soluble polyethylene oxide (PEO) oligomers are also found in the electrolyte breakdown products.[12]

On way to improve the cyclability of silicon anodes is to form an SEI with good mechanical stability, which reduces cracking of the SEI during cycling. The use of electrolyte additives, such as vinylene carbonate (VC) and fluoroethylene carbonate (FEC), have been shown to improve the stability and reduce the cracking of the SEI, which results in improved capacity retention.[12,73,74] These additives have also been shown to improve the thermal stability of lithiated silicon.[75] VC-containing electrolytes show higher cell impedance than the FEC-containing electrolytes, with the best results obtained with electrolytes containing 10% FEC.[73]

1.6 Thesis Outline

In this thesis, solid-state NMR is used to study the lithiation mechanisms and Li ion dynamics, within graphite and silicon-graphene Li ion battery anodes. In Chapter 3 ^{13}C NMR measurements performed on lithiated graphite as a function of state of charge will be presented. It will be demonstrated that these measurements can be used to determine the state of charge of the graphite, and give insight into the electronic structure of lithiated graphite. In Chapter 4, electrochemical, XRD, ^{7}Li NMR and relaxometry measurements of lithiated graphite as a function of state of charge will be presented. It will be shown that these measurements can give insight into the Li-ion dynamics of Li intercalated into graphite. In Chapter 5 the electrochemical cycling performance of silicon-graphene anodes, produced by a conventional shear mixing technique and a novel and highly scalable co-microfluidization technique will

be presented. An investigation of the prelithiation of silicon-graphene anodes by chemical and electrochemical methods, using ^{7}Li NMR, will be shown.

Before presenting this work, the NMR theory underlying the experiments performed in this thesis will be described in Chapter 2. Finally in Chapter 6 some general conclusions of the work are discussed, as well as some potential future directions for this work.

Chapter 2

Solid-state nuclear magnetic resonance spectroscopy

2.1 Key NMR Interactions

Solid-state NMR is a useful tool for probing local structure and dynamics in solids. In solution, rapid molecular tumbling leads to averaging of anisotropic nuclear spin interactions to either zero, or an isotropic value. In the solid state, however, molecules move much more slowly and thus, anisotropic nuclear spin interactions are not averaged, leading to broadening of the NMR signal. However, the anisotropy of the NMR interactions can also provide valuable information about the sample.

The physical basis of NMR lies in the magnetic properties of atomic nuclei that arise due to an intrinsic property known as spin angular momentum, $\boldsymbol{I}$, which has an associated spin quantum number, I (which can be either integer or half-integer values). The spin angular momentum gives rise to the magnetic dipole moment of a nucleus, $\boldsymbol{\mu}$, via the expression

$$\boldsymbol{\mu} = \gamma \boldsymbol{I} \tag{2.1}$$

where γ is the nucleus-specific gyromagnetic ratio. When a nuclear spin is subjected to an external magnetic field, the spin angular momentum is said to be quantized such that

$$I_z = m_I \hbar \tag{2.2}$$

where $\hbar$ is the reduced Plank's constant and m_I is the magnetic quantum number, which has allowed values between $-I$ and $+I$ in integer steps. This gives rise to $2I+I$ degenerate energy levels. Quantum mechanics states that we can only determine the projection of $\boldsymbol{I}$ onto a single axis, which by convention we choose to be the z-axis. The z component of the dipole moment $\boldsymbol{\mu}$ is given as

$$\mu_z = \gamma\hbar m_I. \tag{2.3}$$

The net, or bulk, magnetization of a sample, $\boldsymbol{M}$, is given by the sum of all the magnetic dipole moment vectors such that

$$\boldsymbol{M} = \sum \boldsymbol{\mu}. \tag{2.4}$$

In the absence of a magnetic field, the spins are oriented randomly and $\boldsymbol{M} = 0$. Upon application of a magnetic field, $\mathbf{B}$, the nuclear spins will align with or against the magnetic field and this results a non-zero bulk magnetization. This interaction between $\mathbf{B}$ and $\boldsymbol{\mu}$ causes the degeneracy of these energy levels to be broken; this is known as the Zeeman effect. The perturbation of these energy levels, E, is given by

$$E = -\boldsymbol{\mu}\cdot\boldsymbol{B} = -\mu_z B_0 = -\gamma\hbar m_I B_0. \tag{2.5}$$

Where again by convention, we arbitrarily choose the direction of the $\boldsymbol{B}$ field, which has a magnitude of B_0, to be orientated along the z-axis. Spins which align with the magnetic field are lowered in energy and those that are aligned against it are increased in energy. Selection rules state that only transitions where $\Delta m_I = \pm 1$ are allowed which corresponds to an energy difference of

$$\Delta E = \gamma\hbar B_0. \tag{2.6}$$

which in frequency units gives us

$$\omega_0 = -\gamma B_0 \tag{2.7}$$

where ω_0 is the Larmor frequency. The energy separation between levels is small enough that thermal energy can excite spins to higher levels. The number of nuclei in each spin-state can be described by the Boltzmann distribution. In a two-state system (i.e., $I = 1/2$), the number of nuclei in the higher, N^+, and lower, N^-, energy states is given by

$$\frac{N^+}{N^-} = \exp\left(\frac{-\hbar\omega_0}{k_B T}\right) \tag{2.8}$$

where k_b is Boltzmann's constant and T is temperature. At room temperature, the number of nuclei in the lower energy state slightly outnumbers those in the higher energy state.

In an NMR experiment, a radio frequency (RF) pulse is applied to the system at or near the Larmor frequency which introduces an oscillating magnetic field, B_1. This rotates the nuclear magnetisation vector away from the z-axis, so that after the RF pulse, the magnetization vector precesses about the z-axis at the Larmor frequency.[1] The precession of the magnetisation vector in the xy-plane causes a change in magnetic flux which induces an alternating current (AC) in the coil. The AC signal that is detected is known as the free induction decay (FID). The signal decays exponentially because the magnetisation vector relaxes back to equilibrium, aligning back with the z-axis and this decreases the magnitude of the magnetisation vector in the xy-plane. The associated rate of growth of the z-component of the magnetisation vector is described by $1/T_1$. The signal can also decay due to dephasing of the transverse component of the magnetisation vector with an exponential decay rate $1/T_2$. T_1 and T_2 are known as the spin-lattice and spin-spin relaxation times respectively. These will be described in more detail in Section 2.2.

The total interaction energy of the nuclear spins can be expressed as a linear combination of the Hamiltonians that arise due to all the individual nuclear spin interactions. The total Hamiltonian for these spin interactions, $\hat{H}_T$, is given by

$$\hat{H}_T = \hat{H}_D + \hat{H}_{CS} + \hat{H}_J + \hat{H}_P + \hat{H}_{Q_1} + \hat{H}_{Q_2} + \hat{H}_K \tag{2.9}$$

[1] The negative sign in Equation 2.7 means that a nucleus with a positive γ precesses clockwise whilst a negative γ will result in counterclockwise precession.

where $\hat{H}_D$ is the dipolar interaction, $\hat{H}_{CS}$ the chemical shielding, $\hat{H}_J$ indirect spin-spin coupling, $\hat{H}_P$ paramagnetic interaction, $\hat{H}_{Q_1}$ and $\hat{H}_{Q_2}$ the first and second order quadrupolar coupling (for nuclei with $I > 1/2$) and $\hat{H}_K$ the Knight shift interaction.

The following sections will discuss the interactions pertinent to this thesis.

2.1.1 Chemical Shielding

Chemical shielding arises when a sample is placed in an external magnetic field, B_0, which induces circulation of the electrons, which in turn generate a localized field at the nucleus. This field can be either parallel or antiparallel to B_0, and the nucleus is said to be either deshielded or shielded, respectively. The local field is related to the external field via a second rank tensor, $\ddot{\sigma}$. The chemical shielding effect can be described by the following Hamiltonian:

$$\hat{H}_{CS} = \gamma\hbar B_0 \ddot{\sigma} \cdot \hat{I}_z \tag{2.10}$$

where $\hat{I}_z$ is z-component of the nuclear spin operator. The chemical shielding is orientation-dependent and can be described in 3D Cartesian space by a 3×3 matrix

$$\ddot{\sigma} = \begin{bmatrix} \sigma_{xx} & \sigma_{xy} & \sigma_{xz} \\ \sigma_{yx} & \sigma_{yy} & \sigma_{yz} \\ \sigma_{zx} & \sigma_{zy} & \sigma_{zz} \end{bmatrix} \tag{2.11}$$

where each component σ_{ij} denotes the component of the shielding along i due to a magnetic field applied along j. $\ddot{\sigma}$ is non-symmetric and can be decomposed into symmetric and anti-symmetric parts. Only the symmetric part contributes to frequency shifts of a spectrum in an NMR experiment, while the anti-symmetric part contributes to the relaxation.[76] The symmetric part can be diagonalized into its own principal axis system (PAS) such that

$$\ddot{\sigma}_{\text{PAS}} = \begin{bmatrix} \sigma_{11} & 0 & 0 \\ 0 & \sigma_{22} & 0 \\ 0 & 0 & \sigma_{33} \end{bmatrix} \tag{2.12}$$

where the diagonal elements are known as the principal components.[77]

The chemical shielding is related to the familiar observable, chemical shift, δ via the equation:

$$\delta_{ij} = \frac{\sigma_{\text{iso,ref}} - \sigma_{ij}}{1 - \sigma_{\text{iso,ref}}} \tag{2.13}$$

where $\sigma_{\text{iso,ref}}$ is the isotropic shielding of a chosen reference compound. By convention, $\sigma_{11} < \sigma_{22} < \sigma_{33}$, and this in turn means that $\delta_{11} > \delta_{22} > \delta_{33}$. Each principal component relates to a unique shielding axis, each of which are orthogonal to each other.

Using the Hertzfeld-Berger convention, we define three parameters to describe the chemical shift tensor, the isotropic shift δ_{iso}, the span, Ω, and the skew, κ.[78] These parameters are defined as

$$\delta_{\text{iso}} = \frac{1}{3}(\delta_{11} + \delta_{22} + \delta_{33}) \tag{2.14}$$

$$\Omega = \delta_{11} - \delta_{33} \tag{2.15}$$

$$\kappa = 3\left(\frac{\delta_{22} - \delta_{\text{iso}}}{\Omega}\right) \tag{2.16}$$

The span describes the maximum breadth of the powder pattern, while the skew gives a measure of the asymmetry of the tensor.

There are two contributions to the chemical shielding, the diamagnetic (Lamb) and the paramagnetic (Ramsey) terms, such that $\ddot{\sigma} = \ddot{\sigma}^p + \ddot{\sigma}^d$. Diamagnetic shielding is caused by electrons in their ground state, circulating in response to B_0. The magnetic field induced by these circulating electrons lowers the effective field at the nucleus and therefore results in a positive shielding value. Paramagnetic shielding arises due to the mixing of excited states into the ground state by the external magnetic field. This leads to an increase in the applied field at the nucleus and an increase in the observed shift.

The diamagnetic and paramagnetic shielding terms are given by the equations

$$\sigma_{ij}^{d} = \frac{e^2\mu_0}{8\pi m_e}\langle\Psi_0|\sum_k \frac{\boldsymbol{r}_k\cdot\boldsymbol{r}_{kN}\delta_{ij}^{K} - r_{kNi}r_{kNj}}{r_{kN}^3}|\Psi_0\rangle \tag{2.17}$$

$$\sigma_{ij}^{p} = \frac{e^2\mu_0}{8\pi m_e}\sum_{n\neq 0}\left[\frac{\langle\Psi_0|\sum_k \hat{L}_{ki}|\Psi_n\rangle\langle\Psi_n|\sum_k \frac{\hat{L}_{kNj}}{r_{kN}^3}|\Psi_0\rangle + c.c.}{E_n - E_0}\right] \tag{2.18}$$

where Ψ_0 and Ψ_n are the wavefunctions for the electronic ground state and excited state, respectively, e and m_e are the charge and mass of an electron, μ_0 is the permeability of free space, $\boldsymbol{r_k}$ and $\boldsymbol{r_{kN}}$ are the vector positions of the electron k relative magnetic field and the nucleus N respectively, $\hat{L}_{ki}$ and $\hat{L}_{kNj}$ are the orbital angular momentum operators with respect to the magnetic field and nuclear origins, respectively, and c.c. represents the complex conjugate.[77]

2.1.2 Quadrupolar Interaction

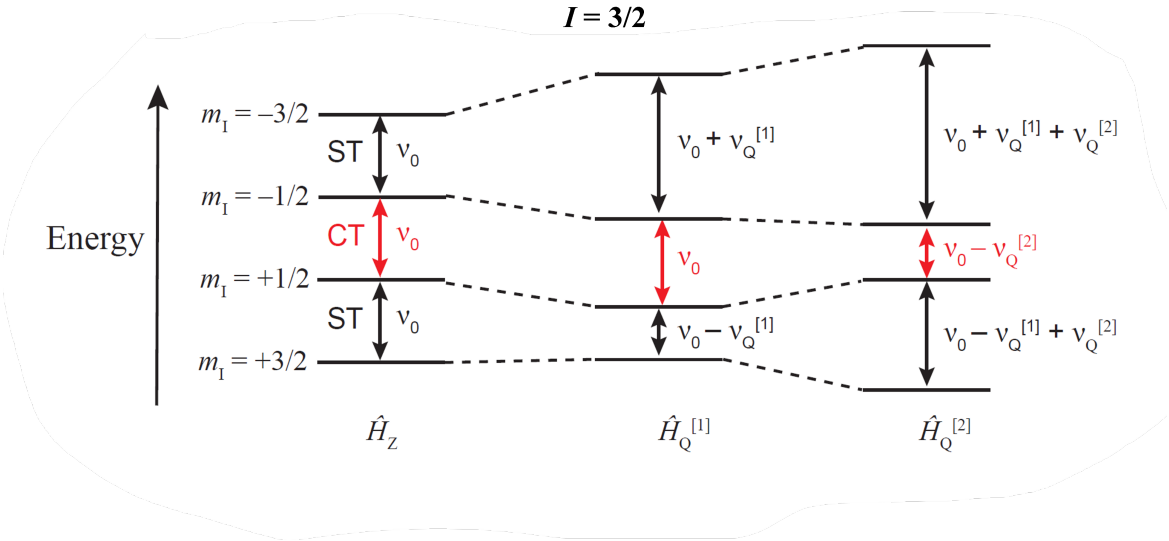

Figure. 2.1 Zeeman energy splitting ($\hat{H}_z$) of spin states for nuclei with spin $\boldsymbol{I} = 3/2$ along with the first ($\hat{H}_Q^{[1]}$) and second ($\hat{H}_Q^{[2]}$) order quadrupolar interactions.

For nuclei with $I > 1/2$, such as ^{7}Li ($I = 3/2$), the electrical charge distribution inside the nucleus is non-spherical and this results in an electric quadrupole moment, Q.[2] This quadrupole moment interacts with an electric field gradient (EFG) caused by a non-spherical distribution of charge around the nucleus, which changes the charge around the nucleus, which causes a perturbation of the nuclear spin energy levels.[3] The Hamiltonian for the quadrupolar interaction is given by

$$\hat{H}_Q = \frac{eQ}{2I(2I-1)}\hat{\boldsymbol{I}} \cdot \ddot{\boldsymbol{V}} \cdot \hat{\boldsymbol{I}} \tag{2.19}$$

where e is the charge of an electron and $\ddot{\boldsymbol{V}}$ is the EFG tensor. $\ddot{\boldsymbol{V}}$ is a 3×3 matrix given by:

$$\ddot{V} = \begin{bmatrix} V_{11} & V_{12} & V_{13} \\ V_{21} & V_{22} & V_{23} \\ V_{31} & V_{32} & V_{33} \end{bmatrix} \tag{2.20}$$

which can be diagonalised into the PAS so that

$$\ddot{V}_{\text{PAS}} = \begin{bmatrix} V_{11} & 0 & 0 \\ 0 & V_{22} & 0 \\ 0 & 0 & V_{33} \end{bmatrix}, \tag{2.21}$$

where the sum of the principal components is 0. This means that the EFG tensor is traceless and can therefore be described by only two paramaters, these are the anisotropy and asymmetry parameters. Since $\ddot{\boldsymbol{V}}$ is traceless, the anisotropy is given by the largest component which is V_{33}. The asymmetry parameter, η_Q, is given by

$$\eta_Q = \frac{V_{22} - V_{11}}{V_{33}}. \tag{2.22}$$

[2]The quadrupole moment can be positive or negative depending on if the nuclear charge distribution is prolate or oblate.

[3]Electrons in *s*-orbitals have a spherical charge distribution and therefore do not contribute to this interaction unless the orbitals become polarised in such a way as to remove the spherical symmetry.

Typically, the magnitude of the quadrupolar coupling is reported in units of frequency as the quadrupolar coupling constant, C_Q, which is given by:

$$C_Q = \frac{e^2 Q V_{33}}{h}. \tag{2.23}$$

The changes in energy of the $m = \pm 1/2$ states due to the first order quadrupolar coupling are identical, as shown in Figure 2.1, this means the central transition (CT) between these states and hence, the lineshape of the central peak is unaffected. Transitions between the $m = +1/2$ and $m = +3/2$ states, as well as the $m = -1/2$ and $m = -3/2$ states are known as satellite transitions (ST) and lead to extra peaks which, in single crystal samples, are spaced by the first order quadrupole frequency. ST are affected by the first order quadrupolar interaction. The second order quadrupolar interaction peturbs both the CT and STs. The quadrupolar interaction is orientation dependent and the signal from the ST is often very broad.

2.1.3 Knight shift

In metallic samples, the magnetic moments of nuclei couple to delocalised electrons in the conduction band via the hyperfine interaction. This interaction, first observed by Walter Knight in 1949, results in a change in resonance frequency known as the Knight shift.[79] Observed shifts are typically much larger than for the same nuclide in insulating materials. The Hamiltonian that describes this interaction is given by:

$$\hat{H}_K = \frac{16\pi}{3}\mu_B \gamma_n \hbar \hat{\boldsymbol{I}} \cdot \hat{\boldsymbol{S}}(\boldsymbol{r})\,\delta(\boldsymbol{r}) - 2\mu_B \gamma_n \hbar \hat{\boldsymbol{I}} \cdot \left[\frac{\hat{\boldsymbol{S}}}{r^3} - \frac{3\boldsymbol{r}\left(\hat{\boldsymbol{S}}\cdot\boldsymbol{r}\right)}{r^5}\right] - \frac{\gamma_n \hbar e}{m_e c}\left[\hat{\boldsymbol{I}} \cdot \frac{(\boldsymbol{r}\times\boldsymbol{L})}{r^3}\right], \tag{2.24}$$

where μ_B is the Bohr magneton, γ_n is the nuclear gyromagnetic ratio, $\hat{\boldsymbol{I}}$ and $\hat{\boldsymbol{S}}$ are the nuclear and electron spin operators, $\boldsymbol{r}$ and $\boldsymbol{L}$ are the radius vector and orbital angular momentum of the electron, respectively, m_e is the mass of an electron and c is the speed light in a vacuum.[80]

The first term represents the Fermi contact interaction, which gives rise to isotropic shifts. It results from the hyperfine interaction between the nucleus and electrons in *s*-orbitals, which are the only orbitals that have non-zero density of states at the nucleus. The second term represents the spin-dipolar interaction between the nuclear and electron spins. It is present in

the absence of cubic symmetry and gives rise to an anisotropic Knight shift.[4] The third term represents the interaction of the nuclear spin with the orbital motion of electrons. Effects of orbital motion are generally quenched in metals.[81] The origin of these three terms will now be described in more detail.

Isotropic Knight Shifts

Fermi-Contact Interaction

The filling of electron energy states follows a Fermi distribution such that only two electrons, one spin up and one spin down, can occupy a particular energy state due to the Pauli exclusion principle. The energy levels are filled from the ground state up to the Fermi level. When no magnetic field is applied, the population of spin up and down electrons is equal,[5] meaning there is no overall net magnetic moment contribution from these electrons. Under an applied magnetic field, electrons with their magnetic moments aligned with the magnetic field (spin down) experience an energy decrease whilst those anti-aligned (spin up) experience an increase. This shift in the energy of the up and down electron spin states must be rebalanced as the electrons share a Fermi level. This means it is energetically favourable for the spin up electrons to flip. This effect, depicted in Figure 2.2 is known as Pauli paramagnetism.

Since the gyromagnetic ratio of an electron is negative, the resulting spin polarisation due to Pauli paramagnetism leads to a net positive magnetisation. If there is any contribution from *s*-orbitals at the Fermi level, they will become polarised such that the effective field at the nucleus increases. This results in a positive Knight shift, towards higher frequencies, given by:

$$K = \frac{8\pi}{3}\chi_s \langle |\psi_s(0)|^2 \rangle_{E_F} \tag{2.25}$$

where χ_s is the Pauli paramagnetic susceptibility,[6] and $\langle |\psi_s(0)|^2 \rangle_{E_F}$ is the average over the Fermi surface of the squared magnitude of the *s*-wave functions evaluated at the nucleus.

[4] It can also be present at cubic sites if spin-orbit coupling is present[81])

[5] Except in materials that display a net magnetic moment in the absence of an external magnetic field i.e. ferromagnets.

[6] Also sometimes known as the spin susceptibility

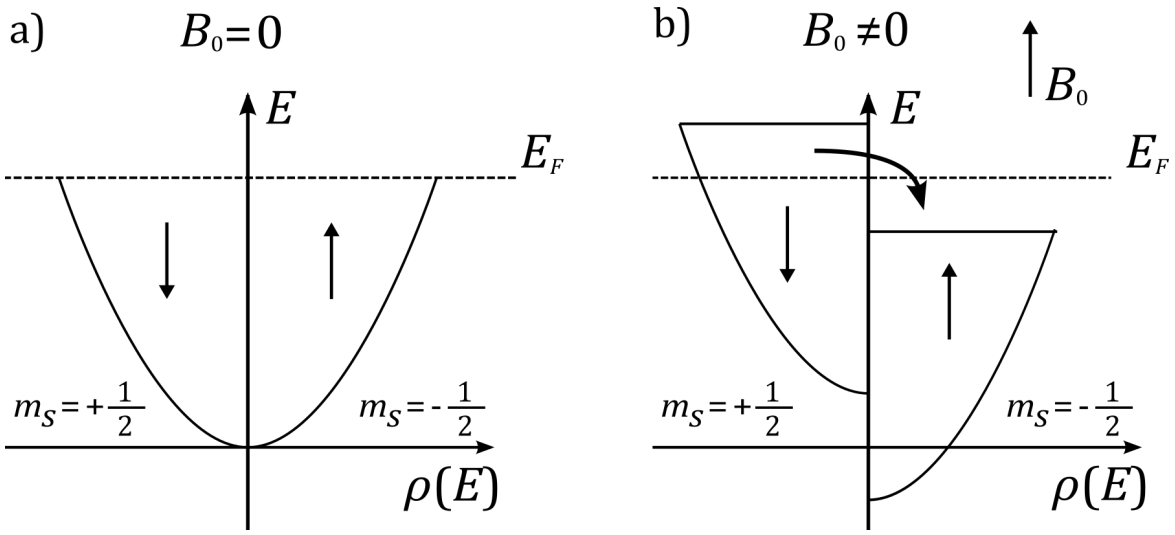

Figure. 2.2 a) When the magnetic field is $B_0 = 0$, the energy levels of the spin-up and spin-down electrons are equal and there is no net population difference. b) In the presence of a magnetic field, the energy of spin-up ($m_s = +1/2$) electrons is increased and lowered for spin-down ($m_s = -1/2$) electrons. Since the Fermi-level must be equal for both spins the spin-up electrons will flip and lead to a net spin-down population which results in an increase of the magnetic field at the nucleus due to the negative gyromagnetic ratio for an electron. Here arrows indicate the direction of the magnetic moment. Figure b is in a non-equilibrium state, at equilibrium the Fermi-level of the spin-up and spin-down electrons is equal.

$\langle|\psi_s(0)|^2\rangle_{E_F}$ therefore gives the probability of finding an *s*-orbital electron from the Fermi level at the nucleus.

The Pauli paramagnetic susceptibility is given by,

$$\chi_s = 2N_0\mu_B^2\rho(E_f) \tag{2.26}$$

where N_0 is number of conduction electrons per unit volume and $\rho(E_f)$ is the electronic density of states at the Fermi level.[81] The induced spins lead to further polarisation of the conduction electrons via an exchange interaction which leads to an enhancement in χ_s which can be given by

$$\chi_s = \frac{\chi_s^o}{1-\alpha}, \tag{2.27}$$

where α is known as the Stoner enhancement factor, which can be calculated using many-body correlation effect theory.[81]

Core Polarisation

In conducting materials where there is no contribution from *s*-orbitals at the Fermi level, no direct contact with the nucleus occurs. However, electrons in the conduction band can induce a polarisation of the core *s*-orbitals. Paired conduction band electrons that lie below the Fermi surface may also become polarised. This polarisation occurs via a spin dependent exchange interaction that arises due to the Pauli exclusion principle. This interaction is known as core polarisation and can produce spin densities at the nucleus which can then interact via the Fermi contact interaction.[81]

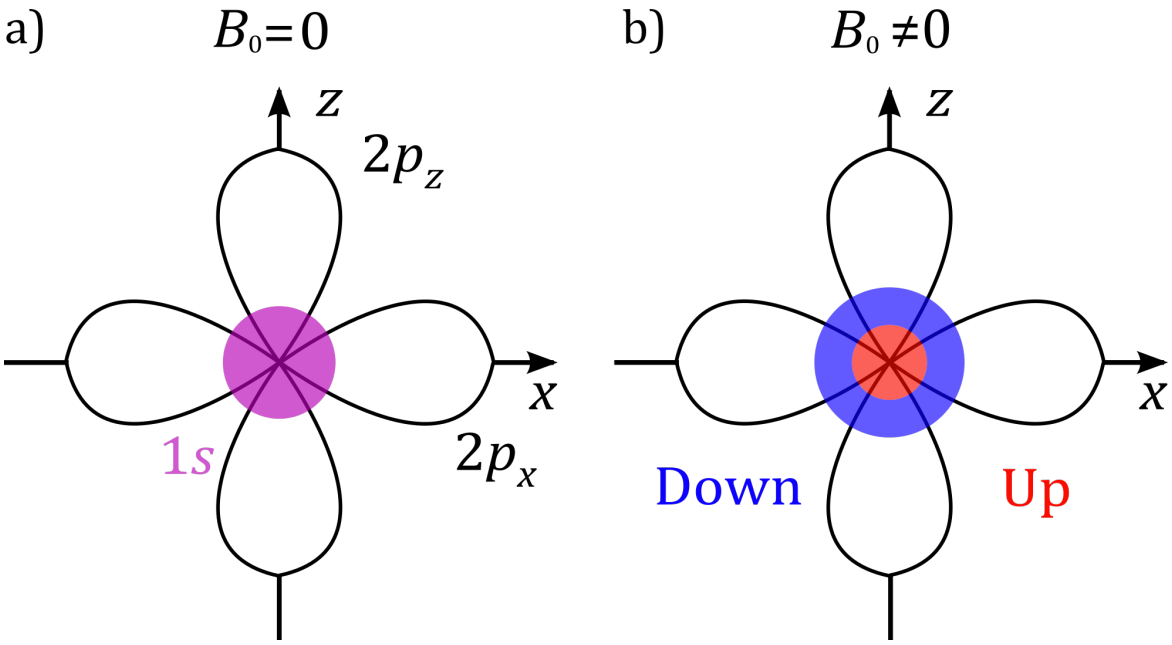

Figure. 2.3 The core polarisation effect depicted for a system such as lithiated graphite where the conduction band lies in the $2p_z$-orbital. a) When $B_0 = 0$, there is no net spin density at the nucleus. b) In the presence of a magnetic field, the magnetic moment of the spin-down electrons in the p_z-orbital will align with the magnetic field. The spatial extent of the spin-down electrons in the 1*s*-orbitals will then expand slightly due to the exchange interaction. This results in a net spin-up density at the nucleus generating a negative magnetic moment resulting in a smaller local magnetic field at the nucleus. The orbitals shown in Figures a and b are depicted in an equilibrium state.

The magnetic moment of the unpaired electron spins at the Fermi level will align with the magnetic field. Since the gyromagnetic ratio of an electron is negative, the unpaired electrons

will be spin down ($m_s = -1/2$). Parallel spins interact favourably through an exchange interaction, this causes an expansion of the spatial extent the electrons below the Fermi level whose magnetic moments are aligned with those at the Fermi level.[82] Whilst there is no change in the overall spin polarisation, this interaction leads to an increase in the net spin up density ($m_s = +1/2$) at the nucleus. This net spin density interacts with the nucleus through the Fermi contact interaction and typically results in a negative Knight shift.

Estimates of the core polarisation effect from experimental data and calculations for single unpaired electrons were given by Bennet *et al.*[81] For d, f and np-shells, where n, the principal quantum number, is 4 or greater, the hyperfine field from this interaction is negative whilst for $2p$ and $3p$ it is positive. This is because typically the spatial extent of $2s$ and $3s$-orbitals are larger than that for the $2p$ and $3p$-orbitals. However, exact values for p-orbitals are not certain, since most experimental evidence are from atoms that also contain a contribution from polarised closed shell s-orbitals. These would also give a positive hyperfine field and hence, to find the magnitude and sign of the core polarisation of p-orbitals these terms must be separated out, which is non-trivial.[81]

Inter-atomic exchange interactions with neighbouring atoms may also contribute to the core polarisation, as an applied magnetic field will also polarise the spins on neighbouring atoms. These can then interact as described previously, except this time, the spin interaction will be through bonds. In monatomic metals, the atom being "observed" will also have an equal and opposite polarising effect on the neighbouring atom. These terms therefore cancel each other out and do not contribute to the isotropic shift. In principle, however, these interactions can still contribute to relaxation as will be discussed in Section 2.2.4. These inter-atomic interactions could also be relevant in polyatomic metals.

Nuclear-electron dipole-dipole coupling/Anisotropic Knight shift

If the symmetry of the system is no lower than cubic, then the Knight shift is purely isotropic. However, in the absence of cubic symmetry, there is an anisotropic Knight shift interaction, given by the second term in equation 2.24. The interaction occurs via the coupling of the nuclear spin and the electron spin density that arises due to Pauli paramagnetism. The coupling occurs via the spin-dipolar interaction and can occur for any non s-orbital electrons in metallic samples.[82] This term does not lead to an isotropic shift but instead results in changes to the anisotropy of the NMR lineshape. Integrating the nuclear-electron spin dipolar Hamiltonian over all electron spatial coordinates for a p_z-orbital one obtains:

$$\hat{H}_{IS} = \gamma_n \gamma_e \hbar^2 \frac{1}{r^3} \frac{2}{5} \left(2I_z S_z - I_x S_x - I_y S_y\right) \tag{2.28}$$

where I_j and S_j are the j-component of the nuclear and electron spin, respectively.[83,84] From Equation 2.28 we find that the anisotropic Knight shift tensor, $\boldsymbol{K}_{IS}$, is traceless. In powder samples, the p_z-orbitals point in every direction and as a result, the anisotropic Knight shifts vary continuously between K_{ISz} and $K_{ISx,y}$. The angular dependence of the anisotropic Knight shift is given by:

$$K(\theta)_{IS} = \frac{2}{5} \left(\frac{1}{r^3}\right) \chi_s \left(3\cos^2(\theta) - 1\right) \tag{2.29}$$

where θ is the angle between principal axis and the applied magnetic field.[85]

Orbital Knight Shift

The third term in Equation 2.24 represents the orbital Knight shift, K_{orb}. This shift originates, not from Pauli paramagnetism, but rather due to the orbital magnetic moment induced by an applied magnetic field. The interaction has a similar origin as the paramagnetic chemical shielding interaction and is often known as Van Vleck Paramagnetism. The isotropic component has the form:

$$K_{\text{Orb}} = \frac{2\mu_B}{IB_0} \sum_{i_{E<E_f}} \sum_{f_{E>E_f}} \frac{\left\langle i|\boldsymbol{B_0} \cdot \hat{\boldsymbol{L}}|f\right\rangle \left\langle f|\frac{2\hat{\boldsymbol{L}}\cdot\hat{\boldsymbol{I}}}{r^3}|i\right\rangle \delta(\boldsymbol{k_f} - \boldsymbol{k_i})}{E_i - E_f} \tag{2.30}$$

where $\hat{\boldsymbol{L}}$ is the orbital angular momentum operator and δ is the delta function which means that only mixing between states with the same wavevector is allowed. The applied field induces mixing of the occupied and unoccupied Bloch states, i (initial) and f (final). This term is usually negligible since in most metals, the orbital angular momentum is quenched. However, this term can be important in metals with half-filled conduction bands since mixing between occupied and unoccupied states is then maximised. The term in the denominator also means that conduction bands that are narrow in energy lead to larger shift.[81]

In alkali intercalated fullerene molecules, the admixture of *s*-orbitals into the p_z-orbitals due to the curvature of the molecule will unquench the orbital angular momentum resulting in a non-zero value for K_{Orb}.[82] In Li-GICs, where there is no curvature of the molecule, admixture of the Li 2*s*-orbitals into the conduction band, which is mostly composed of the C p_z-orbital, should result in a non-zero contribution from orbital effects to the Knight shift.[81,86]

2.2 Relaxation

When a system is perturbed out of equilibrium in an NMR experiment, the nuclear spins are excited to higher energy states. These excited nuclear spins will return back to thermal equilibrium. The study of the interactions that govern how a system returns back to equilibrium is known as NMR relaxometry. It is powerful tool that can be used to study the Li ion dynamics within battery materials, as well the dynamics of other systems. Measurements at different temperatures can yield information on self-diffusion coefficients and activation energy barriers for Li motion.[87]

2.2.1 T_1 Relaxation

Spin-lattice relaxation, also known as longitudinal relaxation, characterised by the time constant T_1, results in the return of the longitudinal magnetisation back to its equilibrium value. Assuming an initial net magnetisation value of zero, as in a saturation recovery experiment, the return of the net magnetisation vector, M, back to its equilibrium value, M_0, follows an exponential relation such that:

$$M(\tau) = M(0)\left(1 - \exp\left(\frac{-t}{T_1}\right)\right). \tag{2.31}$$

The time constant T_1 is the time taken for the magnetisation to reach $1 - \frac{1}{e} = 63\%$ of its equilibrium value. In principle, multiple relaxation processes occur which will have different time constants. In most cases, the time constants are similar enough so that a single T_1 value can be used to model the relaxation. T_1 relaxation occurs as a result of spins transitioning from a higher to lower energy states. The transitions are induced by fluctuating magnetic fields at the nucleus, which can arise due to variations in NMR interactions (e.g., dipolar, quadrupolar, chemical shielding anisotropy). In metallic and paramagnetic samples, hyperfine interactions

between the nucleus and electrons also cause relaxation and are often the dominant relaxation mechanism.

Motional Relaxation

Molecular and ionic motion induces fluctuations in both the dipolar and quadrupolar coupling. The longitudinal relaxation is most efficient when the motional processes occur on time scales at the Larmor frequency and twice the Larmor frequency. When homonuclear dipolar and quadrupolar coupling are considered, the longitudinal relaxation, R_1, is given by:

$$R_1 = A\left[\frac{1}{3}j(\omega_0) + \frac{4}{3}j(2\omega_0)\right] \tag{2.32}$$

where A is a constant that depends on the strength of the interaction that is driving the relaxation and $j(\omega_0)$ is frequency dependent spectral density function.[87] In an ideal case, A can be calculated analytically. If vibrational motions are ignored, and the homonuclear dipolar interaction between two nuclear spins is considered, then A is given by:

$$A_{\text{dip}} = \frac{3{\mu_0}^2\hbar^2\gamma^4}{160\pi^2 r^6}, \tag{2.33}$$

where r is the separation distance between the spins.[88] In practice, vibrational motion means A_{dip} is smaller than the value determined by Equation 2.33. For isotropic motion of a nucleus with spin $I > 1/2$, A_{q} is given by

$$A_{\text{q}} = \frac{4(2I+3)}{5I^2(2I-1)}\left(1+\frac{\eta_Q^2}{3}\right)\frac{3}{160}C_Q^2.^{89} \tag{2.34}$$

In most cases, quadrupolar relaxation dominates over dipolar relaxation.[88]

For random isotropic motion, the temperature and frequency dependence of the relaxation rates can be described by the model proposed by Bloembergen, Purcell and Pound (BPP). In BPP theory, the motional processes can be described by a correlation function, $G(t)$ such that:

$$G(t) = \exp\left(\frac{-t}{\tau_c}\right), \tag{2.35}$$

where τ_c is the correlation time of the motion. Fourier transforming $G(t)$ results in Lorentzian shaped spectral density function given by:

$$j(\omega_0) = \frac{\tau_c}{1 + (2\omega_0\tau_c)^2}. \tag{2.36}$$

The right-hand side of Equation 2.36 can be simplified in the high temperature limit ($\omega_0\tau_c \ll 1$) and low temperature limit ($\omega_0\tau_c \gg 1$) to τ_c and $4\omega_0^{-2}\tau_c^{-1}$, respectively. In the intermediate regime $\tau_c = 1/1.6\omega_0$.

If the motion follows Arrhenius behaviour then τ_c is given by:

$$\tau_c = \tau_0 \exp\left(\frac{E_a}{k_b T}\right) \tag{2.37}$$

where τ_0 is a pre-exponential factor, E_a is the activation energy for a motional process, k_B is Boltzmann's constant and T is temperature. When this is true, T_1 will also have an Arrhenius dependence such that:

$$T_1 \propto \exp\left(\frac{\pm E_a}{k_B T}\right) \tag{2.38}$$

where the negative sign is used for the high temperature regime and the positive sign low temperature regime. The activation energy for motion can be extracted from the gradient of an Arrhenius plot of $\ln(R_1)$ as a function of inverse temperature as shown in Figure 2.4. In the intermediate regime, a maximum is observed in the relaxation rate. If the relaxation rate maximum can be experimentally observed, then the spectral density can be determined and using Equation 2.32, the dipolar and quadrupolar coupling strengths can be calculated.

In real systems, motion is often correlated, and this means the correlation function can no longer be described by a single exponential function. Often, a stretched exponential function, given by:

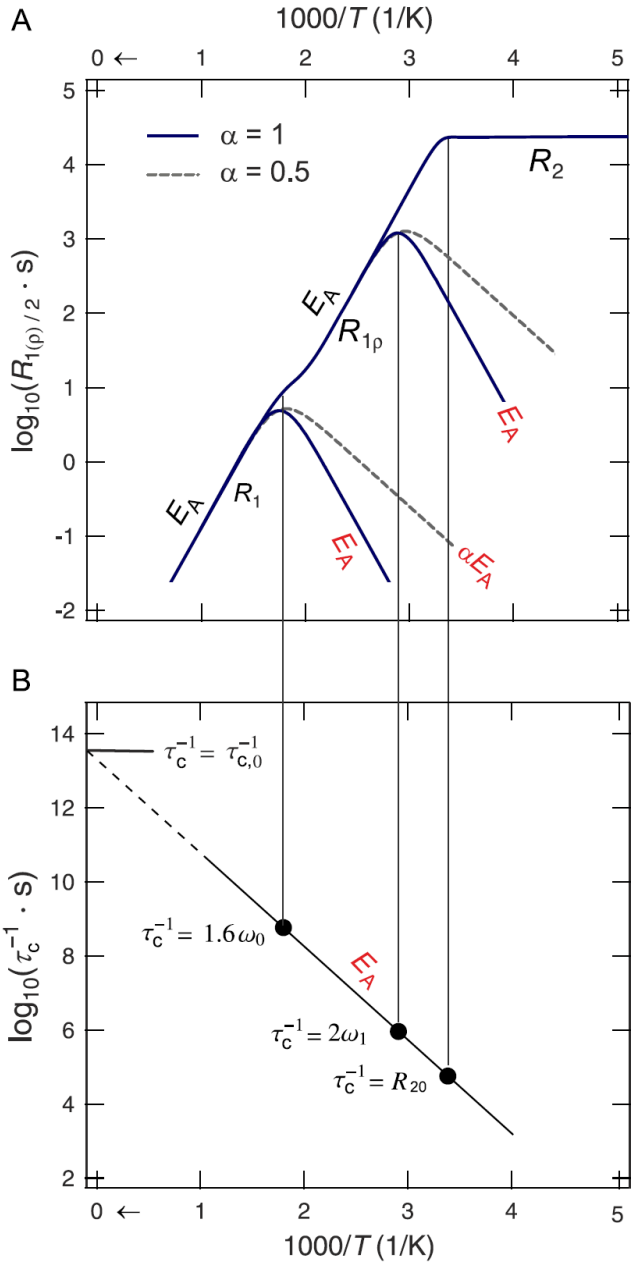

Figure. 2.4 a) Arrhenius plot of the relaxation rates R_1, $R_{1\rho}$ and R_2 where only the homonuclear dipolar coupling interaction is considered and the motion is isotropic. Solid lines represent uncorrelated motion when $\alpha = 1$ and dotted lines show the effect of correlated motion when $\alpha = 0.5$. b) Arrhenius plot which shows how the correlation rates can be determined from the relaxation rates. Figure reproduced with permission from reference.[87] Copyright 2012, Elsevier Ltd.

$$G(t) = \exp\left(\frac{-t}{\tau_c}\right)^{\alpha}, \tag{2.39}$$

gives satisfactory results. The corresponding spectral density function is then

$$j(\omega_0) = \frac{\tau_c}{1 + (2\omega_0\tau_c)^{1+\alpha}} \tag{2.40}$$

where α is an empirical constant that represents the asymmetry of the relaxation rate curve as shown in Figure 2.4. In the low temperature regime, correlated motion causes an increase in the relaxation rate.

2.2.2 $T_{1\rho}$ Relaxation

Measurements of the spin-lattice relaxation in the laboratory frame, characterised by T_1, are sensitive to motion on time scales of the Larmor frequency *i.e.*, in the MHz range.[90] This rapid motion is often only accessible at high temperatures. Spin lattice relaxation in the rotating frame measurements, characterised by $T_{1\rho}$ can be used to probe slower motion.[36]

A spin-locking experiment is used to measure $T_{1\rho}$. After exciting the transverse magnetisation, a continuous wave radio frequency (RF) spin-locking pulse is applied on resonance for a duration, τ. In the rotating frame, the magnetisation is static in the transverse plane. The RF of the spin-locking pulse, $\nu_1 = \omega_1/2\pi$, can be controlled in the experiment and is typically in the kHz range. The decay of the magnetisation, given by:

$$M(\tau) = M(0)\left(\exp\left(\frac{-\tau}{T_{1\rho}}\right)\right), \tag{2.41}$$

now depends on motion at rates similar to the spin-locking frequency ω_1. The spectral density function is given by Equation 2.40, replacing ω_0 with ω_1.

When homonuclear dipolar and quadrupolar coupling are considered, the relaxation rate, $R_{1\rho}$, is given by

$$R_{1\rho} = A\left[j(2\omega_1) + \frac{5}{3}j(\omega_0) + \frac{2}{3}j(2\omega_0)\right]. \tag{2.42}$$

The resulting relaxation rate curve is shown in Figure 2.4 on an Arrhenius plot. The rate maximum occurs when $\tau_c = 1/2\omega_1$.

2.2.3 T_2 Relaxation

Spin-spin relaxation, also known as transverse relaxation, is characterised by a time constant, T_2. Echo pulse sequences are performed to determine T_2. By measuring the signal decay as a function of the echo length, T_2 can be determined. It is a measure of the decay of the magnetisation vector perpendicular to the applied magnetic field. The decay of transverse magnetisation occurs due to a loss of coherence of the transverse nuclear spin magnetization and is given by:

$$M(\tau) = M(0)\left(\exp\left(\frac{-\tau}{T_2}\right)\right). \tag{2.43}$$

Decoherence can occur due spin transitions caused by fluctuating magnetic fields in the same way that longitudinal relaxation occurs. Decoherence can also occur due to differences in the local magnetic field experienced by the nuclear spins in a system. These nuclear spins will have different precession (Larmor) frequencies, and this leads to a loss of coherence which results in a decay and broadening of the NMR signal. The local magnetic field inhomogeneities do not need to vary in time, only in space. This means that the transverse relaxation rate has a term that depends on the spectral density at zero frequency, $j(0)$. These two mechanisms result in the transverse relaxation rate, R_2, given by:

$$R_2 = A\left[j(0) + \frac{5}{3}j(\omega_0) + \frac{2}{3}j(2\omega_0)\right].^{87} \tag{2.44}$$

As a result of the term that depends on $j(0) = \tau_c$, it can be shown that as the correlation time increases, that the relaxation will also increase. In the case of motion induced relaxation that is driven by the homonuclear dipolar interaction, as shown in Figure 2.4, the value of R_2 will reach a steady value at low temperatures when $\tau_c = 1/R_2 = 1/\sqrt{A_{dip}}$.

The observed spectral linewidth is related to T_2 relaxation. In the limit of a perfectly homogeneous magnetic environment:

$$T_2 = \frac{1}{\pi\omega_{1/2}} \tag{2.45}$$

where $\omega_{1/2}$ is given by the full-width-half-maximum (FWHM). However, field inhomogeneities will also lead to broadening of the linewidth and in this case, Equation 2.45 will give the effective transverse relaxation time, T_2^*.

2.2.4 Metallic Relaxation

The dominant relaxation mechanism in most metallic samples is via the hyperfine interaction. For the case of non-interacting electrons, the longitudinal relaxation rate follows Fermi's Golden rule and is proportional to temperature.[84] For the case where the Fermi contact interaction is dominant, the relaxation rate can be given by

$$\frac{1}{T_1} = \frac{64}{9}(\pi\hbar)^3 \left[\gamma_e\gamma_n \left\langle |\psi_s(0)|^2 \right\rangle_{E_f} \rho\left(E_f\right)\right]^2 k_B T, \tag{2.46}$$

where γ_n is the nuclear gyromagnetic ratio. From Equations 2.25, 2.27 and 2.46 we can find the Korringa relation which states that the product of the spin-lattice relaxation time, T_1, temperature, T, and the square of the Knight shift is a constant such that

$$T_1 T K^2 = \frac{\hbar}{4\pi k_B}\left(\frac{\gamma_e}{\gamma_n}\right)^2 \beta = S\beta, \tag{2.47}$$

where S is known as the Korringa constant and β is an experimental factor whose value deviates from unity when electron-electron interactions become important.[82]

Antropov *et al.* calculated the spin-lattice relaxation rates, T_1^{-1} for ^{13}C nuclei in alkali fulleride superconductors where the Fermi level lies in the $2p_z$-orbital, and determined that the T_1 is dominated by the spin-dipolar hyperfine interaction.[91] An angular dependence of the spin-lattice relaxation rate was experimentally confirmed by Pennington *et al.* for alkali fullerides.[85] For ^{13}C nuclei that predominantly interact with electron spins in $2p_z$ orbitals, the T_1 is given by:

$$\frac{1}{T_1} = \frac{1}{4}\left(2+3\sin^2\theta\right)\left(\frac{\pi}{2}\right) k_B\hbar^3\gamma_e^2\gamma_n^2 \left[\frac{4}{5}\left\langle\frac{1}{r^3}\right\rangle \rho\left(E_f\right)\right]^2 T. \tag{2.48}$$

This equation shows that the T_1 is expected to be anisotropic and dependent on the angle, θ, between the p_z-orbital and the applied magnetic field. Since the measurements were performed on powder samples, the z-axis may point in any direction between 0 and $\pi/2$ and T_1 may take any values within this range. Using the Knight shift and relaxation rate in Equations 2.29 and 2.48, a spin-dipolar Korringa relation can be found exactly as in Equation 2.47 except that powder averaged terms must be used.

2.3 Variable Temperature NMR

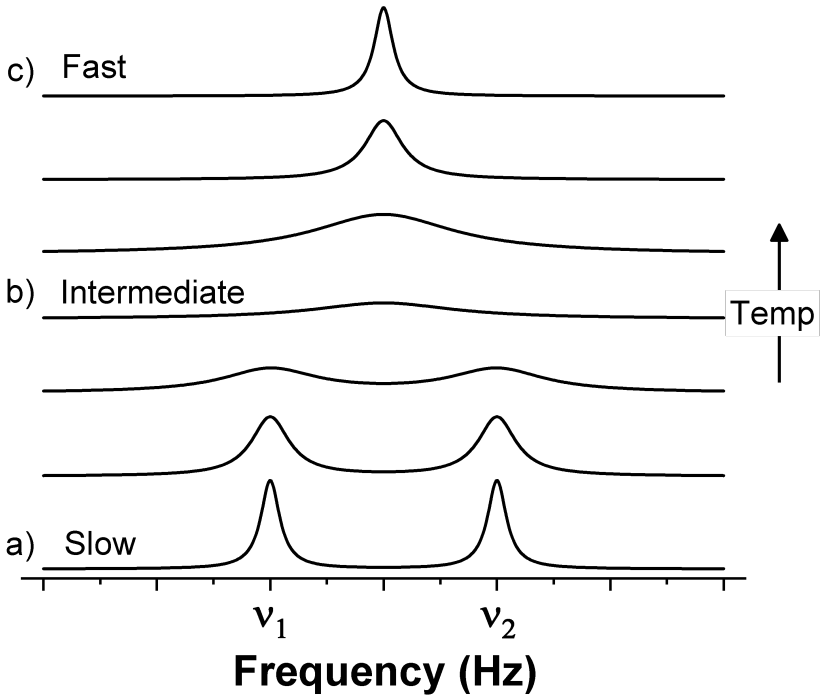

Figure. 2.5 The change in lineshape in a two site system with the exchange rate increasing from a to c. The two sites have a chemical shift frequency of ν_1 and ν_2. The slow and fast intermediate exchange regimes are depicted in a and c, respectively. The two peaks coalesce in b when $k = \Delta\nu/2$.

Variable temperature (VT) NMR is a powerful technique that can be used to study the temperature dependence of the lineshape and position of an NMR signal. As described in Section 2.2, many of the interactions that cause relaxation of the signal are temperature dependent. VT NMR can also be used to study temperature dependent phase transitions.[92] Low temperature VT NMR can increase the signal to noise because the spin populations follow a Boltzmann distribution as described by Equation 2.8 and cooling of the sample leads

to increase population of lower energy states. This increases the extent to which the sample can be polarised and therefore enhances the signal.

Cooling and heating of a sample is typically achieved by flowing a gas, usually dry N_2, over the sample, which is inside a rotor. The gas can be cooled by flowing it through a heat exchanger which can be cooled using a refrigeration unit or by immersing it in liquid N_2. Heating is typically achieved using a heating element that is built into the NMR probe. The temperature is determined using a thermocouple which measures the temperature of the gas flow. In practice, the sample temperature is not the same as that of the gas flow with the main reason due to frictional heating resulting from spinning the sample during magic angle spinning (MAS) experiments. The sample temperature is calibrated using references such as KBr, where the chemical shift of the ^{79}Br nucleus is temperature dependent.[93]

In a two-site system, if a nuclear spin is hopping between both environments, then the lineshape will depend on the time that the nucleus spends in each environment. This in turn depends on the motion of the nucleus, which assuming an Arrhenius relation, will be temperature dependent. We can define an exchange rate constant, k, which gives the transition probability per unit time. The effect that the motion has on the lineshape is dependent on k and on the difference in chemical shift of the two environments, $\Delta\nu = \nu_1 - \nu_2$. The NMR lineshape is particularly sensitive to the exchange rate when $k \sim \Delta\nu$ and this is called the intermediate exchange regime.[88] When $k < \Delta\nu/2$, the system is in a slow exchange regime and this is represented by Figure 2.5a. In this regime, both peaks are sharp and separated by $\Delta\nu$. As the temperature and exchange rate increase, the peaks broaden and coalesce at $(\nu_1 + \nu_2)/2$, when $k = \Delta\nu/2$, as shown in Figure 2.5b. The motion leads to an enhancement in the dephasing of the transverse magnetisation which results in the broadening of the lineshape. A further increase in the temperature and exchange rate leads to a narrowing of this motionally-averaged peak when $k > \Delta\nu/2$ and this is called the fast exchange regime and is depicted in Figure 2.5c. The fast exchange means that the nuclear spins experience the same average chemical shift which means the transverse magnetisation dephases more slowly and hence, the peak narrows. This effect is known as motional narrowing.[88]

Chapter 3

^{13}C NMR of Graphite Lithiation

3.1 Abstract

The ^{13}C NMR peak positions for the lithiated graphite stages 3L - 1 were assigned using *ex-situ* ^{13}C NMR and XRD measurements on a Hitachi MAGE3 graphite anode, lithiated during the first discharge cycle in a Li-ion half-cell. The dense stage LiC_{12} and LiC_6 compounds were shown, via ^{13}C and ^{7}Li NMR, to be metallic in nature, with Korringa relaxation being the dominant relaxation mechanism for both nuclei. The change in colour of the samples with increased Li concentration, also confirmed that the dense stage Li-GIC were metallic. The ^{7}Li NMR shifts in graphite can be described by a direct Fermi-contact Knight shift, while the ^{13}C NMR shifts were described by a combination of an anisotropic spin-dipolar and isotropic Knight shift. The isotropic ^{13}C NMR Knight shift of LiC_6, was smaller than expected for a Knight shift caused purely by the core polarisation of 1s-orbitals. This showed that there must be a contribution of 2s-orbitals at the Fermi level. The density of states at the Fermi level, $\rho(E_F)$, for LiC_6 was estimated and the values, which are dependent on the stoner enhancement factor, α, agree reasonably well with those found in literature.

3.2 Introduction

Li intercalated graphite is part of a class of materials known as graphite intercalation compounds (GICs). These materials show interesting properties such as 2D ion conduction and superconductivity.[94] All alkali metals (AM), with the exception of Na, have been shown to form stable binary GICs.[95] This is due to a change in the chemical bonding between the AM and C atoms. Larger AM ions form stronger ionic bonds, for Na ions the formation energy becomes positive and hence a stable binary compound does not form. For Li-GICs, the bond is stabilized by having some covalent character. This difference in the bonding also results in a change in structure of the GIC, where Li-GIC have a LiC_6 structure unlike other AM which show a AMC_8 structure.[96]

As discussed in Chapter 1 NMR is a powerful tool for understanding the local structure and electronic properties of GICs.[29,36,97–103] Much of the NMR studies on lithiated graphite have focused on the ^{7}Li nuclide, presumably because it is more sensitive, having both a higher gyromagnetic ratio and natural abundance than ^{13}C. Conard *et al.*, Maniwa *et al.*, and Vyalikh *et al.*, reported ^{13}C NMR measurements of GICs.[99–103] Conard *et al.*, measured the change in the peak position in the ^{13}C NMR spectra of LiC_6, LiC_{12} and LiC_{18} compounds relative to pure graphite. They attributed this change to either a change in chemical shielding or a Knight shift, or a combination of the two effects. Since both effects are proportional to the number of electrons in the π orbital, they then estimated charge transfer coefficients.[101] More recently, Vyalikh *et al.*, reported ^{13}C NMR measurements of ^{13}C enriched Li intercalated fine-grained graphite. They observed a narrowing of the ^{13}C lineshape when Li was intercalated due to a reduction of the anisotropic magnetic susceptibility as well as the charge transfer from the Li ions to the graphite. However, it is clear from their voltage profiles that the fine-grained graphite behaves differently to battery-grade graphite as they were not able to synthesize either of the dense stage compounds.[103]

Maniwa *et al.* and Pennington *et al.*, have studied the electronic structure and superconducting properties of AM intercalated fullerides ($AM-C_{60}$) via ^{13}C NMR and T_1 relaxation measurements.[82,85,104,105] Maniwa *et al.*, showed that the ^{13}C NMR lineshape of $AM-C_{60}$ could be described by a combination of the chemical shielding, anisotropic spin-dipolar Knight shift and isotropic Knight shift interactions. They calculated both the anisotropic hyperfine coupling tensor and isotropic hyperfine coupling constant for $AM-C_{60}$. These measurements allowed them to predict the electronic band structure at the Fermi level, as well calculate the density of states.[104,105] The electronic structure of Li-GIC shares some similarities with these materials,[86,100] Though the only Li-GIC compound that exhibits su-

perconductivity is LiC_2, which only forms at high pressure.[94,106] The conduction band in $AM-C_{60}$ consists of mainly p_z-orbitals with some admixture $(1.3\% - 4.2\%)$ of s-orbitals into the p_z-orbital due to the curvature of the C_{60} structure. In LiC_6 the conduction band also mainly consists of p_z-orbitals, with a small contribution of the Li $2s$-orbitals.[86]

In this work ^{13}C and ^{7}Li NMR measurements were performed on a high performance, battery-grade graphite, with Li-GIC samples prepared electrochemically, so that any results deduced from the measurements can accurately reflect our understanding of graphite in LIB anodes. Using a combination of variable temperature (VT) NMR and relaxation measurements, we provide a more complete description of the NMR interactions in Li-GICs and show that the ^{13}C NMR shifts in lithiated graphite can be described via a combination of the spin-dipolar Knight shift, otherwise known as the anisotropic Knight shift, an isotropic Knight shift and a chemical shift. The theory underpinning these Knight shift interactions were described in Sections 2.1.3 and 2.2.4. ^{13}C NMR measurements are used to probe the electronic structure of lithiated graphite and give insight into the degree of charge transfer between the Li ion and the graphite host structure. We show that ^{13}C NMR can also be used to identify and quantify the different stages present in a sample.

3.3 Experimental Methods

3.3.1 Materials

Graphite electrodes were fabricated and provided by the Argonne National Laboratory Cell Analysis, Modeling, and Prototyping (CAMP) facility. The graphite electrodes were composed of 91.83 wt% graphite powder (Hitachi MAGE 3), 2 wt% carbon black (Timcal C45), 6 wt% PVDF binder (Kureha 9300) and 0.17 wt% oxalic acid. The mass loading of the graphite active material is 5.83 mg/cm^2. The graphite electrodes were punched into 15 mm circular disks and dried under dynamic vacuum (10^{-2} mbar) in a Büchi oven at 120° C for at least 12 hours. Once cooled to room temperature, the dried electrodes were then transferred into an Ar atmosphere glovebox ($O_2 \leq 1$ ppm, $H_2O \leq 1$ ppm) for battery assembly. Two separators were used, Celgard 3501, which was punched into 17 mm disks, washed in ethanol and then dried under vacuum at 40 °C for 12 hours, and a 16 mm glass microfibre separator (Whatman). 1 M $LiPF_6$ in ethylene carbonate/ethyl methyl carbonate 3/7 wt:wt (LP57, SoulBrain MI) with 2wt% vinylene carbonate (VC) was used as the electrolyte.

3.3.2 Battery Assembly and Cycling

Graphite half-cells were assembled using 2032 coin cells (Cambridge Energy Solutions) with 15 mm graphite disks, 16 mm lithium chips (Cambridge Energy Solutions) and 180 µL of electrolyte. The Celgard separators were placed between the graphite anodes and the glass fibre separators since they are more inert than the borosilicate glass fibres which, at low voltages, can react with lithiated graphite making battery disassembly difficult. The glass fibre separators were necessary to ensure optimum electrolyte volume and mechanical pressure to homogeneously lithiate the graphite electrodes. Before cycling, the cells were rested at their open circuit voltage (OCV) for a minimum of two hours. The cells were then cycled a rate of C/50, calculated using a theoretical capacity of graphite of 372 mAh/g, using a constant current cycling protocol. For samples prepared for *ex-situ* characterisation, cells were stopped at the desired voltage during the first discharge. For the fully lithiated sample a voltage hold step was implemented after the cut off voltage was reached.

3.3.3 XRD

Powder X-ray diffraction measurements were performed with CuKa(α) radiation (λ = 154.06 pm) at 296 K on a Panalytical Empyrean diffractometer equipped with a Ni filter

and operating under a Bragg-Brentano geometry. Diffraction measurements were carried out to confirm the stages present in the samples prepared for solid-state NMR (ssNMR) measurements. Samples were prepared by disassembling cells and placing them in an air-tight sample holder using Kapton film. For the dense stage samples one electrode was used. While for the dilute stage samples the electrode was cut in half with one half measured via XRD and the other half measured via ssNMR.

3.3.4 ssNMR

Graphite electrodes for ssNMR measurements were electrochemically cycled in half-cells against lithium metal at C/50 until the desired state of charge was reached. The slow cycling was performed to ensure the electrode was homogeneously lithiated. The electrodes were then extracted from the cells and rinsed with 1 mL of DMC to remove residual electrolyte before drying under vacuum for 5 min. The lithiated graphite was then scraped from the copper current collector, diluted with approximately equal amounts of KBr to help with sample spinning, and packed into 4 mm rotors. Four electrodes (15 mm diameter discs) were used to fill each rotor. ^{13}C and ^{7}Li measurements were performed on a 16.4 T magnet ($\nu_0(^1\mathrm{H}) = 700.13$ MHz, $\nu_0(^7\mathrm{Li}) = 272.10$ MHz, $\nu_0(^{13}\mathrm{C}) = 176.05$ MHz) equipped with a Bruker Avance IIIHD spectrometer. A 4 mm Bruker double resonance probe was used with 10 kHz MAS frequency. A rotor-synchronized Hahn-echo pulse sequence was used with a recycle delay that was 5 at least times T_1 to allow for quantitative analysis. Static ^{13}C measurements were also performed so that the CSA parameters could be determined. Simulations of the static spectra were performed using the SOLA function in TopSpin. The ^{13}C chemical shifts were referenced to tetramethylsilane (TMS) using the CH_2 peak in glycine as a secondary reference at 43.7 ppm.[107] The ^{7}Li chemical shifts were referenced to 1 M LiCl in H_2O at 0 ppm. Pulse power calibrations were performed on the Li-GIC samples since the 90° pulse lengths changed significantly from the reference samples due to skin-depth effects as the Li-GIC samples becomes more conductive as more Li is intercalated.

For the dilute stage samples, because of the very small differences in voltage (< 5 mV) and capacity for some of the phase transitions resulting in small variations between cells, it was found to be easier to homogeneously lithiate a smaller volume of graphite to a single stage. For this reason, to identify the ^{13}C shifts of dilute stages, a single electrode was cut in half with half packed into a 1.3 mm rotor and the other half of the same electrode measured via XRD. Static and MAS (50 kHz) measurements were performed using a Carr-Purcell Meiboom-Gill (CPMG) pulse sequence.[108]

Both ^{13}C and ^{7}Li spin-lattice relaxation times, T_1, were recorded using a saturation recovery pulse sequence under 10 kHz MAS. ^{13}C T_1 measurements were also performed at variable temperatures (293 K - 353 K) to determine the Korringa constant for each sample. The sample temperature was determined using an *ex-situ* calibration with the temperature-dependent ^{79}Br NMR shift of KBr.[93] Static ^{13}C spin relaxation measurements were also performed to determine the extent to which the dipolar hyperfine mechanism affects the observed relaxation rate, both in terms of its anisotropy and its effect on the total MAS relaxation rate.

For the room temperature ^{13}C NMR spectra of pure graphite, a CPMG pulse sequence was used to acquire enough signal in a reasonable time (72 hrs) due to the long T_1 times ($\sim$90 s) observed in graphite as well as the low natural abundance of ^{13}C (1.109%)..[109] The measurements was carried out on 4.7 T magnet ($\nu_0(^1\mathrm{H} = 200.13$ MHz, $\nu_0(^{13}\mathrm{C} = 50.3$ MHz) equipped with a Bruker Avance III spectrometer using a 14 mm Chemagnetics double resonance probe under static conditions with a 90 s recycle delay.

3.4 Results and Discussion

3.4.1 Electrochemistry

Figure 3.1 shows the potential profile of a Hitachi Mage3 graphite half-cell cycled at C/50 between 2 and 0.005 V. In the first cycle, the discharge and charge capacities, with respect to the mass of graphite, were 408.5 and 373.7 mAh/g, respectively, resulting in an ICE of 91.5%. In the following 2 cycles, the CE increased to 98.8% and 99.2%. There are two reasons the capacity is larger than the theoretical capacity of 372 mAh/g. First is the capacity from the C45 carbon black. See et al. showed that Super P, which has a similar structure and surface area to C45, has a discharge capacity of 485 ± 28 mAh/g mostly from solid electrolyte interphase (SEI) formation on the high surface area particles.[110,111] This means the C45 could contribute up to 9 mAh/g in the first cycle. Second is the capacity occurring from the initial SEI formation on the graphite surface.[112] The extra capacity (30 mAh/g) from SEI formation occurs largely between 0.8 and 0.2 V in the first cycle. Since graphite forms a stable SEI layer, any capacity from SEI formation in subsequent cycles in less visible than in the first cycle.[113]

Figure 3.2a and 3.2b show the potential profile as a function of stoichiometry, x, and differential capacity as a function of voltage. The potential profile in Figure 3.2a is corrected so that the capacity is only due to lithium intercalated into graphite and any capacity due to SEI formation has been subtracted. This was done by assuming that all the irreversible capacity seen in Figure 3.1 (34.8 mAh/g) occurred before any of the graphite was lithiated. This capacity which corresponded to $x = 0.09$ was taken away from the total capacity shown in Figure 3.2a so that the potential profile begins at $x = -0.09$.

The five points in both Figures 3.2a and 3.2b represent the samples that were characterised by both *ex-situ* NMR and XRD. Cells were stopped at the five points along the voltage profile shown in both Figure 3.2a and 3.2b. These points are at 145, 120, 105, 75 and 1 mV and their x values are 0.14, 0.19, 0.25, 0.51 and 1, respectively. The first three points correspond to compositions of LiC_{43}, LiC_{31} and LiC_{24}. The latter two points represent stages LiC_{12} and LiC_6, or dense stages 2 and 1.

To fully form the dense stage 1 compound, a voltage hold at 1 mV was necessary otherwise around 8% of the dense stage 2 compound remained in the sample (see Figure A1). This was done in five successive 10 hour increments from 5 mV down to 1 mV so as to prevent lithium metal plating. Two ssNMR samples were made with nominal compositions LiC_{31}. One sample consisted of four 15 mm diameter electrodes packed into a 4 mm rotor

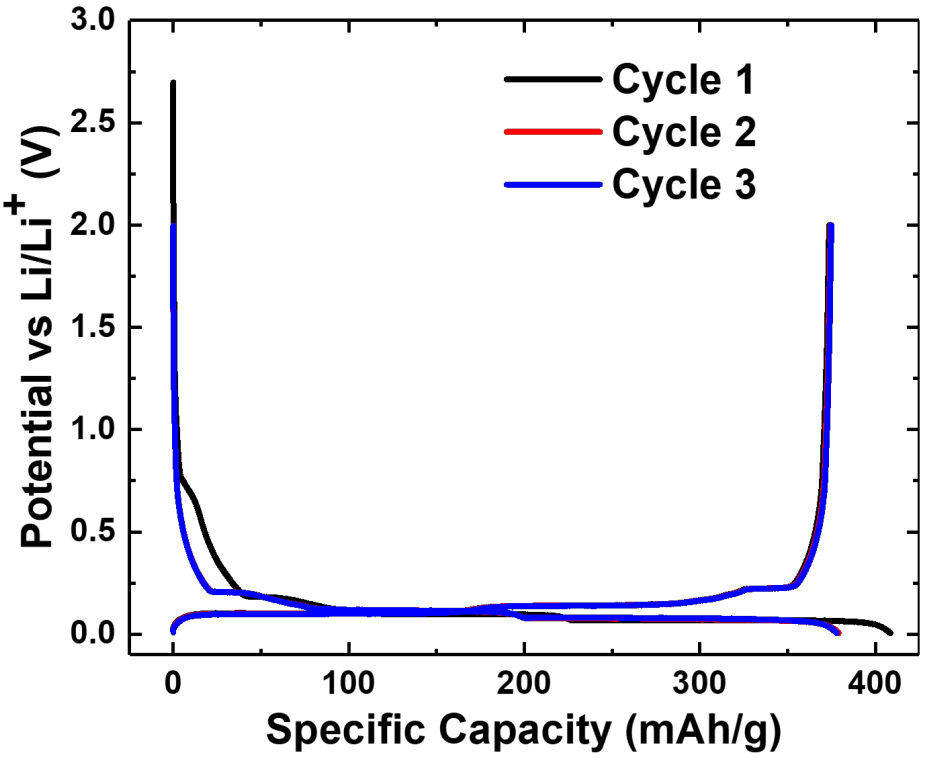

Figure. 3.1 Potential profile of the first three cycles of a Hitachi Mage3 graphite cell cycled galvanostatically between 0.005 - 2 V.

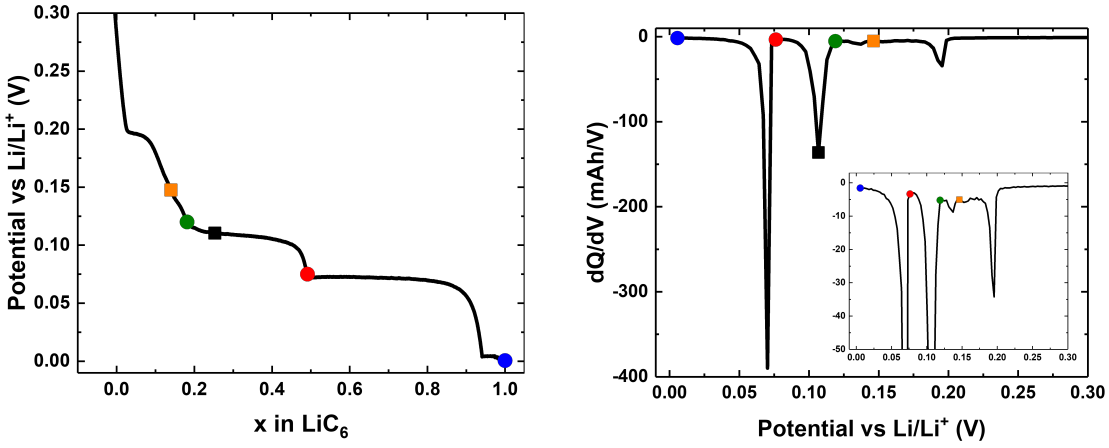

Figure. 3.2 a) Potential profile as function of capacity x, where x represents Li_xC_6. The irreversible capacity due to SEI formation has been accounted for. b) Differential capacity plot as a function of voltage. The points in a and b represent the points at which cells were stopped for *ex-situ* XRD and NMR characterisation. □ points represent samples that were only measured in 1.3 mm rotors using MAS NMR whilst ○ represent those that were measured in a 4 mm rotor with VT, static and MAS NMR.

while the other consisted of one half of an electrode packed into a 1.3 mm rotor. These will now be referred to as LiC_{31}a and LiC_{31}b, respectively.

3.4.2 Optical Images

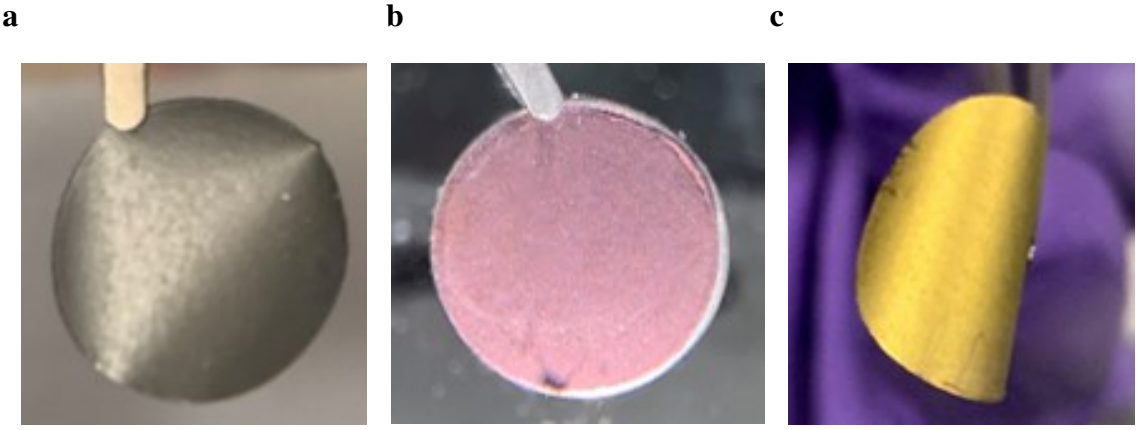

Figure. 3.3 Photographs of a) LiC_{31}, b) LiC_{12} and c) LiC_6 Hitachi Mage 3 graphite electrodes cycled in half-cell configuration and then disassembled.

It is well reported in the literature that Li-GIC stages exhibit distinct colours.[114,115] Figures 3.3a, 3.3b and 3.3c show photographs of Hitachi Mage 3 graphite electrodes discharged to LiC_{31}, LiC_{12} and LiC_6, respectively. LiC_{31} is grey, the same colour as pure graphite. LiC_{12} and LiC_6 are red and gold, respectively. These colours confirm that LiC_{12} and LiC_6 correspond to the stage 2 and 1 Li-GIC compounds respectively.[115] The colour changes can be understood through the Drude model of electrical conduction which can predict the response of conduction electrons to an electromagnetic wave. When an electromagnetic wave is incident on the Li-GIC, it induces a charge density oscillation known as a plasmon, which oscillates at a characteristic frequency known as the plasma frequency which is given by

$$\omega_p = \sqrt{\frac{ne^2}{\varepsilon_0 m^*}} \tag{3.1}$$

where n is the number density of electrons, e is the charge of an electron, ε_0 is the permittivity of free space and m^* is the effective mass of the electrons.[116] An electromagnetic wave that has a frequency below the plasma frequency will be reflected while light above this frequency will penetrate the sample. From Figure 3.3, we can see that the wavelength of the

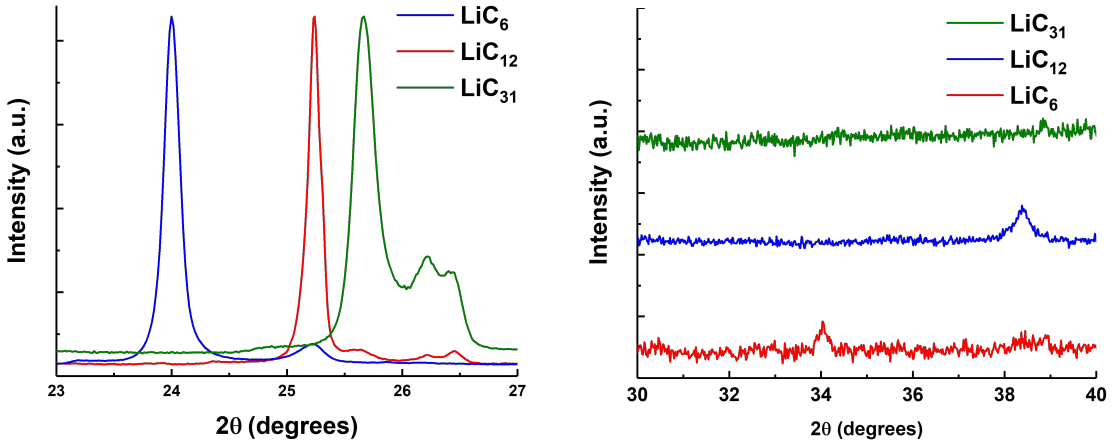

Figure. 3.4 XRD patterns showing the change in the a) 002 peak and b) superlattice peak position for the LiC_6, LiC_{12} and LiC_{31} compounds. The intensity was normalised with respect to 002 peak for all samples.

reflected light decreases, and hence the frequency increases, with increasing Li intercalated into the graphite. From Equation 3.1 we can show that this increase in the plasma frequency is caused by an increase in the electron density.

3.4.3 XRD

Table 3.1 002 peak position and corresponding *d* spacing according to Bragg's Law as well as the peak position and FWHM of the superlattice peak and the correlation length (CL) according to Equation 3.2 of the prepared Li-GIC compounds.

Voltage (mV)	**Formula**	**x in Li_xC_6**	**002 peak**	**d (Å)**	**Superlattice peak**	**FWHM**	**CL (Å)**
145	LiC_{43}	0.14	26.53	3.357			
120	LiC_{31}	0.19	25.68	3.466			
105	LiC_{24}	0.25	25.21	3.530	38.17	0.54	153
			25.43	3.500	34.74	0.58	142
75	LiC_{12}	0.51	25.23	3.527	38.38	0.41	203
1	LiC_6	1.0	24.00	3.705	34.05	0.27	304

The (002) peak gives a measure of average spacing between the graphene layers. The peak shift towards lower angles, seen in Figure 3.4a, is a result of increased layer spacing due to the intercalation on Li between the layers. The superlattice peaks, shown in Figure 3.4b between $30° \leq 2\theta \leq 40°$, can be used to determine the stage number.[24] The Miller indices

for the $(00l)$ for the superlattice peaks for a stage-n compound are given by $l = n+1$. When applying the Scherrer equation,

$$\mathrm{CL} = \frac{0.89\lambda}{\beta \cos(\theta)} \tag{3.2}$$

to a superlattice peak it can be used to estimate the correlation length (CL) of the stages perpendicular to the (00l) plane. Here β is the full width at half maximum (FWHM) of the superlattice peak with a Bragg angle θ measured in radians.[24]

A comparison of the 002 peak positions presented in this work (Table 3.1) to those of Zheng *et al.*, shows that the dilute stage LiC_{31}b sample corresponds to the stage 3L Li-GIC.[24] While Figure A2 and A4 show that the LiC_{24} sample is composed of a mixture of stage 3L and 2L. These can be distinguished by both the 002 and superlattice (SL) peak position at $2\theta_{002} = 25.43^{\circ}$ and $2\theta_{002} = 25.21^{\circ}$ and $2\theta_{SL} = 34.74^{\circ}$ and $2\theta_{SL} = 38.17^{\circ}$. The 002 peak positions for the dense stages also matches well to previously reported measurements.[117]

3.4.4 ^{7}Li NMR

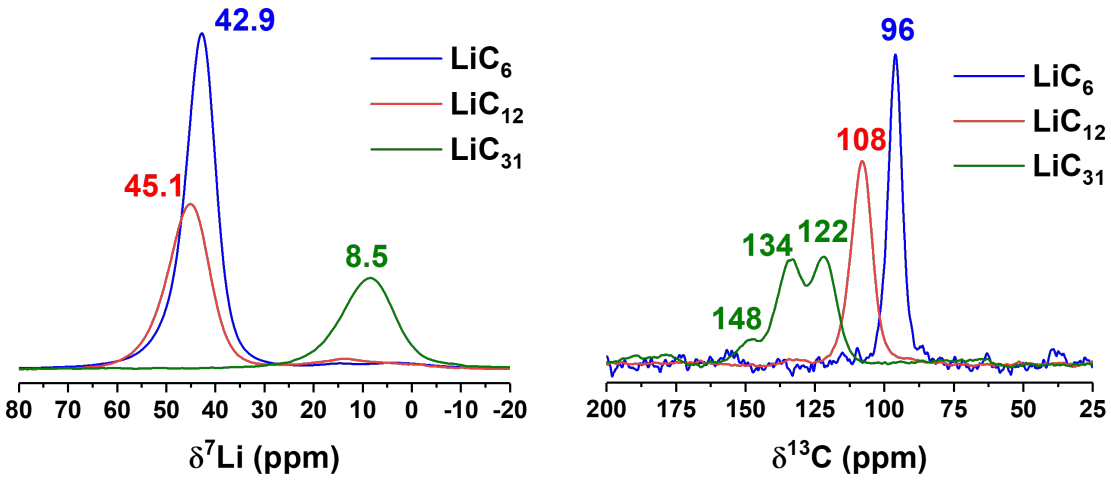

Figure. 3.5 a) ^{7}Li and b) ^{13}C MAS spectra of the LiC_6, LiC_{12} and LiC_{31} compounds. Samples were measured in a 4 mm rotor with a MAS of 10 kHz and a recycle delay that was at least five times T_1.

The ^{7}Li isotropic chemical shifts, shown in Figure 3.5a, are 8.5, 45.1 and 42.9 ppm for LiC_{31}, LiC_{12} and LiC_6, respectively. These shifts agree reasonably well with previously studies by Letallier *et al.*[29,97] The integrated intensities of the LiC_{31} and LiC_{12} peaks compared

to LiC_6 are 45% and 64% respectively. The intensities are slightly higher than expected from the values of x in Li_xC_6. Since we have tried to account for the irreversible capacity, assuming it was equal for all samples, these discrepancies suggest that irreversible reactions continue until 1 mV.

The Fermi contact interaction is important in understanding the shifts observed in lithium metal where the conduction band lies in the 2*s* orbital band. For the dilute stages, the shift lies within the diamagnetic shift range for ^{7}Li whereas the larger shifts seen in the dense stages are due to the Knight shifts. If we assume a linear relationship between the oxidation state and the size of the Knight shift, where Li metal has a charge of 0 and $\delta = 260$ ppm[118] and we take the shift of a Li-ion with charge $+1$ to be $\delta = 0$ ppm, then we can estimate a charge on the Li atom of $+0.84$ and $+0.83$ for dense stage 1 and 2 respectively. It then follows that each carbon atom will have a charge of -0.14 and -0.138 respectively.

3.4.5 ^{13}C NMR

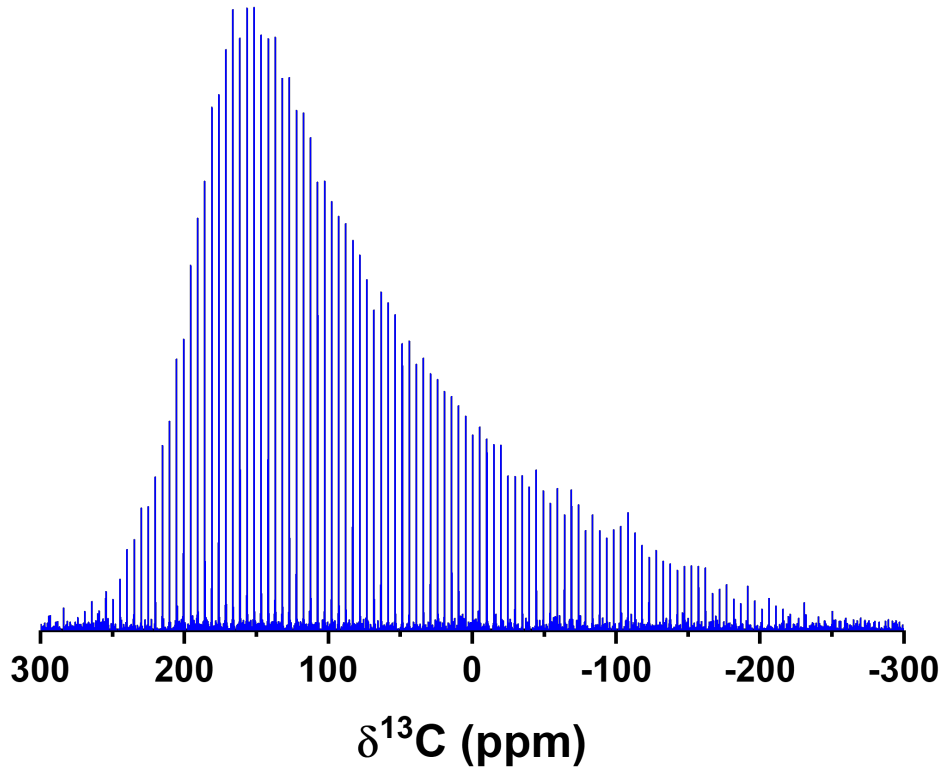

Figure. 3.6 Static ^{13}C CPMG NMR spectra of the pure Hitachi Mage 3 graphite.

Figure 3.6 shows the the static spectrum of the pristine Hitachi MAGE3 graphite powder. The breadth of the static experimental lineshape is denoted by the span, which is defined as $\Omega_\xi = \xi_{11} - \xi_{33}$, where $\ddot{\boldsymbol{\xi}}$ is a tensor that describes the experimental shift. In pristine graphite Ω_ξ = 500 ppm, this large value is in part caused by CSA; however, the lineshape can not be fit by a typical CSA pattern. This is due to the large magnetic susceptibility of graphite in the direction parallel to the *c*-axis of graphite which results in a large demagnetizing field that causes a shift to lower frequencies for graphite particles where the magnetic field is aligned along this same axis.[119,120]

The ^{13}C isotropic shifts, shown in Figure 3.5b, are at 96 and 108 ppm for the LiC_6 and LiC_{12}, respectively. The LiC_{31}a compound showed three peaks at 148, 134, 122 ppm. The total integrated intensities of the ^{13}C NMR signal for the three compounds remains almost constant confirming that all carbon nuclear spins can be excited in all samples. The intensities of the LiC_{31}a peaks relative to LiC_6 are 11%, 44% and 45% whilst for LiC_{12} it is 80%. The deviation from 100% for LiC_{12} is likely due to an inaccuracy in the way the sample was diluted with KBr. Further discussion on the dilute stages will be given in Section 3.4.6

The measured ^{13}C T_1 values, shown in Table 3.2, decrease with increasing lithium content. The values are much lower than in pure graphite where the T_1 is at least 90 s.[109,120] Figure 3.7 shows temperature multiplied by T_1 as a function of temperature for LiC_6, LiC_{12} and the two peaks at 122 ppm and 134 ppm in the LiC_{31}a sample. The data can be fit by with a linear equation where the slope does not vary significantly from 0. Since the isotropic shift does not change with temperature this shows that Korringa relaxation is the dominant mechanism. Fixing the slope to 0, the intercept for LiC_{12} and LiC_6 are 363 $\pm$ 7 sK and 223 $\pm$ 7 sK, respectively. Whilst for the two peaks at 122 and 134 ppm in LiC_{31}a, the intercept is 817 $\pm$ 40 sK and 963 $\pm$ 32 sK. For the two peaks in LiC_{31}a, the higher uncertainty indicates that there may be an additional mechanism driving relaxation such as motion of the lithium ions within the graphite galleries. At higher temperature there is a slight decrease and increase in the value of TT_1 for the peak at 122 ppm and 134 ppm respectively. This could be due to the rearrangement of Li-ions within the graphite that occurs above 320 K in dilute stage graphite compounds. This motion will be further investigated in the following chapter.

Interestingly, given that the ^{7}Li nuclide is quadrupolar, we find that the T_1 values are lower for ^{13}C than for ^{7}Li in all compounds where this was measured. Since Korringa relaxation is the dominant mechanism for both the ^{7}Li (Figure 4.14) and ^{13}C (Figure 3.7) nuclei, for the dense stage Li-GICs, the trend in the T_1 values provide further evidence that more charge is localised near the carbon nuclei.

Table 3.2 Observed shifts and spin-lattice relaxation times for ^{7}Li and ^{13}C nuclei for the Li-GIC compounds.

Formula	^{7}Li		^{13}C	
	δ_{iso} (ppm)	T_1(s)	δ_{iso} (ppm)	T_1(s)
LiC_{31}	8.5 ± 2	7.91	$122 \pm 2, 134 \pm 2, 148 \pm 2$	$3.0 \pm 0.3, 2.7 \pm 0.2, 5.0 \pm 1.0$
LiC_{12}	45.0 ± 1	2.034	108 ± 2	1.21 ± 0.05
LiC_6	42.8 ± 1	1.685	96 ± 2	0.71 ± 0.07

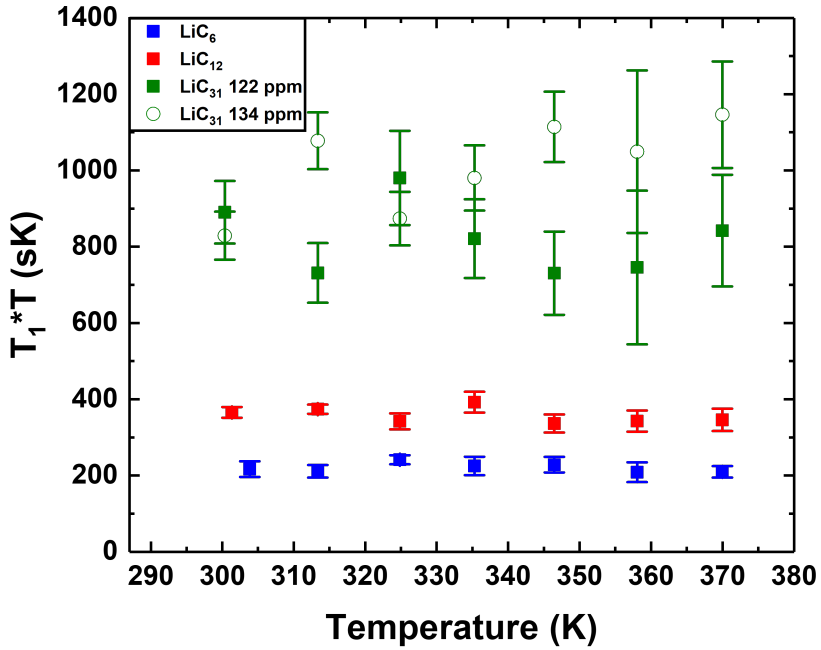

Figure. 3.7 ^{13}C T_1 multiplied by temperature, T, as a function of temperature for the lithiated graphite compounds.

Room temperature, static ^{13}C NMR spectra, shown in Figures 3.8, 3.9a and 3.9b were measured to determine an experimental shift tensor for the Li-GICs. For LiC_6, the principal components of the experimental shift tensor are $\xi_{11} = 141 \pm 3$ ppm and $\xi_{22} = \xi_{33} = 73 \pm 2$ ppm. An accurate simulation of the ^{13}C powder pattern for LiC_6 was found by including a 0.7% contribution of the LiC_{12} phase to the fit. Figure A1 shows the static ^{13}C NMR spectrum of a sample that was discharged to only 5 mV instead of 1 mV. The fraction of the LiC_{12} phase present in the 5 mV sample is 8%, thus confirming the need for the voltage hold to obtain a phase-pure compound. For LiC_{12}, the principal components of the experimental shift tensor are $\xi_{11} = 116 \pm 1$ ppm and $\xi_{22} = \xi_{33} = 104 \pm 1$ ppm. We define the skew $\kappa = 3(\xi_{22} - \xi_{iso})/\Omega_\xi$. For both LiC_6 and LiC_{12}, $\kappa = -1$ and the span $\Omega_\xi = 68 \pm$

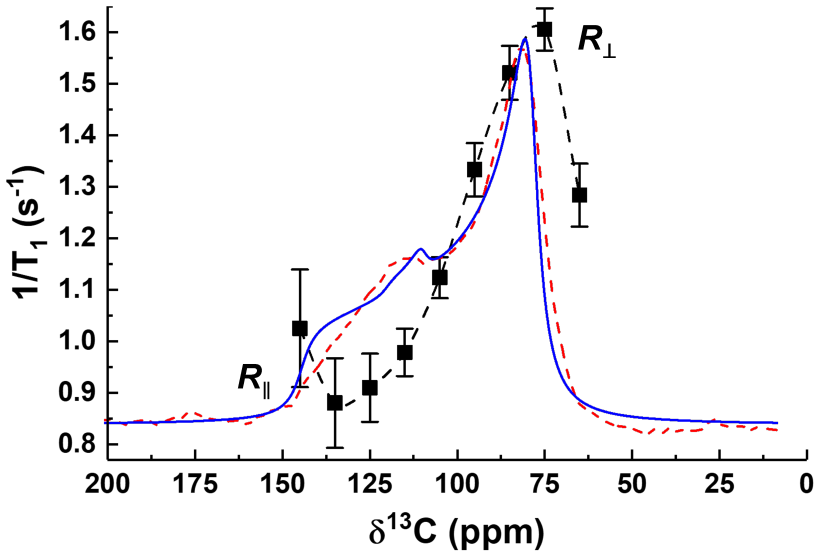

Figure. 3.8 Experimental static ^{13}C NMR powder pattern (blue trace) and simulated spectrum (red trace) for LiC_6. The relaxation rate, $1/T_1$, as a function of chemical shift is overlayed on top of the spectrum.

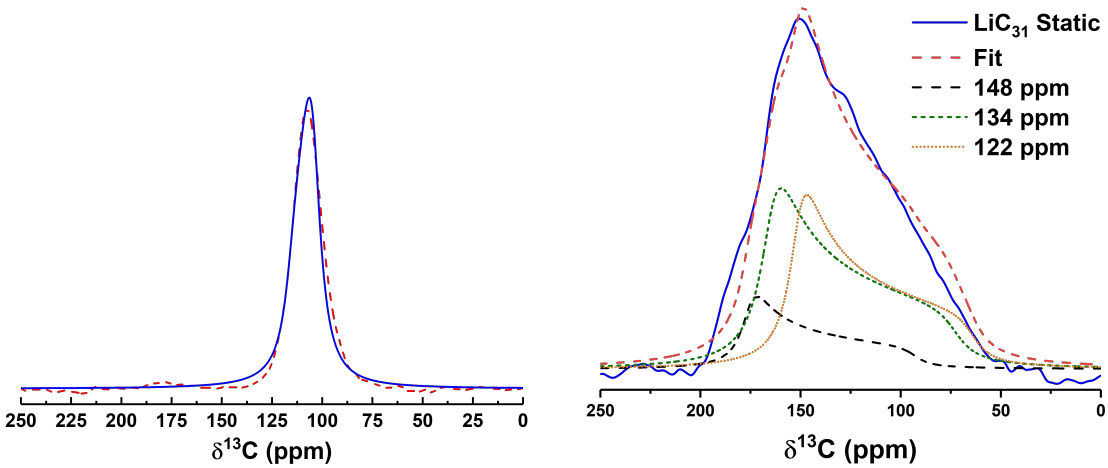

Figure. 3.9 Experimental static ^{13}C NMR powder pattern (blue trace) and simulated spectrum (red trace) for a) LiC_{12} and b) LiC_{31}.

5 ppm and $\Omega_\xi = 12 \pm 2$ ppm, respectively. For LiC_{31}a, three peaks were observed in Figure 3.5b the principal components of the experimental shift tensor are summarised in Table 3.3. All spectra were fit by confining the isotropic shift to the values measured in the MAS experiments as well as assuming an axially symmetric tensor *i.e.* that $\kappa = \pm 1$.

The large change in the anisotropy of the lineshape, with κ changing from $+1$ in pure graphite to -1 in LiC_6, is due to the doping of electrons into graphite to balance the charge

of the Li ions as they intercalate. These electrons then interact with the ^{13}C nuclei via the spin-dipolar hyperfine interaction which results in an anisotropic Knight shift as described by Equation 2.29.

Since the Fermi level in Li-GIC is in the p_z-orbital, the spin-lattice relaxation rate is expected to be dominated by the spin-dipolar mechanism.[91,121,122] Using Equation 2.47 we can use the values of TT_1 from Figure 3.7 for each compound to calculate the anisotropic part of the Knight shift tensor, $\ddot{\boldsymbol{K}}$. If we assume at this point, that the Knight shift is due purely to the spin-dipolar effect then from Equation 2.48 it follows that $\ddot{\boldsymbol{K}}$ will be traceless and $2K_{11} = K_{22} = K_{33}$. It is then possible to calculate a chemical shift tensor $\ddot{\boldsymbol{\delta}}$, such that

$$\ddot{\boldsymbol{\xi}}_{\mathbf{Li_xC_6}} = \ddot{\boldsymbol{\delta}} + \ddot{\boldsymbol{K}} \tag{3.3}$$

where $\ddot{\boldsymbol{\xi}}_{\mathrm{Li_xC_6}}$ is the tensor derived from the experimentally observed pattern. Here we assume that the Knight shift tensor and the chemical shift tensor are co-linear. The Knight shift and chemical shift tensor components for LiC_{31}a, LiC_{12} and LiC_6 are summarised in Table 3.3

The span, Ω_ξ, decreases relative to that of pristine graphite as more lithium is intercalated until the LiC_{12} phase is reached. For the LiC_6 compound, Ω_ξ increases again but with κ changing sign. The reduction in the span is not only due to the spin-dipolar Knight shift, but also due to the reduction of the diamagnetic susceptibility. Mukai *et al.,* showed that the initially large diamagnetic susceptibility of graphite decreases with increasing content, eventually becoming weakly paramagnetic for $x \geq 0.5$ in Li_xC_6.[123]

We can take another approach and calculate the expected Knight shift using the spin-dipolar interaction. Figure 3.8 shows a static spectrum for LiC_6 overlayed with the relaxation rate measured using a static saturation recovery experiment. From Equation 2.48 we can see that the spin-lattice relaxation rate should have an angular dependence such that $R_\perp = 2.5R_\parallel$. Here we define $R_\perp$ and $R_\parallel$ as the relaxation rate for the case when the magnetic field is perpendicular and parallel to the p_z-orbital. By separating the static lineshape into 10 ppm wide columns and finding the relaxation rate for each column, we can determine the angular dependency of T_1. For the LiC_6 sample, we find that $R_\perp = 1.8R_\parallel$. The fact that $R_\perp \neq 2.5R_\parallel$ means there must be some source of relaxation that is isotropic, we denote this term R_{iso}.

If we take these mechanisms to be additive, then we can separate out the contribution of the isotropic relaxation process from the relaxation that is caused purely from the spin-dipolar mechanism

Table 3.3 The experimental span Ω_ξ, skew κ and chemical shift tensor components, Knight shift tensor components calculated using the Korringa relation and the experimental relaxation measurements, and the calculated chemical shielding tensor components from Equation 3.3 for the LiC_{31}a, LiC_{12} and LiC_6 compounds.

Formula	Span[a] (ppm)	Skew[b]	Experimental (ppm)			Knight Shift (ppm)			Chemical Shift[c] (ppm)		
	Ω_ξ	κ	ξ_{11}	ξ_{22}	ξ_{33}	K_{11}	K_{22}	K_{33}	δ_{11}	δ_{22}	δ_{33}
LiC_{31} (148 ppm)	83 ± 19	1	176 ± 9	176 ± 9	93 ± 17						
LiC_{31} (134 ppm)	92 ± 7	1	165 ± 3	165 ± 3	73 ± 6	-47 ± 1	-47 ± 1	93 ± 1	212 ± 3	212 ± 3	-20 ± 6
LiC_{31} (122 ppm)	87 ± 9	1	151 ± 4	151 ± 4	64 ± 8	-50 ± 1	-50 ± 1	100 ± 3	201 ± 4	201 ± 4	-36 ± 9
LiC_{12}	12 ± 1	-1	116 ± 1	104 ± 1	104 ± 1	151 ± 1	-76 ± 1	-76 ± 1	-35 ± 1	180 ± 2	180 ± 2
LiC_6	68 ± 4	-1	141 ± 3	73 ± 2	73 ± 2	194 ± 3	-97 ± 1	-97 ± 1	-53 ± 4	170 ± 2	170 ± 2

[a]The span of the experimental shift tensor is defined as $\Omega_\xi = \xi_{11} - \xi_{33}$ with $\xi_{11} \geq \xi_{22} \geq \xi_{33}$.
[b]The skew of the experimental shift tensor is defined as $\kappa = 3(\xi_{22} - \xi_{\text{iso}})/\Omega_\xi$.
[c]The convention for $\ddot{\boldsymbol{\delta}}$ is such that each component δ_{11}, δ_{22} and δ_{33} points in the same axial direction as ξ_{11}, ξ_{22} and ξ_{33} respectively.

$$\frac{R_\perp}{R_\parallel} = \frac{R_{\text{iso}} + R_{\text{dip}\perp}}{R_{\text{iso}} + R_{\text{dip}\parallel}}. \tag{3.4}$$

We then find that the powder averaged spin-dipolar relaxation rate for the LiC_6 sample is $R_{\text{dip}} = 1.0\pm\ 0.1\,\text{s}^{-1}$ and $R_{\text{iso}} = 0.4\pm\ 0.2\,\text{s}^{-1}$. With this value for R_{dip}, we can then use Equation 2.47 to re-calculate the Knight shift tensor, $\ddot{\boldsymbol{K}} = (169\pm8, -84\pm4, -84\pm4)$ ppm. Following the same procedure as before we can then calculate the chemical shift tensor, $\ddot{\boldsymbol{\delta}} = (-28\pm8, 157\pm4, 157\pm8)$ ppm. The same procedure cannot be applied to the other compounds as the lineshape is too narrow for LiC_{12} and the static T_1 value is difficult to measure for dilute samples due to the broad overlapping peaks.

The span of the chemical shift tensor, as defined by the Herzfeld-Berger notation, for LiC_6, $\Omega_{\ddot{\boldsymbol{\delta}}} = 185$ ppm, matches closely to the chemical shift tensor predicted by DFT calculations for an isolated graphene sheet, $\Omega_{gr} = 185$ ppm ($\ddot{\boldsymbol{\delta}}_{gr} = (195, 195, 10)$ ppm), as well as the measured chemical shift tensor for inner carbon in corannulene molecule, $\Omega_{cor} = 180$ ppm ($\ddot{\boldsymbol{\delta}}_{cor} = (195, 195, 15)$ ppm), both of which should have similar chemical shielding to that of the carbon atoms in LiC_6.[78,124,125] We can see from these results that the isotropic shift of LiC_6, $\delta_{\text{iso}} = 96$ ppm, relative to pure graphite, 133 ppm, and the chemical shift tensor relative to graphene and corannulene is shifted to lower values by around 37 ppm. This negative shift could arise due the core polarisation effect and this effect may also be causing the observed

isotropic relaxation. The same effect might be causing the trend in shifts towards lower ppm with increasing lithium intercalation.

Following a similar treatment that Sato *et al.*, applied to C_{60} superconductors, we can obtain the hyperfine coupling constants as well as estimate the density of states at the Fermi level for LiC_6.[104] First, the anisotropic hyperfine coupling tensor, (d_{11}, d_{22}, d_{33}), can be calculated using the tensor derived from the spin-dipolar effect such that

$$K_i = \left(\frac{d_{ii}}{\gamma_e \gamma_n \hbar^2}\right) \chi_s \qquad (i = 1,2,3) \tag{3.5}$$

and the isotropic hyperfine coupling constant, a_{iso}, is given by

$$K_{\mathrm{iso}} = \left(\frac{a_{iso}}{\gamma_e \gamma_n \hbar^2}\right) \chi_s. \tag{3.6}$$

Here we use the value of $\chi_s = 8.69 \times 10^{-29}$ cm^3 per carbon atom measured by Ikehata *et al.*, with ESR and NMR at 300 K, employing the technique of Schumacher and Slichter to calculate the Pauli spin susceptibility.[126,127] It then follows that $d_{33} = d_{22} = -d_{11}/2 = -2.01 \times 10^{-8}$ eV and $a_{\mathrm{iso}} = d_{33}/2.27 = -8.85 \times 10^{-9}$ eV. In the case of no admixture of *s*-orbitals into the Fermi level, only core polarisation of the 1*s*-orbitals by 2*p*-orbitals is possible, and $a_{\mathrm{iso}} = -1.5 \times 10^{-7}$ eV, as was shown by Karplus and Fraenkel.[128] Since the value of a_{iso} from Equation 3.6 is smaller than this, we must then consider that there may be some contribution of *s*-orbitals at the Fermi level. These contributions could come through a contribution of 2*s*-orbitals into the density of states at the Fermi-Level which would lead to a positive direct Fermi-contact Knight shift. Another possibility is through the core polarisation of 2*s*-orbitals by the 2*p*-orbitals. Since the orbital radius of 2*s*-orbitals are larger than 2*p*-orbitals the shift is expected to be positive. In principle, a change in the chemical shift compared to pristine graphite could be expected as more Li is intercalated. However as we show in the following section this not thought to change significantly between the stages.

Using χ_s and Equation 2.29 for the dipolar Knight shift we find $(1/r^3)$ which gives the average distance between the nucleus and the electron spin over the conduction electron wavefunction normalized in the LiC_6 unit cell at the Fermi level. From the anisotropic Knight shift tensor $\ddot{\boldsymbol{K}} = (169 \pm 8, -84 \pm 4, -84 \pm 4)$ ppm it then follows that $(1/r^3) = 0.36 a_B^{-3}$ where a_B is the Bohr radius. This compares to $(1/r^3) = 1.7 a_B^{-3}$ for a p_z-orbital in a free carbon atom.

The contribution of the 2*s*-orbitals to the wavefunction at the Fermi level can be estimated by assuming that the wavefunction is a linear combination of $2p_z$ and 2*s*-orbitals. Taking a similar approach as before, but instead using Equation 2.25 and χ_s with $K_{\text{iso}} = -37$ ppm, we find $\langle|\psi_s(0)|^2\rangle_{E_F} = 7.5 \times 10^{-3} a_B^{-3}$. For a 2*s*-orbital in a free carbon atom the value is $2.767 a_B^{-3}$. Taking a ratio of these gives an estimate of the contribution of 2*s*-orbitals at the Fermi level, 0.27%. We must however consider the contribution of the core polarisation of 1*s*-orbitals. We can separate the isotropic hyperfine coupling constant such that,

$$a_{\text{iso}} = A_{\text{iso}} + B_{\text{core}} \tag{3.7}$$

where $B_{\text{core}} = -1.5 \times 10^{-7}$ eV and A_{iso} are the hyperfine coupling due to the core polarisation of the 1*s*-orbitals and to the direct Fermi-contact interaction of 2*s*-orbitals respectively.[128] If $A_{\text{iso}} = 1.41 \times 10^{-7}$ eV, using the value of χ_s of Ikehata *et al.*, then Equation 3.6 returns an isotropic shift of $K_{\text{iso}} = -37$ ppm..[126] Using Equation 2.25 and 3.6 we now find $\langle|\psi_s(0)|^2\rangle_{E_F} = 0.12 a_B^{-3}$ meaning the estimated contribution of 2*s*-orbitals at the Fermi level is 4.3%. This value agrees well with the value found by Mansour *et al.*, using soft X-ray emission spectroscopy to study the electronic structure of LiC_6 they gave an upper limit for a Li 2*s* conduction band in LiC_6, as 4% of that in metallic Li.[86]

Next we introduce a modified Korringa relation such that

$$\left\langle \frac{1}{TT_1} \right\rangle = \left\langle \frac{1}{TT_1} \right\rangle_{\text{dip}} + \left\langle \frac{1}{TT_1} \right\rangle_{\text{iso}} = \frac{4\pi k_B}{\beta} \left(\frac{\gamma_n}{\gamma_e} \right)^2 (2\langle K_{33}^2 \rangle + \langle K_{\text{iso}}^2 \rangle) \tag{3.8}$$

where $T_{1\text{iso}} = 1/R_{\text{iso}} = 2.5 \pm 1$ s and $T_{1\text{Dip}} = 1/R_{\text{iso}} = 1 \pm 0.1$ s. Using Equation 3.4.5 and the value of $TT_1 = 223 \pm 7$ sK we find that $\beta = 0.8 \pm 0.$ does not deviate greatly from 1 meaning that electron-electron interactions are not so important in LiC_6. Though the value of $\beta < 1$ suggesting there are additional mechanisms that contribute to the relaxation, this will be discussed further in the next chapter.

Finally we can calculate the density of states at the Fermi level, $\rho(E_F)$, by combining Equations 2.27, 3.5, 3.6 and 3.4.5 such that

$$\frac{1}{TT_1} = \frac{\alpha^2 \pi k_B}{\beta} \left(2d_{33}^2 + a_{\text{iso}}^2\right) \rho\left(E_F\right)^2 . \tag{3.9}$$

where α is the dimensionless Stoner enhancement factor. This gives us $\rho\left(E_F\right) = 3.2$ states/eV per LiC_6 when $\alpha = 1$. If we use $A_{\text{iso}} = 1.41 \times 10^{-7}$ eV instead of $a_{\text{iso}} = -8.85 \times 10^{-9}$ eV in Equation 3.9 then $\rho\left(E_F\right) = 0.66$ states/eV per LiC_6 when $\alpha = 1$. This value is close to the value of Ikehata *et al*, $\rho\left(E_F\right) = 0.77$ states/eV per LiC_6.[126] This approach can be rationalised since the hyperfine coupling arising from core polarisation should not emerge as a result of an increase in the density of states.

3.4.6 Dilute stages

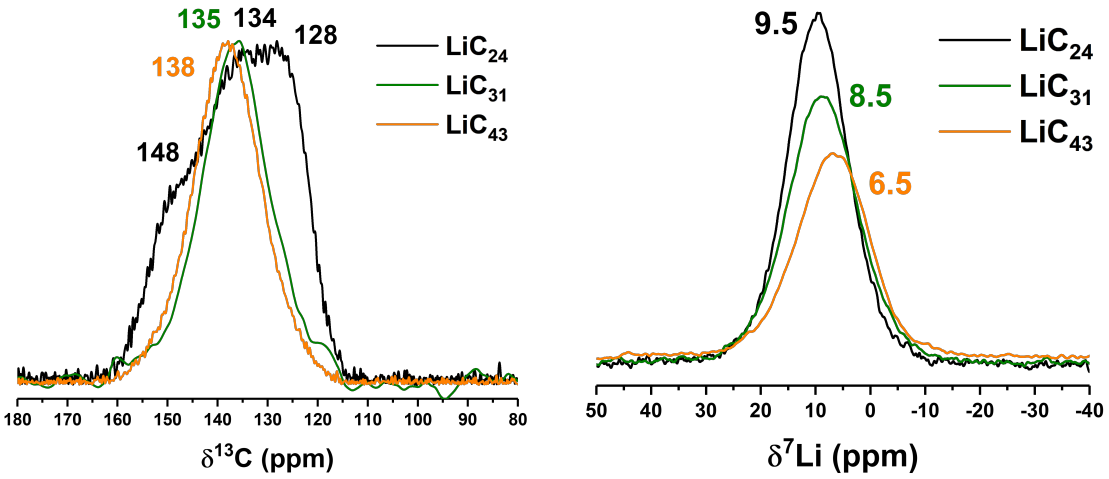

Figure. 3.10 a) ^{13}C and b) ^{7}Li NMR of the dilute stage samples LiC_{24}, LiC_{31} and, LiC_{43}. The intensity of the ^{13}C NMR peaks were normalised as it's not possible to be quantitative when using a CPMG pulse sequence.

We now take a closer look at the dilute stages and will attempt to assign the multiple peaks seen in the LiC_{31}a sample in Figure 3.5b. One might assume that the peaks at 134 and 122 ppm in Figure 3.5b, given their similar intensities, might originate from the same phase and could result from carbon atoms in graphite layers that are bound and not bound to a lithium layer, as would be expected for a dilute stage Li-GIC with an AB stacking structure. Kume *et al*. observed multiple ^{13}C NMR peaks per stage in higher stage K-GIC using highly orientated pyrolitic graphite (HOPG). They observed peaks corresponding to bound and unbound layers with signals originating from carbon atoms that were more tightly bound

to the K layer having a shorter T_1.[99,102] However, since in this work powdered graphite was used instead of HOPG, it may not be possible to distinguish the bound and un-bound layers. It is also clear from the XRD data that the dilute stages are heterogeneous and contain multiple phases. Some of this heterogeneity occurs because at room temperature, as shown by the *in-situ* XRD results of Dahn, stages 4L and 3L and stages 3L and 2L do co-exist for part of the phase diagram.[25] Some of the heterogeneity is also likely a result of the variability in the electrochemical performance between cells, since more than one coin-cell was needed to pack a 4 mm rotor. The variability in the electrochemical performance is most likely due to the variation of the surface of the Li-metal counter electrode which results in differences in overpotential. When fresh Li-metal electrodes were used ($<$ few weeks) the variability was greatly reduced.

To reduce the heterogeneity resulting from sample preparation, the dilute stage samples were measured using a 1.3 mm rotor, where the electrode from one coin cell is sufficient to fill the rotor. ^{13}C NMR measurements, in Figure 3.10a, show that the LiC_{31}b compound now only has one peak at 135 ppm. The 002 peak for this sample is at $2\theta = 25.68°$. From this we can conclude that the peak at 135 ppm corresponds to a stage 3 compound. After further lithiation to the LiC_{24} compound, a peak at 128 ppm is observed in Figure 3.10a however we still observe some heterogeneity in the sample in both the ^{13}C NMR and the XRD data. From the XRD data in Figure A2 we see that the sample is mostly composed of stage 2 ($2\theta = 25.21°$) with some stage 3 phase (($2\theta = 25.43°$)) also present. We do not see any dense stage peak in the ^{7}Li NMR and using the Scherrer equation on the superlattice peak we can calculate a crystallite size of 153 Å. From this we conclude the peaks at 122 ppm (Figure 3.5) and 128 ppm (Figure 3.10a) correspond to the dilute stage 2 compound. The heterogeneity of the LiC_{24} sample also agrees well with the results of Didier *et al*., who concluded through *operando* neutron diffraction measurements that a pure dilute stage 2 compound does not form during lithiation of graphite.[26] Further evidence for this can be seen in Figure A3 which shows the ^{13}C MAS NMR spectra of two samples composed of 4 electrodes each that stopped cycling after reaching a nominal composition of LiC_{20}. The differences observed in the two spectra are again due to variability in the electrochemical performance of the cells. However we see in the first sample that the stage 2L coexists with stage 3L while in the second sample it coexists with both stage 3L and dense stage 2.

From our results we can see that the main differences between stage 2L and stage 2 compounds is the correlation length of the stages which increases from 153 Å for stage 2L to 203 Å for stage 2. The difference in correlation length between stage 2L and stage 2, measured by Ohzuku *et al*, was even larger, this may depend on the graphite as well as the

charging rate used.[23] ^{13}C and ^{7}Li NMR measurements show the onset of peaks corresponding to the dense stage 2 at 108 ppm and 45 ppm respectively. With only a comparatively small change in the ^{13}C isotropic shift between LiC_{43} and LiC_{31}, as shown in Figure 3.10a, we suggest that changes in the chemical shielding are not likely to be the cause of the change in isotropic shift between the different Li-GIC stages seen in Figure 3.5b. Saito *et al*. also showed, through calculations based of the band structure derived by Ohno and Kamimura, that the changes in the chemical shift between different GIC stages are negligible.[121,129] We also see, in Figure 3.5b that the isotropic shift changes linearly, by -13 ± 1 ppm, when going from Stage 3L to dense stage 1. This gives further evidence that the observed shifts are due to Knight shifts.

3.5 Conclusions

The ^{13}C NMR of lithiated graphite as a function of capacity, during the first discharge cycle, has been reported for the first time and the isotropic resonances of stage 1, 2, 2L and $n \geq 3$L were assigned as 96, 108, 122, 134 ppm, respectively. Mukai *et al*, showed that the showed that the initially large diamagnetic susceptibility of graphite decreases with increasing content.[123] This was also evidenced in this work by the decreasing span of the static lineshape, with $\xi_{33} = -250$ ppm in pure graphite decreasing to $\xi_{33} = 73$ for the stage 3L Li-GIC. For Li-GIC stages with $n \geq 3$L the isotropic resonance did not change significantly as a function of state of charge showing that the chemical shielding was similar for these compounds and likely for all Li-GICs. Between stages 3L and dense stage 1 the ^{13}C NMR isotropic resonance decreases by approximately -13 ppm with each change of stage. MAS ^{13}C NMR $T1$ measurements as a function of temperature showed, that for LiC_{12} and LiC_6, the Korringa relation holds and hence the dominant relaxation mechanism for these compounds is Korringa relaxation. This, as well as the change in colour of the samples due to increased plasma frequency, and ^{7}Li NMR measurements, show that LiC_{12} and LiC_6 are metallic. From the static ^{13}C NMR Hahn-echo measurements we found that the lineshape of the spectra could be described by a combination of the chemical shielding, anisotropic spin-dipolar Knight shift as well as an isotropic Knight shift. The angular dependence of this anisotropic Knight shift is such that it increases the shift when the c-axis of graphite is parallel to the bulk magnetic field and decreases when it is perpendicular. The anisotropic Knight shift therefore opposes the shifts due to chemical shielding in graphite. In the case of LiC_{12}, the chemical shielding and anisotropic Knight shift are equal and opposite, leading to a narrow lineshape, with $\omega_\xi = 12 \pm 1$ ppm. For LiC_6, the anisotropy changes sign, with $\kappa = 1$ for $n \geq 2L$ and $\kappa = -1$ for LiC_6.

Static ^{13}C T_1 measurements showed that the anisotropic spin-dipolar Knight shift is the dominant relaxation mechanism in LiC_6, responsible for 71% of the relaxation at room temperature. The ^{13}C NMR measurements also allowed for the determination of anisotropic and isotropic hyperfine coupling strengths in LiC_6. The isotropic hyperfine coupling strength and isotropic Knight shift of LiC_6 ($\delta_{iso} = -37$ ppm) is smaller (less negative) than that expected for the case where only core polarisation of 1s-orbitals occurs. This shows that there must be a contribution of 2s-orbitals, as well as 2p-orbitals, at the Fermi level. Using the value of χ_s of Ikehata *et al.*, we estimate the contribution of 2s-orbitals to be 4.3% in good agreement with the value found by Mansour *et al.*[86]

The density of states at the Fermi level was found to be $\rho(E_F) = 0.66$ states/eV per LiC_6 in good agreement with the value of Ikehata *et al*.[126]

We have shown how ^{13}C NMR shift can be used to identify and quantify the stages present in a lithiated graphite electrode. In this work we only looked at Li-GICs formed during the first discharge cycle. Didier *et al*, have shown that the delithiation mechanism of graphite is different to the lithiation mechanism.[26] ^{13}C NMR could therefore be used to probe the differences during charge and discharge, including stage quantification and any differences in the electronic structure.

This technique can be further applied to understand the intercalation mechanism of sodium and other AM into graphite, as graphite could be an important anode material in n beyond Li-ion batteries.[96,130] It could also be used to understand the differences in lithiation mechanisms of natural and synthetic graphite. With a push towards using natural instead of synthetic graphite due to its lower cost, ^{13}C NMR may help to elucidate why there are differences in their cycle performance.[32,35] Furthermore the understanding gained from this work can be applied to *operando* NMR and can then be utilised as a non-destructive tool to study battery degradation mechanisms in Li-ion batteries.

Chapter 4

Understanding Lithiation Dynamics During Intercalation into Graphite

4.1 Abstract

The Li-ion dynamics, of Li intercalated into graphite, were studied as a function of discharge capacity during the first discharge cycle, using *ex-situ* and *in-situ* ^{7}Li NMR, relaxometry and GITT measurements. We show that the Li-ion dynamics depend on the state of charge. Diffusion coefficients as a function of state of charge, calculated from GITT and ^{7}Li NMR relaxometry measurements, were shown to follow a similar trend with faster Li motion occurring in the dilute stages compared to the dense stages. The magnitude of diffusion coefficients from the GITT measurements were three order of magnitude larger than that calculated from ^{7}Li NMR $T_{1\rho}$ measurements suggesting that these techniques probe different length scales. $T_{1\rho}$ measurements also showed that Li-motion induced relaxation occurs mainly due to the quadrupolar interaction. The activation energies, calculated from the Arrhenius plots of T_1 and $T_{1\rho}$, showed the Li motion likely proceeds mainly via a two stage interstitialcy mechanism. VT NMR and XRD measurements showed that Li leaching occurs when the temperature is increased above room temperature. The onset of Li leaching, occurred at 286 K, 316 K and 294 K, for LiC_{38}, LiC_{12} and LiC_6, respectively.

4.2 Introduction

To enable the widespread adoption of electric vehicles (EVs), batteries with higher energy and power densities are essential.[131] One of the most important factors limiting the uptake of EVs is the charging rate.[132] As discussed previously in Chapter 1, graphite is one of the most widely used anode materials due to its high energy density. Li diffusion within graphite is one of the most important parameters that determine how fast it can be dis/charged. Manufacturing techniques such as laser patterning of graphite, magnetic aligning of graphite and reducing the electrode thickness, can be used to improve dis/charge rates.[133,134] However, these techniques are often expensive and not scalable or lead to a decrease in energy density and poor solid-state diffusion still remains an important limitation. Li-ion dynamics, which are dependent on temperature, as well as state of charge, are also important in determining whether Li-metal will plate on graphite anodes at a particular charging rate.[41,133] Furthermore, an understanding of Li-ion dynamics is important in producing models that can accurately simulate electrochemical processes in LIBs.

There have been many studies that aim to study Li diffusion within graphite using electrochemical techniques,[135–138] first principles calculations,[139–141] as well as ssNMR and Muon spin resonance (μ^+ SR).[36,98,142,143] Li diffusion coefficients in Li-GIC, determined using electrochemical techniques such as, electrochemical impedance spectroscopy (EIS), galvanostatic intermittent titration (GITT) and potentiostatic intermittent titration technique (PITT) have been reported in the range of $10^{-12} - 10^{-8}$.[135–138] The diffusion coefficients calculated with these techniques, often rely on models that have underlying assumptions that can differ between different studies. They also often depend on geometric terms such as the surface area which can be difficult to determine precisely.[137] The calculated diffusion coefficients also depend on the charging direction and rate as well as the temperature and the type of graphite used.[137,142]

Care should be taken when comparing the diffusion coefficient calculated by GITT measurements, and other electrochemical techniques, to those calculated from NMR techniques. The latter will measure the self-diffusion coefficient, D_S, under equilibrium conditions, while the former measures the chemical diffusion coefficient, D_C, which are related by a thermodynamic factor such that

$$D_C = W D_S \tag{4.1}$$

where W is the thermodynamic factor.[144] The thermodynamic factor term arises because the true driving force for diffusion is a gradient in chemical potential, while the self-diffusion coefficient is derived from Fick's law, where the driving force for diffusion arises from concentration gradients.[140,144]

Toyoura *et al.*, described three different Li hopping mechanisms. They showed that vacancy, interstitial and interstitialcy diffusion mechanisms, were all possible in LiC_6.[141] The vacancy mechanism describes a process where a vacancy is filled by a Li atom hoping from a neighbouring site. The interstitial mechanism describes a process where a Li atom occupying an interstitial site hops to a neighbouring interstitial site. The interstitialcy mechanism proceeds via a two stage process where first a Li atom in a regular site jumps into an unoccupied interstitial site and then a Li atom in an interstitial site jumps and fills the vacant regular site. The vacancy, interstitial and interstitialcy mechanisms are characterised by Li hoping distances of 4.3 Å, 2.5 Å and two hops each of 2.5 Å with activation energies of 0.47, 0.48, 0.29 and 0.13 eV, respectively.[141]

ssNMR relaxometry has been shown to be a powerful tool to study Li-ion dynamics in battery materials and can be used to measure D_S.[87] The calculated values of D_S, unlike those calculated from electrochemical techniques (D_C), are reasonably independent of the diffusion model used.[36,87] Measurements of the spin-lattice relaxation in the laboratory frame, characterised by T_1, are sensitive to Li hoping motion on time scales of the Larmor frequency *i.e.*, in the MHz range.[90] This rapid motion is often only accessible at high temperatures, which can not be accessed in Li−GIC due to degradation of the material, such as Li leaching, that occur at these temperatures.[145] $T_{1\rho}$ is sensitive to Li hoping motion in the kHz range.[87] $T_{1\rho}$ measurements can therefore probe much slower motion, and have been used to study Li-ion motion in battery materials at ambient conditions that are much more relevant to operating conditions in a real battery.[36,87] Langer *et al.*, reported on ^{7}Li NMR relaxometry measurements of LiC_6, synthesized via vapour-phase intercalation of Li into polycrystalline graphite.[36] They used T_1, T_2 and $T_{1\rho}$ measurements to probe the Li-ion dynamics and calculated an activation energy for Li hopping motion, of $E_a = 0.55$ eV and a room temperature (295 K) Li self-diffusion coefficient of $D_S = 10^{-11}$ cm^{2}s^{-1}.

While Langer *et al.*, only studied the LiC_6 compound, Umegaki *et al.*, used μ^+ SR to probe Li-ion diffusion in electrochemically prepared LiC_{12} and LiC_6.[36,142] They determined the thermal activation energy and self-diffusion coefficient in LiC_{12} to be $E_a = 0.17$ eV and $D_S = 14.6 \times 10^{-11}$ cm^{2}s^{-1} respectively. For LiC_6 they were found to be, $E_a = 0.27$ eV and $D_S = 7.6 \times 10^{-11}$ cm^{2}s^{-1} respectively.[142]

An understanding of the Li-ion dynamics as a function of state of charge is important to understand limitations of dis/charging rates as well as to help design cycling protocols that can prevent Li-metal plating on graphite anodes. In this work, the Li-ion dynamics, of Li intercalated into graphite, were studied as a function of discharge capacity during the first discharge cycle. We used both *ex-situ* and *in-situ* ^{7}Li NMR relaxometry and GITT measurements to probe Li motion in a battery grade graphite.[21] T_1, T_2 and $T_{1\rho}$ measurements were performed on three electrochemically prepared compounds with nominal stoichiometries, LiC_6, LiC_{12} and LiC_{38}. From VT XRD and NMR experiments, the importance of the quadrupolar, dipolar and Knight shift interactions on the relaxation rates were estimated. Diffusion coefficients as a function of state of charge, calculated from GITT and ^{7}Li NMR relaxometry measurements were also compared.

4.3 Experimental Methods

4.3.1 Materials

Graphite electrodes were fabricated and provided by the Argonne National Laboratory Cell Analysis, Modeling, and Prototyping (CAMP) facility. The graphite electrodes were composed of 91.83 wt% graphite powder (Hitachi Mage 3), 2 wt% carbon black (Timcal C45), 6 wt% PVDF binder (Kureha 9300) and 0.17 wt% oxalic acid. The Hitachi MAGE 3 graphite has a specific surface area of $4.97\,m^2/g$.[21] The mass loading of the graphite active material is $5.83\,mg/cm^2$. The graphite electrodes were punched into 15 mm circular disks and dried under dynamic vacuum (10^{-2} mbar) in a Büchi oven at 120 °C for at least 12 hours. Once cooled to room temperature, the dried electrodes were then transferred into an Ar atmosphere glovebox ($O_2 \leq 1$ ppm, $H_2O \leq 1$ ppm) for battery assembly. Two separators were used, Celgard 3501, and glass microfibre separator (Whatman). The Celgard 3501 was punched into 17 mm disks, washed in ethanol and then dried under vacuum at 40 °C for 12 hours. The glass microfibre was punched into 16 mm disks and dried under vacuum at 100 °C. 1 M $LiPF_6$ in ethylene carbonate/ethyl methyl carbonate 3/7 wt:wt (LP57, SoulBrain MI) with 2wt% vinylene carbonate (VC) was used as the electrolyte.

4.3.2 Battery Assembly and Cycling

Graphite half-cells were assembled using 2032 coin cells (Cambridge Energy Solutions) with 15 mm graphite disks, 16 mm lithium chips (Cambridge Energy Solutions) and 180 µL of electrolyte. The Celgard separators were placed between the graphite anodes and the glass fibre separators since they are more inert than the borosilicate glass fibres which, at low voltages, can react with lithiated graphite making battery disassembly difficult. The glass fibre separators were necessary to ensure optimum electrolyte volume and mechanical pressure to homogeneously lithiate the graphite electrodes. Before cycling, the cells were rested at their open circuit voltage (OCV) for a minimum of two hours. The cells were then cycled a rate of C/50, calculated using a theoretical capacity of graphite of $372\,mAh/g$, using a constant current cycling protocol. For samples prepared for *ex-situ* characterisation, cells were stopped at the desired cut off voltage or capacity during the first discharge. Four samples were prepared by discharging to cut off voltages 120, 75 mV, 10 and 5 mV, respectively. The two samples with a nominal composition of LiC_6 were prepared by discharging to a cut-off of 5 mV and 10 mV, respectively. For both samples a 10 hour voltage hold step was

implemented to more completely form the LiC_6 phase. Three further samples were prepared by discharging to a capacity corresponding to a value for x in Li_xC_6 of 0.29, 0.32 and 0.68, respectively.

For *in-situ* NMR measurements, capsule cells fabricated from polyether ether ketone (PEEK), shown in Figure 4.2, were used as described by Pecher et al.[146] The cells were assembled in an Ar atmosphere glovebox ($O_2 \leq 1$ ppm, $H_2O \leq 1$ ppm) with a graphite anode, a Li metal counter electrode and a glass fibre separator. 1 M $LiPF_6$ in ethylene carbonate/ethyl methyl carbonate 3/7 wt:wt (LP57, SoulBrain MI) with 2wt% vinylene carbonate (VC) was used as the electrolyte.

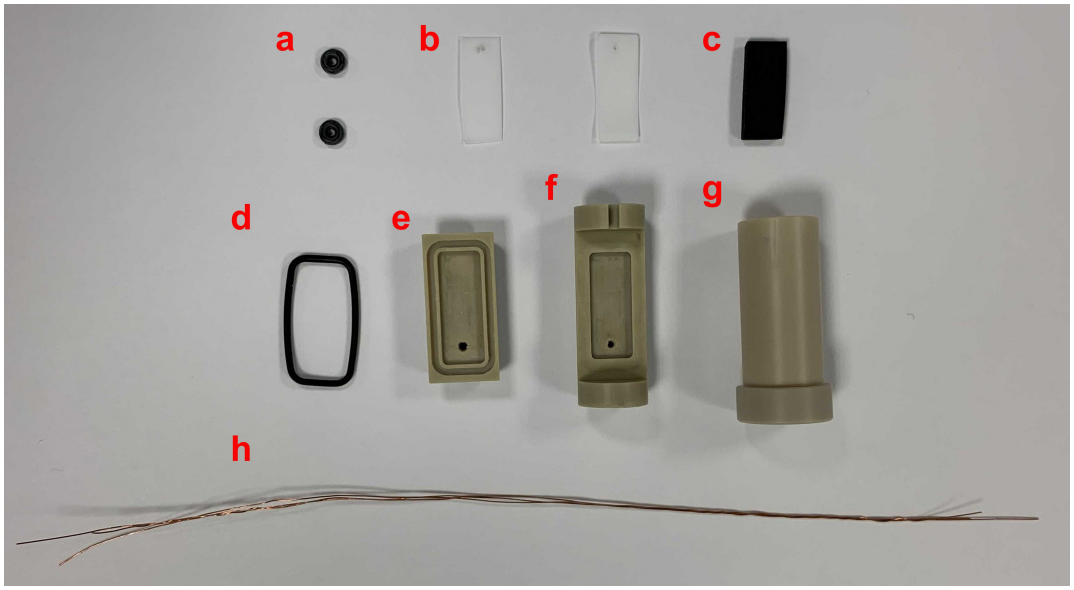

Figure. 4.1 Photo of components of PEEK capsule cell used for *in-situ* NMR experiments. The components are a) small o-rings, b) PTFE spacers, c) Viton spacer, d) large o-ring, e) bottom, f) top, g) sleeve and h) copper wire.

GITT

A GITT measurement was performed during the first lithiation of graphite between the open circuit voltage (OCV), $E_{OCV} = 2.65$ V, and 0.005. The measurements were conducted to extract the chemical diffusion coefficient, D_C, of lithium in graphite at different states of charge.

GITT measurements were performed by applying current pulses which were then followed by periods of relaxation where no current was applied but the change in potential was measured. When a current pulse is applied, the potential quickly drops due to ohmic

resistance and this is known as the IR drop. The potential then gradually decreases as Li-ions are inserted into the graphite leading to a concentration gradient from the surface to the centre of the graphite particles. During the subsequent relaxation periods, this concentration gradient equilibriates due to Li-ion diffusion and the potential, after a sharp increase which occurs because there is no longer any Ohmic resistance, gradually increases back to E_{OCV} when $\Delta E/\Delta t \sim 0$. The chemical diffusion coefficient can be calculated using the equation first derived by Weppner and Huggins[144] such that,

$$D_C = \frac{4}{\pi\tau}\left(\frac{m_B V_M}{M_B S}\right)^2 \left(\frac{\Delta E_s}{\Delta E_t}\right)^2, \qquad (\tau \ll \frac{L^2}{D_C}) \tag{4.2}$$

where τ is the length of time that the current pulse is applied, m_b and S are the mass and surface area of the active material, V_M is the molar volume and M_B is the molecular weight. ΔE_s is the change in E_{OC} after a current pulse, while ΔE_t is the change in potential that occurs during a current pulse, excluding the IR drop. The equation holds as long as the current pulses are sufficiently short such that, $\tau \ll L^2/D_C$. In the case where a liquid electrolyte is used, we can take L to be the graphite particle radius to ensure an accurate approximation of the Fickian diffusion principles.[147]

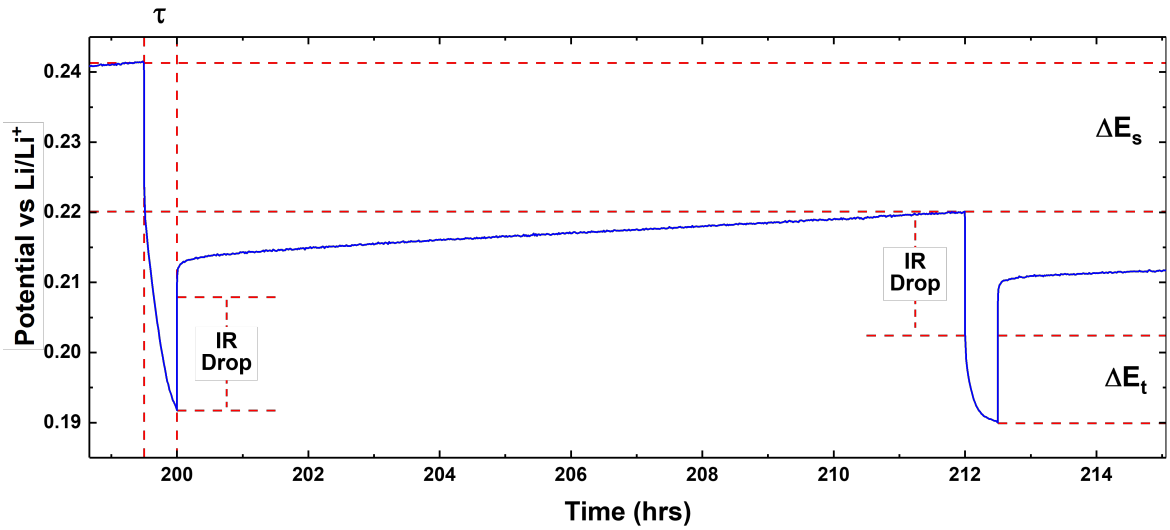

Figure. 4.2 Illustration of the a single step during a GITT experiment. ΔE_t is the change in potential that occurs during a current pulse of length τ. ΔE_s is the change in E_{OC} after a current pulse. The IR drop after the current is applied and removed is also shown.

For the GITT measurement, the amplitude of the current pulses was 66 µA which corresponds a cycling rate of C/58, *i.e.*, the cell is set discharge in 58 hours in a galvanostatic experiment. The current pulses were applied for $\tau = 30$ minutes, followed by a 12 hour rest period. The active mass, m_B, of graphite in the 15 mm diameter electrodes was 10.29 mg. The molecular weight and volume of graphite (C_6) are $M_B = 72.064$ g/mol and $V_M = 5.267$ cm^3/mol, respectively. Using the Brunauer–Emmett–Teller (BET) surface area, typically results in an overestimation of the surface area. Instead, in this work we used the equation derived by Yang *et al.*, for the actual electrochemical interfacial specific surface area (in m^2/g), using the dimensions of the graphite crystal structure and assuming that the Li ions only enter the graphite through the edge planes such that,

$$A_{es} = \frac{8 d_{100}^2 d_{002} N_{\mathrm{A}}}{3 B M_B} \tag{4.3}$$

where $d_{100} = 2.4612$ Å and $d_{002} = 3.354$ Å are the in-plane lattice constant and the interlayer distance, respectively, N_A is Avogadro's constant and $B = 15$ µm is the radius of basal plane.[137]

4.3.3 NMR

Graphite electrodes for ssNMR measurements were electrochemically cycled in half-cells against lithium metal at C/50 until the desired state of charge was reached. The slow cycling was performed to ensure the electrode was homogeneously lithiated. The electrodes were then extracted from the cells and rinsed with 1 mL of DMC to remove residual electrolyte before drying under vacuum for 5 min. The lithiated graphite was then scraped from the copper current collector, diluted with approximately equal amounts of KBr to help with sample spinning, and packed into 4 mm rotors. Four electrodes (15 mm diameter discs) were used to fill each rotor. ^{7}Li measurements were performed on a 4.7 T magnet ($\nu_0(^1\mathrm{H}) = 200.13$ MHz, $\nu_0(^7\mathrm{Li}) = 77.78$ MHz), equipped with a Bruker Avance IIIHD spectrometer. A 4 mm Bruker double resonance probe was used, with measurements performed at 10 kHz MAS spinning frequency. A rotor-synchronized Hahn-echo pulse sequence was used with a recycle delay that was at least 5 times T_1 to allow for quantitative analysis.

Static ^{7}Li NMR measurements, using a solid echo pulse sequence, were also performed to acquire the full ^{7}Li powder pattern including the satellite transitions and to determine the quadrupolar coupling constant, C_q. The ^{7}Li chemical shifts were referenced to 1 M LiCl in

H_2O at 0 ppm. Pulse power calibrations were performed on the Li-GIC samples since the 90° pulse lengths changed significantly from the reference samples due to skin-depth effects as the Li-GIC samples becomes more conductive as more Li is intercalated.

VT NMR

Variable temperature (VT) measurements were performed between 234 - 346 K to observe changes in the lineshape and phase evolution in the sample as function of temperature, as well as to probe different relaxation phenomena. The temperature was first lowered from room temperature and then raised. The sample temperature was determined using an *ex-situ* calibration with the temperature-dependent ^{79}Br NMR shift of KBr.[93]

Hahn-echo measurements were performed as described in the previous section. For the LiC_{12} compound, static VT measurements, using a solid-echo pulse sequence, were performed to observe the change in C_q as a function of temperature. For the LiC_{38} and LiC_6 compounds, the C_q was determined by fitting MAS spectra using the SOLA function in TopSpin. For LiC_{38} and LiC_6, static measurements at different temperatures were not performed since a different probe was used.

Relaxometry

The T_1, T_2 and $T_{1\rho}$, were recorded under 10 kHz MAS over the temperature range 234 - 346 K. A saturation recovery pulse sequence was used to measure T_1 with the delay time, τ, varied between 100 µs and 30 s. For T_2 a Hahn-echo experiment was used with τ varied between 50 µs and 100 ms.

A spin-locking experiment was used to measure $T_{1\rho}$. After a $\pi/2$ pulse, a spin-locking pulse is applied for a duration, τ. The radio frequency (RF) of the spin-locking pulse used in the experiments was $\nu_1 = 12$ kHz. For LiC_{12}, additional $T_{1\rho}$ measurements were performed with three additional spin-locking frequencies $\nu_1 = 8$, 18 and 24 kHz, to probe different motional regimes. For the $T_{1\rho}$ measurements performed on LiC_{18} and LiC_{12}, τ was varied between 100 µs and 1 s, while for LiC_6, τ was varied between 100 µs and 25 ms. The recycle delay used for the $T_{1\rho}$ measurements was set to $1.3 \times T_1$.

T_1 times were were obtained by integrating the area under the dense stage peak for LiC_{12} and LiC_6 and the dilute stage peak for LiC_{18}, before fitting the intensity as a function of the delay time with equation

$$I(\tau) = I(0)\left(1 - \exp\left(\frac{-\tau}{T_1}\right)\right). \tag{4.4}$$

For T_2 and $T_{1\rho}$, the same procedure was applied, except the decay in intensity was fit with the following equation

$$I(\tau) = I(0)\left(\exp\left(\frac{-\tau}{T_{2,1\rho}}\right)\right). \tag{4.5}$$

All relaxation times were satisfactorily fit with mono exponential functions.

4.3.4 *In-situ* NMR Relaxometry

In-situ static ^{7}Li T_1 measurements were performed as a function of state of charge. To perform these measurements, a GITT experiment was conducted where a 30 minute current pulse was applied at a rate of C/20, followed by a rest period of 30 minutes. Once the rest period began, a trigger was sent from the potentiostat to the NMR console. A Hahn-echo experiment was then performed with a recycle delay of 30 s and 60 scans. The recycle delay was chosen so that it would be greater than five times T_1 for the majority of the species recorded along the voltage profile. Following the 30 minute rest period, a saturation recovery experiment was carried out to determine T_1. The T_1 was determined as described in the previous section. Next, a trigger was sent from the NMR console to the potentiostat and the subsequent current pulse was applied. This was repeated until the graphite was fully discharged and the cut-off voltage of 5 mV was reached. Automatic matching and tuning was performed throughout the experiment as described in the work by Pecher *et al.*[148]

4.3.5 XRD

Powder X-ray diffraction measurements were performed with CuKa(α) radiation (λ = 154.06 pm) at 296 K on a Panalytical Empyrean diffractometer equipped with a Ni filter and operating under a Bragg-Brentano geometry.

VT XRD measurements were performed for the LiC_6 sample. The temperature was increased in 10 °C steps from room temperature to 100 °C. At each step, the sample was given 10 minutes to heat up followed by a further 10 minutes for the temperature to equilibriate.

A diffraction pattern was then collected in 10 minutes between $2\theta = 10 - 55°$. The sample was held at 100 °C overnight and diffraction patterns collected every 10 minutes to monitor the re-equilibration of Li within the graphite host structure.

4.4 Results and Discussion

4.4.1 Electrochemical

Galvanostatic cycling

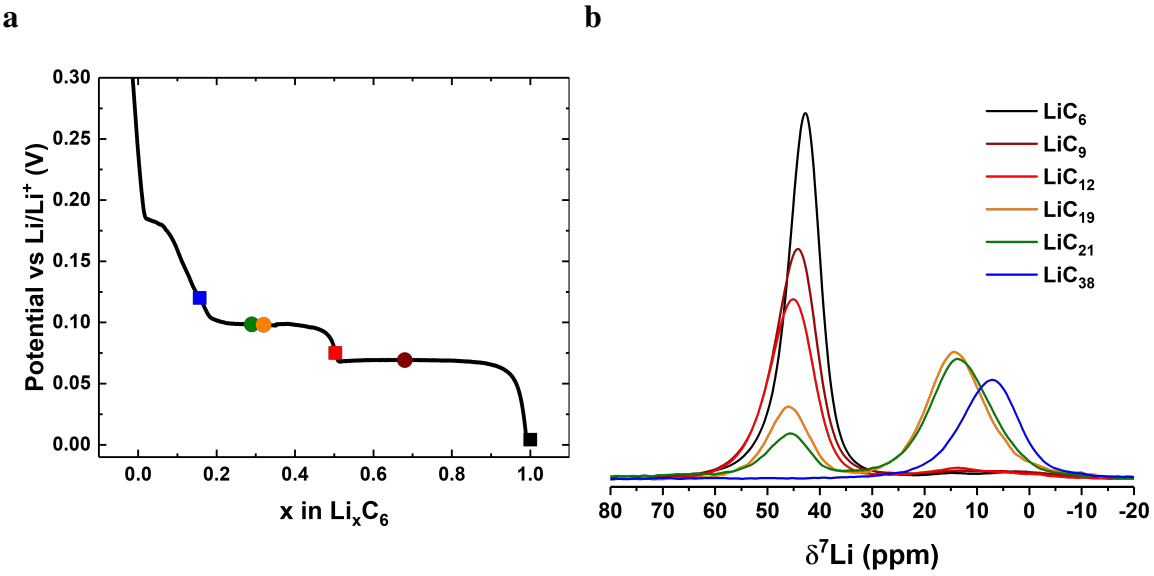

Figure. 4.3 a) Potential profile of the Hitachi Mage 3 graphite half-cell as a function of x in Li_xC_6. Samples were stopped at six points along the voltage profile before being characterised by ^{7}Li NMR. Squares denote samples that were characterised by VT NMR and relaxometry, while samples denoted by circles were characterised only by *ex-situ* NMR. b) The corresponding ^{7}Li NMR spectra for all six samples.

Figure 4.3a shows the potential profile of the Hitachi Mage 3 graphite half-cell as a function of x in Li_xC_6. As described in Chapter 3, the potential profile is corrected so that the capacity is only due to lithium intercalation into graphite, and any capacity due to SEI formation has been accounted for.

The six points in Figure 4.3a represent the potential and capacity at which cells were stopped before being characterised by *ex-situ* NMR. The corresponding ^{7}Li NMR spectra are shown in Figure 4.3b. Three samples, corresponding to LiC_{38}, LiC_{12} and LiC_6 are represented by square points in Figure 4.3a. From the ^{7}Li NMR shifts in Figure 4.3b, and the ^{13}C NMR and XRD results in Chapter 3, we assign the LiC_{38}, LiC_{12} and LiC_6 samples to the stage 3L, 2 and 1 Li-GIC compounds, respectively. These three samples were characterised via VT NMR and relaxometry. Samples where cells were stopped part way along a plateaus are represented by circles in Figure 4.3a. The potential at which the cells were stopped were 120, 103, 98, 98, 75, 68 and 5 mV, and their x values are 0.16, 0.29, 0.32, 0.51, 0.68 and 1,

respectively. The samples will be denoted by their corresponding compositions which are LiC_{38}, LiC_{21}, LiC_{19}, LiC_{12}, LiC_9 and LiC_6. An additional sample, not shown in Figure 4.3 for clarity, was stopped at 10 mV. The two samples stopped at 5 mV and 10 mV both had the same capacity, 369 mAh, but showed differences when measured via ^{7}Li NMR, as will be described in the following sections. Unless specified, the data corresponding to the LiC_6 sample refers to the sample prepared with a 5 mV cut-off voltage.

GITT

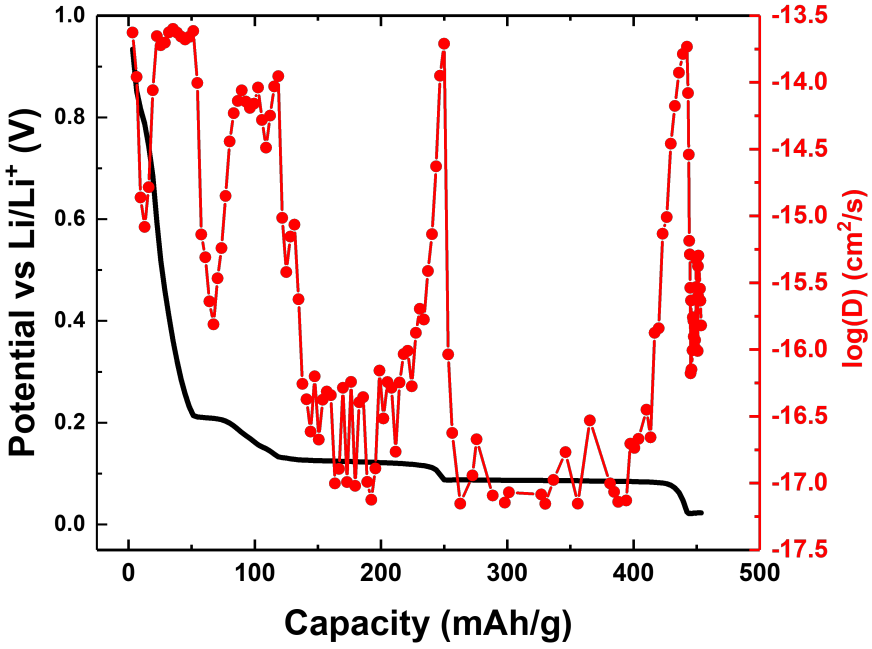

Figure. 4.4 OCV profile as a function of capacity for graphite half-cell (black). The diffusion coefficient, D, (red), calculated using Equation 4.2, is shown as a function of capacity and overlayed on top of the potential profile.

Figure 4.4 shows the OCV profile as a function of capacity for the graphite half-cell as measured during a GITT experiment. The OCV was measured in a quasi-equilibrium state after a 12 hour rest period following a 30 minute, C/58 current pulse. Overlayed onto the potential profile is the diffusion coefficient, calculated using Equation 4.2, as a function of capacity. The diffusion coefficient shows a trend of peaks and minima as a function of capacity that are closely correlated with the different stages. The minima coincide with the plateaus in the voltage profile which occur during first-order phase transitions. The peaks coincide with sloped regions in the voltage profile which occur at the end of the two phase regions. The plateau at 210 mV corresponds to the first-order phase transition between stage

1L and 4L. The diffusion coefficient minima during this phase transition is $D_C = 1.5 \times 10^{-16}$ cm^2s^{-1}. The sloped region in the voltage profile from 210 - 130 mV corresponds to the two solid-solution phase transitions between stages 4L - 3L and stages 3L - 2L. The diffusion coefficient peak during these phase transitions is $D_C = 9.2 \times 10^{-15}$ cm^2s^{-1}. The next plateau at 120 mV corresponds to the two-phase first-order phase transition between stage 2L and stage 2. The diffusion coefficient minima during this phase transition is $D_C = 2.6 \times 10^{-17}$ cm^2s^{-1}. The diffusion coefficient then peaks when $D_C = 1.9 \times 10^{-14}$ cm^2s^{-1}, at the end of the plateau, when there is a single phase solid-solution reaction and only the dense stage 2 phase is present. Another minima occurs during the two-phase first-order phase transition between dense stages 2 and 1 at 85 mV. The diffusion coefficient minima during this phase transition is $D_C = 1.0 \times 10^{-17}$ cm^2s^{-1}. Following this a peak at $D_C = 1.9 \times 10^{-14}$ cm^2s^{-1}, is observed when the reaction proceeds via a single phase solid-solution reaction and only the dense stage 1 phase is present. Further lithiation leads to a plateau at 25 mV, similar to that which occurs during a voltage hold at the end of discharge. At this point, the diffusion coefficient decreases to $D_C = 1.9 \times 10^{-18}$ cm^2s^{-1}. The diffusion coefficient is higher during the phase transitions between dilute stages, compared to the diffusion coefficient minima observed during the formation of the dense stages 2 and 1. This is in part because, the transitions from stage 4L to 3L and 3L to 2L proceed via solid-solution reactions, while transitions from 2L to 2 and 2 to 1 proceed via first-order phase transitions.

The values for D_C found here are lower than values typically reported in literature which are $10^{-8} - 10^{-12}$.[36,135,137,139] The lower values could be due an overestimation of the surface area in Equation 4.3, or because of the slow discharge rate (C/58), as the charging rate can affect the measured diffusion coefficient in a GITT experiment if the time between pulses is not long enough.[149] The lower values could also be affected by the validity of Equation 4.2 as it assumes that Fick's law of diffusion applies. The theory holds true in a solid solution reaction when Li ions enter from the surface of a particle and diffusion away from the surface into the bulk. This may not be valid during the lithiation of graphite in the two phase regions when phase boundaries are also diffusing.

A similar trend in the diffusion coefficient, of peaks and minima in single and two-phase regions, respectively, was observed by Yang *et al.*, via GITT experiments, and Levi *et al.*, with both electrochemical impedance spectroscopy (EIS) and potentiostatic intermittent titration technique (PITT) experiments.[135,137,150] The trend can be explained by taking into account the attractive interactions between Li ions. During a first-order phase transition, the new phase forms as droplets within the existing phase. The growth of the new phase can be modelled by a Frumkin isotherm with strong attraction between the Li ions.[135] These

attractive interactions lead to a decrease in D in two-phase regions compared to single-phase regions.

4.4.2 NMR

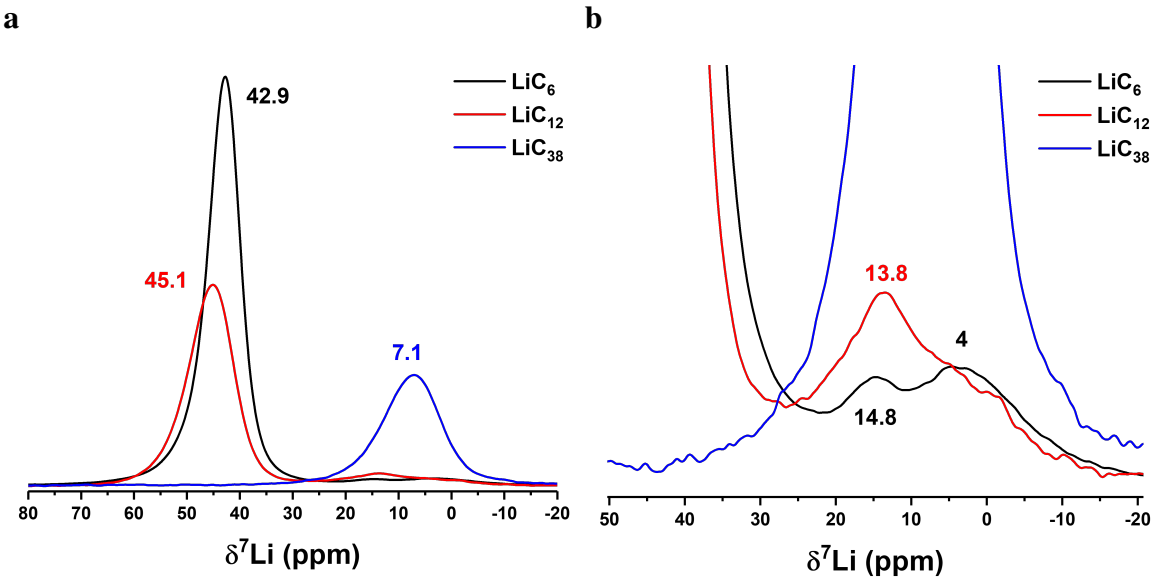

Figure. 4.5 a) ^{7}Li MAS NMR spectra of the LiC_{38}, LiC_{12} and LiC_6 samples. b) An expanded view of the dilute stage ^{7}Li NMR peaks present in the LiC_{12} and LiC_6 samples.

Figure 4.5a shows the ^{7}Li NMR spectra of the LiC_{38}, LiC_{12} and LiC_6 samples. Figure 4.5b shows an expanded view of the dilute stage ^{7}Li NMR peaks present in the LiC_{12} and LiC_6 samples. LiC_{12} and LiC_6 have peaks at 45.1 and 42.9 ppm and these shifts correspond well to those expected for stage 2 and 1, respectively.[29] The peaks at 13.8 ppm and 14.8 ppm in LiC_{12} and LiC_6 are due to residual stage 2L and 3L present in the sample. The broad peak at 4 ppm in LiC_6 is likely due to diamagnetic SEI components. LiC_{38} has a peak at 7.1 ppm which corresponds to stage 3L.[29]

Figure 4.6 shows the static ^{7}Li NMR spectra for the LiC_{38}, LiC_{12} and LiC_6 samples. The satellite transitions are clearly visible in Figure 4.6 and can be used to determine the magnitude of the quadrupolar coupling, C_q, for each Li-GIC compound. We find that $\eta_q = 0$ for all all the Li-GIC compounds which makes sense due the axial symmetry of the Li environments. While the isotropic shifts of the LiC_{12} and LiC_6 differ only by 2.2 ppm, the values of C_q differ more significantly. At room temperature, the value of C_q is 44.7, 35.2 and 38.9 kHz for LiC_6, LiC_{12} and LiC_{38}, respectively. The values of C_q agree well with previously reported values.[29,151] The quadrupolar interaction occurs due to the coupling of the nuclear quadrupolar moment of the ^{7}Li nuclei to the EFG produced by the graphite host

structure and the surrounding Li-ions. Our results agree well with those of Letellier *et al.*, who showed that the quadrupolar coupling increases from $C_{q,4L} = 36$ kHz to $C_{q,2L} = 38$ kHz between stages 4L and 2L, and then decreases in stage 2 where $C_{q,2} = 34$ kHz, before increasing again in stage 1 where $C_{q,1} = 45.2$ kHz.[29] The increase in C_q with capacity could be due to the increasing charge in the graphite host structure, as well as the increase in intercalated Li could lead to an increase in the EFG. The decrease in the C_q between stage 2L and 2 could be due to the change in the graphite stacking structure from AABB to AA.[27]

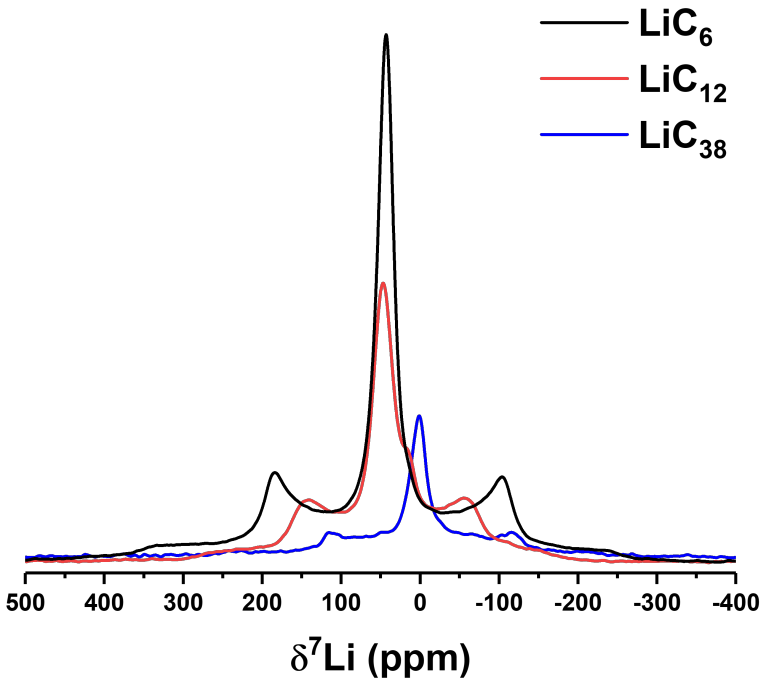

Figure. 4.6 a) ^{7}Li static NMR spectra of the LiC_{38}, LiC_{12} and LiC_6 samples. The spectra are normalised by mass.

Billaud *et al.*, reported on structural refinements of stage 2L and 2 Li-GIC, using Li-intercalated HOPG.[27] They determined for stage 2L, that the interlayer spacing between graphene sheets in the empty layers is 3.33 Å, while the graphene sheet spacing in the Li containing layer is 3.735 Å.[27] For dense stage 2, the interlayer spacing in the empty layer was 3.245 Å and 3.78 Å in the filled layer.[27] The decrease in the interlayer spacing of the empty layer in dense stage 2, compared to the average interlayer spacing of graphite, 3.35 Å, is an agreement with the DFT model of Li-GIC of Hazrati *et al.*[152] The increase in d-spacing of the graphene sheets, with increasing Li concentration, occurs due to increased electrostatic repulsion between the graphene sheets. The decrease and increase in the interlayer spacing of the empty and filled layer respectively, in dense stage 2, therefore suggests that the

electrostatic repulsion is weaker between empty layers and stronger in the filled layer. The difference in the interlayer spacing of the empty layer, between stage 2L and 2, could also be because of the change in the stacking structure. The decrease in C_q between stage 2L and 2, could be because of the larger interlayer spacing of the filled layer in stage 2.

VT NMR and XRD

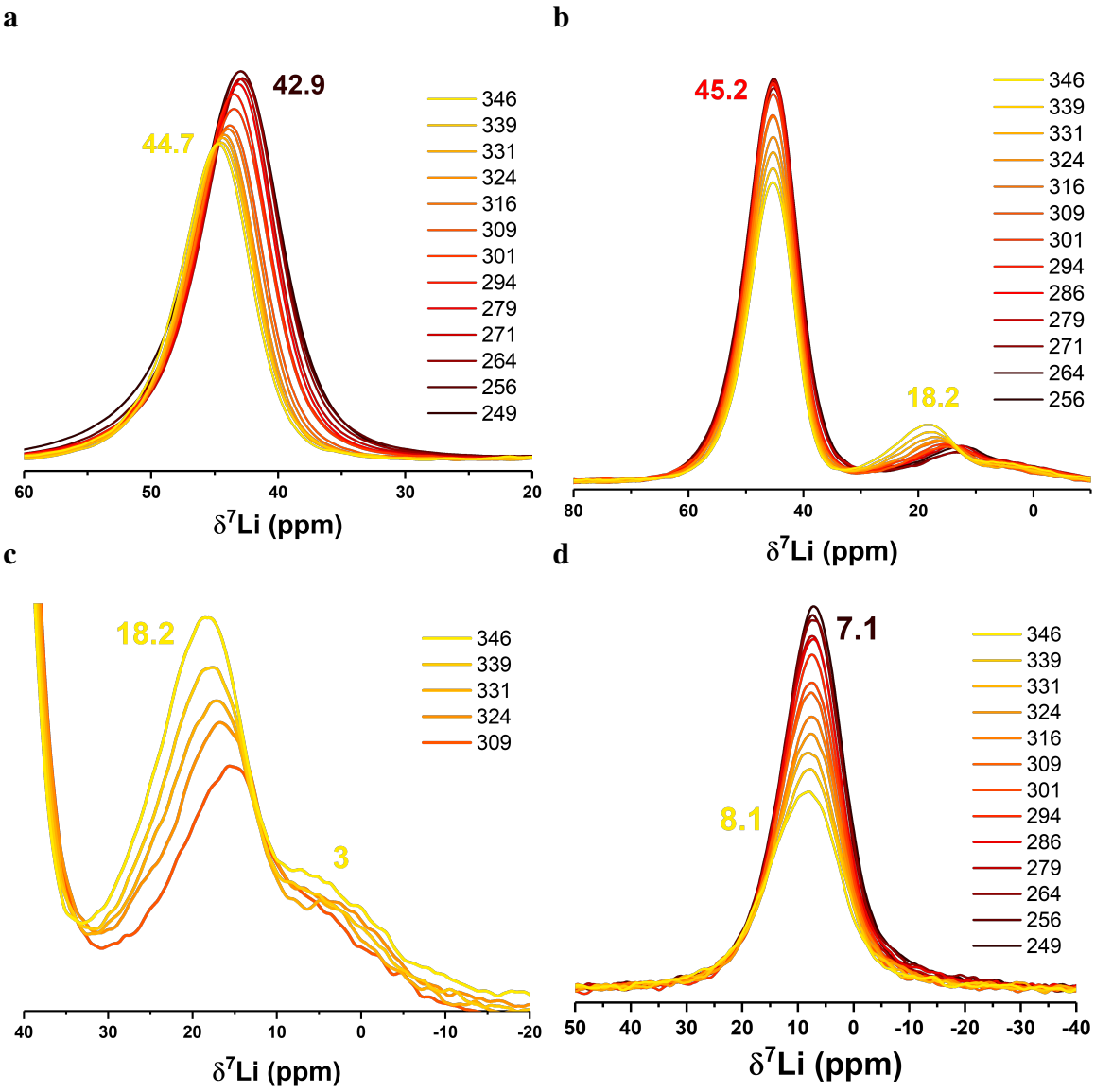

Figure. 4.7 ^{7}Li NMR spectra as a function of temperature for a) LiC_6, b,c) LiC_{12} and d) LiC_{38}. The temperature, in Kelvin, is shown in the legend of each figure. The recycle delays used were set to five times the T_1 of the Li-GIC compound in each sample. The T_1 was measured at each temperature.

The ^{7}Li NMR spectra, shown in Figure 4.7, were recorded as a function of temperature for LiC_{38}, LiC_{12} and LiC_6. As the temperature increases a decrease in intensity is observed for all samples. The decrease can not be totally explained by the change in Boltzmann distribution, as the changes are not reversible upon cooling back to room temperature as shown in Figure 4.8. The isotropic shift of the LiC_6 sample also changes from 42.9 ppm at 249 K to 44.7 at 346 K, which correspond to a shift from stage 1 to stage 2, respectively. For LiC_{12}, a decrease in intensity of the dense stage 2 peak at 45 ppm was observed. Simultaneously, an increase in the intensity of the dilute stage peak was seen which also shifted from 14 ppm at 256 K to 18 ppm at 349 K. In LiC_{38}, the dilute stage peak at 7.1 ppm decreased in intensity as the temperature increased. The onset of the observed changes in the spectra occurred at 286 K, 316 K and 294 K, for LiC_{38}, LiC_{12} and LiC_6, respectively

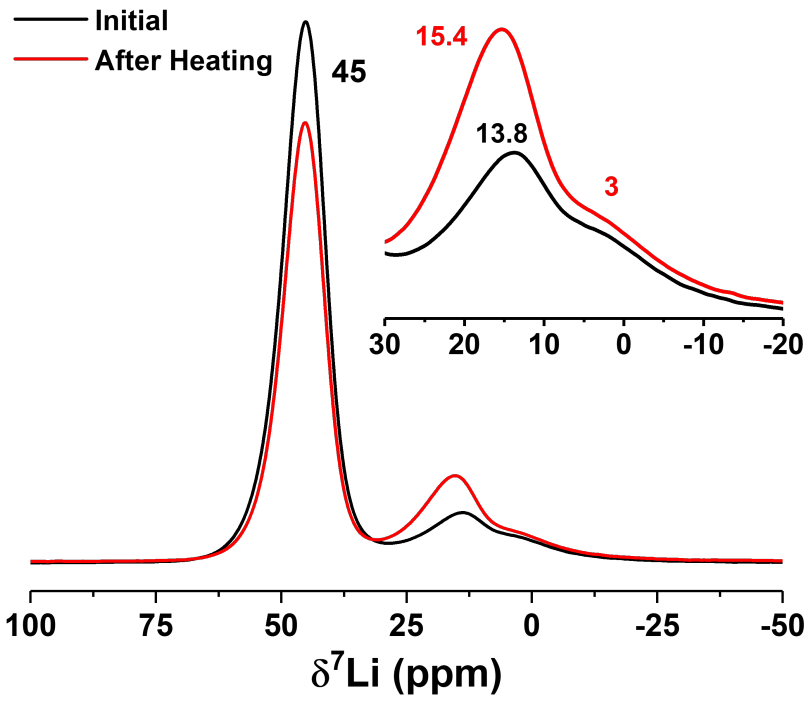

Figure. 4.8 ^{7}Li NMR spectra of LiC_{12} at room temperature before and after heating to 346 K. The inset shows a magnified view of the peaks observed between $-20-30$ ppm.

Similar observations were also seen via VT XRD measurements. Figure 4.9 shows the diffraction pattern of LiC_6 as a function of time spent at 100 °C. The sample temperature was initially increased from 25 to 100 °C over 4 hours and then held at this temperature overnight. When the sample temperature reached 80 °C, a peak at $2\theta = 25.15°$ corresponding to stage 2 became visible with the intensity increasing with temperature. After 5.5 hours at 100 °C,

a peak emerges at $2\theta = 26.35°$ and increases in intensity. This peak also has a shoulder at $2\theta = 26.1°$ which emerges after 3 hours. The peaks at $2\theta = 26.35°$ and $26.1°$ correspond to stage 4L and 1L, respectively. The observed changes were also not reversible upon cooling back to room temperature.

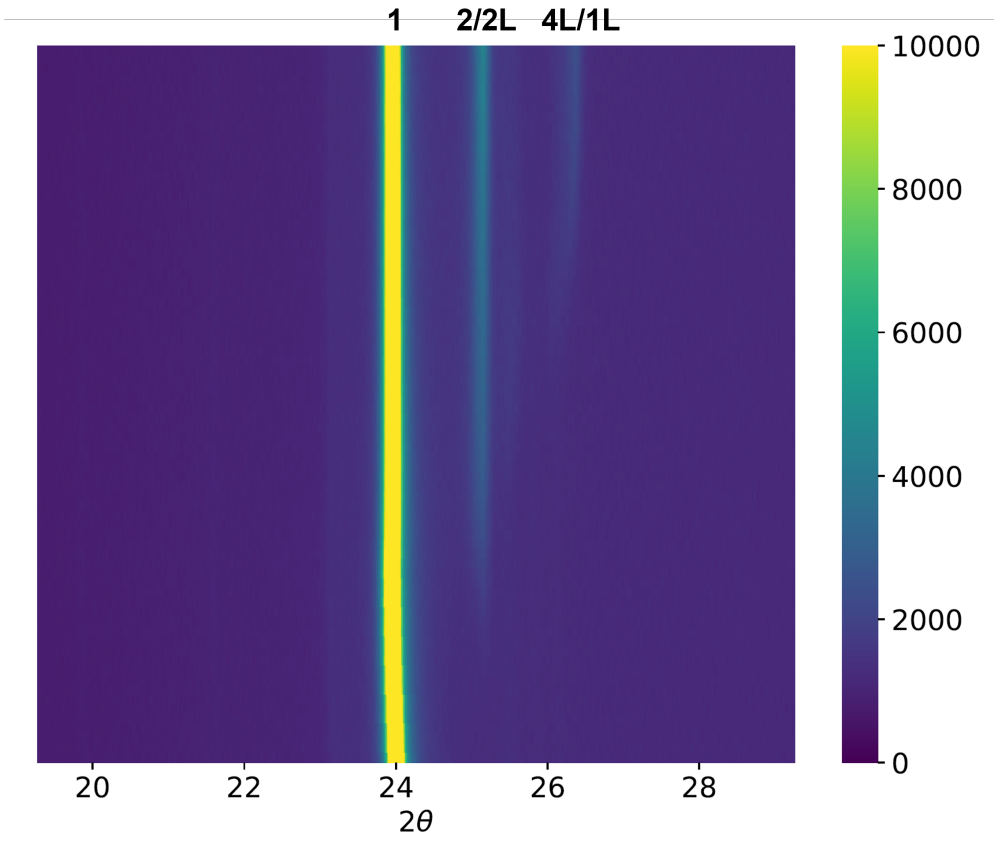

Figure. 4.9 Diffraction pattern, between $2\theta = 20° - 28°$, of LiC_6 sample held overnight at 100 °C. Initially as the sample temperature was increased from room temperature to 100 °C the 001 peak, of the stage 1 Li-GIC, at $2\theta = 24°$ shifts to a lower angle. At 80 °C a peak appears at $2\theta = 25.15°$, corresponding to the stage 2 Li-GIC. After 5.5 hours at 100 °C a peak emerges at $2\theta = 26.35°$ corresponding to either the stage 4L or 1L Li-GIC compound.[23] The peaks are labelled at the top of the figure.

Figure 4.10 shows the values of C_q as a function of temperature for LiC_{38}, LiC_{12} and LiC_6. The LiC_6 sample was prepared with a cut off voltage of 5 mV. For LiC_{12}, C_q was determined by simulation of the powder pattern from the satellite transitions in static spectra as described in the previous section. For LiC_{38} and LiC_6 C_q was determined by fitting the manifold of spinning sidebands from the satellite transitions. From Figure 4.10 we see that C_q is temperature dependent and decreases approximately linearly with increasing

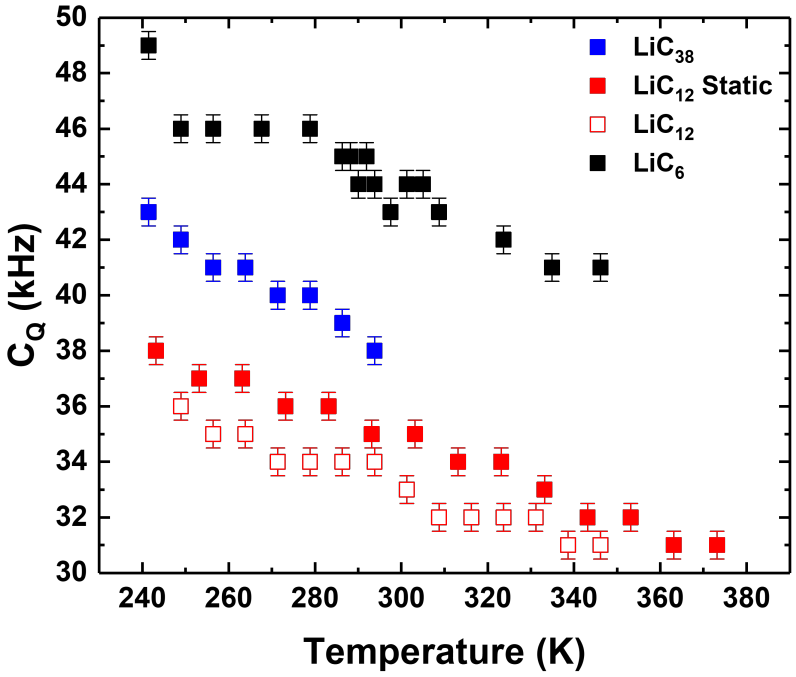

Figure. 4.10 C_q as a function of temperature for LiC_{38}, LiC_{12} and LiC_6. For the LiC_{12} sample, both the static and MAS NMR spectra were fit to determine the C_q, while for LiC_{38} and LiC_6, only MAS NMR measurements were performed. The C_q was determined from the MAS NMR spectra by fitting the manifold of spinning sidebands from the satellite transitions, while C_q was determined by simulation of the powder patterns from the satellite transitions in the static spectra.

temperature. A linear fit to the data shows that for LiC_{38}, LiC_{12} and LiC_6, C_q changes by -64 ± 5, -55 ± 2 and -48 ± 6 Hz/K. Figure 4.11 shows the d-spacing of the 001 reflection of LiC_6 as a function of temperature which increases linearly with temperature. This is caused by the lattice expansion of the graphite along c-axis at elevated temperatures. At room temperature, $d = 3.705$ Å while at at 100 °C, $d = 3.715$ Å. The d-spacing therefore increases by $\Delta d = 13.3$ fm/K. Since the largest component of the ^{7}Li EFG tensor, V_{33}, points towards the graphite layers, parallel to the c-axis, the increase in d-spacing leads to a decrease in V_{33}, and hence C_q. A proportionality constant, A_{LiC6}, between C_q and Δd can be calculated for LiC_6, as $A_{\mathrm{LiC6}} = 3.6 \pm 0.5$ Hz/fm.

4.4.3 Motional Narrowing

Figure 4.12 shows the full width at half maximum (FWHM) of the central transition for LiC_{12} as a function of temperature. At low temperatures, when the Li motion is slow compared to

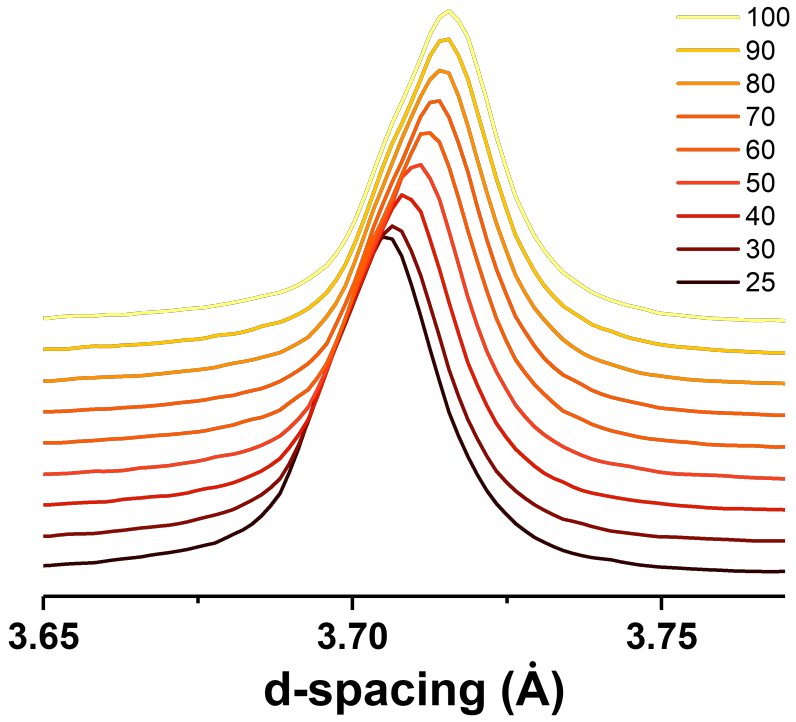

Figure. 4.11 d-spacing of the 001 peak of LiC_6 as a function of temperature from 25 - 100 °C. At 25 °C, the 001 peak is at $d = 3.705$ Å. As the temperature increases the d-spacing also increases. At 100 °C, $d = 3.715$ Å.

the spectral linewidth, the peak is broadened by dipolar interactions. The low temperature FWHM is 2875 kHz. This value is slightly lower than that measured by Langer *et al.*, 3.5 kHz for LiC_6.[36] This is expected since the measurements in this work were performed at a lower field, 4.7 T compared to 7.0 T and 11.7 T. Also the dipolar and quadrupolar couplings are lower in LiC_{12} than in LiC_6 (See Table 4.1).

The FWHM begins to slowly decrease at 241 K and then more rapidly decreases from 273 K. This is due to increased Li hoping which leads to motional averaging of dipolar coupling. The linewidth begins to narrow when the Li hoping frequency is on the order of the dipolar coupling strength *i.e.*, a few kHz. The temperature at which the motional narrowing begins, $T_{Mn} = 241$ K, allows us to estimate the activation energy for this Li hoping using the relation of Waugh *et al.* This gives $E_a = 1.62 \times 10^{-3} \times T_{Mn} = 0.39$ eV.[90,153] The point of inflection in Figure 4.12 occurs at 303 K. The Li hoping rate τ^{-1} can be estimated at this temperature from the linewidth in the low temperature limit ($\nu_0 = 2875$ Hz) such that $\tau^{-1} = 2\pi\nu_0 = 18$ kHz. At high temperatures, the residual linewidth of the central peak could be due to internal inhomogeneous magnetic fields that are not averaged by the Li hoping motion.

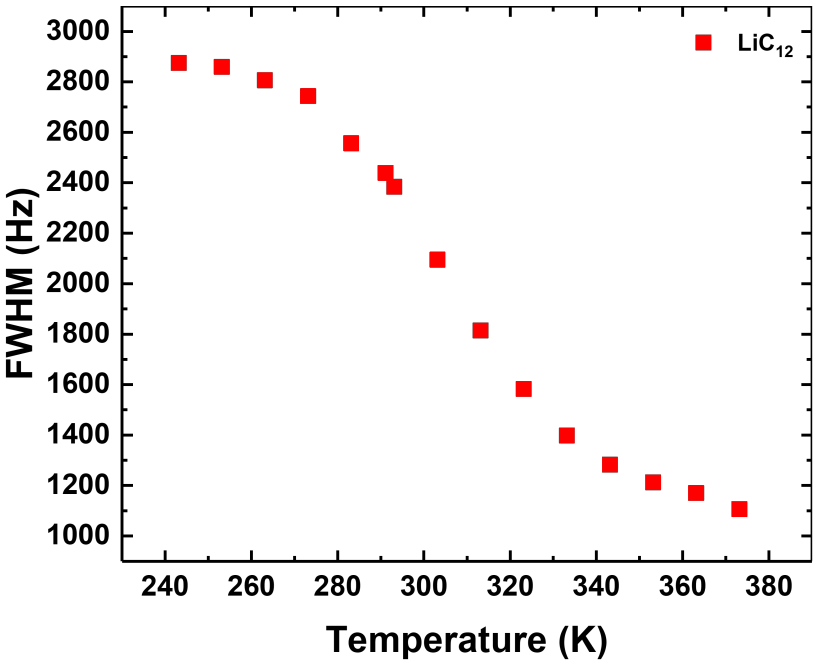

Figure. 4.12 The full width at half maximum (FWHM) of the ^{7}Li NMR central transition peak of LiC_{12} as a function of temperature. The linewidth decreases due to motional narrowing.

4.4.4 Relaxometry

T_1 Relaxation

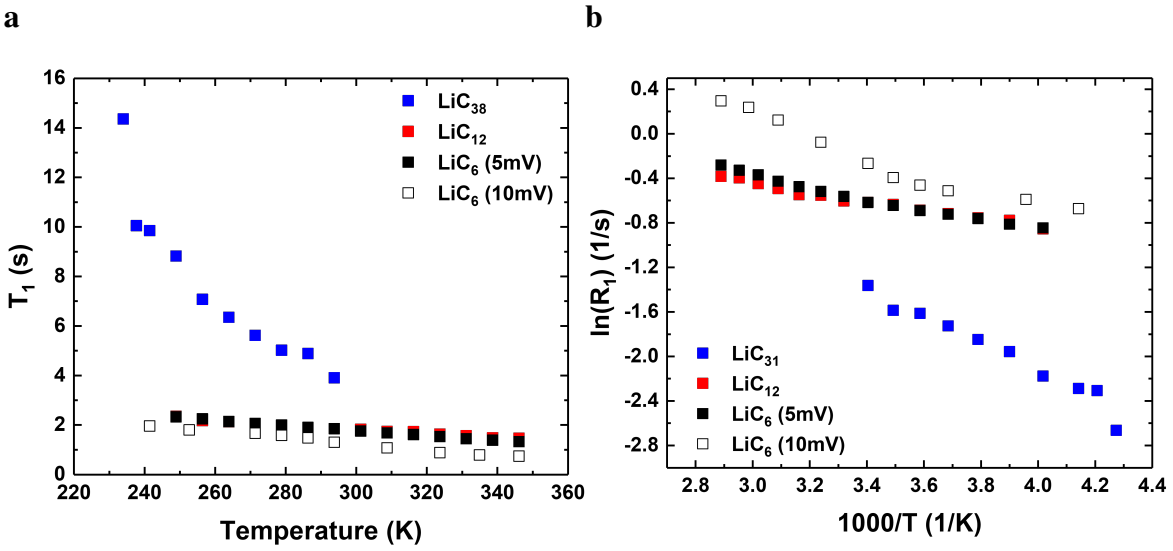

Figure. 4.13 a) ^{7}Li NMR spin-lattice relaxation times, T_1, as a function of temperature and b) the corresponding Arrhenius plot for LiC_{38}, LiC_{12} and LiC_6. Two LiC_6 samples are shown, one with a cut off voltage of 10 mV and the other 5 mV.

Figure 4.13a shows the spin-lattice relaxation times as a function of temperature and Figure 4.13b shows the corresponding Arrhenius plot for LiC_{38}, LiC_{12} and LiC_6. Two samples with a nominal composition of LiC_6 are shown in Figures 4.13a and 4.13b, one which had a cut off voltage of 10 mV and the other 5 mV. For LiC_{38}, $T_1 = 3.9$ s which is more than double that for LiC_{12} and LiC_6 which have the same room temperature spin-relaxation time $T_1 = 1.85$ s. The main reason for this difference is due to Korringa relaxation. At room temperature, the sample with a 10 mV cut-off voltage had a $T_1 = 1.31$ s, while for the sample with a 5 mV cut-off voltage it was 1.85. The differences in the capacities were small, with the 10 mV sample reaching 408 ± 5 mAh/g and the 5 mV sample reaching 418 ± 5 mAh/g.

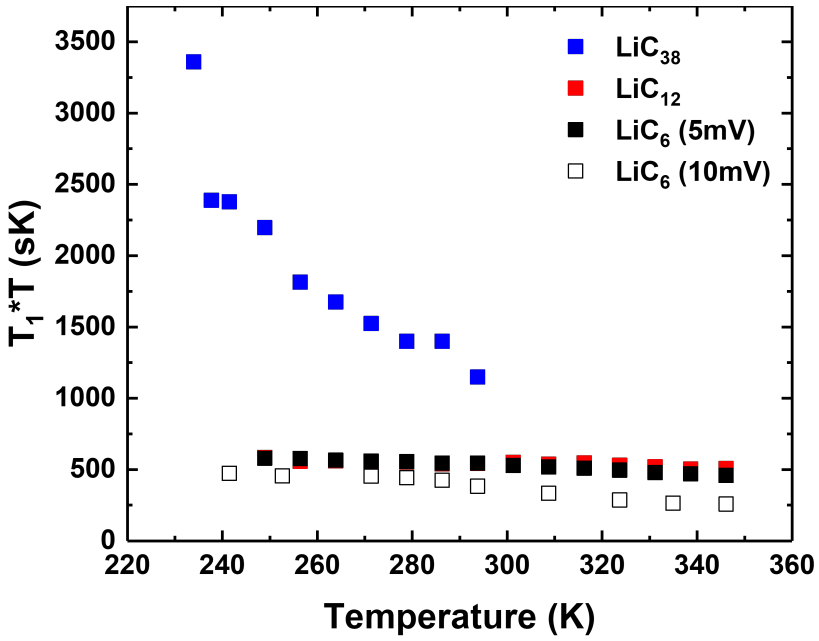

Figure. 4.14 ^{7}Li T_1 multiplied by temperature, T, as a function of temperature for LiC_{38}, LiC_{12} and LiC_6. Two LiC_6 samples are shown, one with a cut off voltage of 10 mV and the other 5 mV.

Figure 4.14 shows T_1 multiplied by temperature as a function of temperature. It is clear that T_1T is not constant with temperature for LiC_{38}. This shows the T_1 relaxation does not follow the Korringa relation and shows that motional effects dominate the T_1 relaxation. LiC_{12} and LiC_6 can both be fit well by a linear relation with $T_1T = 542 \pm 21$ sK and $T_1T = 528 \pm 39$, respectively. This shows that LiC_{12} and LiC_6 are metallic and the dominant relaxation mechanisms is Korringa relaxation. These values agree well with the values reported by Langer *et al.*, of $T_1T = 650 \pm 15$ sK and Estrade *et al.*, $T_1T = 600 \pm 120$ sK for LiC_6..[36,98] Dividing Equation 2.47 by the measured Knight shift for LiC_{12} ($\delta_{iso,LiC12} = 45.1$)

and LiC_6 ($\delta_{iso,LiC6} = 42.9$) gives $T_1T = 857$ sK and $T_1T = 947$ sK, respectively, in the case of non-interacting electrons *i.e.*, $\beta = 1$. The experimentally determined values of β for LiC_{12} and LiC_6 are $\beta = 0.63$ and $\beta = 0.55$, respectively. These were calculated by taking the ratio of T_1T determined from Figure 4.14 and from Equation 2.47 using the experimental Knight shift. The deviation from $\beta = 1$ shows that the relaxation is faster than that expected from purely metallic relaxation. This could be because electron-electron interactions are important or more likely, given that the ^{7}Li nuclide has a spin $I = 3/2$, that other relaxation mechanisms such as quadrupolar and dipolar relaxation are also important as well as motion of the Li ions.

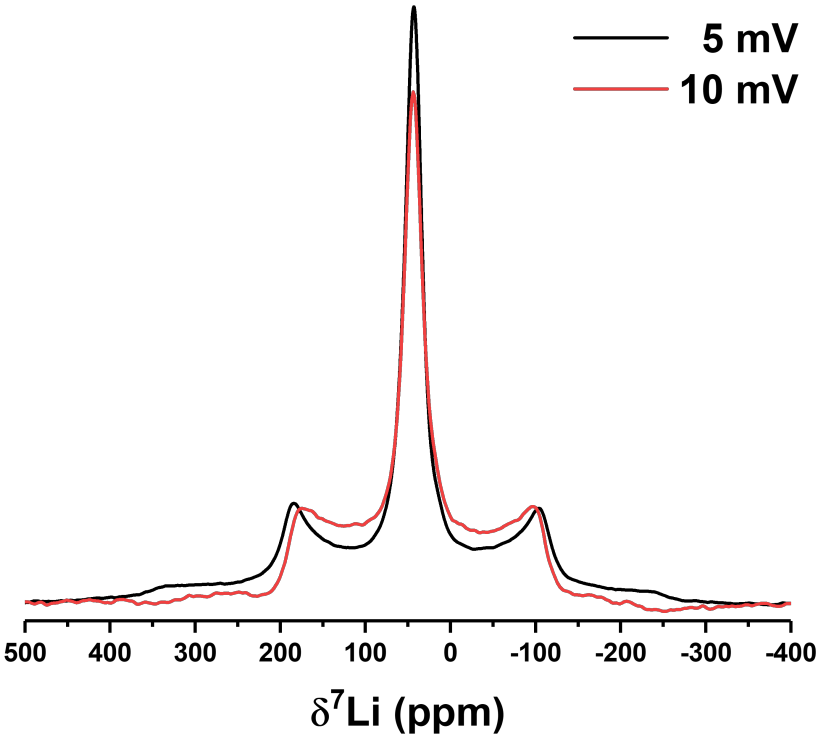

Figure. 4.15 ^{7}Li static NMR spectra of two LiC_6 samples. The samples were prepared by discharging a graphite half-cell to 10 mV and 5 mV, respectively, before holding the cells at this voltage for 10 hours.

A slight decrease in T_1T for LiC_{12} and LiC_6 away from their constant value is observed at high temperatures in Figure 4.14. Figures 4.13 and 4.14 also show that the T_1 relaxation of an LiC_6 sample with a higher cut off voltage, 10 mV instead of 5 mV, has a lower T_1 over the whole temperature range measured. Figure 4.15 shows a comparison of the room temperature static spectra of the 10 mV and 5 mV LiC_6 samples. From Figure 4.15 we find that the room temperature quadrupolar coupling is 42 kHz for the 10 mV sample compared to

Table 4.1 Nearest and next nearest Li-Li distances and corresponding dipolar coupling strengths calculated from Equation 2.33 for LiC_{38}, LiC_{12} and LiC_6. The quadrupolar coupling constant, C_q, measured at 241 K for LiC_{12} and LiC_6 and at 243 K for LiC_{38}. The corresponding quadrupolar coupling strength, calculated from Equation 2.34 is also shown for each sample.

Formula	**Li-Li Distance (Å)[a]**		**A_{dip} (Hz^2)**		**C_q**	**A_q**
	Nearest	**Next Nearest**	**Nearest**	**Next Nearest**	**(kHz)**	**10^6 (Hz^2)**
LiC_{38}	4.272	8.543	412	6.43	43	37.0
LiC_{12}	4.288	7.032[b]	403	20.7	38	28.9
LiC_6	3.700[b]	4.316	975	387	49	48.0

[a]The Li-Li distances are found from the crystal structure of stage 3 (LiC_{18}), stage 2 (LiC_{12}) and stage 1 (LiC_6) from the Inorganic Crystal Structure Database (ICSD).[154]
[b]These nearest and next nearest Li atoms in these cases are Li atoms in the adjacent graphite gallery.

48 kHz for the 5 mV sample. Both the 10 mV and 5 mV samples are mostly composed of the stage 1 compound as shown by the isotropic ^{7}Li shifts, 43.6 ppm and 42.9 ppm, respectively, this means the ^{7}Li nuclei should have similar local environments and therefore the dipolar coupling should be similar. This suggests that the decrease in $T_1 * T$ at higher temperatures is due to faster Li motion in the 10 mV sample.

For the case of spins interacting via homonuclear dipolar and quadrupolar coupling and undergoing isotropic random motion, the relaxation rate is given by Equation 2.32. The relaxation due to the dipolar and quadrupolar coupling interactions is additive. The interaction strength, A, is a linear combination of A_{dip} (Equation 2.33) and A_q ((Equation 2.34)) such that

$$R_1 = \left(C_1 A_{dip} + C_2 A_q\right)\left[\frac{1}{3}j(\omega_0) + \frac{4}{3}j(2\omega_0)\right] + \frac{TK^2}{S} \tag{4.6}$$

where and $0 < C_1, C_2 < 1$ are constants that determine the relative weight of each interaction on the relaxation rate.[87] A term TK^2/S, for Korringa relaxation, is also included in Equation 4.6 where $S = 1.744 \times 10^6$ sK^2 is the Korringa constant for ^{7}Li nuclei, T is temperature and K is the Knight shift. Table 4.1 gives a summary of the nearest and next nearest Li-Li distances that are used to calculate the strength of the homonuclear dipolar coupling, as well as the quadrupolar coupling at the lowest measured temperature for LiC_{38}, LiC_{12} and LiC_6.

The measured T_1 times are in the low temperature (slow motion) regime so we can simplify the correlation function (Equation 2.36) using $\omega_0\tau_c \gg 1$. For $I = 3/2$ and $\eta_Q = 0$ and inserting Equations 2.33 and 2.34, Equation 4.6 now becomes

$$R_1 = \frac{5}{6}\left(C_1\left(\frac{3{\mu_0}^2\hbar^2\gamma^4}{160\pi^2 r^6}\right) + C_2\left(\frac{{C_Q}^2}{50}\right)\right)\frac{1}{\omega_0^2\tau_0}\exp\left(-\frac{E_a}{k_B T}\right) + \frac{TK^2}{S}. \tag{4.7}$$

For LiC_{38}, the Knight shift contribution is small and motional effects dominate and we can determine the activation energy for Li ion motion from the gradient in Figure 4.13b. For LiC_{12} and both the 10 mV and 5 mV LiC_6 samples, where the relaxation is dominated by Korringa relaxation, to determine the activation energy for Li motion we first need to separate the diffusion induced relaxation from Korringa relaxation. To do this we subtract the Korringa relaxation rate from Equation 4.7 such that

$$R_1^{'} = R_1 - \frac{TK^2}{S}. \tag{4.8}$$

An Arrhenius plot of $R_1^{'}$ is shown in Figure 4.16. For comparison, the relaxation rate R_1 of LiC_{38} is also shown in Figure 4.16. Again we can find the activation energy of Li motion from the gradient of Figure 4.16. The activation energy for LiC_{38} is $E_a = 0.11 \pm 0.01$ eV. For LiC_{12} and both the 10 mV and 5 mV LiC_6 samples, we find an inflection point, where the gradient increases at $T = 301$, 279 and 294 K, respectively. This increase in gradient shows that above these temperatures the activation energy for Li motion increases, possibly because longer range Li motion occurs. The activation energy before (lower temperatures) and after (higher temperatures) the inflection point for LiC_{12} is $E_a = 0.04 \pm 0.01$ eV and $E_a = 0.07 \pm 0.01$ eV, respectively. For the 10 mV LiC_6 sample the activation energy before and after the inflection point is, $E_a = 0.04 \pm 0.01$ eV and $E_a = 0.14 \pm 0.01$ eV, respectively. While for the 5 mV LiC_6 sample, the activation energy before and after the inflection point is $E_a = 0.05 \pm 0.01$ eV and $E_a = 0.09 \pm 0.01$ eV.

The activation energies are highest in LiC_{38} and the 10 mV LiC_6 samples. This is compared to LiC_{12} and the 5 mV LiC_6 sample where the activation energy $E_a < 0.1$ eV. This suggests that the Li motion occurs over longer ranges in the LiC_{38} and the 10 mV LiC_6 samples than in the LiC_{12} and the 5 mV LiC_6 samples.[36,141] From Equation 4.7, the only reason the relaxation rate could be faster in the 10 mV sample compared to the 5 mV sample

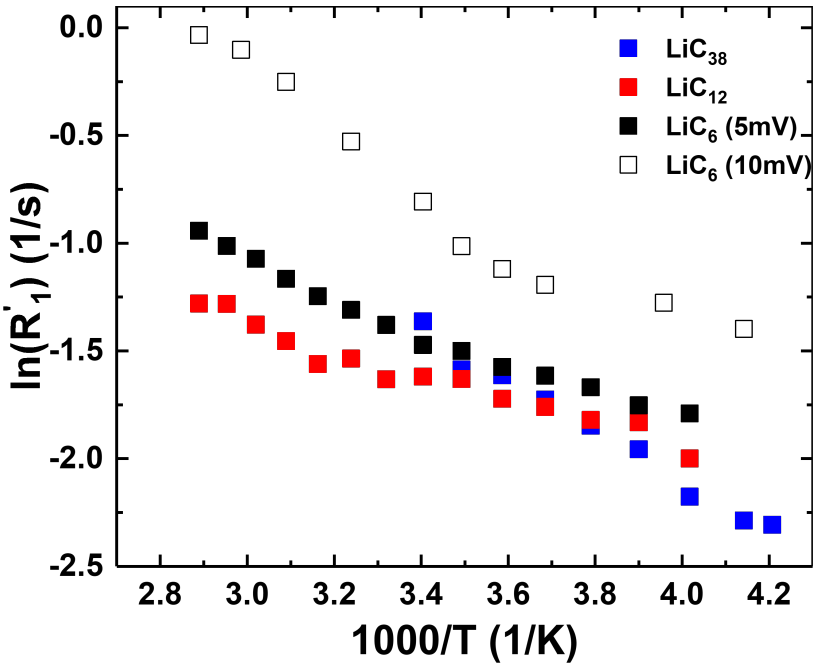

Figure. 4.16 Arrhenius plot ^{7}Li NMR spin-lattice relaxation rates, $R_1^{'}$, as a function of temperature for LiC_{38}, LiC_{12} and LiC_6. Two LiC_6 samples are shown, one with a cut off voltage of 10 mV and the other 5 mV. The relaxation rates for LiC_{12} and both LiC_6 samples were corrected to remove the relaxation rate due to Korringa relaxation and leave only relaxation due to Li motion, $R_1^{'}$. Using R_1 from Equation 4.7 this relaxation rate is given by $R_1^{'} = R_1 - TK^2/S$. The T_1 relaxation in LiC_{38} does not follow the Korringa relation as the relaxation is dominated by motional effects. For this reason the relaxation rate for this sample was not corrected.

is a higher Li jump rate, therefore the 10 mV sample must have faster Li motion. We also see in Figure 4.16 that this motion is activated at lower temperatures, 279 K in the 10 mV sample compared to 294 K in the 5 mV sample. This leads to the conclusion that the more completely lithiated the graphite is, the slower the Li motion. This intuitively makes sense since there would be less vacancies for the Li-ions to hop to.

In-situ NMR Relaxometry

The dependence of Li ion motion on the capacity was further examined by performing *in-situ* T_1 measurements. A GITT cycling protocol was used with 30 minute discharge pulses and an effective C-rate of C/20. Figure 4.17 shows the voltage profile of a graphite half-cell and the T_1 times as a function of capacity. The T_1 times for the dilute and dense stage ^{7}Li NMR environments are shown separately in Figures 4.17a and Figures 4.17b for clarity. The

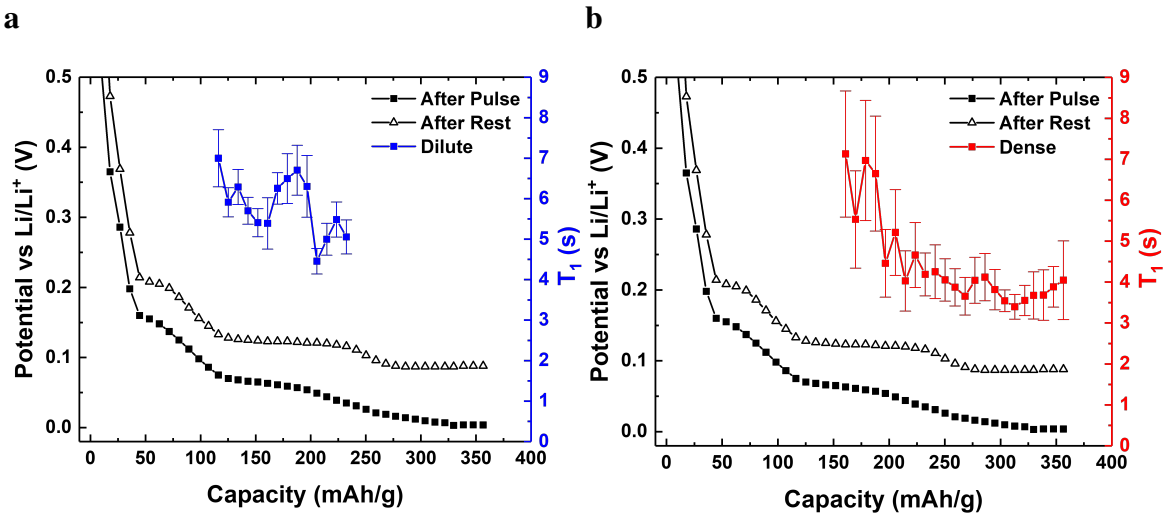

Figure. 4.17 voltage profile of a graphite half-cell and the T_1 times as a function of capacity for a) the dilute stage and b) dense stage ^{7}Li NMR peaks. Here the dilute stage peak is the peak that is observed when stages 4L - 2L are present and the peak occurs between 2 - 14 ppm. The dense stage peak is the peak that is observed when stages 2 and 1 are present and occurs between 50 - 43 ppm.

pressure in the PEEK capsule cells (Figure 4.2) is not as high as that which can be achieved in a steel coin cells and this leads to a higher overpotential. The lithiation staging mechanism of graphite is particularly sensitive to overpotentials since the difference in potential between some stages is < 30 mV. For this reason, both the potential after applying the 30 minute pulse and after the rest period are plotted as the transitions between stages are more clearly visible in the latter.

The overall trend observed in Figure 4.17 is that the ^{7}Li T_1 decreases with capacity, in agreement with the previous discussion. There are two points that deviate from this trend. Between $150-200$ mAh/g and $300-350$ mAh/g, the dilute and dense stage T_1 increases. The first point corresponds well with the point at which the dense stage 2 begins to form. We suggest that the increase in T_1 of the dilute stage environment could be due slower Li motion as a result of a "filling" of the 3L and 2L Li-GIC stages. It could also be due to an increase in the activation barrier for lithium intercalation into the stage 2 Li-GIC. We can see from Figure 4.10 that the quadrupole coupling also decreases between stages 2L and 2 and this could also lead to an increase in T_1. From 300 mAh/g onwards, during the formation of the LiC_6 phase, T_1 of the dense stage increases. With C_q increasing with capacity, at this point the only explanation for the increase in T_1 is slower Li motion. The final capacity was 360 mAh/g, but it is possible this trend could continue further if the lithiation continued to the

theoretical capacity of 372 mAh/g. Persson *et. al.*, also observed a decrease in the chemical diffusivity of Li ions with increasing "filling" of the dense stage 2 and stage 1 phases.[139]

$T_{1\rho}$ Relaxation

The T_1 is sensitive to Li hoping motion on time scales of the Larmor frequency *i.e.*, in the MHz range.[90] This rate of motion is only accessible at high temperatures which can not be accessed in Li−GIC due to degradation of the material, such as Li leaching, that occurs at these temperatures.[145] Therefore, in order to probe Li motion at temperatures which are more relevant to those used during operation of Li-ion batteries, $T_{1\rho}$ measurements were performed. The motion induced relaxation rate, $R_{1\rho} = 1/T_{1\rho}$ is governed by Equation 2.42 instead of Equation 2.32 for R_1.[87] The $T_{1\rho}$ measurements are therefore sensitive to Li hoping motion occurring on time scales on the order of $1/\nu_1$ *i.e.*, in the kHz range[36,87] This means that the motion induced maximum in the relaxation rate occurs at lower temperatures. It also means that the high temperature regime, where $\omega_1 \tau \ll 1$, is accessible at lower temperatures allowing us to probe ion dynamics occurring at longer length scales.[36]

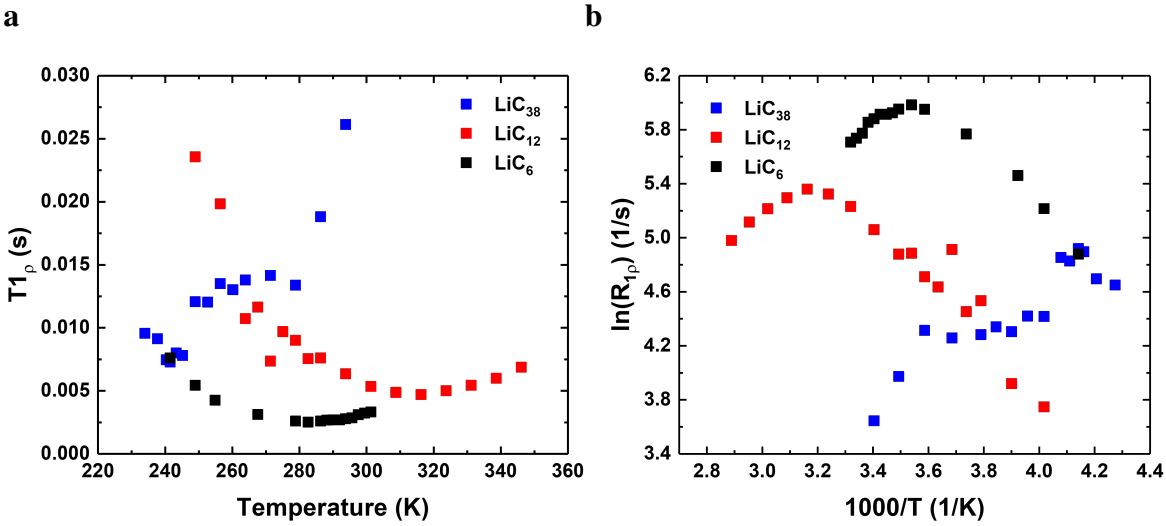

Figure. 4.18 a) ^{7}Li NMR spin-lattice relaxation in the rotating frame, $T_{1\rho}$, as a function of temperature and b) the corresponding Arrhenius plot for LiC_{38}, LiC_{12} and LiC_6.

Figures 4.18a and 4.18b show $T_{1\rho}$ and $R_{1\rho}$ as a function of temperature for LiC_{38}, LiC_{12} and LiC_6. $R_{1\rho}$ in Figure 4.18b is shown on an Arrhenius plot. For all three samples, a motion induced maximum in the relaxation rate is observed. For LiC_6, at 283 K, the maximum in the relaxation rate is $R_{1\rho} = 397\,s^{-1}$. For LiC_{12} the maximum, found at 316 K, is $R_{1\rho} = 213\,s^{-1}$. For LiC_{38}, we observe a maximum at 241 K of $R_{1\rho} = 137\,s^{-1}$ as well as a shoulder at 279

K where $R_{1\rho} = 75\,\mathrm{s}^{-1}$. This indicates there could be two motional processes driving the relaxation in the dilute stage LiC_{38} sample.

We can describe the $T_{1\rho}$ relaxation rates with a Bloembergen, Purcell and Pound (BPP) model.[155] Equation 2.42 can be simplified since $\omega_0\tau_c \gg \omega_1\tau_c$ so that the equation now becomes

$$R_{1\rho} = \left(C_1 A_{\mathrm{dip}} + C_2 A_{\mathrm{q}}\right)\left[j(2\omega_1)\right] \tag{4.9}$$

where again $0 < C_1, C_2 < 1$ are constants that determine the relative importance of the dipolar and quadrupolar interactions on the relaxation rate.[87] The spectral density function is given by

$$j(2\omega_1) = \frac{\tau_c}{1 + (2\omega_1\tau_c)^{\alpha}} \tag{4.10}$$

where α is an empirical constant that represents the asymmetry of the diffusion related peak in $R_{1\rho}$ which may occur as a result of any correlation effects.[36] The right hand side of Equation 4.10 can be simplified in the high temperature limit ($\omega_1\tau_c \ll 1$) and low temperature limit ($\omega_1\tau_c \gg 1$) to τ_c and $\omega_1^{-\alpha}\tau_c^{1-\alpha}$, respectively. Therefore, the relaxation rate in the high temperature limit is given by

$$R_{1\rho} = \left(C_1 A_{\mathrm{dip}} + C_2 A_{\mathrm{q}}\right)\tau_0 \exp\left(\frac{E_a}{k_B T}\right) \tag{4.11}$$

where τ_c is given by Equation 2.37 and in the low temperature limit by

$$R_{1\rho} = \left(C_1 A_{\mathrm{dip}} + C_2 A_{\mathrm{q}}\right)\frac{1}{\omega_1^{\alpha}\tau_0^{\upsilon-1}}\exp\left(\frac{-E_a}{k_B T}\right). \tag{4.12}$$

From the Arrhenius plot in Figure 4.18b, we can then extract the activation energies for the Li hoping motion from the gradient of the high and low temperature flanks of the maximum. For both LiC_6 and LiC_{12}, the activation energy of the high temperature and low temperature

flanks is $E_a = 0.18 \pm 0.2$ eV and therefore the relation rate curve is symmetric and so $\alpha = 1$. This shows that Li motion is similar in the high and low temperature regime for both LiC_6 and LiC_{12}.For LiC_{38}, the activation energy is difficult to extract, due to the multiple points of inflection but different fits give a range of $E_a = 0.1 - 0.4$ eV. The activation energies measured in this work are lower than that of LiC_6 ($E_a = 0.55$) eV determined by Langer *et al.*, via $T_{1\rho}$ and T_2 measurements.[36] The activation energy we measured is closer to the activation energy for an interstitialcy diffusion mechanism calculated by Toyoura *et al.*, and also agree well with the activation barriers determined by Perrson *et al.*[139,141] This suggests that diffusion via this mechanism is more important in the samples prepared in this work.

From Equation 4.10 we find the maximum relaxation rate occurs when $\omega_1 \tau_c = 0.5$. Using $\omega_1 = 2\pi \times 12$ kHz, this gives us a correlation time, $\tau_c = 6.63\,\mu$s. We can calculate a diffusion coefficient, D, from the correlation time can be using the Einstein-Smoluchowki Equation,

$$D = \frac{x^2}{2d\tau_c} \tag{4.13}$$

where x is the mean Li hopping distance and d is the dimensionality of the diffusion process. Here we used $d = 3$ and a hopping distance of 3 Å based on the mean hoping distance of all the mechanisms described by Toyoura *et al.*[141] We can then show that the diffusion coefficient for LiC_{38}, LiC_{12} and LiC_6 at 241 K, 316 K and 283 K, respectively is $D = 2.3 \times 10^{-11}$ cm^2s^{-1}. Figure 4.19 shows the dependence of the relaxation rate, $R_{1\rho}$, on the spin-locking frequency ω_1. As expected, using a lower frequency leads to a shift to lower temperatures of the relaxation rate maximum. These measurements were performed to try to probe the diffusive motion at temperatures closer to those relevant for Li-ion batteries. From Figure 4.19 we can see that when $\omega_1 = 2\pi \times 8$ kHz a diffusion induced maximum in the relaxation rate occurs at 309 K with $R_{1\rho} = 833\,s^{-1}$. The resulting diffusion coefficient from Equation 4.13 is $D = 1.5 \times 10^{-11}$ cm^2s^{-1}. The diffusion coefficients for LiC_{12} and LiC_6, are extrapolated to room temperature assuming Arrhenius behaviour. The results are summarised in Table 4.2 and are in good agreement with those found in the literature.[36,135,142] The diffusion coefficients found by $T_{1\rho}$ measurements differ by three orders of magnitude from the diffusion coefficient calculated from the GITT measurements (Figure 4.4). The diffusion coefficient, determined from GITT measurements, gives the chemical diffusion coefficient, D_C, while the $T_{1\rho}$ measurements are measured under equilibrium conditions and gives the self-diffusion coefficient, D_S. Typically D_C is larger than D_S, as it is enhanced by the thermodynamic factor (Equation 4.1).[140] The difference could also be because NMR

probes local Li motion while GITT measurements probe bulk Li diffusion as well as a possible over estimation of the surface area in Equation 4.2. Additionally, the diffusion coefficient from the GITT measurement is calculated assuming Fickian diffusion which may not be valid during the lithiation of graphite, whereas, the diffusion coefficient measured by NMR has no such assumptions.

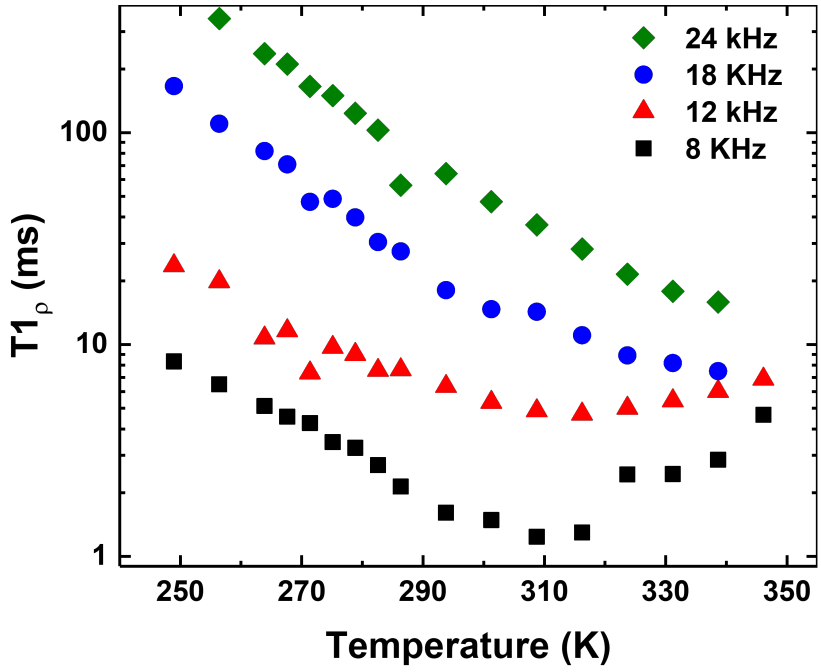

Figure. 4.19 ^{7}Li NMR $T_{1\rho}$ as a function of temperature and and spin-locking pulse frequency, $\omega_1 = 2\pi\nu_1$, for LiC_{12}.

The relative importance of the dipolar and quadrupolar interactions towards Li motion dependent relaxation can also be determined from the rate peak maximum. At the rate peak maximum $\tau_c\omega_1 = 0.5$. Inserting this limit into Equation 4.9 we find

$$A = \left(C_1 A_{\text{dip}} + C_2 A_{\text{q}}\right) = \frac{2R_{1\rho}}{\tau_c}, \tag{4.14}$$

where we use the value of $\tau_c = 6.63\,\mu$s that was previously calculated. From this we can show that for LiC_{38}, LiC_{12} and LiC_6 the interaction strength is 41, 64 and 120 $\times 10^6$ Hz^2, respectively. Comparing to the values in Table 4.1, indicates that the quadrupolar interaction is the dominant interaction that drives $T_{1\rho}$ relaxation. For LiC_{38}, the interaction strength is close to A_q in Table 4.1, while for LiC_{12} and LiC_6, is larger than that predicted from the

Table 4.2 Comparison of lithium diffusion coefficients, D_{Li}, and activation energies, E_a, measured with different techniques. Where E_a was determined, the diffusion coefficient at room temperature (298 K) was also calculated, assuming Arrhenius behaviour.

Compound	**Technique**	D^*_{Li} **cm^{2}s^{-1}**	E_a **(eV)**	D_{Li} **at 298 K cm^{2}s^{-1}**
LiC_6	$T_{1\rho}$ (314 K)[36]	1.9×10^{-11}	0.55	6.4×10^{-12}
	$T_{1\rho}$ (283 K)**	2.3×10^{-11}	0.18	3.3×10^{-11}
	μ^+ SR (310 K)[142]	7.6×10^{-11}	0.27	5.1×10^{-11}
	PITT & EIS (298 K)[135]	1×10^{-9}		
	GITT (298 K)**	1.9×10^{-14}		
LiC_{12}	μ^+ SR (310 K)[142]	14.6×10^{-11}	0.17	1.1×10^{-11}
	$T_{1\rho}$ (316 K)**	2.3×10^{-11}	0.18	1.5×10^{-11}
	PITT & EIS (298 K)[135]	1×10^{-9}		
	GITT (298 K)**	1.9×10^{-14}		
LiC_{38}	$T_{1\rho}$ (241 K)**	2.3×10^{-11}	0.1 - 0.4	$5.8-91.6\times10^{-11}$
	PITT and EIS (298 K)[135]	3×10^{-10}		
	GITT (298 K)**	9.5×10^{-15}		

*D_{Li} calculated via electrochemical techniques, represent the chemical diffusion coefficient, while D_{Li} from ^{7}Li NMR $T_{1\rho}$ and Muon spin relaxation measurements, represent the self-diffusion coefficient.
**This work

values of A_q and A_{dip} in Table 4.1. This could be because the value of C_q, used in Equation 2.34 to calculate A_q, should be the low temperature steady state value, which we were not able to measure at the temperatures used in this work. If we assume that the quadrupolar interaction dominates the Li induced relaxation, then we can use the calculated values of A to estimate the low temperature steady state values of C_q for each sample. For LiC_{38}, LiC_{12} and LiC_6 the estimated steady values of C_q are 45, 57 and 77 kHz, respectively.

Figure 4.20 shows the temperature at which the maximum in the relaxation rate $R_{1\rho}$ occurs LiC_{38}, LiC_{12} and LiC_6 when $\omega_1 = 2\pi\times12$ kHz. The data is overlayed on to the voltage profile to show the capacity at which the relaxation rates were found. Assuming an Arrhenius behaviour, Figure 4.20 therefore shows that the Li motion at ambient temperatures is fastest for the dilute stage LiC_{38} and slowest for LiC_{12}. The trend in the Li motion as a function of state of charge agrees well with the observations of Persson *et al.*[139] For LiC_{12} and LiC_6, the Li hoping rates at room temperature (298 K) are $\omega_{LiC12} = 14$ kHz and $\omega_{LiC6} = 31$ kHz. We can also show that the Li diffusion coefficients are the same for LiC_{38}, LiC_{12} and LiC_6 at 241 K, 316 K and 283 K, respectively. The faster Li diffusion in the dilute

stages could be one reason, along with the steady state potential of the dilute stages being further above 0 V than the dense stages, why Li metal does not plate on to graphite at lower temperatures at low states of charge, while for similar charging rates at high states of charge Li metal plating does occur at low temperatures.[41]

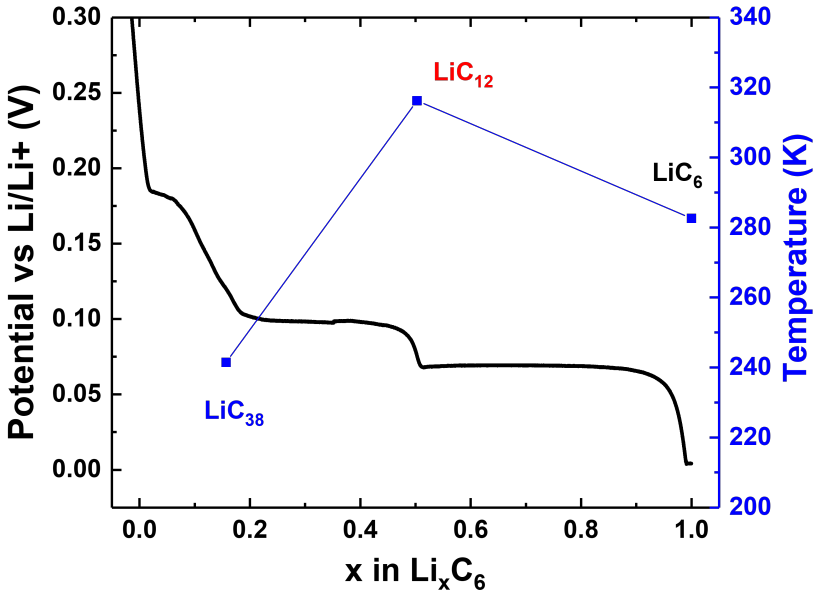

Figure. 4.20 Room temperature $T_{1\rho}$ values for LiC_{38}, LiC_{12} and LiC_6 as a function of capacity and x in Li_xC_6 overlayed on to the potential profile of a graphite half-cell.

T_2 Relaxation

Figures 4.21a and 4.21b show the T_2 as a function of temperature for LiC_{38}, LiC_{12} and LiC_6. Figure 4.21a shows the relaxation time, T_2 while Figure 4.21b shows an Arrhenius plot of the relaxation rate R_2. For LiC_{12} and LiC_6, T_2 initially increases with temperature. For LiC_{12} T_2 increases from 2.3 ms at 249 K to 5.1 ms at 301 K while for LiC_6 T_2 increases from 1.8 ms at 241 K to 3.3 ms at 268 K. Between 301 - 324 K and 268 - 288 K T_2 remains constant at 5 ms and 3.3 ms for LiC_{12} and LiC_6, respectively. Then as the temperature increases further T_2, increases reaching 7 ms and 10.8 ms, respectively for LiC_{12} and LiC_6 at 346 K.

The initial increase in the T_2 from 249 - 310 K for LiC_{12} coincides well with the decrease in the FWHM of the central transition (Figure 4.12). This shows that the reason that T_2 increases with temperature is due to increasing Li hoping which leads to averaging of dipole-dipole interactions. The same explanation can therefore be given for the increase in T_2 for LiC_6 between 241 - 268 K. The temperature at which the T_2 begins to increase after the

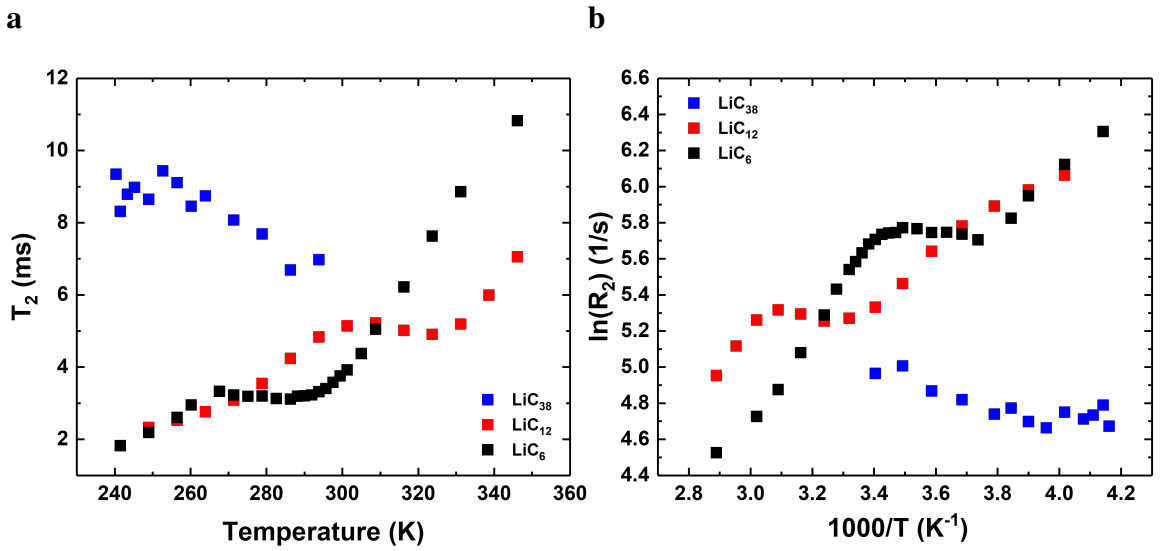

Figure. 4.21 a) ^{7}Li NMR spin-spin relaxation times, T_2, as a function of temperature and b) the corresponding Arrhenius plot for LiC_{38}, LiC_{12} and LiC_6.

plateau, coincides well with the temperature at which the $T_{1\rho}$ minima occur for both LiC_{12} and LiC_6. Beyond these temperatures we therefore enter the fast motional regime. This means that the further increase in T_2 observed for LiC_{12} and LiC_6 could be due to further averaging of dipolar couplings or could be due to the decrease in the C_q that occurs due to lattice expansion.

For LiC_{38}, the T_2 remains relatively constant in the temperature range that was probed. As shown by the $T_{1\rho}$ measurements we expect to be in the high temperature regime above 240 K. This means that the dipolar coupling, which is smaller than in LiC_{12} and LiC_6 (Table 4.1), should already be averaged out at this point. Owing to the lower temperature range probed for LiC_{38} it is unclear whether the T_2 will increase at higher temperatures as for LiC_{12} and LiC_6. From Figures 4.13, 4.18 and 4.13 we can see that for LiC_{38}, LiC_{12} and LiC_6 that R_2 and $R_{1\rho}$ are approximately equal and R_1 is around 2 to 3 orders of magnitude slower. This shows that the R_1 relaxation is less sensitive to the motionally driven relaxation that drives the R_2 and $R_{1\rho}$ relaxation.

4.5 Discussion

The ^{7}Li NMR and XRD results, in Section 4.4.2, show that electrochemically lithiated graphite is not stable at elevated temperatures. These results agree well with those of Liu *et al.*, who reported synchrotron XRD and mass spectroscopy results of thermal degradation

of electrochemically lithiated graphite.[145] They showed that beginning as low as 40 °C, polyethylene oxide (PEO), a major component in the organic layer of the SEI in LIBs, begins to decompose.[145,156] They also showed that at the same time as the SEI breaks down, lithium leaching also occurs. the Upon further heating, the graphite continues to delithiate until, at 280°C, the graphite returns to the 2H phase with the extracted Li mainly converted to LiF and Li_2O. These results explain why a decrease in the intensity observed in the VT ^{7}Li NMR experiments and suggest that Li leaches out of the graphite due to redox reactions between SEI breakdown products and the Li in the Li-GIC.

The recycle delays used in ^{7}Li VT Hahn-Echo experiments (Figure 4.7) were based on the T_1 of the Li-GIC compounds. LiF and Li_2O are expected to have a longer T_1 than that of lithiated graphite as they are diamagnetic and the contribution of quadrupolar relaxation is likely small. The signals, $\delta_{\mathrm{LiF}} = -1$ ppm and $\delta_{\mathrm{Li2O}} = 2.8$ ppm will also overlap with those of residual SEI components, as well as dilute stage Li-GIC.[157] A summation of the last 10 XRD scans (Figure B1) acquired at 100 °C show the presence of a broad peak at $2\theta = 38.55°$ which can be attributed to the 111 peak of LiF.[145]

The Li leaching could also explain the differences in the activation energies for Li motion in LiC_6 in this work ($E_a = 0.18 \pm 0.2$ eV) and in the work of Langer *et al.*, ($E_a = 0.55$ eV).[36] The different diffusion mechanisms could occur due to differences in sample preparation.[36] While both activation energies were determined using ^{7}Li NMR $T_{1\rho}$ measurements, Langer *et al.*, prepared the LiC_6 compound via vapour-phase intercalation of Li into polycrystalline graphite.[36] This means there was either no SEI or the SEI was very different to the SEI on the Li-GIC samples prepared electrochemically in this work. The crystallite size was 500 µm, while the Hitachi Mage 3 graphite used in this work had a crystallite size of 200 nm and particle size of 30 µm.[21,36] The SEI and higher surface area of the Li-GIC samples prepared in this work, will lead to greater Li leaching than in the samples prepared by Langer *et al.* The increased rate of Li leaching, may have an effect on Li dynamics and could be one reason why the activation energy was found to be lower in this work, as greater Li leaching could introduce more Li vacancies.

Langer *et al.*, had a better fit to their $T_{1\rho}$ results in LiC_6 when they used a modified BPP model.[36] BPP models are typically used to describe three dimensional isotropic diffusion. When low dimensional diffusion occurs $(d < 3)$, the high temperature regime will have a smaller slope than expected by the BPP model. The slopes in Figure 4.18b for LiC_{12} and LiC_6 in both the high and low temperature regimes are equal suggesting the three dimensional BPP mode should fit well. This would be clearer if more data points were taken at higher temperatures. For LiC_{38}, only the high temperature regime is observed. Persson *et al.*, also

showed that three dimensional diffusion occurs in graphite. They found that the diffusion coefficients of Li motion perpendicular and parallel to the graphene planes in HOPG graphite are, $D = 8.7 \times 10^{-12}$ cm^{2}s^{-1} and $D = 4.4 \times 10^{-6}$ cm^{2}s^{-1}, respectively.[139] Three dimensional diffusion may occur through defects in the graphite basal plane.

The observed trends in T_2 (Figure 4.21) are more complex than those shown by Langer *et al.*, for LiC_6.[36] This could again be due to the difference in how the samples are prepared and the size of the graphite particles used. The change in structure with temperature, with the *d* spacing increasing (Figure 4.11) and Li leaching occurring also complicates the analysis since the Equations in Section 2.2.3 are derived based on the assumption that the structure does not change with temperature.[87]

4.6 Conclusions

The Li-ion dynamics, of Li intercalated into graphite, were studied as a function of discharge capacity during the first discharge cycle, using *ex-situ* and *in-situ* ^{7}Li NMR, relaxometry and GITT measurements. Previous ^{7}Li NMR studies of Li-ion dynamics in graphite have focused on HOPG graphite prepared through a chemical route, whereas in this work we used a battery grade graphite prepared electrochemically meaning the results should reflect more closely the Li-ion dynamics in a commercial LIB.

Diffusion coefficients calculated using GITT measurements, exhibited a trend of peaks and minima as a function of capacity. The minima coincide with the plateaus in the voltage profile which occur during first-order phase transitions. The peaks coincide with sloped regions in the voltage profile which occur during solid solution phase transitions. The trend was explained by taking into account the attractive interactions between Li-ions, with new phases, that form during a first-order phase transition, growing as droplets within the existing phase. The growth of the new phase was shown to follow a Frumkin isotherm, with strong attraction between the Li-ions. These attractive interactions, lead to a decrease in D_c in two-phase regions, compared to single-phase regions. The diffusion coefficient minima during first-order phase transitions, is higher in the dilute stage regions compared to dense stage regions. D_c is also higher during the solid-solution phase transitions between dilute stages, compared to the minima in D_c, observed during the first-order phase transitions that occur during the formation of the dense stages.

VT NMR (Figure 4.7) and XRD measurements (Figure 4.9) showed that Li leaching occurs when the temperature is increased above room temperature. The onset of Li leaching, occurred at 286 K, 316 K and 294 K, for LiC_{38}, LiC_{12} and LiC_6, respectively. In agreement with the results of Liu *et al.*, an increase in Li in diamagnetic regions as well as the LiF and LiO_2 seen in the VT XRD and NMR measurements.[145] This was due to the breakdown of the SEI which occurs above 40 °C and results in Li leaching out of the Li-GIC structure due to redox reactions that occur between the Li and the SEI. This shows a clear degradation pathway for lithiated graphite anodes at temperatures near to their operating temperatures. VT XRD measurements also showed that the d-spacing in LiC_6 increases by $\Delta d = 13.3$ fm/K between room temperature and 373 K. The increase in d-spacing leads to a decrease in V_{33}, and hence C_q. A proportionality constant, A_{LiC6}, between C_q and Δd was calculated for LiC_6, as $A_{\mathrm{LiC6}} = 3.6 \pm 0.5$ Hz/fm. The increased d-spacing at elevated temperatures, could also contribute to Li leaching reaction, as the energy barrier for Li-migration decreases, when d increases.[158]

^{7}Li T_1 measurements showed, through the Korringa relation, and in agreement with the results in Chapter 3, that LiC_{12} and LiC_6 are metallic, while LiC_{38} is not. The relaxation for LiC_{12} and LiC_6 was found to be faster than expected from purely Korringa relaxation. This was shown via $T_{1\rho}$ measurements to be due to Li motion which leads to relaxation via the dipolar and quadrupolar coupling interactions, with the quadrupolar coupling shown to be the more important interaction. The activation energy for Li motion, suggests that Li motion proceeds mainly via a two stage interstitialcy mechanism. Diffusion coefficients calculated from $T_{1\rho}$ measurements, using the Einstein-Smoluchowki Equation showed that $D = 2.3 \times 10^{-11}$ cm^{2}s^{-1} for LiC_{38}, LiC_{12} and LiC_6 at 241 K, 316 K and 283 K, respectively. Assuming an Arrhenius behaviour, this shows that the Li motion at ambient temperatures is fastest for the dilute stage LiC_{38} and slowest for LiC_{12}.

The trend in the Li motion as a function of state of charge agrees well with observations of Persson *et al.*[139] The trend also agrees well with the GITT measurements shown in this work, though D is three orders of magnitude lower when measured via GITT. The difference could be because NMR probes local Li motion while GITT measurements probe bulk Li diffusion as well as a possible over estimation of the surface area in Equation 4.2. The lower values could also be affected by the validity of Equation 4.2 as it assumes that Fick's law of diffusion applies which may not be valid during the lithiation of graphite in the two phase regions when phase boundaries are also diffusing. This trend in Li motion as a function of stage of charge could help to explain why Li metal does not plate on to graphite at lower temperatures at low states of charge, while for similar charging rates at high states of charge Li metal plating does occur at low temperatures.[41]

In this work we have shown that the Li-ion dynamics depend on the state of charge. Although the magnitude of the diffusion coefficients from the GITT and ^{7}Li NMR relaxometry measurements differed by three orders of magnitude, likely due to probing of different length scales, the trend in the Li-dynamics as a function of state of charge was similar. We can conclude that faster Li motion occurs in the dilute stages compared to the dense stages during Li-intercalation into graphite. This understanding could help design advanced charging protocols in batteries for fast charging applications which prevent Li-metal plating. The results presented here could also be used to improve computational models of graphite lithiation. The understanding gained in the work can be further applied to investigate the lithiation mechanism of different graphite materials, such as natural graphite. It is important to understand any differences in the Li-ion dynamics which determines how fast these materials can be dis/charged. Only the first discharge cycle was looked at in this work. The

study could be extended to look at the Li-ion dynamics during charging as well as to look how the Li dynamics change as a function of cycle number.

Chapter 5

Prelithiation of Silicon Graphene Anodes

5.1 Abstract

The electrochemical cycling performance of silicon-graphene anodes, produced by a conventional shear mixing technique and a novel and highly scalable co-microfluidization technique, were tested in half-cell and full-cell configurations. The performance of electrodes produced with two different silicon nanoparticles were compared. Co-microfluidization of silicon-graphene anodes produced with 300 nm silicon nanoparticles outperformed electrodes produced by conventional shear mixing.

Prelithiation via chemical lithiation was investigated as a means to enhance the cycle life of the silicon-graphene anodes and compensate for Li loss due to SEI formation. It was shown via Raman spectroscopy and *ex-situ* and *in-situ* ^{7}Li NMR to lead to a deeper lithiation than could be achieved by electrochemical lithiation during initial formation cycles. This deeper lithiation leads to an increase in the coulombic efficiency compared to when the electrodes were cycled without prelithiation. Prelithiation of silicon-graphene anodes was also shown to improve the cycle performance when cycled against an NMC622 cathode in a full-cell configuration.

Variable temperature ^{7}Li NMR and relaxometry measurements showed that the peak attributed to the crystalline c-$Li_{3.75}Si$ phase was the result of two chemically exchanging ^{7}Li environments. At low temperatures, the c-$Li_{3.75}Si$ peak separated into two peaks which were attributed to Li near isolated Si and Li tetrahedrally coordinated to Si.

5.2 Introduction

As discussed in Chapter 1, Si anodes are one of the most promising materials that could enable higher energy density batteries. Commercial Si anodes with high Si content have still not been realised due to the large volume expansion (300%) that occurs when silicon is fully lithiated to the c-$Li_{3.75}Si$, this should be compared to graphite which expands by $\sim$ 10%.[25,43] This large volume expansion and contraction, and concomitant continuous SEI formation during cycling, leads to increased impedance and capacity fade. In full-cell testing, the irreversible consumption of Li and the decomposition of the electrolyte that occur due continuous SEI formation both contribute to capacity fade.[159]

In half-cell testing, the CE is an important parameter that can be used to predict the cycle performance of a material in a full-cell. This is because the CE, or coulombic inefficiency (CI) ($CI = 1 - CE$), is a good measure of the irreversible capacity lost due to SEI formation.[160] A commonly accepted industry standard is that a battery is "dead" when the capacity has reached 80% of its initial value. If the average CE value is 99.9%, then the cumulative CI exceeds 20% after 200 cycles. During cycling of silicon nanoparticle (SiNP) electrodes, the initial coulombic efficiency (ICE) typically does not exceed 90% for anodes with high silicon content ($\geq$ 10%) that are not prelithiated.[161–165] The ICE has been shown to depend on the particle size, morphology and surface oxidation of the SiNPs, as well as the additive concentration in the electrolyte.[162,163] During further cycling, the CE increases and eventually stabilizes as the SEI becomes more stable.[160] For silicon anodes with high Si content, the CE typically stabilises to values around 99.5% though in some cases, it reaches 99.9%.[160] For a CE value of 99.5%, the cumulative CI exceeds 20% after 45 cycles.

The size and morphology of SiNPs affects the cycle performance of silicon anodes. Zhu *et al*. reported on the differences in cycle performance of flaky and spherical SiNP electrodes.[162] They showed that flaky SiNPs have a higher surface area to volume ratio than spherical SiNPs, as well as a thicker surface oxide layer. The cycle performance of the spherical SiNPs is greater than for flaky SiNPs. They also showed that this was due to the increased stability of the SEI formed on the spherical SiNPs and that SiNP agglomeration is detrimental to the cycle performance of silicon anodes.[162]

Carbon coatings and additives have been widely used as a method to enhance cyclability as well as the electronic conductivity of silicon electrodes.[166–170] The carbon coatings can also help manage the stress and strain of the electrode that occurs when the silicon is lithiated, as well as reduce pulverisation.[171] The SEI formed on carbon is also much more stable than that formed on silicon due to the lower volume expansion, and so carbon coatings

can help improve the CE of silicon anodes.[167] Liu *et al.*, synthesized silicon nanoparticles encapsulated in carbon. The structure contained void space that silicon nanoparticles could expand into without cracking the carbon coating and resulted in a stable SEI formation. As a result, they were able to achieve 97% capacity retention with a capacity of 1160 mAh/g after 1000 cycles.[167]

Graphene has also been widely used in silicon electrodes.[172–176] The high strength and good electrical conductivity, even under strain, of graphene has been shown to improve cyclability as well as conductivity of silicon anodes, which is important for long cycle life and fast charging.[172,175] Also, the high aspect ratio of graphene improves the connectivity of silicon nanoparticles and helps to prevent pulverisation of the electrode.[177] Graphene has also been shown to increase the capacity retention of high silicon content anodes by preventing agglomeration of silicon particles during cycling.[178,179]

Prelithiation of anodes is an important technique that can improve capacity retention in LIBs by reducing the amount of Li from the cathode that is irreversibly consumed during the first cycle during SEI formation.[180] This is particularly important in silicon anodes, where the first cycle CE is lower than in graphite and is one of the main causes of capacity loss in full-cells. Various prelithiation techniques exist, such as the introduction of stabilized Li metal powder or Li_xSi nanoparticles into the electrode slurry before casting.[181,182] Lithiation via shorting of the anode against a Li metal electrode has also been used as a method for prelithiation.[183,184] The later technique is done in the presence of electrolyte and so an SEI is formed during this process.[184] A further benefit of prelithiation of anodes is that they can then be made into a full-cell with high capacity cathodes such as sulfur and MnO_2, which do not contain Li, unlike more conventional cathodes such as LCO.[185,186] Kim *et al.* also showed that controlled prelithiation of silicon monoxide (SiO_x, $x \approx 1$) anodes, accelerated the activation of Si domains that usually take a few cycles to become electrochemically active.[183,187] These Si domains are lithiated once the electrode has expanded and the electrolyte can penetrate more easily.[187] Kim *et al.* were able to show a high ICE of 94.9% with SiO_x anodes (which usually suffer from low ICE) prelithiated via this technique.

In many SiNP electrodes, after an initial increase, the CE dips in the first ~ 50 cycles before recovering again and increasing with cycle number.[161–163] Ogata *et al.* found that the dip in CE was more pronounced and the CE recovered to a higher value more quickly when the depth of lithiation was higher.[161] They found that the dip in CE was associated with the formation of the c-$Li_{3.75+\delta}Si$ phase, with parasitic reactions that occur between this metastable phase and the electrolyte resulting in an increase in irreversible Li consumption.[54,161] They then showed that as the CE increases to a stable value after the dip, that the

overlithiated c-$Li_{3.75+\delta}Si$ phase no longer forms at the end of discharge, which also results in a decrease of the specific capacity. They attributed this, using electron microscopy measurements, to structural changes in the Si, which becomes dominated by smaller, more uniform a-Si regions after long-term cycling. These structural changes lead to more homogeneous lithiation of the silicon. Repeated formation of the c-$Li_{3.75+\delta}Si$ was also shown to accelerate the structural changes of the silicon.[161]

Four crystalline lithium silicide phases have been reported in the binary phase diagram, $Li_{12}Si_7$, Li_7Si_3, $Li_{13}Si_4$ and $Li_{21}Si_5$; however, none of these form during the electrochemical lithiation of Si at room temperature.[54,188] ^{7}Li NMR has been shown to be an important tool to understand the lithiation mechanism Si anodes.[54,189] The ^{7}Li resonances of Li near large Si clusters, with stoichiometry $Li_{0-2}Si$, occur between 0 - 10 ppm. For Li near small Si clusters with stoichiometry $Li_{2-3.5}Si$, the resonances occur at higher frequencies between 10 - 25 ppm. For stoichiometries between $Li_{3.5-3.75}Si$, including the crystalline phase c-$Li_{3.75}Si$), the resonances decrease in frequency to 0 - 6 ppm. For the overlithiated crystalline phase, c-$Li_{3.75+\delta}Si$, the resonances decrease further in shift to 0 - -10 ppm.[54] The c-$Li_{3.75+\delta}Si$ phase can accommodate around $\delta = 0.55 - 0.6$ extra Li ions without any structural changes compared to the c-$Li_{3.75}Si$ phase.[54] The c-$Li_{3.75+\delta}Si$ phase is metastable as it reacts with the electrolyte via a self-charge (half-cell) mechanism.[54] *In-situ* and *operando* ^{7}Li NMR measurements are useful techniques to study this phase, Key *et al.* observed a gradual decrease in the intensity of the c-$Li_{3.75+\delta}Si$ peak after a cell was discharged to 0 V and allowed to rest at OCV.[54] If the sample is washed to remove residual electrolyte and soluble SEI components and quickly packed into a rotor then the c-$Li_{3.75+\delta}Si$ signal can be observed in *ex-situ* ^{7}Li NMR measurements.[54]

Dupke *et al.* investigated the Li ion dynamics within chemically synthesized lithiated silicon by measuring the motional narrowing of static ^{6}Li and ^{7}Li NMR peaks as a function of temperature.[190] They showed that with increasing Li content, the mobility of the Li ions decreases. This trend was understood in terms of an increasing amount of charge localized on the Si atoms, with an increasing Li to Si ratio leading to stronger Coulomb interactions.[190] They also showed, in agreement with the PDF results of Key *et al.*, that the c-$Li_{3.75}Si$ contains two local Li environments.[53,190] Li is located slightly below a triangle of isolated Si in one environment (c-$Li_{3.75}Si$ a) (d(Li–Si) = 2.61, 2.71 and 2.81 Å) and tetrahedraly coordinated to Si in one environment (c-$Li_{3.75}Si$ b) (d(Li-Si) = 2.86 Å) All Si-Si bonds are broken within this phase. The c-$Li_{3.75}Si$ a environment possesses a lower positive charge than the c-$Li_{3.75}Si$ b environment.[190]

Baran *et al.* measured the ^{7}Li T_1 as a function of temperature of chemically synthesized c-$Li_{3.75}Si$ and showed that it could be modelled by a BPP relaxation model.[155,191] Two motional regimes were found; below 350 K, they found that Li motion leads to relaxation via the dipolar and quadrupolar coupling interactions. Above this temperature, the relaxation rates increase more rapidly with temperature. The increase in the relaxation rate was attributed to faster relaxation of decomposition products, which begin to form at 350 K, as was shown by the evolution of the MAS lineshape as a function of temperature.[191] The lithiated Si compounds of Dupke *et al.* and Baran *et al.*, were both synthesized chemically at high temperature in furnace.[190,191]

In this work, we compare the electrochemical cycle performance of silicon-graphene anodes produced via a conventional shear mixing and a novel co-microfluidization technique. The co-microfluidization technique can produce silicon-graphene electrodes on a large scale, in a one-step process.[1] Two different SiNPs, with diameters of 80 nm and 300 nm, were used and their cycle performances are compared in both half-cells and full-cells, using NMC622 as the cathode.

Prelithiation, via chemical lithiation at room temperature, was investigated as a technique to improve the cycle life of silicon anodes. Prelithiation is shown to improve the CE of silicon-graphene anodes in half-cells. NMR and Raman spectroscopies were used to understand the mechanism that leads to the increase in CE. Full-cells were cycled with prelithiated silicon-graphene anodes and these full-cells show improved performance over electrodes that were not prelithiated.

VT ^{7}Li NMR was used to study changes in the lineshape between 261 and 331 K. At lower temperatures, the peak corresponding to c-$Li_{3.75}Si$, in lithiated silicon-graphene anodes, is shown to originate from two local environments (c-$Li_{3.75}Si$a and c-$Li_{3.75}Si$b) that are chemically exchanging and coalesce to into one peak at higher temperatures. ^{7}Li T_1 relaxation measurements were used to probe the differences in the Li ion dynamics in chemically and electrochemically lithiated silicon-graphene anodes. The results give mechanistic insight into how different prelithiation techniques affect cycle performance of anodes with high Si content.

[1] The co-microfluidized silicon-graphene composite electrodes were produced in collaboration with Jeremiah Marcellino.

5.3 Experimental Methods

5.3.1 Materials

Two types of Si nanoparticles (SiNPs) were used in this work; laser synthesized 80 nm SiNPs (US Research Nanomaterials), which have very uniform size distribution, and Si nanopowder (Elkem - Silgrain e-Si 1030) which was prepared via ball milling of micron sized Si particles. The ball milled Si nanopowder had a purity of 99.7% and a distribution of particles sizes with $d_{50} = 300$ nm, $d_1 = 90$ nm and $d_{100} = 1.6\,\mu$m The binder used was Na polyacrylic acid (NaPAA) (Mw $\sim$ 450k, Sigma-Aldrich) which is soluble in both water and IPA, both of which were used as solvents to prepare electrode slurries in this work. The graphite used to produce the graphene was a Timrex KS25 graphite (Imerys). Graphene was produced via microfluidization of graphite in water as described by Karagiannidis *et al* using 70 process cycles.[192] Karagiannidis *et al*. reported on the microfluidization of graphite to produce graphene, they found that the thickness of the graphene produced using 100 microfluidization process cycles, shows a log-normal distribution with a maximum at $\sim$7.4 nm and a mean thickness of $\sim$12 nm.[192] They showed that $\sim$4% of the flakes were few layer (1 - 10 layers) graphene with a thickness of <4 nm. The mean lateral dimension of the graphene after 100 process cycles, which was initially 32 µm, was $\sim$1 µm[192] The graphene ink produced in this work had a concentration of 100 mg/ml of graphene, and 5 mg/ml of sodium deoxycholate (SDC - Sigma Aldrich) was used as a surfactant to stabilise the dispersion. No other conductive carbon additive was used as graphene provides sufficient enhancement of the electrical conductivity.

Two electrode slurry preparation techniques were used in this work and their electrochemical performances were compared. In the first, conventional shear mixing was used to prepare the slurry. First, NaPAA was added to deionized water (DI) at a concentration of 3% by mass, before mixing at 3500 rpm using a SpeedMixer (DAC 150 FVZ-K, FlackTek) until the NaPAA had fully dissolved. Next, graphene ink, followed by SiNPs were added, such that the final dry mass ratios of NaPAA:Graphene:Si were 10:30:60. After each step the slurry was further mixed at 3500 rpm for 10 minutes. Finally, the slurry was further mixed at 10,000 rpm using a Dispermat LC30 shear mixer (VMA-Getzmann).

The second method used a novel co-microfluidization technique, which used a high-pressure homogenizer (HPH) (PSI Instruments) to both mix the electrode slurry together while at the same time, exfoliate the graphite into graphene. The process is depicted in Figure 5.1. Malik *et al*. reported on a similar technique, known as wet jet milling, to

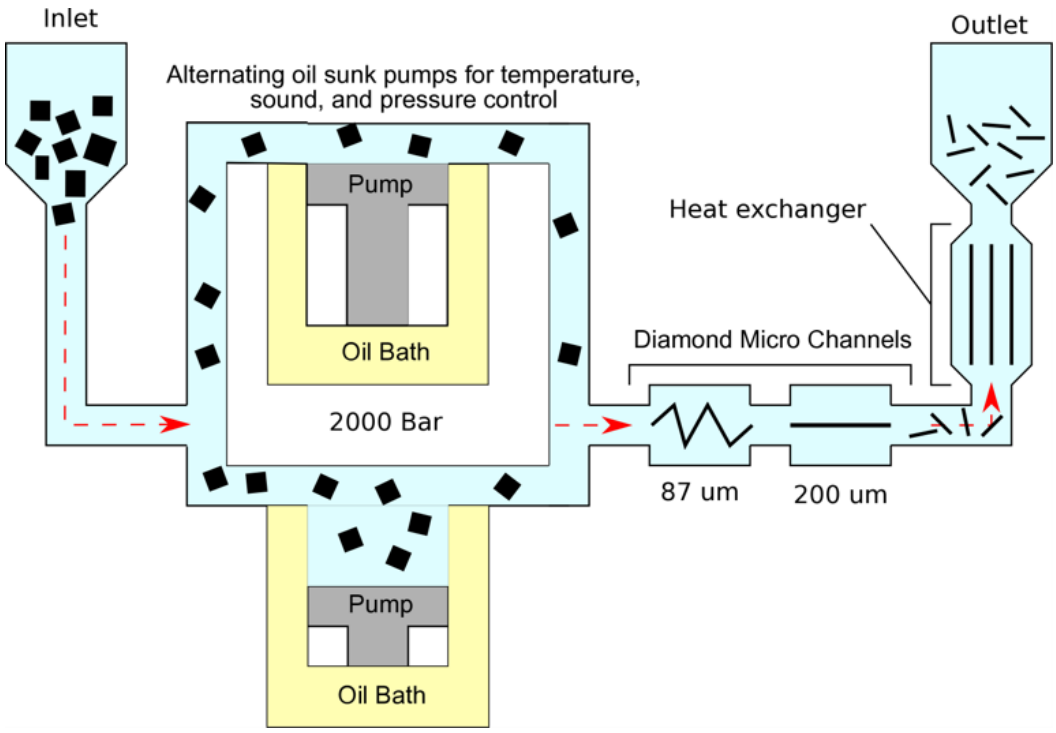

Figure. 5.1 A high pressure homogenizer was used to co-microfluidize SiNPs and graphite. The process combined the materials to form a homogeneous composite material and at the same time exfoliated the graphite to make graphene. Figure produced by Jeremiah Marcellino.

produce a silicon-graphene composite electrode.[178] The graphene produced during the co-microfluidization of Si and graphite in this work has a similar morphology to that produced by both Malik *et al.* and Karagiannidis *et al.*[178,192] The benefit of the co-microfluidization technique is that it is easily scalable to industrially relevant levels, with a pilot-scale HPH capable of volumetric flow rates of ∼60 L/hr. Based on the chosen number of processing cycles, this can produce up to 1 kg/hr dry mass of silicon-graphene composite anode material. The HPH has ∼50 ml of dead volume, which limits the minimum amount of material that can be processed via this technique.

The HPH uses high pressure (∼2000 bar) and high-speed flow (∼700 m/s) through microchannels (87 µm diameter) to generate shear rates of $\sim 10^8$ s^{-1}, around three orders of magnitude higher than other mixing techniques, such as shear mixers $\sim 10^5$ s^{-1}. These shear rates allow scalable, rapid deagglomeration, exfoliation, mixing, and dispersion of materials at the nanometer scale.

The first step in producing the co-microfluidized silicon-graphene electrodes was to add the NaPAA binder to IPA at a concentration of 100 g/L. This mixture was then processed by the HPH for 10 cycles at 2000 bar through an 87 µm channel to fully dissolve the NaPAA. Next, SiNP and graphite dry powders were mixed together in a large glass flask, before IPA and the NaPAA-IPA solution were added such that the final concentration of the mixture was 400 g/L and the dry mass concentrations of NaPAA:Graphene:Si were 10:30:60. Thirty HPH process cycles were used to co-microfluidize the silicon-graphene composites, as this was found to be the optimum number for the best electrochemical performance in terms of coulombic efficiency (CE), specific capacity and capacity retention as shown in Figure C1.

After the slurries were prepared, electrodes were then cast onto 9 µm copper foil (Pi-KEM) with a wired bar, using a K101 Control Coater System (RK Print Coat Instruments), producing a wet film thickness of ∼75 µm. The electrode was left to dry in air before 15 mm diameter electrodes were punched out (Heavy Duty Disk Cutter, MTI) and further dried at 80 °C for 3 hours under vacuum. The coated electrodes had an areal loading between 1 - 2 mg/cm^2. Four electrode coatings are presented in this work and will be denoted by S80, C80, S300, and C300 for the electrodes produced by shear mixing (S) and co-microfluidization (C) using the 80 nm and 300 nm Si, respectively. Thinner S80 electrodes were also produced with an areal loading of ∼0.25 mg/cm^2.

The dried electrodes were transferred into an Ar atmosphere glovebox ($O_2 \leq 1$ ppm, $H_2O \leq 1$ ppm) for battery assembly. Two types of separators were used, either Celgard 3501 which were punched into 17 mm disks, washed in ethanol and then dried under vacuum at 40 °C for 12 hours or a 16 mm glass microfibre separator (Whatman) which was dried at 100 °C under vacuum. 1 M $LiPF_6$ in ethylene carbonate/dimethyl carbonate 1:1 v/v (LP30, Sigma Aldrich) with 10wt% fluoroethylene carbonate (FEC) was used as the electrolyte.

5.3.2 SEM

Scanning Electron Microscopy (SEM) images of the pristine silicon-graphene electrodes were taken with a FEI Magellan 400 SEM using a secondary electron detector. The electrodes were coated on copper current collectors and were fixed in place using conductive carbon-coated tape. Samples were studied at a working distance of 4.3 mm from the objective lens and images were acquired using a 10 kV acceleration voltage.

5.3.3 Electrochemistry

Silicon-graphene anode half-cells were assembled using 2032 coin cells (Cambridge Energy Solutions) with 15 mm silicon-graphene disks, 16 mm lithium chips (Cambridge Energy Solutions) and 150 µL of electrolyte. Full-cells were assembled similarly, using commercial $LiNi_{0.6}Mn_{0.2}Co_{0.2}O_2$ (NMC622) as the cathode. For long term cycling, borosilicate glass fibre separators were used, while for cells that were disassembled for post-mortem analysis, Celgard separators were used.

Before cycling, the cells were rested at their open circuit voltage (OCV) for a minimum of two hours to allow the electrolyte to wet the electrode. The C-rates were calculated using an estimated capacity, for the silicon-graphene anodes with 60% Si (3759 mAh/g) and 30% graphene (372 mAh/g, assuming that graphene has the same capacity as graphite), of 2367 mAh/g. The cells underwent two formation cycles at C/20 to slowly and homogeneously form the SEI which improves its stability.[193] This slow step also helps to "activate" the crystalline Si nanoparticles.[161] After the formation cycles, the cells were cycled at C/5, which corresponds to around 475 mA/g, between 0.01 - 1 V.

The commercial NMC622 cathode used in full-cell testing had an areal capacity of around 2.2 mAh/cm^2 at C/5. The areal loading of the silicon-graphene electrodes produced for full-cell was targeted so that the anode (negative) to cathode (positive) capacity ratio (N:P) was between 1.1 and 1.2. This was done to prevent Li metal plating on the graphene which can occur if the potential at the anode drops below 0 V. Full-cells of shear mixed and co-microfluidised silicon-graphene electrodes were cycled between 3 and 4.2 V versus the NMC622 cathodes. The first two formation cycles were again performed at C/20 and the subsequent cycles were performed at C/5.

Chemical lithiation was investigated as a prelithiation technique to improve the cycle performance of the silicon-graphene anodes. Chemical lithiation of the anodes was achieved by placing a 15 mm silicon-graphene electrode in the top half of a 2032 coin cell case, before adding 50 µL of electrolyte. Next, a 16 mm lithium chip was placed directly on top of silicon-graphene anode and pressure was applied using stainless steel spacers and a plastic clamp. This induced an electrical short circuit and the silicon-graphene electrode is then spontaneously lithiated via a galvanic corrosion reaction. The cyclability of both half and full-cells using S80 electrodes prelithiated for 3 hours were studied and compared to the cycle performance of pristine S80 electrodes.

5.3.4 Raman Spectroscopy

Raman spectroscopy measurements were carried with a Horiba HRT800 spectrometer using a 514 nm laser wavelength with a laser power < 1 μW to ensure that the samples were not heated or damaged during the measurements. Measurements were calibrated using the T_{2g} peak of a crystalline Si wafer at 520 cm^{-1}.[194] Post-mortem analysis was carried out on the shear mixed Si-graphene electrodes in order to understand the impact of prelithiation on the electrode structure in relation to how this affected the cyclability of the electrodes. Samples were prepared by cycling the electrodes in coin cells using a half-cell format. Prior to disassembly in a glove box, the cells were charged to 1 V, so that they were measured in the delithiated state. After the cells were disassembled, the electrodes were dried under vacuum for ∼5 minutes. The Raman measurements were then carried out in ambient conditions.

5.3.5 NMR

Silicon-graphene anodes for ssNMR measurements were electrochemically cycled in half-cells against lithium metal at C/30 from OCV to 10 mV. Cells that were prepared by chemical lithiation were assembled around 5 days before the measurement was carried out. The electrodes were then extracted from the cells before being dried under vacuum for ∼ 5 minutes. The lithiated silicon-graphene electrodes were scraped from the copper current collector, diluted with approximately equal amounts of KBr to help with sample spinning and packed into 2.5 mm rotors. One electrode (comprising a 15 mm diameter disc) was used to fill each rotor.

^{7}Li measurements were performed on a 11.75 T magnet ($\nu_0(^{1}H) = 500.13$ MHz, $\nu_0(^{7}Li) =$ 194.37 MHz), equipped with a Bruker Avance IIIHD spectrometer. A 2.5 mm Bruker double resonance probe was used with a 30 kHz MAS frequency. A rotor-synchronized Hahn-echo pulse sequence was used with a recycle delay that was at least 5 times T_1 to allow for quantitative analysis.

Variable temperature (VT) measurements were performed between 269 - 331 K to observe changes in the lineshape as function of temperature, as well as to probe different relaxation phenomena. The sample temperature was determined using an *in-situ* calibration with the temperature-dependent ^{79}Br NMR shift of KBr.[93] The measurements were performed by cooling the sample using a BCU II cooling unit (Bruker). Due to frictional heating of the 2.5 mm rotor spinning at 30 kHz, room temperature corresponded to 331 K.

The ^{7}Li spin-lattice relaxation times, T_1, were determined under 30 kHz MAS over the temperature range 269 - 331 K. A saturation recovery pulse sequence was used to determine

T_1, with the delay time, τ, varied between 250 µs and 10 s. ^{7}Li T_1 times were obtained for the dense stage Li-GIC, and lithiated Si compounds with small Si clusters, isolated Si^{4-} anions including c-$Li_{3.75}Si_4$ and the overlithiated crystalline phase, c-$Li_{3.75+\delta}Si_4$.[189] All relaxation times were satisfactorily fit with mono-exponential functions.

Operando ^{7}Li NMR measurements were performed during electrochemical (EL) and chemical (CL) lithiation of C300 electrodes using a 7.05 T magnet ($\nu_0(^1\mathrm{H}) = 300.13$ MHz, $\nu_0(^7\mathrm{Li}) = 116.64$ MHz). Capsule cells, as described in the previous chapter, were assembled with a silicon-graphene anode and a Li metal counter electrode. For the chemical lithiation experiment, no separator was used, and the experiment was started within 5 minutes of the cell being closed as the reaction began immediately and spontaneously.

For the electrochemical lithiation measurement, the cell was cycled using a galvanostatic experiment with a 2 hour potential hold at the end of discharge. The cell was cycled at C/20 between 0.01 - 1 V for one full cycle, a second cycle was performed but the experiment was stopped at 0.4 V during the delithiation step. Hahn-echo experiments were performed while the cell was cycled. The recycle delay was 1.875 s and 32 scans were summed together so that each spectra took 1 minute to acquire. Automatic matching and tuning of the probe resonance circuit was performed throughout the experiment as described in the work by Pecher *et al.*[148]

5.4 Results

5.4.1 SEM

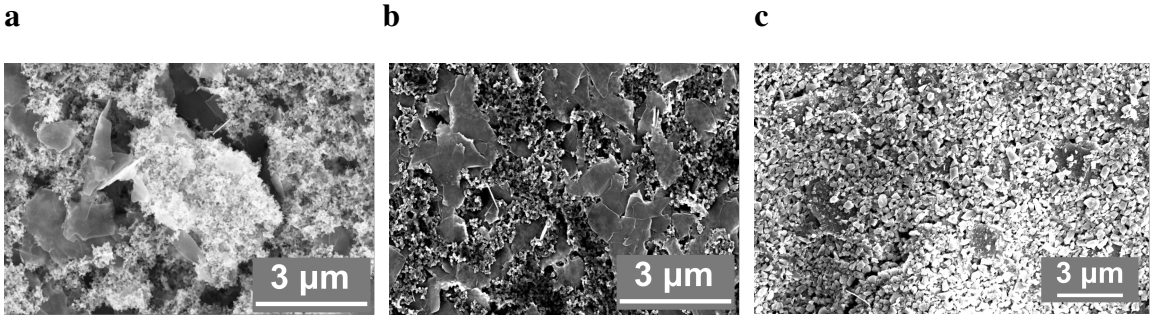

Figure. 5.2 High magnification SEM of silicon-graphene electrodes produced by a) shear mixing (S80), b,c) co-microfluidization (C80 and C300). The electrodes shown in a and b were produced using the 80 nm Si, while for the electrode shown in c, the 300 nm Si was used.

The two graphene-silicon composites were first characterized via SEM so as to help rationalize the subsequent electrochemical performance. The ideal electrode structure would have silicon and graphene homogeneously dispersed throughout the electrode. This would allow the graphene to maximise its ability to prevent silicon particle agglomeration during cycling.[179] It would also improve electrical conductivity of the composite compared to a material where the graphene is not well dispersed which is beneficial for increasing the rate capability of a material.

Figure 5.2 shows high magnification SEM images of silicon-graphene electrodes coated onto copper foil. Lower magnification SEM images are shown in Figure C3. For the C80 electrode (Figures 5.2b and C3b), the contrast between the SiNPs and graphene flakes is higher than that for the C300 electrode. This is because the 300 nm SiNPs have a flaky morphology which is similar to the graphene flakes and they both have similar diameters. The $\sim$1 µm flakes observed in Figures 5.2a and 5.2b are the few layers graphene flakes produced by microfluidization. While measurements to characterise the thickness of the graphene flakes were not performed it is assumed that the graphene flake thickness will show a similar log-normal distribution to those produced by microfluidization by Karagiannidis *et al.*[192] Since 30 co-microfluidization process cycles were found to result in a silicon-graphene composite with optimum electrochemical performance, the thickness distribution is expected to shift to larger values than for the graphene produced by 70 microfluidization cycles used in the shear-mixed electrodes.[192] This means the co-microfluidized electrodes may also contain some small graphite fragments. Electrodes produced by shear mixing (S80) (Figures 5.2a and

C3a) show areas of well dispersed silicon and graphene and regions with large agglomerates (∼3 µm) of Si nanoparticles. In comparison, the electrodes produced by co-microfluidization (Figures 5.2b,c and C3b,c), show much a more homogeneous composition.

From Figure 5.2b, we can conclude that the high shear forces that occur during the co-microfluidization process are able to break apart the SiNP agglomerations. We can also see, by the reduced brightness of Figure 5.2b compared to Figure 5.2a, that the charging of the electrode by the electrons in the SEM is lower, which suggests the electrical conductivity is also improved by co-microfluidization.

5.4.2 Electrochemistry

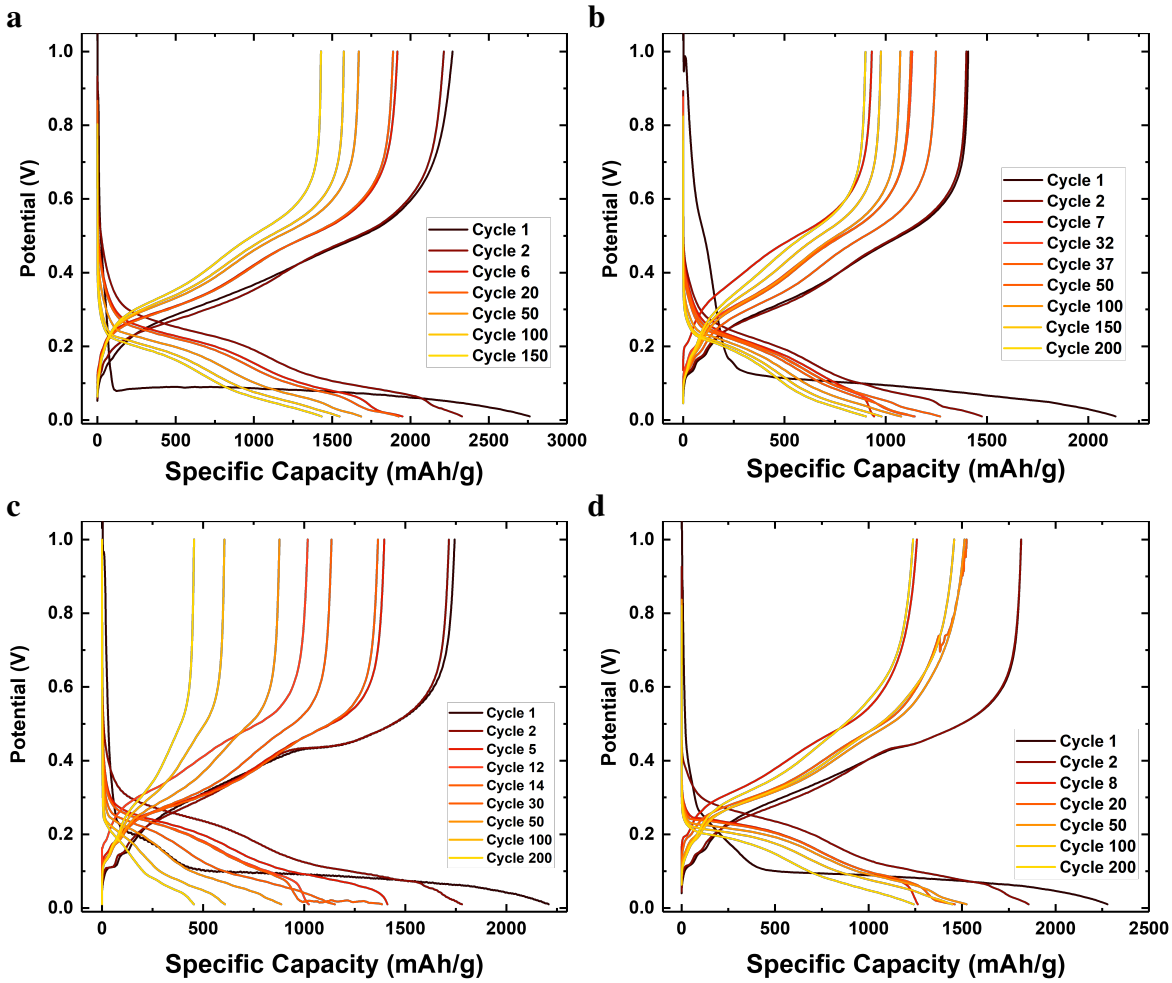

Figure. 5.3 Potential profiles of the silicon-graphene anodes produced by shear mixing and co-microfluidization of a,b) 80 nm (S80, C80) and c,d) 300 nm (S300, C300) Si nanoparticles, respectively.

Figure 5.3a-d show the potential profiles of the S80, C80, S300 and C300 electrodes, respectively. The first discharge profiles of all the electrodes show an initial sharp drop from OCV and a bump between bump between 0.8 and 1 V which is due to the reduction of FEC.[159] This peak is most prominent in the C80 sample.

For the S80, C80, S300 and C300 electrodes, the capacity above 0.23 V in the first cycle is 67, 187, 81, 150 mAh/g, respectively. This capacity is ascribed to initial SEI formation. This assumption can be rationalised because 0.23 V is close to the potential at which lithium begins to intercalate into graphite and is also the potential at which SiO_2 reacts with Li to form Li_4SiO_4, which is partially reversible,[195] meaning any capacity above this voltage is unlikely to be associated with reactions involving the active materials. The total irreversible capacity in the first cycle is larger than the capacity measured above 0.23 V for all the electrodes. This is due to continuous electrolyte degradation that occurs during the whole low voltage process as the Si is gradially lithiated to eventually for the c-$Li_{3.75}Si$ phase.[54] The sloped region between 0.23 V and 0.1 V in the electrodes with 300 nm SiNPs is not observed in the electrodes with 80 nm SiNPs. The unprocessed 80 nm SiNPs have an oxide layer that is ~ 5 nm, while that of 300 nm SiNPs is unknown. The S300 and C300 anodes show (Figure 5.3) show higher capacity between 0.23 V and 0.1 V than the S80 and C80 anodes, the capacity in this region is attributed to the lithiation of SiO_2 to form Li_4SiO_4. This suggests that the native oxide layer is thicker in the 300 nm SiNPs. Preparation of SiNPs via ball milling has been shown to increase the surface oxide layer.[162] The thicker oxide layer would also explain the lower ICE observed for the 300 nm Si anodes compared to the S80 electrodes.[162] Zhu *et al.* also showed that the increase in surface oxidation is correlated to a decrease in the intrinsic Si peak during XPS measurements.[162] This shows that surface oxidation leads to a decrease in the crystalline Si and could be one reason the initial specific capacity of the 300 nm Si is lower than S80 electrode. The increased surface oxidation will also result in higher impedance and higher overpotentials which could also decrease the initial specific capacity achieved.

Following the SEI formation, a long plateau at ~ 0.1 V is observed which corresponds to the conversion of crystalline Si to amorphous lithium silicide a$-Li_xSi$.[43] Further lithiation leads to the formation of the crystalline phase, c-$Li_{3.75}Si$. The formation of the c-$Li_{3.75}Si$ can be confirmed by the characteristic process at ~ 0.4 V during the delithiation potential profile. This feature in the potential profile corresponds to the delithiation of c-$Li_{3.75}Si$, which forms amorphous Si. This process is more clearly observable in the 300 nm silicon (Figure 5.3c and 5.3d). This could in part be due to the smaller size of the 80 nm Si. The XRD results of results of Wang *et al.* showed that the c-$Li_{3.75}Si$ phase did not form at the

end of the first lithiation of nanoparticle Si anodes but did form when micro-sized Si was used.[196] One suggested reason for this was that the higher surface area of smaller Si particles increases the rate of self-discharge that occurs due to reaction of the c-$Li_{3.75}Si$ phase with the electrolyte.[54,196] The subsequent lithiation potential profile shows two pseudo plateaus at ~0.25 V and ~0.1 V, which are characteristic of the lithiation of amorphous Si. The plateaus at 0.25 V and 0.1 V correspond to the formation of phases with approximate stoichiometry a-$Li_{2.5}Si$ and a-$Li_{3.5}Si$, respectively.

During the first two slow formation cycles, two plateaus at 0.12 V and 0.15 V are observed at the beginning of delithiation. Plateaus in this voltage range are not seen for Si and must correspond to the delithiation of graphite fragments within the lithiated composite electrodes, the plateau at 0.12 V is due to the transition of LiC_6 to LiC_{12} and the plateau at 0.15 V is due to the transition of LiC_{12} to LiC_{18} (Dilute stage 2 and dilute stage 3).[197] In subsequent cycles, the higher current density (C/5) leads to a larger overpotential and these plateaus occur at ~ 0.2 V and are much shorter, indicating that the graphite is less lithiated at higher current densities.

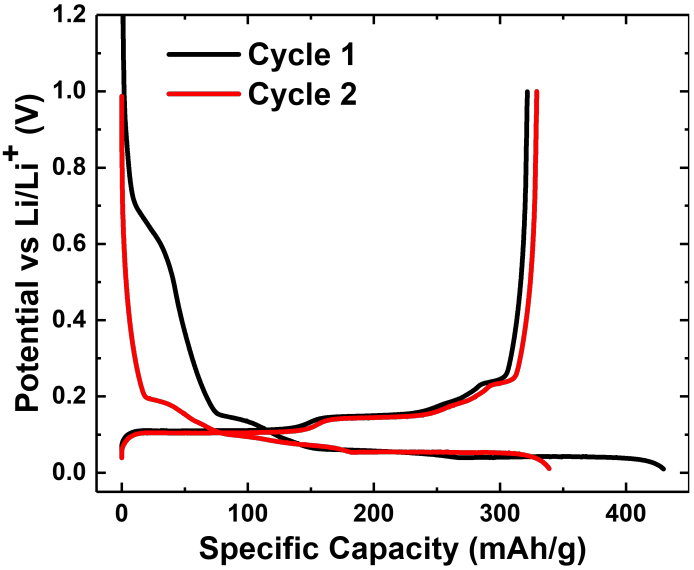

Figure. 5.4 Potential profile of a graphene anode half-cell. The graphene was produced microfluidisation of graphite using 70 process cycles.

Figure 5.4 shows the potential profile of a graphene anode half-cell. The graphene was produced microfluidisation of graphite using 70 process cycles and is the same graphene used within the S80 and S300 electrodes. The first cycle dis/charge specific capacities are 428 mAh/g and 322 mAh/g. The potential profile is similar to that of graphite (Figure

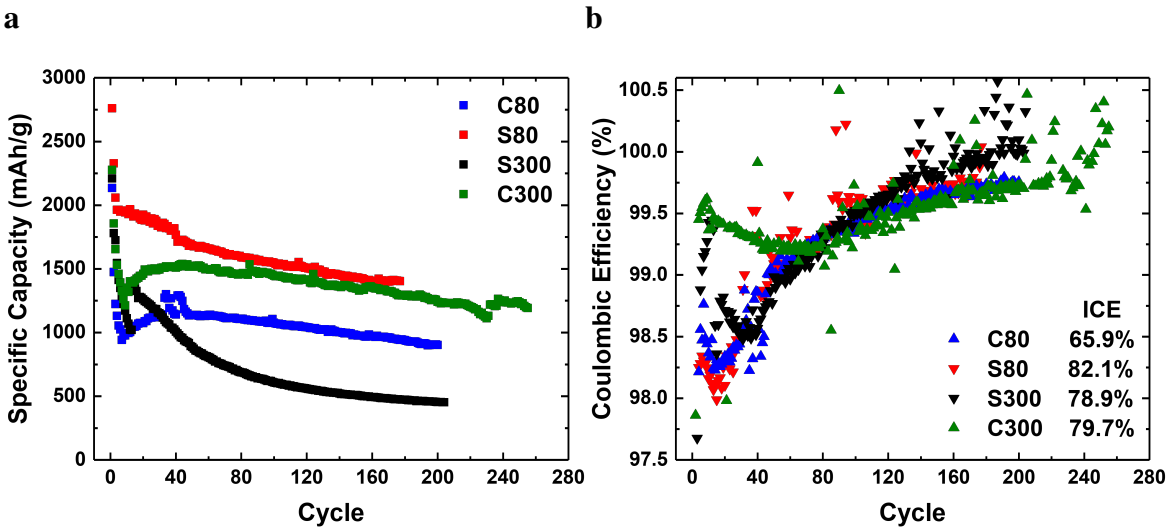

Figure. 5.5 a) Discharge specific capacity and b) coulombic efficiency for the silicon-graphene anodes produced by shear mixing and co-microfluidization of 80 nm (S80, C80) and 300 nm (S300, C300) Si nanoparticles, respectively. All samples shown achieved an areal capacity > of 2 mAh/cm^2.

3.1), though the ICE is lower for the graphene electrodes (75.2%) compared to the graphite electrodes (91.5% - Figure 3.1). This is due to the higher surface area of the graphene compared to the graphite, which leads to increased SEI formation, as evidenced by the larger capacity observed above 0.2 V in the graphene electrode. The graphene produced during the co-microfluidisation of silicon and graphite is expected to have a similar morphology and electrochemical performance to that of the graphene electrode shown in Figure 5.4.

Figure 5.5a and 5.5b show the discharge specific capacity and coulombic efficiency, respectively, as a function of cycle number for the S80, C80, S300 and C300 silicon-graphene anode half-cells. The specific capacities reported in this work are given per mass of the electrode material. The data, summarised in Table 5.1, is representative of at least 3 cells that were cycled for each sample. The results are also compared in Table 5.1 to those in the literature for different silicon-carbon anodes, including those that use graphite, graphene and reduced graphene oxide (RGO).[178,198–202] Figure 5.6 shows the ICE for S80, C80, S300 and C300, as well as a prelithiated S80 anode (S80 Pl). The data shows the range and mean ICE values for each material.

Care must be taken when comparing results as differences in electrochemical cycling protocols, such as, whether galvanostatic cycling (CC), galvanostatic cycling followed by a potential hold (CCCV), or capacity limited cycling, is used. CCCV cycling can improve capacity retention in half-cell testing, since increased impedance, due to continuous SEI

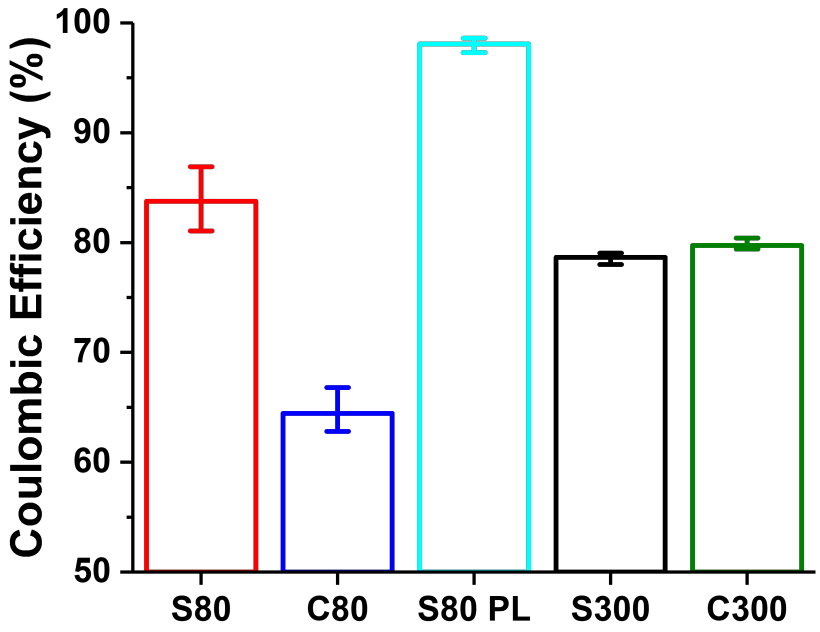

Figure. 5.6 Initial coulombic efficiency (ICE) for the silicon-graphene anodes produced by shear mixing and co-microfluidization of 80 nm (S80, C80) and 300 nm (S300, C300) Si nanoparticles, respectively, as well as a prelithiated S80 anode (S80 Pl). The error bars represent the range of ICE values found for each sample with at least 3 half-cells tested for each material.

degradation (which occurs on both the Si and Li electrodes), is typically the dominant cause of capacity loss. A higher low cut-off voltage can also limit the stress and volume expansion of the Si and improve cyclability by reducing electrode pulverisation.[203] Low mass loading, defined as the electrode mass per unit area on the current collector, can also increase the achievable specific capacity. With increasing thickness, the mass transport of Li ions through the electrodes becomes increasingly limited. This leads to higher overpotentials, which results in a lower specific capacities when CC cycling is used.[204] On the other hand, increasing the areal capacity can improve the energy density of LIBs as it reduces the mass of inactive components[205] Additionally, capacity retention values are often reported with respect to either the charge (delithiation) capacity or the discharge (lithiation) capacity after the formation cycles. This misrepresents the true performance since in a half-cell, the Li metal counter electrode provides a large excess of Li meaning the degradation mechanism is due to increased impedance as a result of continuous SEI break down and repair, as well as a reduction in the usable active material due to electrode pulverisation. In full-cells, the

main degradation mechanism is loss of Li inventory and therefore the capacity lost due to the initial formation cycle is important.[14]

Table 5.1 Comparison of the electrochemical performance of silicon-carbon anodes in the literature and in this work. Data in the second half of the table is from this work.

Synthesis Method	Silicon	Silicon (wt%)	Carbon	Current Density* (mA/g)	Voltage Range (V)	Capacity Retention**	ICE (%)	Discharge Specific Capacity (mAh/g)*	Initial Areal Capacity (mAh/cm^2)	Comments
Wet Jet Milling[178]	SiNP <100 nm	50	Few layer graphene	179	0.05 - 1	98% @450 cycles	84	900	1.0	Capacity limited
CVD[198]	Si nanolayer	9	Graphite	358	0.005 - 1	96% @100 cycles	92	517	3.3	
Ball milling[200]	SiNP 100 nm	66	Carbon Black	200	0.01 - 1	100% @110 cycles	96	900	3.2	Capacity limited Prelithiated
Ball milling and spray coating[199]	SiNP	10	Graphite and amorphous carbon coating	500 (100)	0.01 - 1.5	83.6% @300 cycles	80	756 (818)	0.83	
Self assembly[202]	SiNP <100 nm	54	Graphite and polyaniline	1125 (56)	0.02 - 1.5	76% @500 cycles	86.2	1800 (2090)	1.5	CCCV cycling
Spray coating and heat treatment[201]	SiNP 30 nm	16	Graphite and RGO	100	0.01 - 2	83.4% @20 cycles	78	800	-	
Shear mixing	SiNP 80 nm	60	Few layer graphene	473 (118)	0.01 - 1	68.2% @177 cycles	84 ± 3	2058 (2672)	3.45	High loading
Shear mixing	SiNP 80 nm	60	Few layer graphene	473 (118)	0.01 - 1	75.8% @130 cycles	84 ± 3	2577 (3106)	0.8	Low loading
Shear mixing	SiNP 80 nm	60	Few layer graphene	473 (118)	0.01 - 1	79.3% @120 cycles	98.1 ± 0.7	2392 (2610)	0.6	Prelithiated
Shear mixing	SiNP 300 nm	60	Few layer graphene	473 (118)	0.01 - 1	26% @200 cycles	78.6 ± 0.5	1725 (2209)	2.28	
Co-microfluidisation	SiNP 80 nm	60	Graphite and graphene	473 (118)	0.01 - 1	73.7% @200 cycles	64 ± 2	1224 (2135)	2.56	
Co-microfluidisation	SiNP 300 nm	60	Graphite and graphene	473 (118)	0.01 - 1	72.1% @255 cycles	79.7 ± 0.5	1654 (2277)	2.99	

*All capacities and current densities are shown are with respect to the mass of the whole electrode *i.e.* active material, carbon and binder. The values in brackets are the current density and specific capacity during the formation cycle.

**The capacity retention values shown are relative to the discharge capacity after the formation cycles. This was done for easier comparison to other results in the literature. In reality, the capacity retention relative to the first formation cycle is equally important in determining the performance in a full-cell.

For easier comparison to previously reported results in the literature, the capacity retention in Table 5.1 is given relative to the capacity after the formation cycles. For the S80, C80, S300 and C300 electrodes (Figure 5.5a), the capacity retention with respect to the capacity after the formation cycles are 68.2% (1403 mAh/g @177 cycles), 73.7% (902 mAh/g @200 cycles), 26% (452 mAh/g @200 cycles) and 72.1% (1193 mAh/g @255 cycles), respectively. For full-cell performance, what is important is the capacity retention with respect to the initial discharge capacity. This is because the initial capacity lost during the formation cycles will reduce the available Li in the cathode that is paired with the Si anode and reduce the cycle life of the full-cell. For the S80, C80, S300 and C300 electrodes (Figure 5.5a), the capacity retention with respect to the first discharge capacities are 52.5% (@177 cycles), 42.3% (@200 cycles), 20.3% (@200 cycles) and 52.4% (@255 cycles), respectively.

From Figure 5.5a, it can be seen that for C80, S300 and C300, at around cycle 10, a dip in the capacity to 942, 1020 and 1213 mAh/g, respectively, occurs. The capacity then increases to 1141, 1384 and 1539 mAh/g for C80 (cycle 40), S300 (cycle 14) and C300 (cycle 44), respectively. The theoretical capacity of these electrodes, 2367 mAh/g, is not achieved in the first cycle, suggesting that not all of the Si is lithiated, particularly when the irreversible capacity due to SEI formation in the first cycle is considered. The reason the capacity increases after the dip could be due to the structure of the silicon-graphene composite opening up as a result of the volume expansion during cycling, which would make further lithiation of Si easier.[206,207] The lower capacity in the initial cycles could also be due a difficulty in lithiating the core of the Si particles, particularly the larger Si particles when the distribution in particle size is considered. The same trend is not observed for the S80 electrode, where the capacity decreases gradually with cycle number. The sharp increase in capacity at around cycle 40 for C80 was due to temperature fluctuations in the lab, similar results were seen in other samples cycled at the same time.

From Figure 5.5b, it can be seen that for all four samples, the CE initially increases from the initial value at around cycle 4, it then dips before increasing again. For S80 and C80, the CE dips to 98% and 98.22%, respectively, at cycle 14. For S300 and C300, the CE dips to 98.5% and 99.1% at cycle 35 and 60, respectively. The C80 and C300 electrodes show a lower dip in the CE. The C300 and S300 electrodes have similar ICE, while the ICE of C80 is 16% lower than S80, this is likely due to the increased surface area, as the SiNPs aggregates were broken apart during cycling (Figure 5.2). The CE increased to more than 99% at around 50 cycles for S80, C80 and S300, while it only took 4 cycles for c300 to reach 99.4%. The cumulative CI reaches 100% after 103, 40, 61 and 110 cycles for S80, C80, S300 and C300, respectively.

Prelithiation

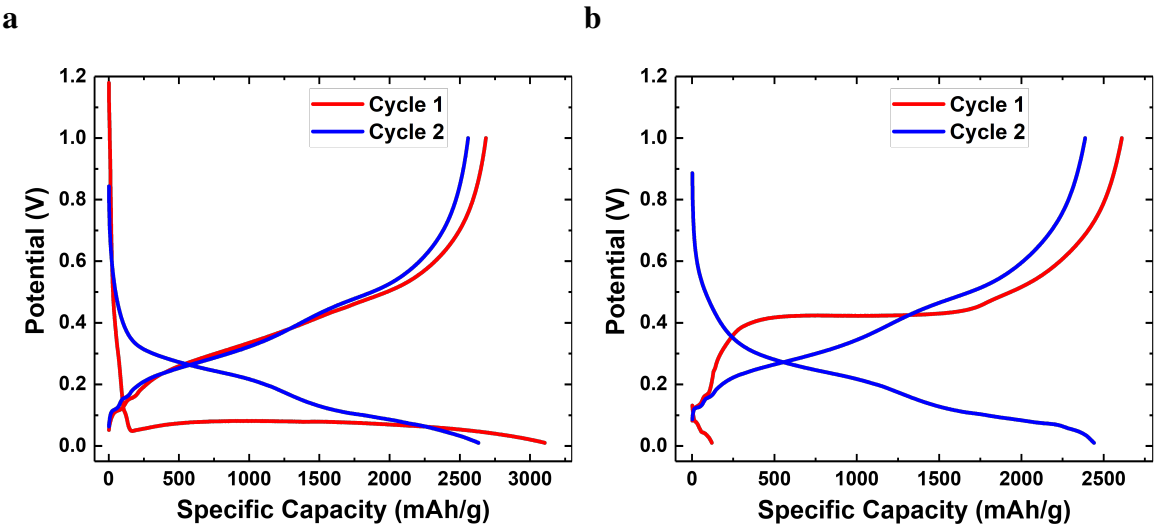

Figure. 5.7 Potential profile of S80 electrodes during the first two dis/charge cycles a) without and b) with prelithiation.

Figure 5.7 shows the potential profile of the pristine and prelithiated S80 electrode. The first discharge potential profile, for the pristine electrode shows a rapid initial drop in potential, followed by a long plateau at ∼100 mV, which is characteristic of the lithiation of c-Si and the formation of a−Li_xSi as discussed previously.[52] In the prelithiated S80 electrode (Figure 5.7b), the OCV is 130 mV and initial discharge capacity is 120 mAh/g. The reason the OCV was not 0 V, which would be expected since the electrode had been electrically short circuited by being placed in contact with the Li metal, is because of self-discharge. This has been reported by Key *et al.*, who observed the self-discharge of fully lithiated Si anode due to the metastable c-$Li_{3.75}Si$ phase reacting with the electrolyte.[54] The discharge profile shows two pseudo-plateaus at ∼80 mV and ∼50 mV. The voltage of these plateaus indicate the capacity could be from the lithiation of dense stage 2 and stage 1 graphite as the voltages are similar (see Chapter 3). More likely, the capacity is from the lithiation of Si which has self-discharged in the period between prelithiating the cell and assembling the fresh half-cell. The first charge (delithiation) capacities for the pristine and prelithiated electrodes are 2687 and 2610 mAh/g, respectively, suggesting similar amount of Li were inserted into Si. However, the first charge profile of the prelithiated electrode shows a large plateau at 0.42 V, characteristic of the delithiation of c-$Li_{3.75}Si$.[52] The pristine S80 electrode profile showed two pseudo plateaus at ∼ 0.3 V and ∼ 0.45 V, these features correspond to the

delithiation of the amorphous a-$Li_{2.5}Si$ and a-$Li_{3.5}Si$ phases, respectively.[52] In subsequent cycles, the charge potential profile are similar in the pristine and prelithiated electrodes.

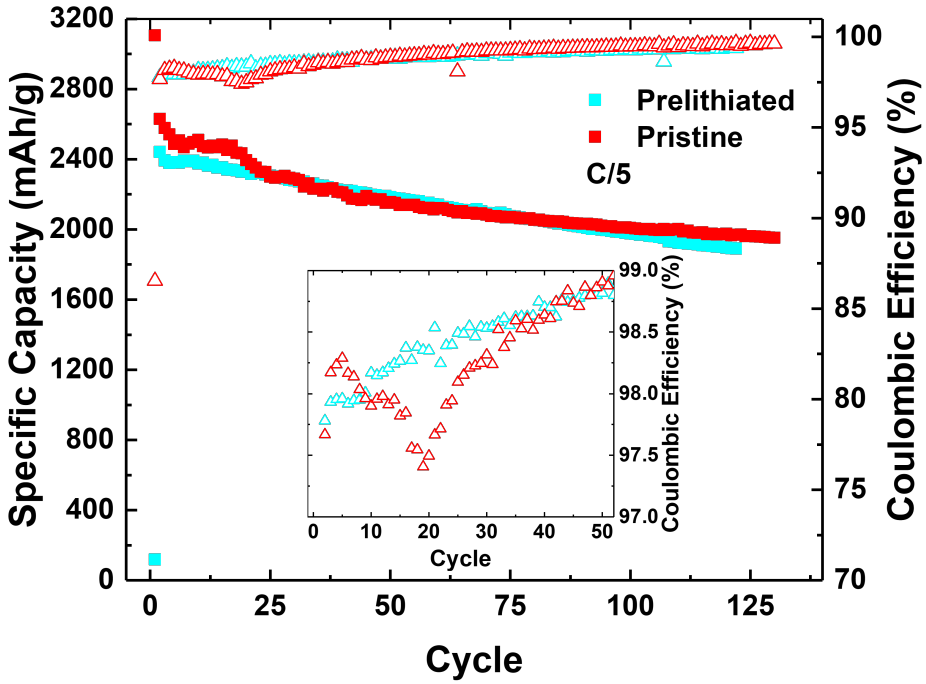

Figure. 5.8 Cycle performance of prelithiated and pristine S80 electrodes. Inset shows the CE in the first 50 cycles. The CE increases with cycle number from an initial value of 97.8% for the prelithiated electrode, while for the pristine electrode, the CE initially increases from 86.5% to 98.3% at cycle 5. The CE then decreases to 97.4% at cycle 19 before increasing with cycle number. Beyond cycle 50 the CE is similar for the pristine and prelithiated electrodes, and plateaus at $\sim$ 99.5%. Small variations were seen between cells but the observed trends remained the same.

Figure 5.8 shows the specific discharge capacity and coulombic efficiency of a pristine and prelithiated S80 electrode. The inset shows the CE during the first 50 cycles. Electrodes with similar areal loadings (0.25 mg/cm^2) were used so that the results were comparable. The specific capacities are comparable but different trends are observed in the CE. The ICE of the pristine electrode is 86.5% compared to 97.8% for the prelithiated electrode. The CE of the pristine electrode, similarly to that shown in Figure 5.5b, drops from 98.3% at cycle 5 to 97.4% at cycle 19, before increasing with cycle number. The prelithiated electrode shows no dip in the CE and increases in CE with cycle number. After cycle 50, the CE of both electrodes is similar and at >99%. The cumulative irreversible capacity reaches 100% at cycle 50 for the pristine electrode, meaning a full-cell would have no capacity remaining at this point. For the prelithiated electrode, the cumulative irreversible capacity is just 77% at

50 cycles and exceeds 100% after 73 cycles. For the prelithiated and pristine electrodes, the capacity retention drops below 80% after 63 cycles and 107 cycles, respectively.

Full-cells

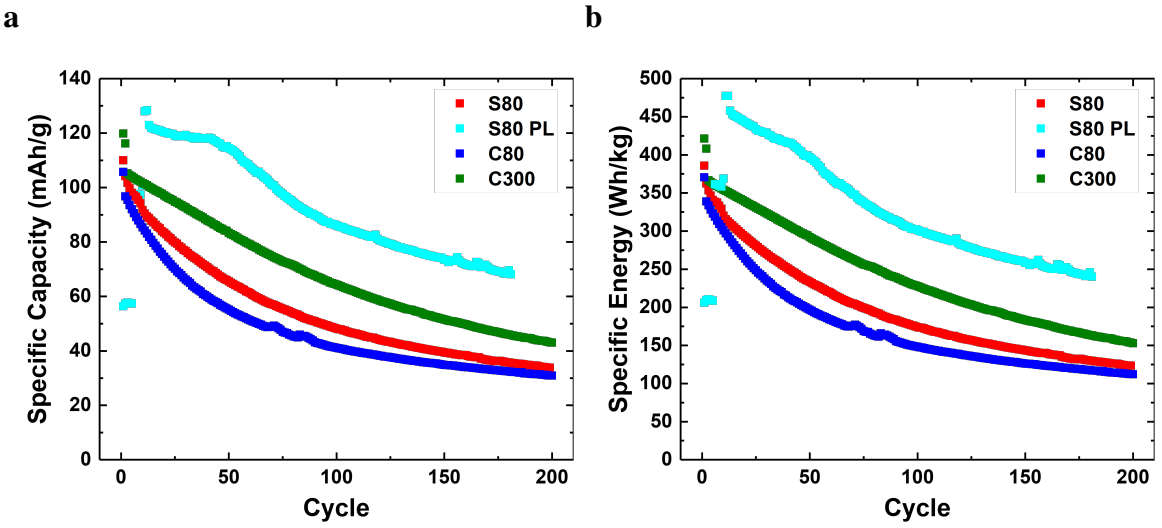

Figure. 5.9 Discharge specific capacity and energy density of C80, C300 and pristine and prelithiated S80 electrodes cycled against commercial NMC622 cathodes between 3 - 4.2 V at C/5. For the prelithiated S80 electrode, to prevent Li metal plating, the upper cut off voltage was limited to 3.8 V in the first 5 cycles and 4.0 in cycle 6 - 10. Formation cycles for all cells were performed at C/20. The specific capacities and energy densities were calculated with respect to the total mass of the cathode and anode coatings.

Figures 5.9a and 5.9b show the discharge specific capacity and energy density of C80, C300 and pristine and prelithiated S80 electrodes cycled against commercial NMC622 cathodes. The specific capacities and energy densities were calculated with respect to the total mass of the cathode and anode coatings. Each silicon-graphene anode tested had an areal loading between 1 - 1.5 mg/cm^2 and an N:P ratio between 1 and 1.2. These are considered optimal values for full cells with silicon-graphite anodes and NMC cathodes.[11] If the N:P ratio is too low, the end of charge potential on the anode side can drop below 0 V which would lead to Li metal deposition on the graphite. This could lead to dendrite formation, which can lead to short circuiting of the battery.[41] If the anode loading is too high, the capacity loss due to SEI formation is too high and this can lead to capacity loss and reduced cycle performance.[11] The similar loading levels mean the electrochemical performances are more comparable since the capacity of thicker electrodes can be kinetically limited.[205]

The initial specific discharge capacities of the S80, C80 and C300 cells were 110, 106 and 120 mAh/g, respectively. The initial discharge energy densities of the S80, C80 and C300 cells were 386, 371 and 421 Wh/kg. For the prelithiated S80 cell, the initial specific discharge capacity and energy density was 56 mAh/g and 206 Wh/kg, respectively. After the initial formation cycles this increased to 128 mAh/g and 477 Wh/kg. The capacity retention is highest for the prelithiated S80 electrode, the capacity drops to 80% after 61 cycles with respect to the capacity after the formation cycles. For the C300 cell, the capacity drops to 80% after 50 cycles with respect to the capacity after the formation cycles. For the S80 and C80 cells, the capacity drops to 80% after 21 and 18 cycles, respectively.

5.4.3 Raman Spectroscopy

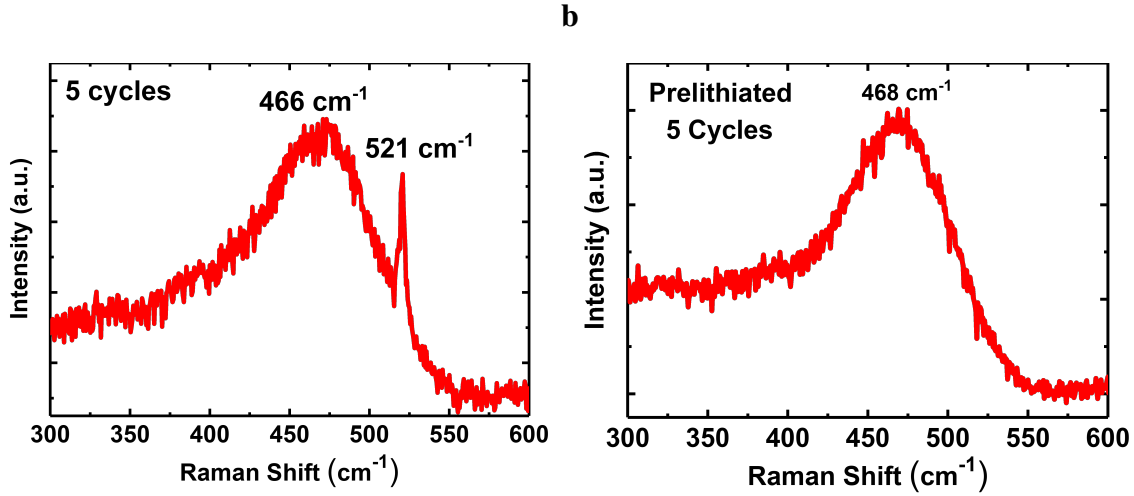

Figure. 5.10 Raman spectra of S80 electrodes after 5 dis/charge cycles a) without and b) with prelithiation. The spectral ranges have been chosen to highlight the amorphous (a-Si) and crystalline (c-Si) Si peaks. Samples were measured in the delithiated state.

Raman spectroscopy provides a convenient method of determining whether a silicon sample is crystalline or amorphous. C-Si has a single, triply degenerate Raman active mode, the T_{2g} mode which gives rise to a peak at 521 cm^{-1}.[208] As the Si crystallite size decreases, this peak gradually red shifts and becomes broader. a-Si consists of extremely small, randomly orientated crystallites. The lack of long-range order means that the fundamental Raman selection rules are relaxed and all phonon modes are allowed.[208] Variations in bond lengths and bond angles also lead to a larger range of vibrational energies within a-Si as compared to c-Si. This leads to a Raman spectra with a broad peak centred at $\sim$480 cm^{-1}.[208] Figure 5.10 shows the Raman spectra of pristine and prelithiated S80 electrodes after 5 electrochemical

dis/charge cycles. Two peaks are observed in the Raman spectra of the S80 electrode cycled without prelithiation, one at 521 cm^{-1} which corresponds to the T_{2g} mode of c-Si and the other at 466 cm^{-1} which corresponds to a-Si. In the Raman spectra prelithiated electrode, only the peak at 466 cm^{-1}, corresponding to a-Si, is observed.

5.4.4 NMR

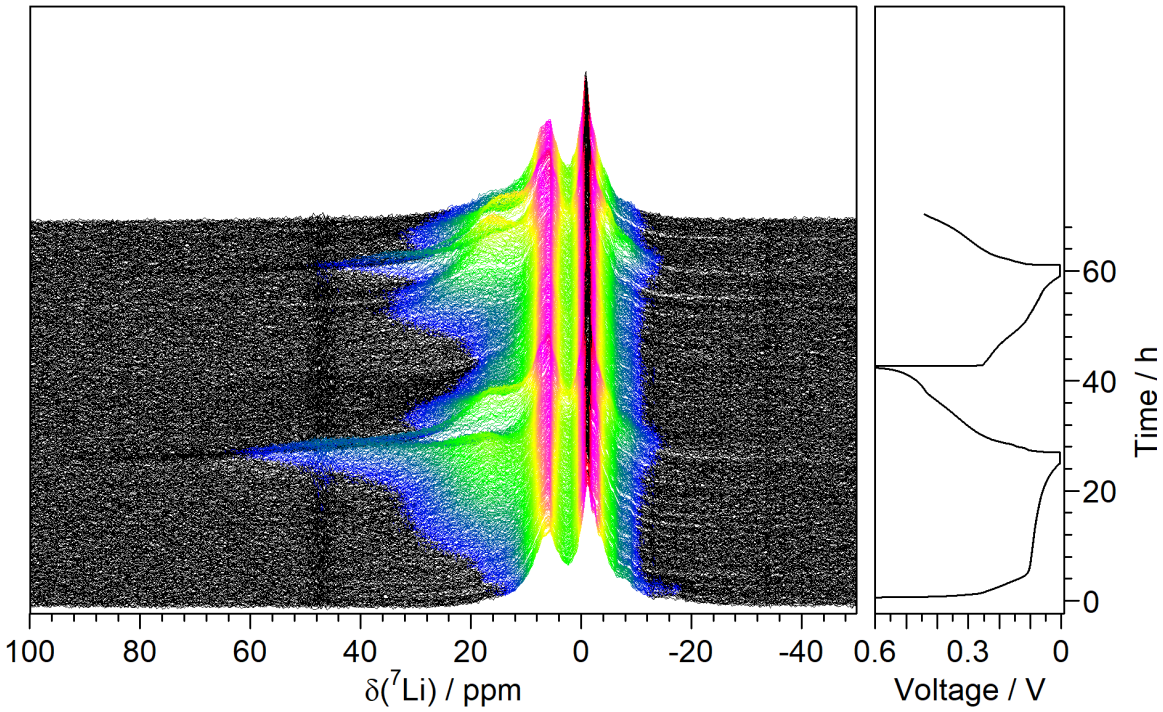

Figure. 5.11 *Operando* ^{7}Li NMR spectra of a C300 silicon-graphene anode half-cell. The potential profile as a function of time is shown on the right. The cell was electrochemically lithiated at C/20 between 0.005-1 V with a two hour potential hold at 5 mV at the end of discharge. The signal of Li metal at $\sim$ 260 ppm is not visible in this frequency range.

Figure 5.11 shows the *operando* ^{7}Li NMR spectra of a C300 anode during the first two dis/charge cycles. The cell was cycled between 5 mV and 1 V at C/20 with a two hour potential hold at 5 mV, where the current decayed to C/80. In the second cycle, the charging was stopped when the cell reached 0.4 V. Figures 5.12a and b also show the *operando* ^{7}Li NMR spectra acquired at 2.73 V (OCV), 95 mV, 87 mV, 62 mV and 5 mV during the first discharge and at 5 mV, 0.20 V, 0.31 V and 1.0 V during the first charge, respectively. The points in Figure 5.12c represent the potential and capacity of the corresponding spectra in

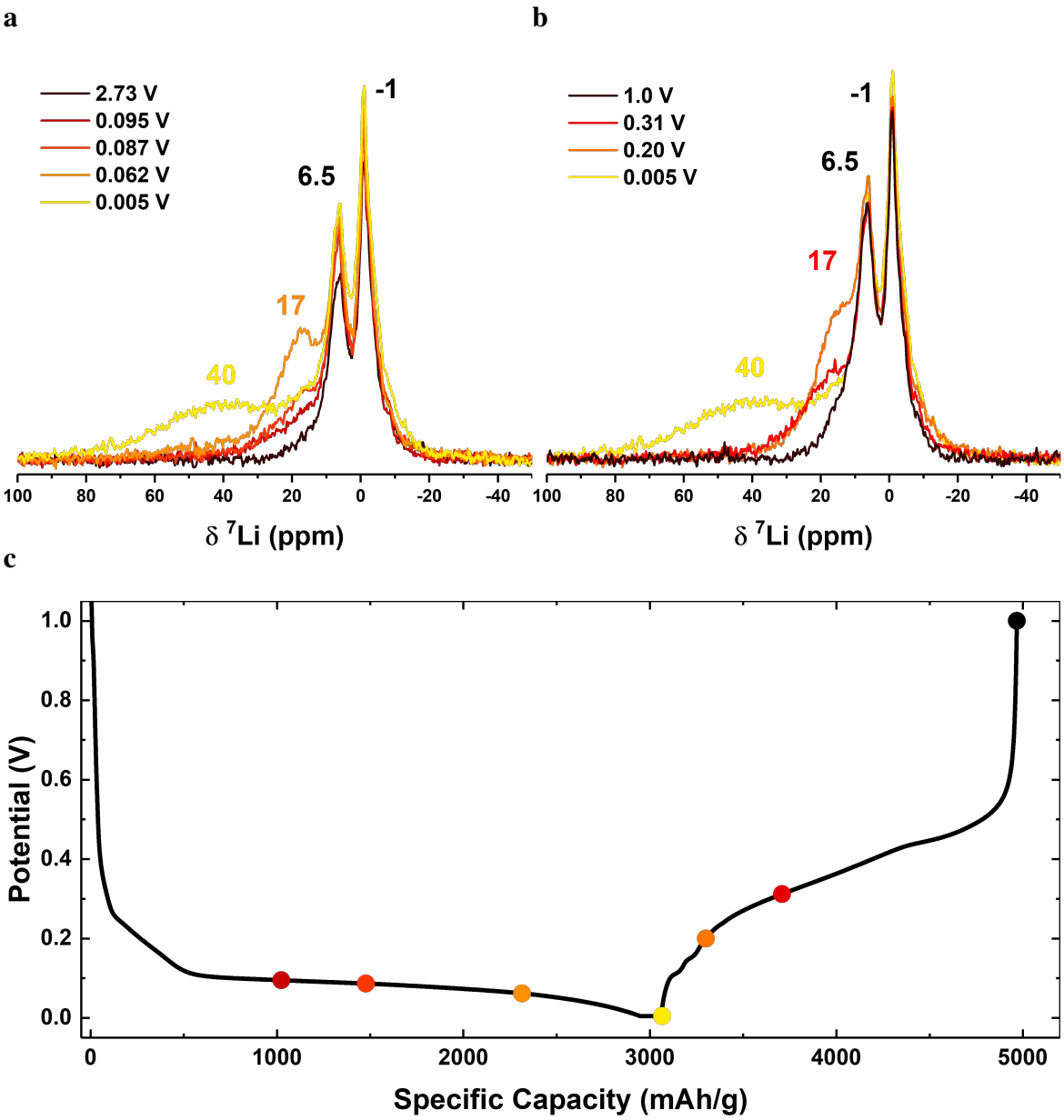

Figure. 5.12 *Operando* ^{7}Li NMR spectra of a C300 anode during the first a) discharge and b) charge. c) The potential profile as a function of specific capacity. Spectra shown in a and b are represented by the points along the potential profile in c.

Figures 5.12a and b. The initial specific capacity of the electrode is 3065 mAh/g with an ICE of 62.1%. The second cycle discharge specific capacity is 2077 mAh/g. Two peaks at 6.5 ppm and -1 ppm in the ^{7}Li NMR spectrum ppm are observed at OCV. The peaks do not change significantly during cycling of the battery. In previous studies by Key *et al.*, peaks in this region were attributed to Li in electrolyte and in the SEI on the silicon and Li

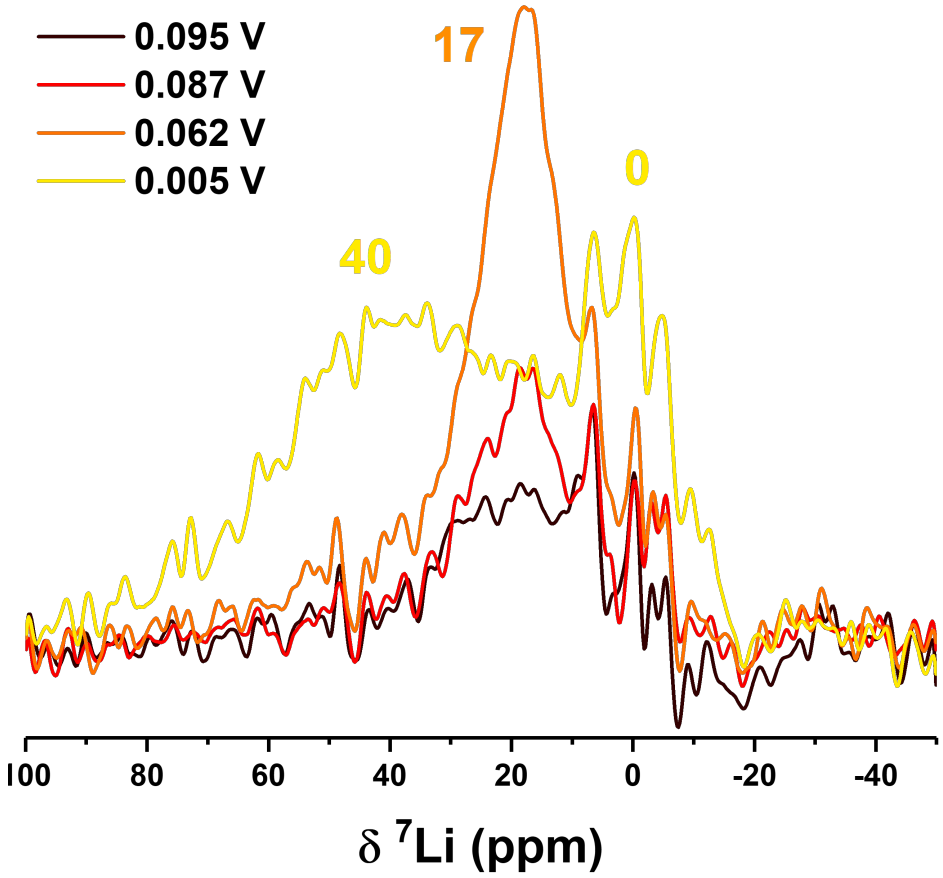

Figure. 5.13 *Operando* ^{7}Li NMR difference spectra of a C300 anode during the first discharge. The spectra plotted show the difference in intensity compared to the spectrum acquired at OCV before starting the first discharge.

metal electrodes. This peak at 6.5 ppm has not been observed during *in-situ* NMR studies of graphite anodes suggesting the SEI is different on silicon anodes than on graphite anodes.[209] The peak at 6.5 ppm could also be arise due to a shift of the electrolyte signal caused by bulk magnetic susceptibility (BMS) effects which arise due to the different magnetic susceptibilities of all the components within the capsule cell (Figure 4.2). The peak at -1 ppm could correspond to Li in the electrolyte, with rapid molecular tumbling leading to averaging of the dipolar and quadrupolar interactions, resulting in a sharp peak. The peak at -1 ppm could also correspond to LiF and Li containing SEI components.[157] At 95 mV, 87 mV and 62 mV during the first discharge, a peak 17 ppm is observed and corresponds to Li near small Si clusters.[189] The peak increases in intensity with capacity. Upon further lithiation, a broad peak at 40 ppm appears as well as a weak peak centered at approximately 0 ppm and the peak at 17 ppm decreases in intensity. The peak at 0 ppm is more clearly

observed in Figure 5.13, which shows the difference spectra relative to the spectrum acquired at OCV before the first discharge. The peak at 0 ppm disappears when the electrode is fully delithiated at 1 V. The peak corresponds to the crystalline c-$Li_{3.75}Si$ phase.[189] The reduction in intensity of the peak at 17 ppm is consistent with the breaking up of small Si clusters during lithiation.[53]

The broad peak at 40 ppm could correspond to the dense stage lithiated graphite.[209] In Chapter 3 this peak was much sharper therefore we suggest this peak could also correspond to metallic Li_xSi phases, which have also been observed in this region by Kitada *et al.* in lithiated SiO anodes, where the SiO had been heat treated at 1000 - 1100 °C.[195] The large ^7Li shift seen for the metallic Li_xSi phase is caused by a Knight shift with contribution from the Li 2*s* and Si 3*p* orbitals.[195] The heat treatment of SiO leads to disproportionation of the SiO and increases the domain size of Si crystallite that form. Heat treatment at 1000 - 1100 °C was shown, via XRD measurements, to result in crystallite sizes of $3-5$ nm.[195] The signal at 40 ppm therefore suggests that the 300 nm silicon may contain similarly small Si crystallites within the particles.

Figure 5.14 shows the *operando* ^7Li NMR spectra as a function of time during chemical lithiation of a C300 anode. The measurement was started within 5 minutes of closing the cell. Three peaks are observed at 6.5, -1 and -12 ppm. The two peaks at 6.5 and -1 ppm were also observed at OCV in the electrochemical cell, they are assigned to Li in the SEI and electrolyte, respectively, with the peak at 6.5 ppm likely shifted due to BMS effects. The peak at -12 ppm corresponds to the overlithiated crystalline c-$Li_{3.75+\delta}Si$ phase.[189] The peak at -12 ppm is observed in the first spectrum that was acquired after 5 minutes and increases in intensity over time. The largest change in intensity occurs between 10 and 200 minutes, suggesting that after this point, the reaction becomes rate limited, probably due to slow solid-state diffusion of the Li in the Si. No peak was observed around 40 ppm suggesting that the graphite did not lithiate during this experiment and no metallic Li_xSi phase was formed.

Figure 5.15 shows the *ex-situ* ^7Li MAS NMR spectra of an electrochemically (EL) and chemically (CL) lithiated C300 electrode, performed so as to obtain higher resolution spectra than is possible to obtain from *in-situ* experiments. The spectra are normalised so that the total intensity of each spectrum is equal. The EL sample was prepared by discharging a half-cell at C/30 while the CL sample was lithiated for 5 days prior to measurement. Three peaks are observed in the spectrum for the EL sample at 42, 11.8 and -1 ppm. In the spectrum for the CL sample, three peaks are also observed at 42, 6.1 and -0.8 ppm. The peaks at 42 ppm in the EL and CL samples correspond to the lithiated GIC LiC_6. The peak at 11.8 ppm in the EL sample corresponds to lithium near small Si clusters (a-$Li_{2.0-3.5}Si$).[54] The peak

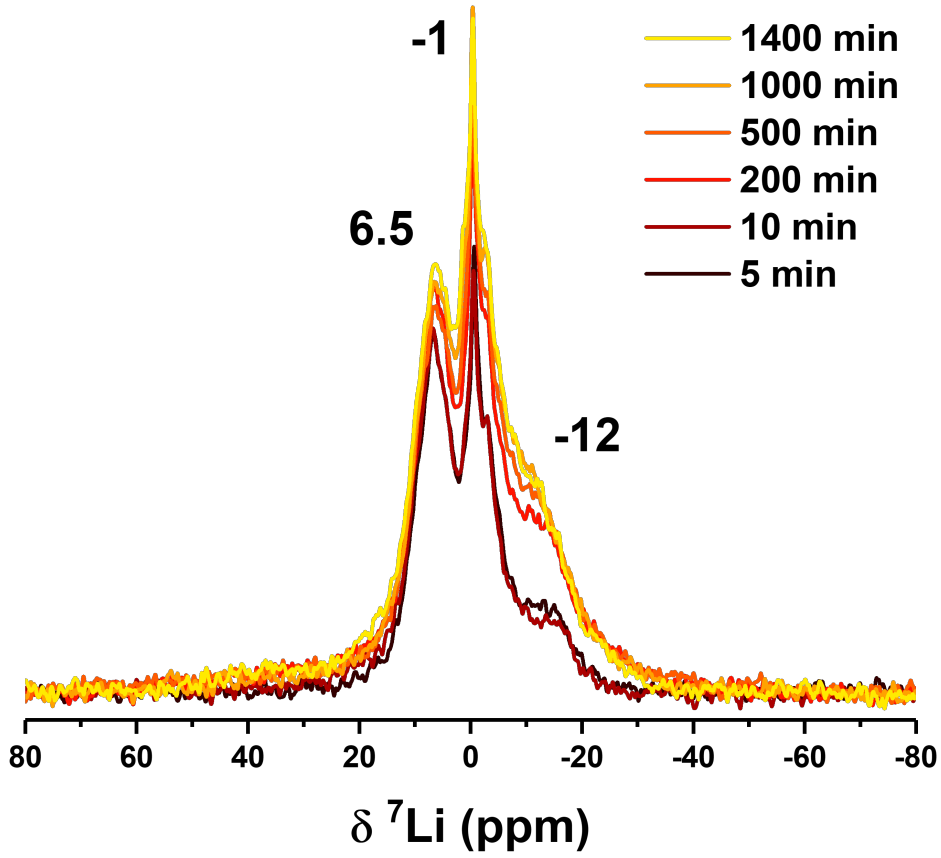

Figure. 5.14 *Operando* ^{7}Li NMR spectra as a function of time during chemical lithiation of a C300 anode.

at 6.1 ppm in the CL sample corresponds to the c-$Li_{3.75}Si$ phase.[54] Unlike in the *operando* NMR measurements, no peak corresponding to the overlithiated c-$Li_{3.75+\delta}Si$ was observed in the CL sample. This is in agreement with the results of Key *et al.*, who did not observe this c-$Li_{3.75+\delta}Si$ phase during *ex-situ* measurements.[54] They found that the phase was metastable and spontaneously reacts with the electrolyte which results in self-discharge of the lithiated silicon.[54]

The peak at -0.8 ppm in the CL sample is narrow, with a FWHM of 0.89 ± 0.06 ppm, suggesting that the Li is relatively mobile, leading to an averaging of dipolar, quadrupolar and CSA interactions. Since the electrodes were not washed before packing into the NMR rotor, the peak likely corresponds to residual electrolyte on the electrode surface or mobile Li in the SEI. The peak at -1 ppm in the EL sample is broader with a FWHM max of 6.99 ± 0.05 ppm, suggesting that the Li is less mobile than in the peak at -0.8 ppm in the CL sample.

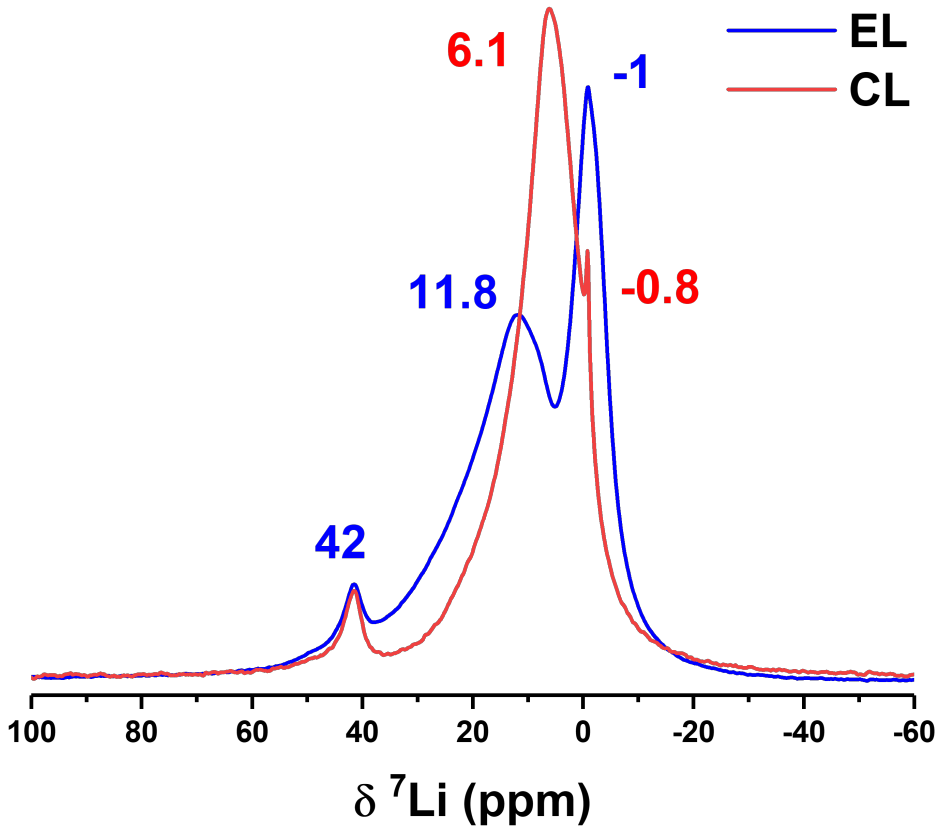

Figure. 5.15 *Ex-situ* ^{7}Li MAS NMR spectra of chemically (CL) and electrochemically (EL) lithiated co-microfluidized silicon-graphene anode with 300 nm silicon (C300). Spectra were processed with 100 Hz of line broadening. The spectra were normalised so that the total intensity is equal. The spectra were acquired with 64 scans, using a quantitative recycle delay that was fives time the T_1 of the slowest relaxing component.

This could be due to a difference in the SEI layer that forms during the different lithiation techniques.

5.4.5 VT NMR and Spin Lattice Relaxation

Figures 5.16a and 5.16b show the ^{7}Li NMR spectra of EL and CL C300 electrodes at temperatures between 261 - 331 K. Due to frictional heating of spinning the 2.5 mm rotor at 30 kHz during MAS experiments, 'room temperature' measurements actually corresponded to a temperature of 331 K, as determined by internal temperature calibration using the temperature dependent ^{79}Br NMR shift of KBr. The sample was cooled from this temperature down to 270 K and 261 K for the EL and CL samples, respectively, with T_1 measurements

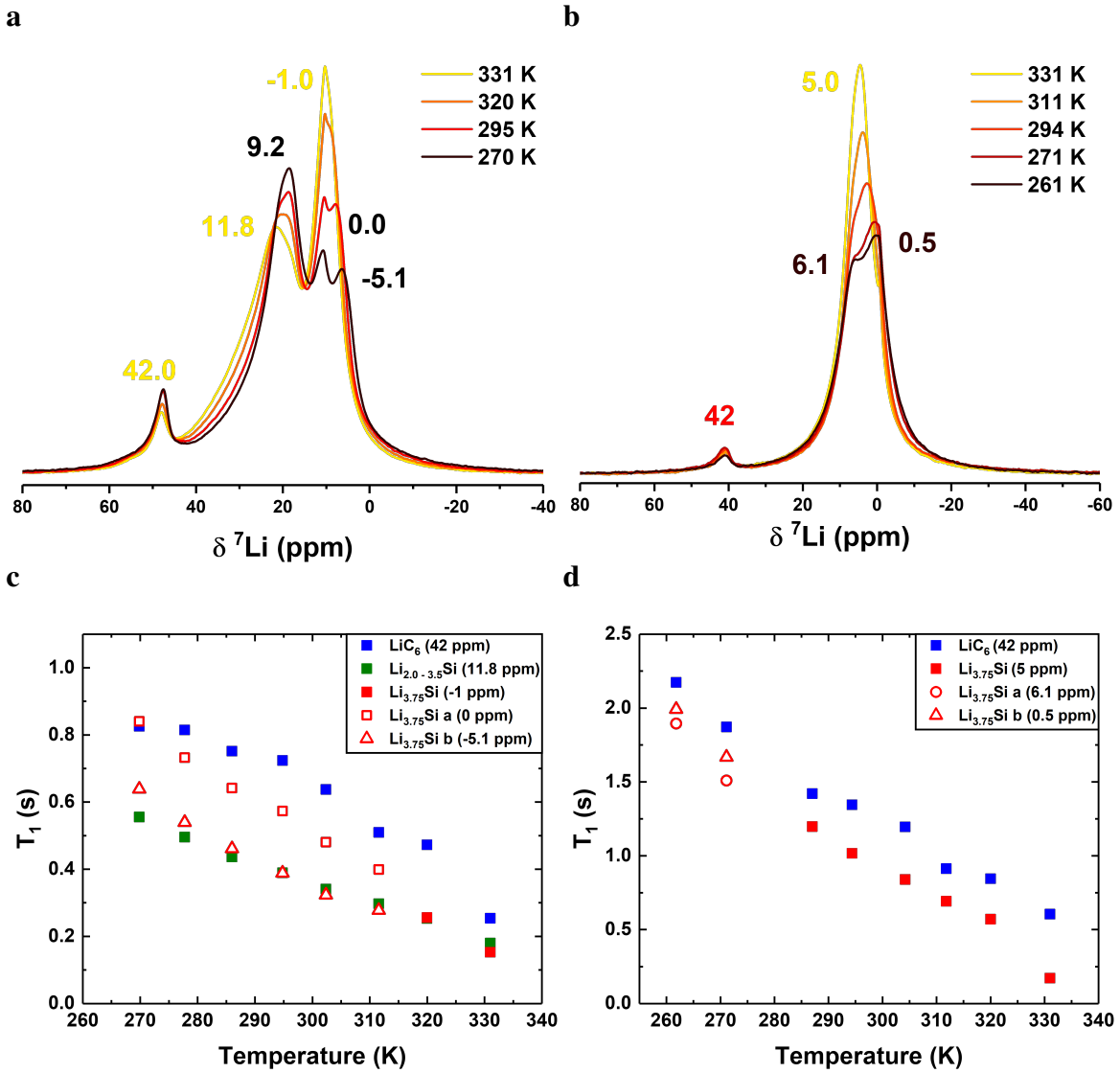

Figure. 5.16 ^{7}Li NMR spectra of a) electrochemically (EL) and b) chemically (CL) lithiated C300 electrodes at temperatures between 261 - 331 K. T_1 measurements as a function of temperature for the c) electrochemically (EL) and d) chemically (CL) lithiated C300 electrodes. The T_1 relaxation of each peak observed in a and b were satisfactorily fit with single exponentials. The peaks at 0 ppm and 6.1 ppm in the EL and CL samples were labelled c-$Li_{3.75}Si$ a and were assigned to a Li located slightly below a triangle of isolated Si. The peaks at -5.1 ppm and 0.5 ppm in the EL and CL samples were labelled c-$Li_{3.75}Si$ b and were assigned to Li tetrahedrally coordinated to Si.

performed at each temperature, shown in Figures 5.16c and 5.16d. Upon cooling of the EL sample to 270 K, the peak at -1 ppm splits into two peaks at 0.0 ppm and -5.1 ppm. The results show that the single peak at -1 pm is the result of the coalescence of signals from multiple environments: at 331 K, the two environments are undergoing chemical exchange

and have a coalescence temperature of 320 K. Cooling the sample slows the exchange rate such that is slower than the NMR timescale enabling the observation of both environments. A similar phenomenon is observed for the peak at 5.0 ppm in the CL sample, two peaks being observed at 6.1 ppm and 0.5 ppm at 261 K, with a coalescence temperature of 294 K. The peaks are separated by 995 Hz and 1088 Hz, respectively, for the EL and CL samples at 270 K and 262 K. At the coalescence temperature, the exchange rate constant for a two-site system is approximately equal to half the frequency separation of the two environments.[88] This means the exchange rate constant between the two environments in the EL and CL samples is at least 0.5 kHz at the coalescence temperatures of 320 K and 294 K, respectively. Baran *et al*., observed the onset of motional narrowing in static ^{7}Li NMR measurements of the c-$Li_{3.75}Si$ phase occurs at 200 K.[191] The results of Baran *et al*. suggests that the peaks are likely to separate further if the temperature was decreased to 200 K. Such low temperatures could not be achieved with a 2.5 mm rotor at 30 KHz MAS. The changes in the lineshape for the EL spectra are reversible upon returning back to 320 K (Figure C5). The peak at 11.8 ppm increases in intensity and shifts to 9.2 ppm as the sample is cooled. The increase in intensity is consistent with that expected from Equation 2.8, 20%, due to a change in the Boltzmann distribution of the nuclear spins. The peak shift, from 11.8 ppm to 9.2 ppm, suggests that there might be multiple Li environments in this region that are also undergoing chemical exchange. The decrease in intensity of the peak at -1 ppm and 5 ppm in the EL and CL samples, respectively, is due to the splitting of the peaks.

Similar observations were reported by Dupke *et al*. using VT ^{7}Li and ^{6}Li NMR of lithiated silicon, synthesized chemically at high temperatures in a furnace.[190] They observed two peaks at 200 K for the $Li_{15}Si_4$ compound, one at 7.5 ppm corresponding to Li located slightly below a triangle of isolated Si (c-$Li_{3.75}$Si a), and another at -8 ppm corresponding Li tetrahedrally coordinated to Si (c-$Li_{3.75}$Si b).[190] This is also consistent with the structural representation of $Li_{3.75}Si$ reported by Key *et al*., which predicted two Li environments in $Li_{3.75}Si$, though only one ^{7}Li NMR peak was observed at room temperature.[54] Dupke *et al*., also showed that the c-$Li_{3.75}$Si a environment possesses a lower positive charge than the c-$Li_{3.75}$Si b environment which explains why the c-$Li_{3.75}$Si b environment appears at a lower frequency.[190]

At 300 K, Dupke *et al*. showed that the relative positions of the two ^{7}Li NMR peaks change. The c-$Li_{3.75}$Si a peak at 7.5 ppm shifts towards lower frequencies and is found at 2.5 ppm at 300 K, while the weaker c-$Li_{3.75}$Si b peak originally at -8 ppm, shifts towards higher frequencies and is found at 7.5 ppm at 300 K.[190] We therefore suggest that the peak at 0.0 ppm and 6.1 ppm in the EL and CL samples, respectively, correspond to c-$Li_{3.75}$Si a, while

the lower frequency peaks at −5.1 and 0.5 ppm correspond to c-$Li_{3.75}$Si b. At 270 K in the EL sample, the relative intensity of the c-$Li_{3.75}$Si a to c-$Li_{3.75}$Si b peaks is ∼1:2, while for the CL sample the relative intensity is ∼2:1. The inconsistent peak positions could be due to differences in Li mobility or different Li to Si ratios within the c-$Li_{3.75}$Si/c-$Li_{3.75+\delta}$Si phase, which may lead to differences in the electronic interactions in the samples. The differences in intensity could be due to the because the EL sample has a higher ratio of the c-$Li_{3.75}$Si a to c-$Li_{3.75}$Si b within the c-$Li_{3.75}$Si phase. This can occur since the c-$Li_{3.75}$Si is not a line phase.[53] There were more Li environments observed in the EL sample and this made fitting more challenging which adds uncertainty to the relative intensities for this sample.

Figures 5.16c and 5.16d show the T_1 as a function of temperature of the different compounds found in the EL and CL samples, the data is summarised in Table 5.2. The room temperature (295 K) T_1 values for the LiC_6 compound in the EL and CL samples are 0.72 s and 1.35 s, respectively. These are shorter than the T_1 time constants for LiC_6 found for the Hitachi MAGE 3 graphite found in Chapters 4 and 3. $T_{1LiC6} = 1.80$ s at 4.7 T and $T_{1LiC6} = 1.69$ s at 16.4 T, while the measurements on the silicon-graphene anodes were carried out at 11.7 T. This suggests that there is faster Li motion within the graphite/graphene in the silicon-graphene anodes, which could be due to smaller particle size of the graphite in silicon-graphene anodes (< 3 µm) compared to the Hitachi MAGE 3 graphite (∼30 µm).[21,192] The activation energies for Li motion within the LiC_6 compound in the EL and CL samples are $E_a = 0.09 \pm 0.01$ eV and $E_a = 0.13 \pm 0.01$ eV, respectively. These activation energies are comparable to those found for Li motion in LiC_6 above 279 K in Chapter 4. The relaxation also does not follow the Korringa relation, (i.e. $T_1 * T =$ constant), which suggests that relaxation via the dipolar and quadrupolar interactions, mediated by Li motion, are the dominant relaxation mechanisms. This is in contrast to the ^{7}Li T_1 relaxation seen in LiC_6 (Chapter 4), where Korringa relaxation was the dominant mechanism.

The T_1 of Li near small Si clusters (a-$Li_{2.0-3.5}$Si), which results in a peak at 9.2 - 11.8 ppm in the spectrum for the EL sample, is 0.39 s and the activation energy for lithium motion within this phase is $E_a = 0.13 \pm 0.01$ eV. For c-$Li_{3.75}$Si a (0.0 ppm) and c-$Li_{3.75}$Si b (−5.1 ppm) the $T_1 = 0.57$ s and $T_1 = 0.39$ s, respectively. The activation energy for Li motion within these phases is $E_a = 0.13 \pm 0.01$ eV and $E_a = 0.146 \pm 0.004$ eV, respectively. For the c-$Li_{3.75}$Si compound at 5 ppm in the CL sample, the $T_1 = 1.02$ s at 295 K and the activation energy for Li motion within the phase is $E_a = 0.18 \pm 0.01$ eV. This activation energy for Li motion in c-$Li_{3.75}$Si is lower than that determined by Dupke *et al.* (0.25 eV) but closer to Baran *et al.* (0.16 eV).

Table 5.2 Room temperature (294 K) T_1 relaxation times and activation energies E_a for lithium motion for the phases observed in the electrochemically (EL) and chemically (CL) silicon-graphene electrodes. The activation energies were determined from the gradient of T_1 versus temperature on an Arrhenius plot.

Sample	Phase	Peak Position (ppm)	T_1 @ 294 K (s)	E_a (eV)
EL	LiC_6	42	0.72	0.09 ± 0.01
CL	LiC_6	42	1.35	0.13 ± 0.01
EL	$Li_{2.0-3.5}Si$	9.2 - 11.8	0.39	0.13 ± 0.01
EL	$Li_{3.75}Si$	-1.0	-	-
EL	$Li_{3.75}Si$ a	0.0	0.57	0.13 ± 0.01
EL	$Li_{3.75}Si$ b	-5.1	0.39	0.146 ± 0.004
CL	$Li_{3.75}Si$	5.0	1.02	0.18 ± 0.01
CL	$Li_{3.75}Si$ a	6.1	-	-
CL	$Li_{3.75}Si$ b	0.5	-	-

The results of Dupke *et al.* lead us to conclude from the longer T_1 times in the CL sample, that the CL sample is more lithiated than the EL sample. This is also consistent with the smaller plateau at 0.4 V (Figure 5.7), in the EL sample compared to PL sample, which corresponds to the delithiation of the c-$Li_{3.75}Si$ phase. We can also conclude, from the activation energies, that the compound assigned to c-$Li_{3.75}Si$ in the CL sample is closer to the chemically synthesized c-$Li_{3.75}Si$ of Dupke *et al.* and Baran *et al.* than the compound assigned to c-$Li_{3.75}Si$ in the EL sample.[190,191]

5.5 Discussion

For the 80 nm silicon used in this work, co-microfluidization of graphite and silicon was shown to lead to electrodes with a much more homogeneous composite structure. The high pressures involved in the co-microfluidization process were able to break apart the micron sized SiNP agglomerates. This, however, led to electrodes with a lower specific capacity. This could be because the breakup of the SiNP agglomerates leads to an electrode with lower porosity and higher tortuosity, which could also be the cause for the difference in rate capabilities of the C80 and S80 anode half-cells, as shown in Figure C2. However, for the C300 and S300 anodes, this trend was reversed (Figure C2) suggesting that the improved dispersion of the graphene within the composite structure increased the rate capability

of the electrodes, possibly due to improved conductivity of the composite produced by co-microfluidisation.

The breakup of the SiNPs also leads to a lower ICE due to the increased surface area. During further cycling, the CE in half cell testing is similar. In full-cell testing, the S80 electrode has a slightly higher specific capacity, 110 mAh/g, and energy density, 386 Wh/kg, compared to the C80 electrode, where these values are 106 mAh/g and 371 Wh/kg, respectively. The S80 electrode also has a slightly higher capacity retention, reaching 70% capacity retention at cycle 37 instead of cycle 27 for the C80 electrode. The higher capacity and cyclability of the S80 electrode in full-cell testing, could be due to lower Li loss due to the improved CE of the S80 material, as well as the better rate capability compared to the C80 material (Figure C2).

Co-microfluidization of the 300 nm silicon leads to more significant improvements in the capacity and cyclability of the electrodes compared to the shear mixed 300 nm silicon electrodes. The ICE, at 79.7% and 78.9% for the C300 and S300 electrodes, respectively, are comparable. However, the capacity retention is significantly improved with 72.1% capacity retained after 255 cycles for the C300 electrode and just 26% retained after 200 cycles for the S300 electrode. The CE as of function of cycle number for the C300 electrode is also improved compared to the S300 electrode. In full-cell testing, the C300 electrode shows the best performance out of the silicon-graphene electrodes that were not prelithiated and was able to achieve a specific energy density of 421 Wh/kg at C/20 and 367 Wh/kg at C/5. The energy density was maintained above 70% of this value for 75 cycles.

For both the C300 and C80 electrodes, 30 co-microfluidic cycles were found to give the optimum performance. This could be due to a balance of the graphite and graphene contents within these electrodes, with more process cycles leading to greater graphene content due to increased exfoliation of the graphite. The graphene is beneficial due to its high aspect ratio which improves the mechanical properties of the composite. It also prevents the silicon particles from agglomerating during repeated volume expansion during cycling.[179] The graphene also acts as a conductive additive and will improve the electrical conductivity of the composite.[192] Graphite is beneficial because it will contribute to the capacity of the composite material. It also has a lower surface area which will lead to a higher CE as less SEI will form. We believe that the graphite and graphene produced during the thirty co-microfluidic cycles offers an optimum balance between these properties.

We have shown that prelithiating the silicon-graphene anodes via chemical lithiation leads to a deep lithiation. *Operando* ^{7}Li NMR measurements (Figure 5.14) show that electronically short circuiting the silicon-graphene electrodes leads to a spontaneous reaction where the c-Si

converts to c-$Li_{3.75+\delta}Si$. This reaction proceeds via the surface of the silicon particles and the reaction becomes kinetically limited after around 200 minutes with the C300 electrodes, as shown by the lower rate of increase of the peak at -12 ppm after 200 minutes in Figure 5.14. This is likely due to the slow Li ion mobility in the c-$Li_{3.75+\delta}Si$ phase and because Li has to diffuse through the Si.[190] Electrochemical lithiation, on the other hand, does not result in a deep lithiation of the electrode. *Operando* ^{7}Li NMR measurements (Figure 5.11) show that even with a low current density (C/20) and a two hour potential hold at 5 mV, that the silicon does not fully convert to the c-$Li_{3.75}Si$ phase; a portion of the silicon is only lithiated to the c-$Li_{2.5}Si$ phase with a signal still remaining at 17 ppm at the end of discharge. This is also observed in the *ex-situ* ^{7}Li NMR MAS (Figure 5.15) measurements, with the peak at 11.8 ppm remaining at the end of discharge. The Raman spectra of the electrochemically lithiated S80 electrodes also shows that some Si, likely the large agglomerates observed in Figure 5.2, is still crystalline, and therefore, has not reacted with Li even after 5 cycles. The chemically lithiated Si shows no peak in the Raman spectrum due to crystalline Si after 5 cycles, showing that all the Si has reacted with the Li. The deeper lithiation is also confirmed by the potential profiles of the electrochemically and chemically lithiated S80 electrodes (Figure 5.7)

The deeper lithiation achieved by chemical lithiation compared to electrochemical lithiation is also confirmed by ^{7}Li T_1 measurements (Figure 5.16). In Chapter 4 we showed that the ^{7}Li T_1 of Hitachi MAGE 3 graphite, lithiated to the LiC_6 phase, had a longer T_1 when the sample had a lower cut-off voltage and higher capacity. When the cut-off voltage was set to 10 mV, the capacity reached was 408 ± 5 mAh/g in the first cycle and the T_1 was 1.85 s at room temperature. When the cut-off voltage used was 5 mV, the capacity was 418 ± 5 mAh/g and $T_1 = 1.31$ s. The difference in T_1 for the 5 mV and 10 mV samples was ascribed to faster Li motion in the 10 mV sample. Faster relaxation was observed in the EL sample ($T_1 = 0.72$ s) compared to the CL sample ($T_1 = 1.35$ s). This suggests that the intercalated Li in the graphite/graphene in the CL sample has slower motion and the Li-GIC is more lithiated than in the EL sample. The shorter T_1 times compared to those measured for the Hitachi MAGE 3 graphite could be due faster Li motion as a result of the smaller crystallite size of the graphite/graphene produced by co-microfluidization.

The results of Dupke *et al.* lead us to conclude from the longer T_1 times seen for ^{7}Li spins in the CL sample, that the CL sample is more lithiated than the EL sample. We can also conclude, from the activation energies, that the Li motion within the c-$Li_{3.75}Si$ phase in the CL sample is closer to the Li motion in the chemically synthesized c-$Li_{3.75}Si$ sample of Dupke *et al.* and Baran *et al.* than the Li motion in the c-$Li_{3.75}Si$ phase in the EL sample.

This deeper lithiation could be the reason for the increase in CE observed in the prelithited S80 electrode observed in Figure 5.8. The ICE of the prelithiated sample, 97.4%, is higher than that of the pristine electrode, 86.5%. This is because the SEI has already formed during the prelithiation process, and this mitigates the first cycle losses in the prelithiated sample. This does not explain why there is a dip in CE observed in the pristine sample between cycle 5 and 19 and not in the prelithiated sample. This dip was also observed by Ogata *et al.* during the cycling of SiNP electrodes.[161]

The dip in CE is caused by the parasitic reactions between the metastable c-$Li_{3.75+\delta}Si$ phase and the electrolyte which causes self-discharge of the lithiated Si. Ogata *et al.* found that the dip in CE was more pronounced and recovered to a higher CE value more quickly when the depth of lithiation was higher.[161] They attributed the differences in the rate of recovery of the CE, to structural changes as a result of the repeated formation of the c-$Li_{3.75+\delta}Si$ which rearranges the Si-Si bonds. These structural changes lead to more homogeneous lithiation of the silicon and a decrease in the proportion of the metastable c-$Li_{3.75+\delta}Si$ phase formed at the end of discharge.[161] This decreases the amount of parasitic reactions that occurs which leads to an increase in the CE.

The difference in CE between the chemically lithiated and pristine electrode shows that the deep lithiation achieved by the chemical lithiation of Si leads to a larger change in the structure of Si than is achieved by electrochemical lithiation. This leads to a more homogeneous lithiation of the silicon in subsequent cycles, which results in higher CEs in the prelithiated sample. The higher CE results in improved cycle performance with the total cumulative irreversible capacity exceeding 100% after 50 cycles for the pristine electrode and 73 cycles for the prelithiated electrode. The prelithiated electrode may also have a more stable SEI, as the SEI has more time to form during chemical lithiation than during electrochemical lithiation. The more stable SEI in the prelithiated electrode may also contribute to the improved cycle performance.

The reduction in the cumulative irreversible capacity is reflected in the full-cell testing shown in Figure 5.9, with the capacity fading to 70% after 91 and 37 cycles with and without prelithiation, respectively. The increase in the cyclability between the prelithiated and pristine electrodes is larger in the full-cells compared to the half-cells. This suggests that as well as the reduction in Li loss in the anode, that the capacity is also increased by the increase in Li inventory achieved by prelithiating the S80 electrode.

These results suggest that a deep lithiation during the formation cycle, which leads to full lithiation the Si to the c-$Li_{3.75}Si$ and c-$Li_{3.75+\delta}Si$ phases, is beneficial to the long term cyclability of the silicon-graphene anodes. This is because of the restructuring of the Si

bonds, and the formation of smaller a-Si clusters upon delithiation that occurs after as a result of charging to a high depth of charge.[161] These results are supported by the work of Ogata *et al*. and are contrary to previous results that show that the formation of the c-$Li_{3.75}Si$ is detrimental to the cyclability of silicon anodes.[54,161,210] While chemical lithiation may not be the most practical route to prelithiate a silicon anode, other routes such as using stabilised lithium metal particles could be used.[211] This would allow a high depth of charge to be achieved in the first cycles, which would improve the cyclability in subsequent cycles.

5.6 Conclusions

The electrochemical cycle performance of silicon-graphene anodes produced by conventional shear mixing and a novel, highly scalable co-microfluidisation technique were compared. Silicon-graphene anodes were tested with realistic mass loadings, achieving areal capacities between 2.28 - 3.45 mAh/cm^2. Co-microfluidization was shown to increase the homogeneity of the silicon-graphene anodes compared to electrodes prepared via conventional shear mixing, and was also able to break apart SiNP agglomerates. This led to improved cycle performances for the co-microfluidized silicon-graphene anodes, in both half-cells and full-cells, when 300 nm silicon was used. In half-cells the capacity retention, relative to the initial discharge capacity increased from 52.4% after 255 cycles for the co-microfluidized electrode compared to 20.3% after 200 cycles for the shear mixed electrode. For electrodes that used the 80 nm SiNPs, the breakup of the SiNP agglomerates led to a decrease in the ICE, likely due to an increase in the surface area. The initial discharge capacity also decreased from 2672 mAh/g to 2135 mAh/g, which has been ascribed to an increase in tortuosity of the electrode. From these results, we showed that the electrochemical performance of the silicon-graphene anodes, in agreement with Zhu *et al*., was dependent on the size and morphology of the SiNPs.[162] The capacity of the flaky (300 nm) silicon used in this work was lower than the spherical silicon (80 nm) as was observed by Zhu *et al*., the capacity retention of C300 was higher than C80, while Zhu *et al.* observed the capacity retention to be higher in spherical silicon particles. This highlights the complexity in drawing conclusions from the performance of composite silicon anodes that can be applied to other systems.

The superior half-cell performance of the C300 electrode translated to better cycle performance in full-cells. When using an NMC622 cathode, an initial energy density of 421 Wh/kg and 80% capacity retention after 50 cycles were achieved.

Prelithiation, via chemical lithiation, was shown to be an effective technique to improve the cycle performance of silicon-graphene anodes. In half-cells, the CE increased from $84 \pm 3\%$ in pristine electrodes to $98.1 \pm 0.7\%$ in prelithiated electrodes. The capacity retention also increased from 68.2% to 79.3% in half-cells. In full-cells, prelithiation led to an increase of cycle life, with the capacity dropping below 80% after 21 cycles for pristine electrodes and 55 cycles for prelithiated electrodes.

The improvement in performance was shown via Raman and NMR spectrocopies to be due to a deeper initial lithiation achieved by chemical lithiation compared to electrochemical lithiation. In chemically lithiated electrodes, the silicon was fully lithiated to the c-$Li_{3.75+\delta}Si$ phase. In the electrochemically lithiated samples, despite slow C/20 cycling with a potential

hold, not all the silicon was converted to the c-$Li_{3.75}Si$ phase. This deeper lithiation resulted in an increase in the CE in the first 50 cycles of silicon-graphene half-cell with dip in CE observed for electrodes that were not prelithiated. The increase in CE, in agreement with the results of Ogata *et al*., is due to all the Si reaction with Li in the first cycle which leads to greater structural rearrangement of the Si-Si bonds.[161]

Variable temperature ^{7}Li NMR and relaxometry measurements showed that the peak attributed to the crystalline c-$Li_{3.75}Si$ phase was the result of two chemically exchanging ^{7}Li environments. At low temperatures the peak separated into two peaks. The higher frequency peak was attributed to Li located slightly below a triangle of isolated Si (c-$Li_{3.75}$Si a), while the lower frequency peak was attributed to Li tetrahedraly coordinated to Si (c-$Li_{3.75}$Si b).

The longer T_1 relaxation times and higher activation energies for Li motion in the CL sample compared to the EL sample showed Li motion is slower in the CL sample. The T_1 times of LiC_6 in the graphite/graphene within the silicon-graphene electrodes were shorter in both cases than the T_1 measured for the Hitachi MAGE 3 graphite in Chapters 4 and 3. This was likely due to faster Li motion within the smaller graphite particles used within the silicon-graphene anodes.

Chapter 6

Conclusions and Further Work

The lithiation of graphite has been widely studied for many decades,[25,100,212,213] yet many questions remain about the exact lithiation mechanism, particularly within the dilute stage Li-GICs.[26] In this work we have shown that ssNMR is a useful technique to study the lithiation of graphite and can provide insight into the kinetics of the reactions, by probing Li motion within the Li-GICs. NMR unlike diffraction and electrochemical techniques can provide information on the local structure and electronic properties of Li instead of showing average or bulk properties of the lithiated graphite.

While *ex-situ* ^{13}C measurements have been useful in determining the electronic structure and state of charge of lithiated graphite, *in-situ* and *operando* measurements could provide more insight into how the transitions between Li-GIC stages proceed. The assignment of the ^{13} NMR peak positions presented in this work offer a good starting point for these studies. *In-situ* and *operando* measurements, which are typically performed without MAS due to hardware limitations, will be challenging because of the broad NMR signals that are obtained during static experiments, particularly for the dilute stage Li-GICs, as shown in Chapter 3. The narrower lineshape of the dense stage compounds might be easier to study, though more questions remain on the stage transitions between dilute stages, so a study of these compounds would be more interesting. The *in-situ* MAS technique developed by Freytag *et al*. may provide one method to overcome these issues.[42] A further challenge of *in-situ* and *operando* measurements, is that much of the components of the cell, e.g., the electrolyte and the PEEK casing used in this work, contain carbon and therefore overlapping signals may occur, making it more difficult to discern any changes in peak position and shape. Using ^{13}C enriched graphite, as in the work of Vyalikh *et al*., could help overcome some of these issues, though the electrochemical performance of the ^{13}C enriched graphite studied, differed from that of typical battery grade graphite.[103]

Another direction for future work from this project is to perform heteronuclear double resonance ssNMR measurements, such as the cross polarisation (CP) or rotational-echo double-resonance (REDOR) measurements, which can provide a measure of the dipolar coupling between a heteronuclear spin pair.[214] Such techniques could be used to correlate the ^{13}C and ^{7}Li NMR peaks of each Li-GIC stage. This would be particularly useful to study the dilute stage Li-GIC as it could help determine whether the multiple ^{13}C NMR peaks observed for the LiC_{24} sample in Figure 3.10 arise from multiple Li-GIC phases present in the sample or from ^{13}C atoms next to and not next to a Li layer. CP measurements for the LiC_6 sample, shown in Figure A5, were performed and as expected, showed that all the ^{13}C atoms are near to Li. However, for the dilute stage compounds, these experiments have proved to be more challenging, due to the faster Li motion within these samples even when performed at $-40\,^{\circ}$C, where the Li motion is slower. Performing these measurements at even lower temperatures could help overcome these issues. The $1/r^3$ dependence of the dipolar coupling in REDOR measurements, also means these experiments could be exploited to determine the distance between the ^{13}C and ^{7}Li nuclear spins.

Previous works have shown how the lithiation of graphite is sensitive to the kinetics of the reaction, which are affected by temperature as well as charging rate and direction.[24,26,30] In this work, we have used ^{7}Li NMR and relaxometry measurements to study the Li motion as a function of state of charge. We showed that the Li motion at room temperature is faster within the dilute stages than in the dense stages. Additionally, we showed that as the stages "fill-up", that the Li motion is reduced. In this work we focused on studying the lithiation of graphite during the first discharge. Didier *et al.* showed that the delithiation of graphite follows a different staging mechanism than during.[26] They showed that during delithiation, the stage 2L Li-GIC can be electrochemically synthesized without any other Li-GIC stages coexisting in the sample and in agreement with the work presented here, they showed that this was not possible during lithiation of graphite.[26] As such it would be interesting to apply the same techniques in this work to study the delithiation mechanism of graphite and this could give further insight into the differences between the stage 2L and stage 2 Li-GIC. The techniques in this work could also be applied to study any degradation mechanisms within graphite as a function of cycle number. They could also be used to study any differences in the lithiation mechanisms or Li motion between different graphites e.g., NG and SG and could help rationalise a choice of graphite for a particular application.

In-situ ^{7}Li T_1 measurements gave insight into the Li dynamics during the first lithiation of graphite. We showed that ^{7}Li $T_{1\rho}$ measurements could probe Li motion at lower frequencies (kHz) at ambient conditions, close to those of a real battery. *In-situ* ^{7}Li $T_{1\rho}$ measurements

could provide more insight into the Li motion within Li-GICs. Also, most of the relaxometry measurements in this work were performed at one magnetic field strength, measurements at different field strengths could provide further insight into the Li dynamics within the Li-GICs.

In Chapter 5, co-microfluidization was shown to be a promising technique to scalably produce silicon-graphene anodes which showed promising electrochemical performance in both half-cell and full-cell configurations, however, the capacity retention still needs to improve for these anodes to become commercially relevant.To further improve the cycle performance, future work should explore using lower silicon content than used in this work (60%) as well as explore different silicon materials such as silicon monoxide.[195] The Timrex KS25 graphite used in this work was chosen as it has been found to produce high quality graphene flakes via microfluidization.[192] This means it is not necessarily an optimal graphite for LIB applications, so different graphite materials could be explored to try and improve the cycle performance.

The effect of the co-microfluidization process on the binder, surface oxide layer of silicon and adhesion between the binder, active materials and the current collector should also be studied as any changes during the process can have important impacts on the cycle performance.[215]

Prelithiation was shown to be a useful technique to improve the cycle life of full-cells with an NMC622 cathode and silicon-graphene anode. However, the chemical lithiation method used in this work is not easily scalable. Instead, the use of stabilized lithium metal salt to prelithiate the silicon-graphene anodes should be explored.[211] This material could be directly added into the high pressure homogenizer and co-microfluidized with the silicon and graphite to homogeneously distribute it throughout the composite electrode. This technique would be more scalable and the amount of Li that is prelithiated could be more precisely controlled. The prelithiated silicon-graphene anodes could also be paired with next-generation high-capacity lithium-free cathodes, such as sulfur cathodes to produce high energy LIBs.[184,216]

The impact of the lithiation method (chemical or electrochemical) on the SEI of the silicon-graphene anode should also be studied as this could be one reason for the difference in cycle performance observed in Figure 5.8. ssNMR has already been shown by Jin *et al*. to be a powerful technique to study the SEI of silicon anodes.[12] ssNMR was also used to give insight into the different local environments within lithiated silicon. The VT and relaxometry measurements performed on the chemically and electrochemically lithiated samples (Figure 5.16), could be extended to study silicon anodes as a function of state of charge to study the Li motion in these samples.

In this thesis, NMR has been shown to be a powerful tool to study the lithiation mechanisms of graphite and silicon-graphene anodes. The techniques developed in this work could be further applied to other LIB materials as well as other graphite intercalation compounds. These techniques have also provided insights into the electronic structure and Li ion dynamics within these materials.

References

(1) Masson-Delmotte, V. P. et al. Climate Change 2021 The Physical Science Basis. Contribution of Working Group I to the Sixth Assessment Report of the Intergovernmental Panel on Climate Change, 2021.

(2) COP26 Outcomes, 2021.

(3) Linden, D.; Reddy, T. B. *McGraw-Hill* **2002**.

(4) Nagaura, T. *Progress in Batteries & Solar Cells* **1990**, *9*, 209.

(5) Nitta, N.; Wu, F.; Lee, J. T.; Yushin, G. *Materials today* **2015**, *18*, 252–264.

(6) Muratori, M.; Alexander, M.; Arent, D.; Bazilian, M.; Dede, E. M.; Farrell, J.; Gearhart, C.; Greene, D.; Jenn, A.; Keyser, M., et al. *Progress in Energy* **2021**, *3*, 022002.

(7) Roni, M. S.; Yi, Z.; Smart, J. G. *Transportation Research Part D: Transport and Environment* **2019**, *76*, 155–175.

(8) Smith, A.; Burns, J.; Trussler, S.; Dahn, J. *Journal of The Electrochemical Society* **2010**, *157*, A196–A202.

(9) Dose, W. M.; Xu, C.; Grey, C. P.; De Volder, M. F. *Cell Reports Physical Science* **2020**, *1*, 100253.

(10) Kim, C.-S.; Jeong, K. M.; Kim, K.; Yi, C.-W. *Electrochimica Acta* **2015**, *155*, 431–436.

(11) Chen, Z.; Zhang, L.; Wu, X.; Song, K.; Ren, B.; Li, T.; Zhang, S. *Journal of Power Sources* **2019**, *439*, 227056.

(12) Jin, Y.; Kneusels, N.-J. H.; Magusin, P. C.; Kim, G.; Castillo-Martınez, E.; Marbella, L. E.; Kerber, R. N.; Howe, D. J.; Paul, S.; Liu, T., et al. *Journal of the American Chemical Society* **2017**, *139*, 14992–15004.

(13) Ruff, Z.; Xu, C.; Grey, C. *Journal of The Electrochemical Society* **2021**.

(14) Wagner, N. P.; Asheim, K.; Vullum-Bruer, F.; Svensson, A. M. *Journal of Power Sources* **2019**, *437*, 226884.

(15) Obrovac, M.; Chevrier, V. *Chemical reviews* **2014**, *114*, 11444–11502.

(16) Cheng, X.-B.; Zhang, R.; Zhao, C.-Z.; Zhang, Q. *Chemical reviews* **2017**, *117*, 10403–10473.

(17) Peled, E.; Menkin, S. *Journal of The Electrochemical Society* **2017**, *164*, A1703–A1719.

(18) Goodenough, J. B.; Kim, Y. *Chemistry of materials* **2009**, *22*, 587–603.

(19) Goodenough, J. B. *Nature Electronics* **2018**, *1*, 204.

(20) Asenbauer, J.; Eisenmann, T.; Kuenzel, M.; Kazzazi, A.; Chen, Z.; Bresser, D. *Sustainable Energy & Fuels* **2020**.

(21) Mao, C.; Wood, M.; David, L.; An, S. J.; Sheng, Y.; Du, Z.; Meyer III, H. M.; Ruther, R. E.; Wood III, D. L. *Journal of The Electrochemical Society* **2018**, *165*, A1837.

(22) Daumas, N.; Herold, A. *Comptes Rendus Hebdomadaires Des Seances De L Academie Des Sciences Serie C* **1969**, *268*, 373.

(23) Ohzuku, T.; Iwakoshi, Y.; Sawai, K. *Journal of The Electrochemical Society* **1993**, *140*, 2490–2498.

(24) Zheng, T.; Dahn, J. *Physical Review B* **1996**, *53*, 3061.

(25) Dahn, J. *Physical Review B* **1991**, *44*, 9170.

(26) Didier, C.; Pang, W. K.; Guo, Z.; Schmid, S.; Peterson, V. K. *Chemistry of Materials* **2020**, *32*, 2518–2531.

(27) Billaud, D.; Henry, F.; Lelaurain, M.; Willmann, P. *Journal of Physics and Chemistry of Solids* **1996**, *57*, 775–781.

(28) Allart, D.; Montaru, M.; Gualous, H. *Journal of The Electrochemical Society* **2018**, *165*, A380–A387.

(29) Letellier, M.; Chevallier, F.; Béguin, F. *Journal of Physics and Chemistry of Solids* **2006**, *67*, 1228–1232.

(30) Cañas, N. A.; Einsiedel, P.; Freitag, O. T.; Heim, C.; Steinhauer, M.; Park, D.-W.; Friedrich, K. A. *Carbon* **2017**, *116*, 255–263.

(31) Taminato, S.; Yonemura, M.; Shiotani, S.; Kamiyama, T.; Torii, S.; Nagao, M.; Ishikawa, Y.; Mori, K.; Fukunaga, T.; Onodera, Y., et al. *Scientific reports* **2016**, *6*, 1–12.

(32) Glazier, S.; Li, J.; Louli, A.; Allen, J.; Dahn, J. *Journal of The Electrochemical Society* **2017**, *164*, A3545.

(33) Shi, H.; Barker, J.; Saidi, M.; Koksbang, R. *Journal of the Electrochemical Society* **1996**, *143*, 3466.

(34) Yoshio, M.; Wang, H.; Fukuda, K.; Hara, Y.; Adachi, Y. *Journal of the Electrochemical Society* **2000**, *147*, 1245.

(35) Schmuch, R.; Wagner, R.; Hörpel, G.; Placke, T.; Winter, M. *Nature Energy* **2018**, *3*, 267–278.

(36) Langer, J.; Epp, V.; Heitjans, P.; Mautner, F.-A.; Wilkening, M. *Physical Review B* **2013**, *88*, 094304.

(37) Inaba, M.; Yoshida, H.; Ogumi, Z.; Abe, T.; Mizutani, Y.; Asano, M. *Journal of the Electrochemical Society* **1995**, *142*, 20.

(38) Eklund, P.; Dresselhaus, G.; Dresselhaus, M.; Fischer, J. *Physical Review B* **1980**, *21*, 4705.

(39) Imanishi, N.; Kumai, K.; Kokugan, H.; Takeda, Y.; Yamamoto, O. *Solid State Ionics* **1998**, *107*, 135–144.

(40) Fujimoto, H.; Mabuchi, A.; Tokumitsu, K.; Chinnasamy, N.; Kasuh, T. *Journal of Power Sources* **2011**, *196*, 1365–1370.

(41) Märker, K.; Xu, C.; Grey, C. P. *Journal of the American Chemical Society* **2020**, *142*, 17447–17456.

(42) Freytag, A. I.; Pauric, A. D.; Krachkovskiy, S. A.; Goward, G. R. *Journal of the American Chemical Society* **2019**, *141*, 13758–13761.

(43) Obrovac, M.; Christensen, L. *Electrochemical and Solid-State Letters* **2004**, *7*, A93–A96.

(44) Besenhard, J.; Yang, J.; Winter, M. *Journal of Power Sources* **1997**, *68*, 87–90.

(45) Yaroshevsky, A. *Geochemistry International* **2006**, *44*, 48–55.

(46) Michan, A. L.; Divitini, G.; Pell, A. J.; Leskes, M.; Ducati, C.; Grey, C. P. *Journal of the American Chemical Society* **2016**, *138*, 7918–7931.

(47) Cui, L.-F.; Hu, L.; Choi, J. W.; Cui, Y. *Acs Nano* **2010**, *4*, 3671–3678.

(48) Zhang, J.; Zhang, C.; Wu, S.; Zhang, X.; Li, C.; Xue, C.; Cheng, B. *Nanoscale research letters* **2015**, *10*, 395.

(49) Luo, J.; Zhao, X.; Wu, J.; Jang, H. D.; Kung, H. H.; Huang, J. *The journal of physical chemistry letters* **2012**, *3*, 1824–1829.

(50) Jia, H.; Stock, C.; Kloepsch, R.; He, X.; Badillo, J. P.; Fromm, O.; Vortmann, B.; Winter, M.; Placke, T. *ACS applied materials & interfaces* **2015**, *7*, 1508–1515.

(51) Limthongkul, P.; Jang, Y.-I.; Dudney, N. J.; Chiang, Y.-M. *Acta Materialia* **2003**, *51*, 1103–1113.

(52) Obrovac, M.; Krause, L. *Journal of The Electrochemical Society* **2007**, *154*, A103–A108.

(53) Key, B.; Morcrette, M.; Tarascon, J.-M.; Grey, C. P. *Journal of the American Chemical Society* **2011**, *133*, 503–512.

(54) Key, B.; Bhattacharyya, R.; Morcrette, M.; Seznec, V.; Tarascon, J.-M.; Grey, C. P. *Journal of the American Chemical Society* **2009**, *131*, 9239–9249.

(55) Li, H.; Huang, X.; Chen, L.; Wu, Z.; Liang, Y. *Electrochemical and Solid-State Letters* **1999**, *2*, 547–549.

(56) Chan, C. K.; Peng, H.; Liu, G.; McIlwrath, K.; Zhang, X. F.; Huggins, R. A.; Cui, Y. *Nature nanotechnology* **2008**, *3*, 31–35.

(57) Rahman, M.; Song, G.; Bhatt, A. I.; Wong, Y. C.; Wen, C., et al. *Advanced Functional Materials* **2016**, *26*, 647–678.

(58) Byles, B.; Palapati, N.; Subramanian, A.; Pomerantseva, E. *APL Materials* **2016**, *4*, 046108.

(59) Orikasa, Y.; Gogyo, Y.; Yamashige, H.; Katayama, M.; Chen, K.; Mori, T.; Yamamoto, K.; Masese, T.; Inada, Y.; Ohta, T., et al. *Scientific reports* **2016**, *6*, 26382.

(60) Smekens, J.; Gopalakrishnan, R.; Steen, N. V. d.; Omar, N.; Hegazy, O.; Hubin, A.; Van Mierlo, J. *Energies* **2016**, *9*, 104.

(61) Suthar, B.; Northrop, P. W.; Rife, D.; Subramanian, V. R. *Journal of The Electrochemical Society* **2015**, *162*, A1708–A1717.

(62) Landesfeind, J.; Hattendorff, J.; Ehrl, A.; Wall, W. A.; Gasteiger, H. A. *Journal of The Electrochemical Society* **2016**, *163*, A1373–A1387.

(63) Ischenko, A. A.; Fetisov, G. V.; Aslalnov, L. A., *Nanosilicon: properties, synthesis, applications, methods of analysis and control*; CRC Press: 2014.

(64) Graetz, J.; Ahn, C.; Yazami, R.; Fultz, B. *Electrochemical and Solid-State Letters* **2003**, *6*, A194–A197.

(65) Cui, L.-F.; Ruffo, R.; Chan, C. K.; Peng, H.; Cui, Y. *Nano letters* **2008**, *9*, 491–495.

(66) Li, W.; Guo, X.; Lu, Y.; Wang, L.; Fan, A.; Sui, M.; Yu, H. *Energy Storage Materials* **2017**, *7*, 203–208.

(67) Pharr, M.; Zhao, K.; Wang, X.; Suo, Z.; Vlassak, J. J. *Nano letters* **2012**, *12*, 5039–5047.

(68) Watanabe, M.; Thomas, M. L.; Zhang, S.; Ueno, K.; Yasuda, T.; Dokko, K. *Chemical reviews* **2017**, *117*, 7190–7239.

(69) Manthiram, A.; Yu, X.; Wang, S. *Nature Reviews Materials* **2017**, *2*, 16103.

(70) Younesi, R.; Veith, G. M.; Johansson, P.; Edström, K.; Vegge, T. *Energy & Environmental Science* **2015**, *8*, 1905–1922.

(71) Ein-Eli, Y.; Markovsky, B.; Aurbach, D.; Carmeli, Y.; Yamin, H.; Luski, S. *Electrochimica Acta* **1994**, *39*, 2559–2569.

(72) Dudley, J.; Wilkinson, D.; Thomas, G.; LeVae, R.; Woo, S.; Blom, H.; Horvath, C.; Juzkow, M.; Denis, B.; Juric, P., et al. *Journal of power sources* **1991**, *35*, 59–82.

(73) Nguyen, C. C.; Lucht, B. L. *Journal of The Electrochemical Society* **2014**, *161*, A1933–A1938.

(74) Dalavi, S.; Guduru, P.; Lucht, B. L. *Journal of The Electrochemical Society* **2012**, *159*, A642–A646.

(75) Profatilova, I. A.; Stock, C.; Schmitz, A.; Passerini, S.; Winter, M. *Journal of power sources* **2013**, *222*, 140–149.

(76) Anet, F. A.; O'Leary, D. J. *Concepts in Magnetic Resonance* **1991**, *3*, 193–214.

(77) Widdifield, C. M.; Schurko, R. W. *Concepts in Magnetic Resonance Part A: An Educational Journal* **2009**, *34*, 91–123.

(78) Herzfeld, J.; Berger, A. E. *The Journal of Chemical Physics* **1980**, *73*, 6021–6030.

(79) Knight, W. D. *Physical Review* **1949**, *76*, 1259.

(80) Bloembergen, N.; Rowland, T. *Acta metallurgica* **1953**, *1*, 731–746.

(81) Bennett, L.; Watson, R.; Carter, G. *Journal of Research of the National Bureau of Standards. Section A, Physics and Chemistry* **1970**, *74*, 569.

(82) Pennington, C. H.; Stenger, V. A. *Reviews of modern Physics* **1996**, *68*, 855.

(83) Abragam, A. *Chap. IX, Oxford Univ. Press, London/New York* **1961**.

(84) Slichter, C., *Principles of Magnetic Resonance, volume 1*; Springer: 1990.

(85) Pennington, C.; Stenger, V.; Recchia, C.; Hahm, C.; Gorny, K.; Nandor, V.; Buffinger, D.; Lee, S.; Ziebarth, R. *Physical Review B* **1996**, *53*, R2967.

(86) Mansour, A.; Schnatterly, S. *Physica Scripta* **1987**, *35*, 595.

(87) Kuhn, A.; Kunze, M.; Sreeraj, P.; Wiemhöfer, H.-D.; Thangadurai, V.; Wilkening, M.; Heitjans, P. *Solid state nuclear magnetic resonance* **2012**, *42*, 2–8.

(88) Levitt, M. H., *Spin dynamics: basics of nuclear magnetic resonance*; John Wiley & Sons: 2013.

(89) Werbelow, L. G. *eMagRes* **2007**.

(90) Wilkening, M.; Heitjans, P. *Physical Review B* **2008**, *77*, 024311.

(91) Antropov, V.; Mazin, I.; Andersen, O.; Liechtenstein, A.; Jepsen, O. *Physical Review B* **1993**, *47*, 12373.

(92) Hope, M. A.; Griffith, K. J.; Cui, B.; Gao, F.; Dutton, S. E.; Parkin, S. S.; Grey, C. P. *Journal of the American Chemical Society* **2018**, *140*, 16685–16696.

(93) Thurber, K. R.; Tycko, R. *Journal of magnetic resonance* **2009**, *196*, 84–87.

(94) Klemm, R. A., *Layered superconductors*; Oxford University Press: 2012; Vol. 153.

(95) Li, Y.; Lu, Y.; Adelhelm, P.; Titirici, M.-M.; Hu, Y.-S. *Chemical Society Reviews* **2019**, *48*, 4655–4687.

(96) Moriwake, H.; Kuwabara, A.; Fisher, C. A.; Ikuhara, Y. *RSC advances* **2017**, *7*, 36550–36554.

(97) Letellier, M.; Chevallier, F.; Morcrette, M. *Carbon* **2007**, *45*, 1025–1034.

(98) Estrade, H.; Conard, J.; Lauginie, P.; Heitjans, P.; Fujara, F.; Buttler, W.; Kiese, G.; Ackermann, H.; Guerard, D. *Physica B+ C* **1980**, *99*, 531–535.

(99) Kume, K.; Nomura, K.; Hiroyama, Y.; Maniwa, Y.; Suematsu, H.; Tanuma, S. *Synthetic Metals* **1985**, *12*, 307–312.

(100) Conard, J.; Estrade, H.; Lauginie, P.; Fuzellier, H.; Furdin, G.; Vasse, R. *Physica B+ C* **1980**, *99*, 521–524.

(101) Conard, J.; Gutierrez-Le Brun, M.; Lauginie, P.; Estrade-Szwarckopf, H.; Hermann, G. *Synthetic Metals* **1980**, *2*, 227–236.

(102) Maniwa, Y.; Kume, K.; Suematsu, H.; Tanuma, S.-i. *Journal of the Physical Society of Japan* **1985**, *54*, 666–676.

(103) Vyalikh, A.; Koroteev, V. O.; Münchgesang, W.; Köhler, T.; Röder, C.; Brendler, E.; Okotrub, A. V.; Bulusheva, L. G.; Meyer, D. C. *ACS applied materials & interfaces* **2019**, *11*, 9291–9300.

(104) Sato, N.; Tou, H.; Maniwa, Y.; Kikuchi, K.; Suzuki, S.; Achiba, Y.; Kosaka, M.; Tanigaki, K. *Physical Review B* **1998**, *58*, 12433.

(105) Maniwa, Y.; Saito, T.; Ohi, A.; Mizoguchi, K.; Kume, K.; Kikuchi, K.; Ikemoto, I.; Suzuki, S.; Achiba, Y.; Kosaka, M., et al. *Journal of the Physical Society of Japan* **1994**, *63*, 1139–1148.

(106) Tossici, R.; Janot, R.; Nobili, F.; Guerard, D.; Marassi, R. *Electrochimica acta* **2003**, *48*, 1419–1424.

(107) Hayashi, S.; Hayamizu, K. *Bulletin of the Chemical Society of Japan* **1989**, *62*, 2429–2430.

(108) Carr, H. Y.; Purcell, E. M. *Physical review* **1954**, *94*, 630.

(109) Carver, G. P. *Physical Review B* **1970**, *2*, 2284.

(110) See, K. A.; Lumley, M. A.; Stucky, G. D.; Grey, C. P.; Seshadri, R. *Journal of The Electrochemical Society* **2016**, *164*, A327.

(111) Wang, R.; Mo, H.; Li, S.; Gong, Y.; He, B.; Wang, H. *Scientific reports* **2019**, *9*, 1–6.

(112) Edström, K.; Herstedt, M.; Abraham, D. P. *Journal of Power Sources* **2006**, *153*, 380–384.

(113) Agubra, V. A.; Fergus, J. W. *Journal of Power Sources* **2014**, *268*, 153–162.

(114) Thomas-Alyea, K. E.; Jung, C.; Smith, R. B.; Bazant, M. Z. *Journal of The Electrochemical Society* **2017**, *164*, E3063.

(115) Guo, Y.; Smith, R. B.; Yu, Z.; Efetov, D. K.; Wang, J.; Kim, P.; Bazant, M. Z.; Brus, L. E. *The journal of physical chemistry letters* **2016**, *7*, 2151–2156.

(116) Kittel, C.; McEuen, P., *Introduction to solid state physics*; Wiley: 2005; Vol. 8.

(117) Missyul, A.; Bolshakov, I.; Shpanchenko, R. *Powder Diffraction* **2017**, *32*, S56–S62.

(118) Gutowsky, H.; McGarvey, B. *The Journal of Chemical Physics* **1952**, *20*, 1472–1477.

(119) Goze-Bac, C.; Latil, S.; Lauginie, P.; Jourdain, V.; Conard, J.; Duclaux, L.; Rubio, A.; Bernier, P. *Carbon* **2002**, *40*, 1825–1842.

(120) Hiroyama, Y.; Kume, K. *Solid state communications* **1988**, *65*, 617–619.

(121) Ohno, T.; Kamimura, H. *Journal of the Physical Society of Japan* **1983**, *52*, 223–232.

(122) Holzwarth, N.; Girifalco, L.; Rabii, S. *Physical Review B* **1978**, *18*, 5206.

(123) Mukai, K.; Inoue, T. *Carbon* **2017**, *123*, 645–650.

(124) De Souza, F. A.; Ambrozio, A. R.; Souza, E. S.; Cipriano, D. F.; Scopel, W. L.; Freitas, J. C. *The Journal of Physical Chemistry C* **2016**, *120*, 27707–27716.

(125) Orendt, A. M.; Facelli, J. C.; Bai, S.; Rai, A.; Gossett, M.; Scott, L. T.; Boerio-Goates, J.; Pugmire, R. J.; Grant, D. M. *The Journal of Physical Chemistry A* **2000**, *104*, 149–155.

(126) Ikehata, S.; Milliken, J.; Heeger, A.; Fischer, J. *Physical Review B* **1982**, *25*, 1726.

(127) Schumacher, R. T.; Slichter, C. P. *Physical Review* **1956**, *101*, 58.

(128) Karplus, M.; Fraenkel, G. K. *The Journal of Chemical Physics* **1961**, *35*, 1312–1323.

(129) Saito, R.; Tsukada, M.; Kobayashi, K.; Kamimura, H. *Physical Review B* **1987**, *35*, 2963.

(130) Barsukov, I. V.; Johnson, C. S.; Doninger, J. E.; Barsukov, V. Z., *New Carbon Based Materials for Electrochemical Energy Storage Systems: Batteries, Supercapacitors and Fuel Cells*; Springer Science & Business Media: 2006; Vol. 229.

(131) Meintz, A.; Zhang, J.; Vijayagopal, R.; Kreutzer, C.; Ahmed, S.; Bloom, I.; Burnham, A.; Carlson, R. B.; Dias, F.; Dufek, E. J., et al. *Journal of Power Sources* **2017**, *367*, 216–227.

(132) Zeng, X.; Li, M.; Abd El-Hady, D.; Alshitari, W.; Al-Bogami, A. S.; Lu, J.; Amine, K. *Advanced Energy Materials* **2019**, *9*, 1900161.

(133) Chen, K.-H.; Namkoong, M. J.; Goel, V.; Yang, C.; Kazemiabnavi, S.; Mortuza, S.; Kazyak, E.; Mazumder, J.; Thornton, K.; Sakamoto, J., et al. *Journal of Power Sources* **2020**, *471*, 228475.

(134) Yang, X.-G.; Wang, C.-Y. *Journal of Power Sources* **2018**, *402*, 489–498.

(135) Levi, M. D.; Aurbach, D. *The Journal of Physical Chemistry B* **1997**, *101*, 4641–4647.

(136) Levi, M.; Levi, E.; Aurbach, D. *Journal of Electroanalytical Chemistry* **1997**, *421*, 89–97.

(137) Yang, H.; Bang, H. J.; Prakash, J. *Journal of the Electrochemical Society* **2004**, *151*, A1247.

(138) Takami, N.; Satoh, A.; Hara, M.; Ohsaki, T. *Journal of The Electrochemical Society* **1995**, *142*, 371.

(139) Persson, K.; Sethuraman, V. A.; Hardwick, L. J.; Hinuma, Y.; Meng, Y. S.; Van Der Ven, A.; Srinivasan, V.; Kostecki, R.; Ceder, G. *The journal of physical chemistry letters* **2010**, *1*, 1176–1180.

(140) Persson, K.; Hinuma, Y.; Meng, Y. S.; Van der Ven, A.; Ceder, G. *Physical Review B* **2010**, *82*, 125416.

(141) Toyoura, K.; Koyama, Y.; Kuwabara, A.; Tanaka, I. *The Journal of Physical Chemistry C* **2010**, *114*, 2375–2379.

(142) Umegaki, I.; Kawauchi, S.; Sawada, H.; Nozaki, H.; Higuchi, Y.; Miwa, K.; Kondo, Y.; Månsson, M.; Telling, M.; Coomer, F. C., et al. *Physical Chemistry Chemical Physics* **2017**, *19*, 19058–19066.

(143) Saito, Y.; Kataoka, H.; Nakai, K.; Suzuki, J.; Sekine, K.; Takamura, T. *The Journal of Physical Chemistry B* **2004**, *108*, 4008–4012.

(144) Weppner, W.; Huggins, R. A. *Journal of The Electrochemical Society* **1977**, *124*, 1569.

(145) Liu, X.; Yin, L.; Ren, D.; Wang, L.; Ren, Y.; Xu, W.; Lapidus, S.; Wang, H.; He, X.; Chen, Z., et al. *Nature Communications* **2021**, *12*, 1–11.

(146) Pecher, O.; Carretero-González, J.; Griffith, K. J.; Grey, C. P. *Chemistry of Materials* **2017**, *29*, 213–242.

(147) Kaspar, J.; Graczyk-Zajac, M.; Riedel, R. *Electrochimica Acta* **2014**, *115*, 665–670.

(148) Pecher, O.; Bayley, P. M.; Liu, H.; Liu, Z.; Trease, N. M.; Grey, C. P. *Journal of Magnetic Resonance* **2016**, *265*, 200–209.

(149) Park, J. H.; Yoon, H.; Cho, Y.; Yoo, C.-Y. *Materials* **2021**, *14*, 4683.

(150) Levi, M.; Markevich, E.; Aurbach, D. *The Journal of Physical Chemistry B* **2005**, *109*, 7420–7427.

(151) Lopez, J. L. L.; Grandinetti, P. J., et al. *Journal of Materials Chemistry A* **2018**, *6*, 231–243.

(152) Hazrati, E.; De Wijs, G.; Brocks, G. *Physical Review B* **2014**, *90*, 155448.

(153) Waugh, J.; Fedin, É. I. *Soviet Physics-Solid State* **1963**, *4*, 1633–1636.

(154) Levin, I. NIST Inorganic Crystal Structure Database (ICSD), 2018.

(155) Bloembergen, N.; Purcell, E. M.; Pound, R. V. *Physical review* **1948**, *73*, 679.

(156) Michan, A. L.; Leskes, M.; Grey, C. P. *Chemistry of Materials* **2016**, *28*, 385–398.

(157) Meyer, B. M.; Leifer, N.; Sakamoto, S.; Greenbaum, S. G.; Grey, C. P. *Electrochemical and Solid State Letters* **2005**, *8*, A145.

(158) Xu, B.; Wu, M.; Liu, G.; Ouyang, C. *Journal of Applied Physics* **2012**, *111*, 124325.

(159) Jin, Y.; Kneusels, N.-J. H.; Marbella, L. E.; Castillo-Martınez, E.; Magusin, P. C.; Weatherup, R. S.; Jónsson, E.; Liu, T.; Paul, S.; Grey, C. P. *Journal of the American Chemical Society* **2018**, *140*, 9854–9867.

(160) Jin, Y.; Li, S.; Kushima, A.; Zheng, X.; Sun, Y.; Xie, J.; Sun, J.; Xue, W.; Zhou, G.; Wu, J., et al. *Energy & environmental science* **2017**, *10*, 580–592.

(161) Ogata, K.; Jeon, S.; Ko, D.-S.; Jung, I.; Kim, J. H.; Ito, K.; Kubo, Y.; Takei, K.; Saito, S.; Cho, Y.-H., et al. *Nature communications* **2018**, *9*, 1–17.

(162) Zhu, G.; Wang, Y.; Yang, S.; Qu, Q.; Zheng, H. *Journal of Materiomics* **2019**, *5*, 164–175.

(163) Lin, Y.-M.; Klavetter, K. C.; Abel, P. R.; Davy, N. C.; Snider, J. L.; Heller, A.; Mullins, C. B. *Chemical communications* **2012**, *48*, 7268–7270.

(164) Yoon, T.; Nguyen, C. C.; Seo, D. M.; Lucht, B. L. *Journal of The Electrochemical Society* **2015**, *162*, A2325.

(165) Zhao, X.; Lehto, V.-P. *Nanotechnology* **2020**.

(166) Liu, N.; Lu, Z.; Zhao, J.; McDowell, M. T.; Lee, H.-W.; Zhao, W.; Cui, Y. *Nature nanotechnology* **2014**, *9*, 187–192.

(167) Liu, N.; Wu, H.; McDowell, M. T.; Yao, Y.; Wang, C.; Cui, Y. *Nano letters* **2012**, *12*, 3315–3321.

(168) Hwang, T. H.; Lee, Y. M.; Kong, B.-S.; Seo, J.-S.; Choi, J. W. *Nano letters* **2012**, *12*, 802–807.

(169) Kim, S. Y.; Lee, J.; Kim, B.-H.; Kim, Y.-J.; Yang, K. S.; Park, M.-S. *ACS applied materials & interfaces* **2016**, *8*, 12109–12117.

(170) Wang, C.; Luo, F.; Lu, H.; Rong, X.; Liu, B.; Chu, G.; Sun, Y.; Quan, B.; Zheng, J.; Li, J., et al. *ACS applied materials & interfaces* **2017**, *9*, 2806–2814.

(171) Ng, S.-H.; Wang, J.; Wexler, D.; Konstantinov, K.; Guo, Z.-P.; Liu, H.-K. *Angewandte Chemie International Edition* **2006**, *45*, 6896–6899.

(172) Chou, S.-L.; Wang, J.-Z.; Choucair, M.; Liu, H.-K.; Stride, J. A.; Dou, S.-X. *Electrochemistry Communications* **2010**, *12*, 303–306.

(173) Tao, H.-C.; Fan, L.-Z.; Mei, Y.; Qu, X. *Electrochemistry Communications* **2011**, *13*, 1332–1335.

(174) Zhou, X.; Cao, A.-M.; Wan, L.-J.; Guo, Y.-G. *Nano Research* **2012**, 1–9.

(175) Xiang, H.; Zhang, K.; Ji, G.; Lee, J. Y.; Zou, C.; Chen, X.; Wu, J. *Carbon* **2011**, *49*, 1787–1796.

(176) Cen, Y.; Sisson, R. D.; Qin, Q.; Liang, J. *C* **2018**, *4*, 18.

(177) Chen, J. *Materials* **2013**, *6*, 156–183.

(178) Malik, R.; Huang, Q.; Silvestri, L.; Liu, D.; Pellegrini, V.; Marasco, L.; Venezia, E.; Abouali, S.; Bonaccorso, F.; Lain, M. J., et al. *2D Materials* **2020**, *8*, 015012.

(179) Huang, Q.; Loveridge, M. J.; Genieser, R.; Lain, M. J.; Bhagat, R. *Scientific reports* **2018**, *8*, 1–9.

(180) Zhao, J.; Sun, J.; Pei, A.; Zhou, G.; Yan, K.; Liu, Y.; Lin, D.; Cui, Y. *Energy Storage Materials* **2018**, *10*, 275–281.

(181) Zhao, J.; Lu, Z.; Wang, H.; Liu, W.; Lee, H.-W.; Yan, K.; Zhuo, D.; Lin, D.; Liu, N.; Cui, Y. *Journal of the American Chemical Society* **2015**, *137*, 8372–8375.

(182) Shellikeri, A.; Watson, V.; Adams, D.; Kalu, E.; Read, J.; Jow, T.; Zheng, J.; Zheng, J. *Journal of The Electrochemical Society* **2017**, *164*, A3914–A3924.

(183) Kim, H. J.; Choi, S.; Lee, S. J.; Seo, M. W.; Lee, J. G.; Deniz, E.; Lee, Y. J.; Kim, E. K.; Choi, J. W. *Nano letters* **2015**, *16*, 282–288.

(184) Liu, N.; Hu, L.; McDowell, M. T.; Jackson, A.; Cui, Y. *ACS nano* **2011**, *5*, 6487–6493.

(185) Reddy, A. L. M.; Shaijumon, M. M.; Gowda, S. R.; Ajayan, P. M. *Nano letters* **2009**, *9*, 1002–1006.

(186) Ji, X.; Nazar, L. F. *Journal of Materials Chemistry* **2010**, *20*, 9821–9826.

(187) Kim, K. W.; Park, H.; Lee, J. G.; Kim, J.; Kim, Y.-U.; Ryu, J. H.; Kim, J. J.; Oh, S. M. *Electrochimica Acta* **2013**, *103*, 226–230.

(188) Nesper, R. *Progress in solid state chemistry* **1990**, *20*, 1–45.

(189) Ogata, K.; Salager, E.; Kerr, C.; Fraser, A.; Ducati, C.; Morris, A. J.; Hofmann, S.; Grey, C. P. *Nature communications* **2014**, *5*, 1–11.

(190) Dupke, S.; Langer, T.; Pöttgen, R.; Winter, M.; Passerini, S.; Eckert, H. *Physical Chemistry Chemical Physics* **2012**, *14*, 6496–6508.

(191) Baran, V.; van Wüllen, L.; Fässler, T. F. *Chem.-Eur. J* **2016**, *22*, 6598–609.

(192) Karagiannidis, P. G.; Hodge, S. A.; Lombardi, L.; Tomarchio, F.; Decorde, N.; Milana, S.; Goykhman, I.; Su, Y.; Mesite, S. V.; Johnstone, D. N., et al. *ACS nano* **2017**, *11*, 2742–2755.

(193) Zhang, W.; Cai, T. H.; Sheldon, B. W. *Advanced Energy Materials* **2019**, *9*, 1803066.

(194) Smit, C.; Van Swaaij, R.; Donker, H.; Petit, A.; Kessels, W.; Van de Sanden, M. *Journal of applied physics* **2003**, *94*, 3582–3588.

(195) Kitada, K.; Pecher, O.; Magusin, P. C.; Groh, M. F.; Weatherup, R. S.; Grey, C. P. *Journal of the American Chemical Society* **2019**, *141*, 7014–7027.

(196) Wang, F.; Wu, L.; Key, B.; Yang, X.-Q.; Grey, C. P.; Zhu, Y.; Graetz, J. *Advanced Energy Materials* **2013**, *3*, 1324–1331.

(197) Mercer, M. P.; Peng, C.; Soares, C.; Hoster, H. E.; Kramer, D. *Journal of Materials Chemistry A* **2021**, *9*, 492–504.

(198) Ko, M.; Chae, S.; Ma, J.; Kim, N.; Lee, H.-W.; Cui, Y.; Cho, J. *Nature Energy* **2016**, *1*, 1–8.

(199) Sui, D.; Xie, Y.; Zhao, W.; Zhang, H.; Zhou, Y.; Qin, X.; Ma, Y.; Yang, Y.; Chen, Y. *Journal of Power Sources* **2018**, *384*, 328–333.

(200) Marinaro, M.; Weinberger, M.; Wohlfahrt-Mehrens, M. *Electrochimica Acta* **2016**, *206*, 99–107.

(201) Su, M.; Wang, Z.; Guo, H.; Li, X.; Huang, S.; Xiao, W.; Gan, L. *Electrochimica Acta* **2014**, *116*, 230–236.

(202) Wiggers, H.; Sehlleier, Y. H.; Kunze, F.; Xiao, L.; Schnurre, S. M.; Schulz, C. *Solid State Ionics* **2020**, *344*, 115117.

(203) Sethuraman, V. A.; Nguyen, A.; Chon, M. J.; Nadimpalli, S. P.; Wang, H.; Abraham, D. P.; Bower, A. F.; Shenoy, V. B.; Guduru, P. R. *Journal of the Electrochemical Society* **2013**, *160*, A739.

(204) Singh, M.; Kaiser, J.; Hahn, H. *Journal of The Electrochemical Society* **2015**, *162*, A1196.

(205) Lin, Z.; Liu, T.; Ai, X.; Liang, C. *Nature communications* **2018**, *9*, 1–5.

(206) He, W.; Zhang, T.; Jiang, J.; Chen, C.; Zhang, Y.; Liu, N.; Dou, H.; Zhang, X. *ACS Applied Energy Materials* **2020**, *3*, 4394–4402.

(207) Li, M.; Hou, X.; Sha, Y.; Wang, J.; Hu, S.; Liu, X.; Shao, Z. *Journal of Power sources* **2014**, *248*, 721–728.

(208) Richter, H.; Wang, Z.; Ley, L. *Solid State Communications* **1981**, *39*, 625–629.

(209) Letellier, M.; Chevallier, F.; Clinard, C.; Frackowiak, E.; Rouzaud, J.-N.; Beguin, F.; Morcrette, M.; Tarascon, J.-M. *The Journal of chemical physics* **2003**, *118*, 6038–6045.

(210) Iaboni, D.; Obrovac, M. *Journal of the Electrochemical Society* **2015**, *163*, A255.

(211) Forney, M. W.; Ganter, M. J.; Staub, J. W.; Ridgley, R. D.; Landi, B. J. *Nano letters* **2013**, *13*, 4158–4163.

(212) Reddy, M. V.; Mauger, A.; Julien, C. M.; Paolella, A.; Zaghib, K. *Materials* **2020**, *13*, 1884.

(213) Guerard, D.; Herold, A. *Carbon* **1975**, *13*, 337–345.

(214) Gullion, T. In *Modern Magnetic Resonance*; Springer: 2008, pp 713–718.

(215) Bresser, D.; Buchholz, D.; Moretti, A.; Varzi, A.; Passerini, S. *Energy & Environmental Science* **2018**, *11*, 3096–3127.

(216) Ji, X.; Lee, K. T.; Nazar, L. F. *Nature materials* **2009**, *8*, 500–506.

(217) Ferrari, A. C.; Meyer, J.; Scardaci, V.; Casiraghi, C.; Lazzeri, M.; Mauri, F.; Piscanec, S.; Jiang, D.; Novoselov, K.; Roth, S., et al. *Physical review letters* **2006**, *97*, 187401.

Appendix A

NMR and XRD data for ^{13}C NMR Chapter.

Samples (Figure A3) prepared had some heterogeneity due to multiple coin cell electrodes needed to pack 4 mm rotor. In the sample where we see a dense stage peak in the ^{7}Li

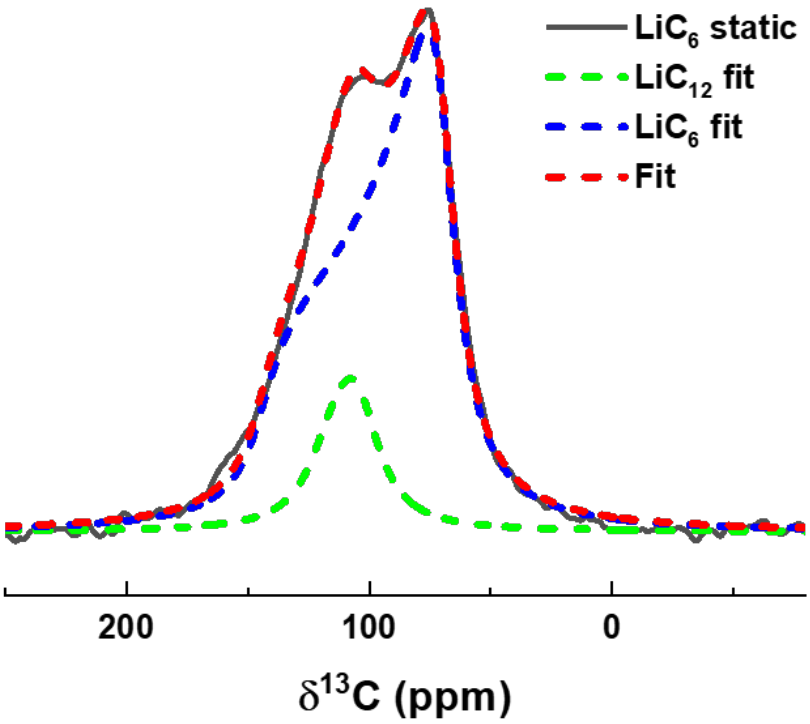

Figure. A1 Static ^{13}C NMR spectra of LiC_6 sample prepared with a cut off voltage of 5 mV showing that there is still a LiC_{12} phase present in this sample.

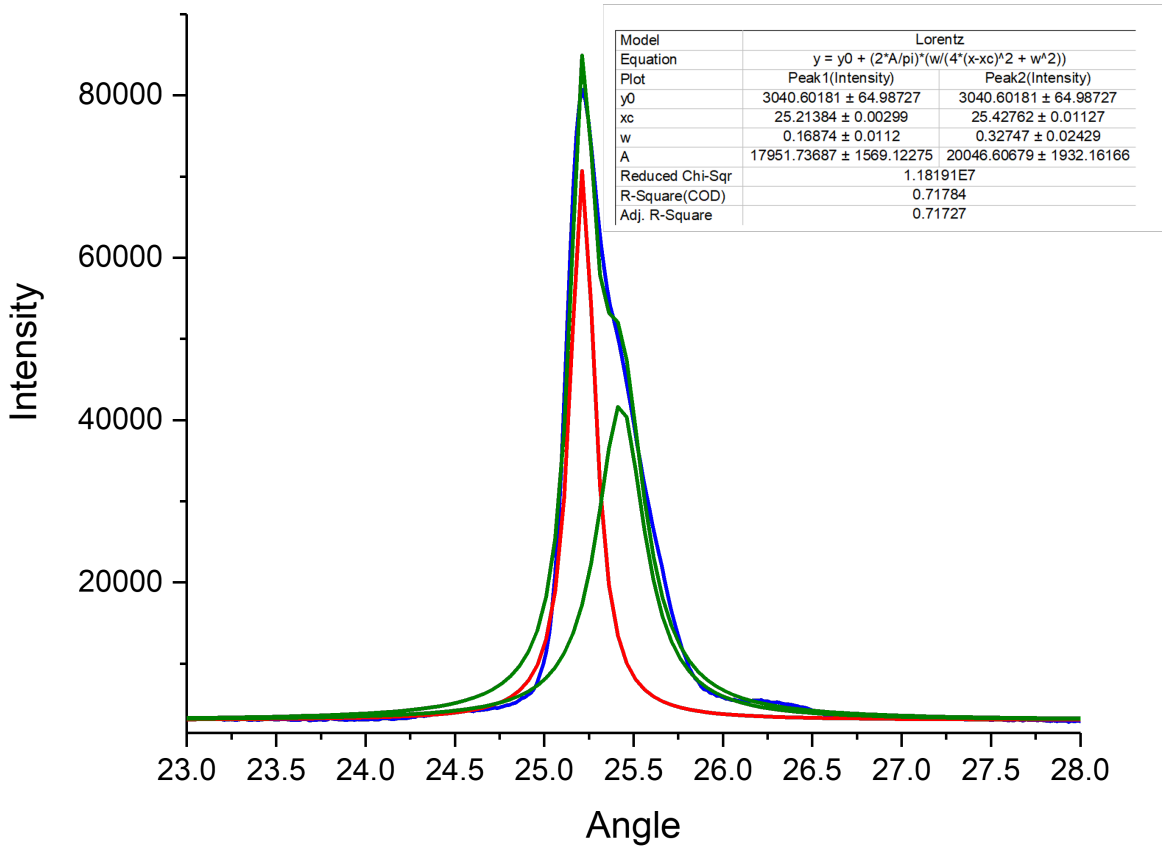

Figure. A2 Lorentzian fits of the two phases present in the LiC_{24} compound.

NMR we see a peak at 109 ppm in the ^{13}C NMR whereas we don't see this peak when no dense stage peak is present in the ^{7}Li NMR. This shows us that the peak at 109 ppm must correspond to the LiC_{12} compound.

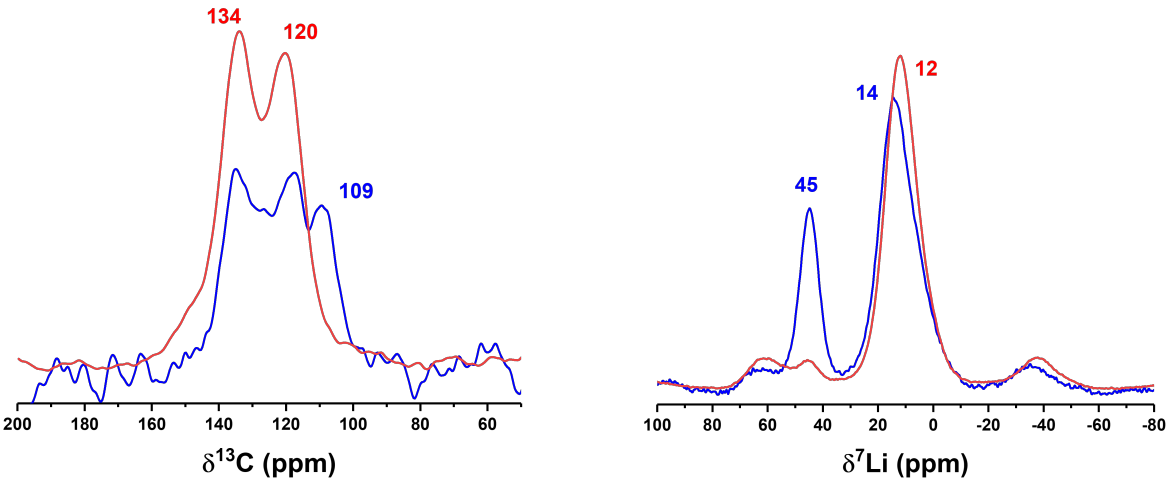

Figure. A3 a) ^{13}C and b) ^{7}Li NMR of the two samples lithiated to a nominal composition of LiC_{20}. Differences in the spectra are due to variation of the electrochemical performance of the cells that were used to pack the 4 mm rotor for this sample. The ^{13}C NMR peaks at 134, 120 and 109 ppm correspond to stage 3L, 2L and 2 respectively. The ^{7}Li NMR peaks at 45 ppm correspond to dense stage 2 while the peaks at 14 and 12 ppm are attributed to dilute stage Li-GIC.

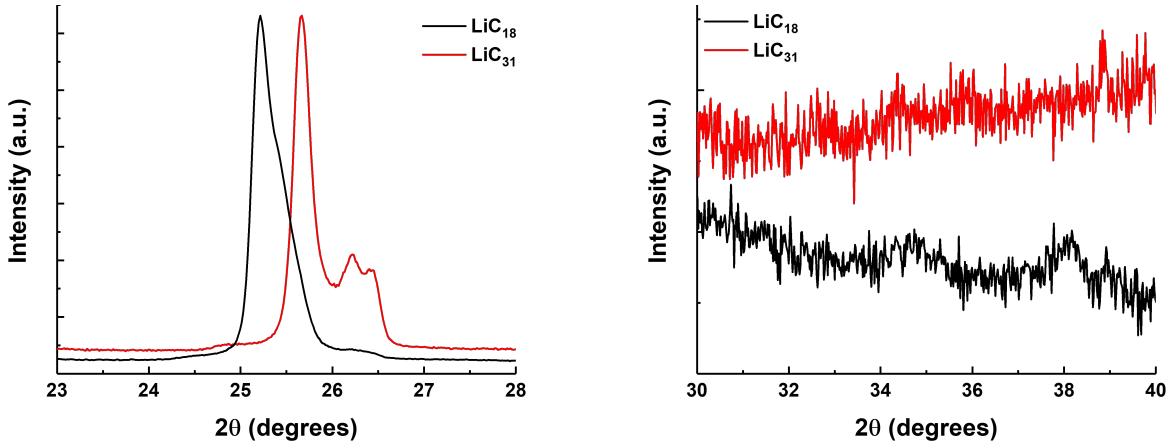

(a) 002 peak

(b) Superlattice peak

Figure. A4 Diffraction data showing the c) 002 peak and d) superlattice peak for the dilute stage samples.

The CP experiment is designed to reintroduce dipolar coupling, which is averaged to zero when MAS is performed. For the CP spectra shown in Figure A5, the ^{7}Li nuclear spins were excited and their spins were transferred to the ^{13}C. This means that any signal observed, arises from ^{13}C nuclear spins that are coupled to ^{7}Li nuclear spins. The spectra is similar to the one observed via direct excitation of the ^{13}C nuclear spins (Figure 3.5).

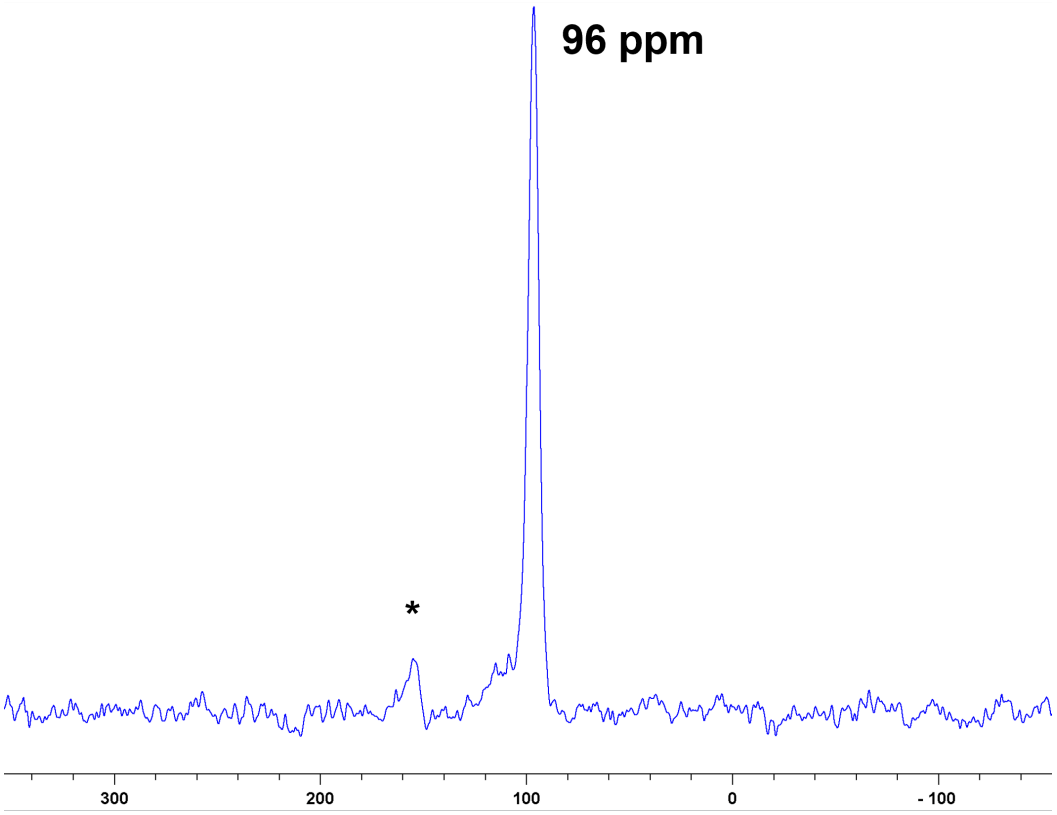

Figure. A5 ^{13}C NMR spectra of LiC_6 measured using a ^{7}Li - ^{13}C CP experiment recorded at 16.4 T using 10 kHz MAS with a recycle delay of 5 s, 6144 scans and a contact time of 5 ms. The * denotes a spinning sideband.

Appendix B

NMR and XRD data for ^{7}Li Dynamics Chapter

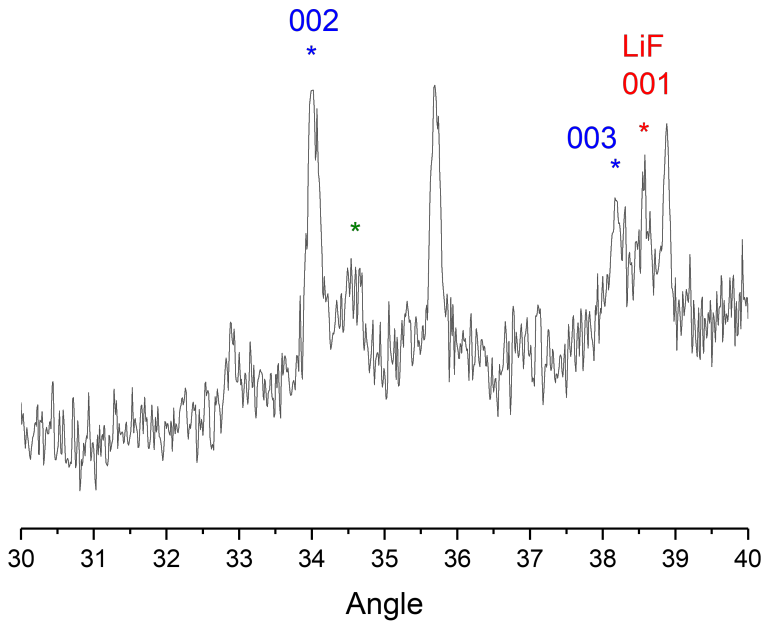

Figure. B1 Diffraction pattern of LiC_6 at 100 °C between $2\theta = 22 - 28°$. Peaks corresponding to the 002 and 003 peaks of stage 1 and stage 2 Li-GIC are observed at $2\theta = 34.0°$, 38.2° denotes by a blue asterisk. A peak, denoted by a red asterisk, at $2\theta = 38.6°$ corresponding to the 001 peak of LiF is also observed. The peak, denoted by green asterisk, at $2\theta = 34.5°$ could be either due to the 003 peak of stage 3L Li-GIC or due to the 111 peak of Li_2O.[25,145]

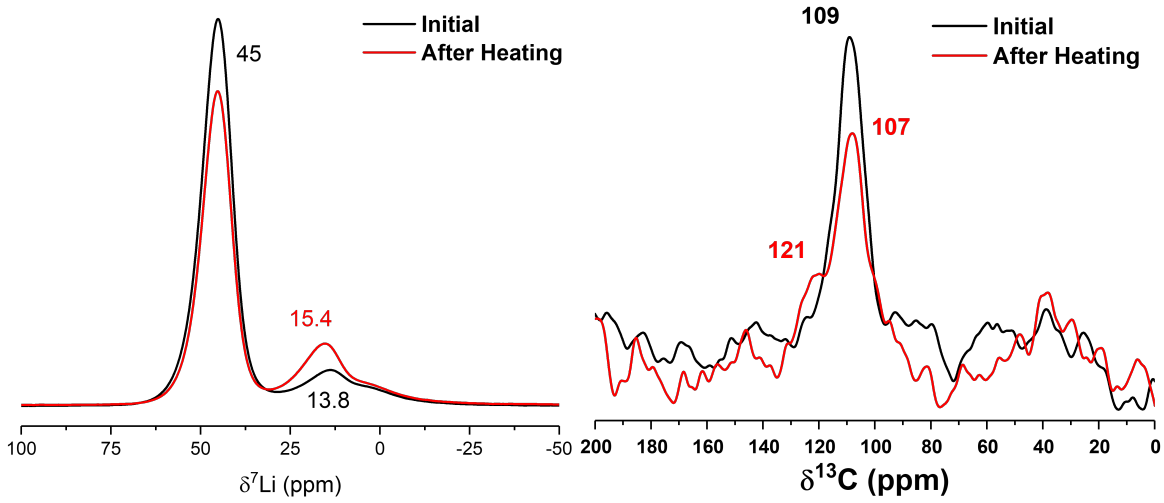

Figure. B2 a) ^{7}Li and b) ^{13}C NMR spectra of the LiC_{12} sample at room temperature before and after heating the sample.

Appendix C

Addition data for Silicon-Graphene Anode Chapter

Figure C1 shows the electrochemical half-cell cycling performance of C80 electrodes prepared with 10 (C80-10), 30 (C80-30) and 70 (C80-70) co-microfluidisation process cycles. From Figure C1 we find the the ICE does not depend on the number of co-microfluidisation process cycles, this is counter-intuitive, since the surface area of the graphite should increase with the number of process cycles. This could be because the irreversible capacity that arises due to SEI formation on the Si nanoparticles is more important in determining the ICE. The CE exceeds 99% fastest (46 cycles) for the C80-30 electrode. The real capacities are similar for each electrode but the gravimetric capacity is highest for the C80-30 electrode. The capacity retention after 200 cycles, of the C80-30 (64%) and C80-70 (62%) electrodes are similar. On balance we found that the electrochemical performance of the C80-30 electrode is best.

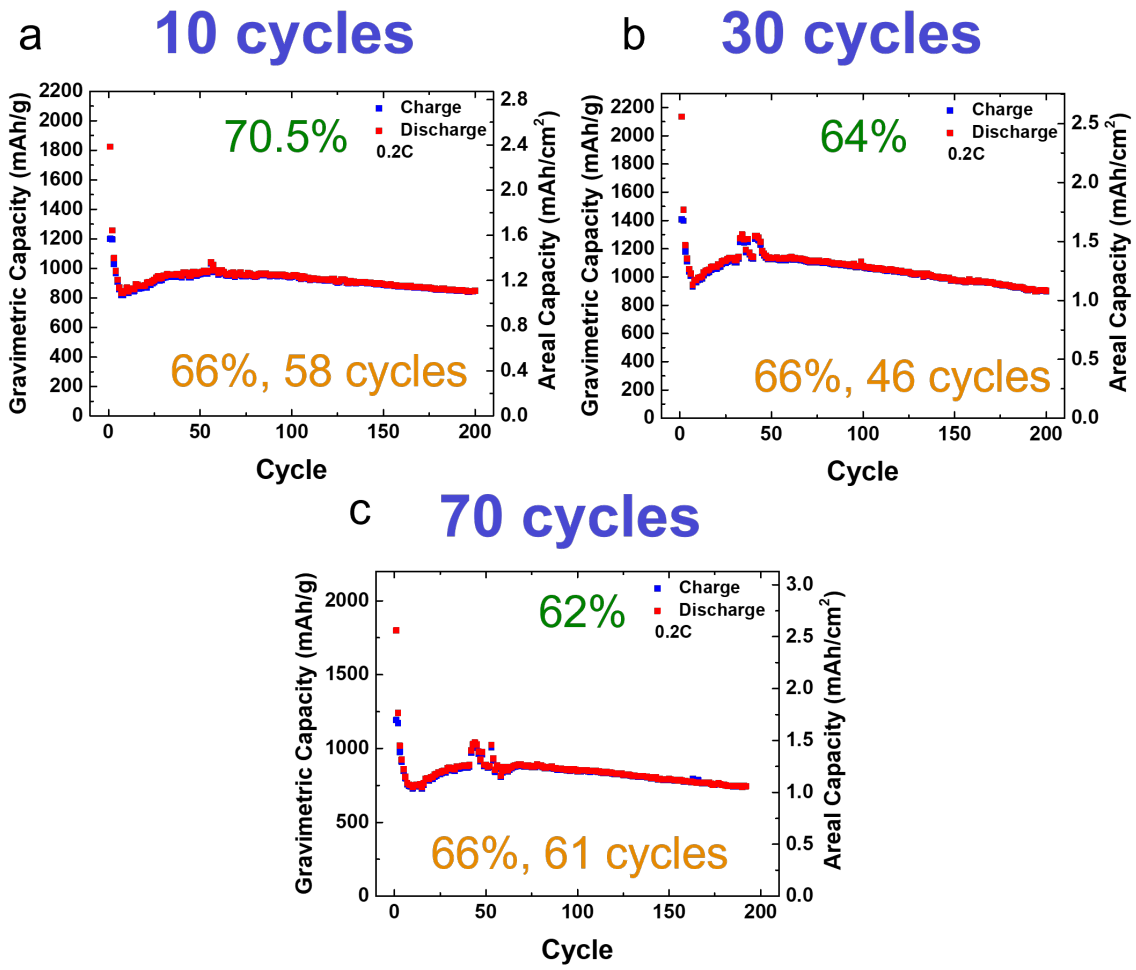

Figure. C1 Electrochemical half-cell cycling performance of C80 electrodes as a function of the number of co-microfluidisation process cycles, shown in blue. The gravimetric and areal capacities as a function of cycle number are shown for a C80 electrode that was prepared with a) 10, b) 30 and c) 70 process cycles. In green is the charge capacity retention after 200 cycles. In yellow is the initial CE and the number of cycles before the CE exceeded 99%.

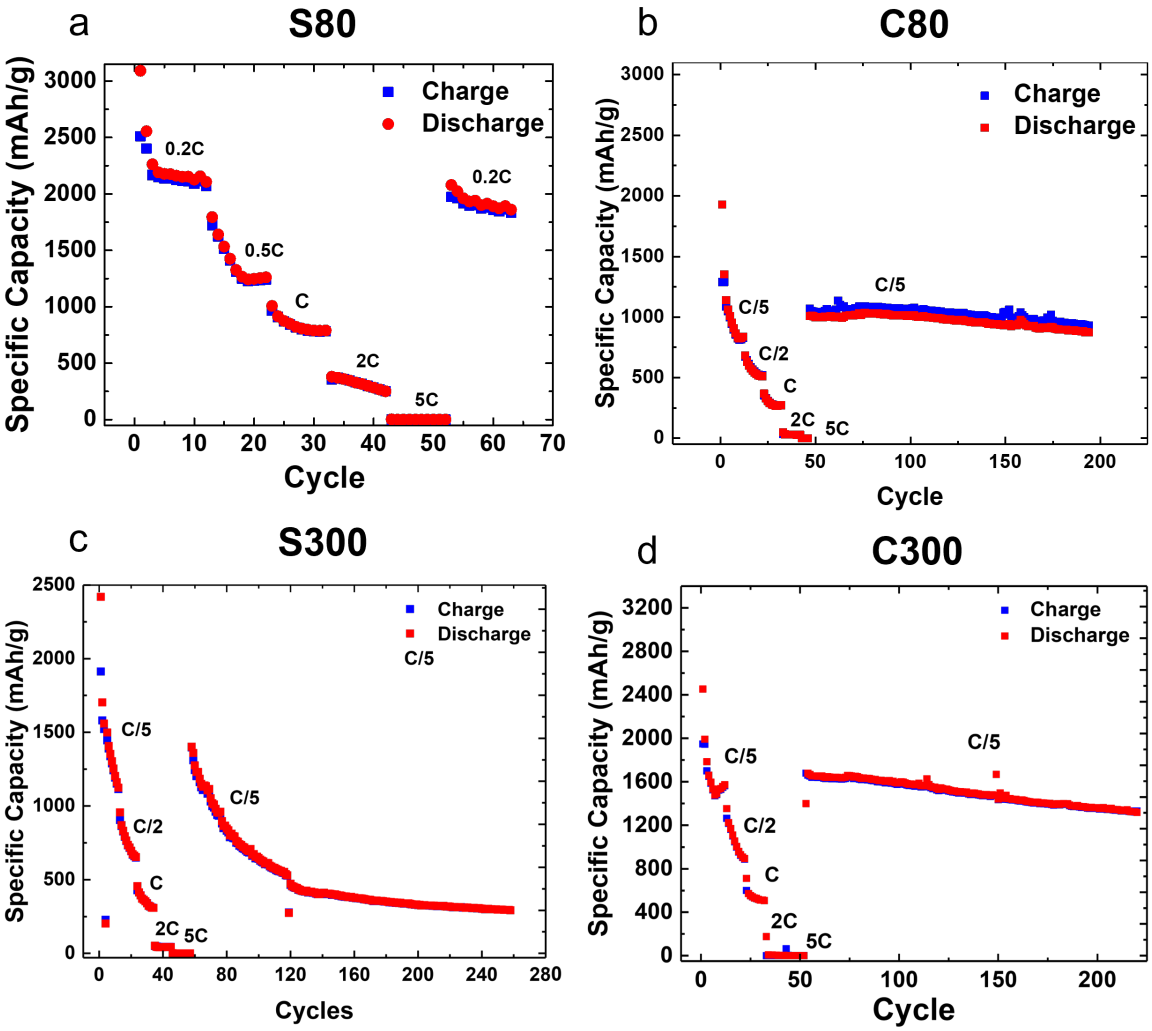

Figure. C2 Specific capacity of a) S80, b) C80, c) S300 and d) C300 silicon-graphene anodes as a function of charge/discharge rate. Cells were charge/discharged at constant currents of C/5 to 5C.

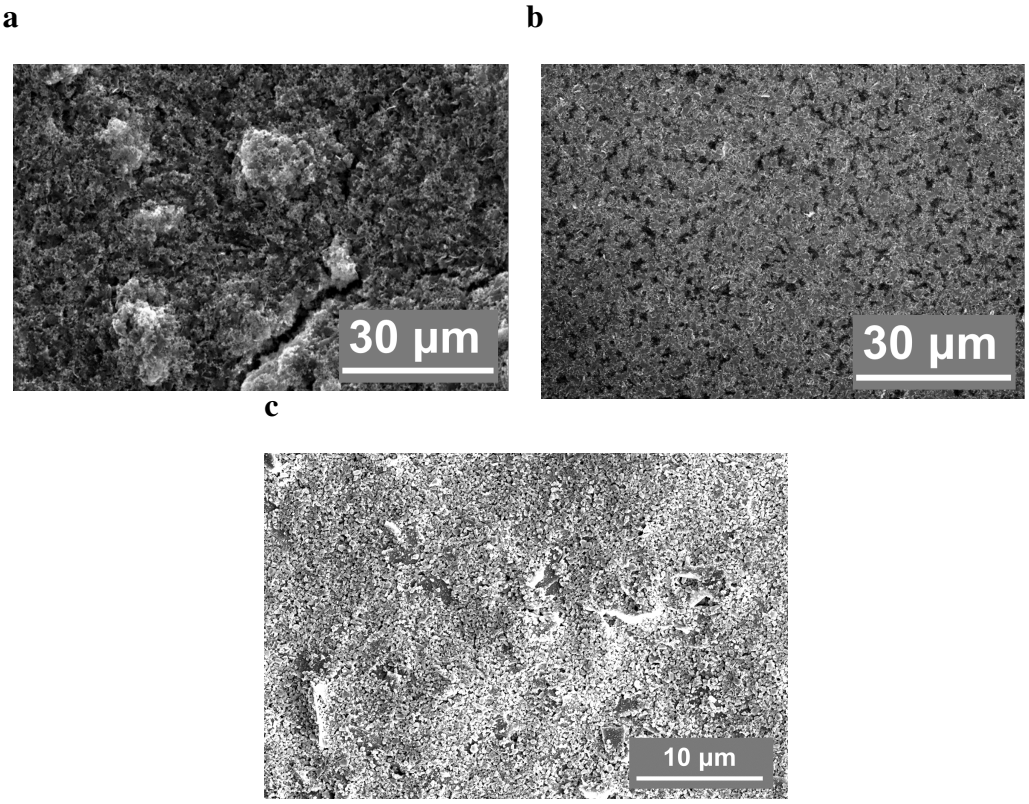

Figure. C3 Low magnification SEM of Silicon-graphene electrodes produced by a) shear mixing (S80), b,c) co-microfluidization (C80 and C300). The electrodes shown a and b were produced using the 80 nm silicon, while for the electrode shown in c, the 300 nm silicon was used.

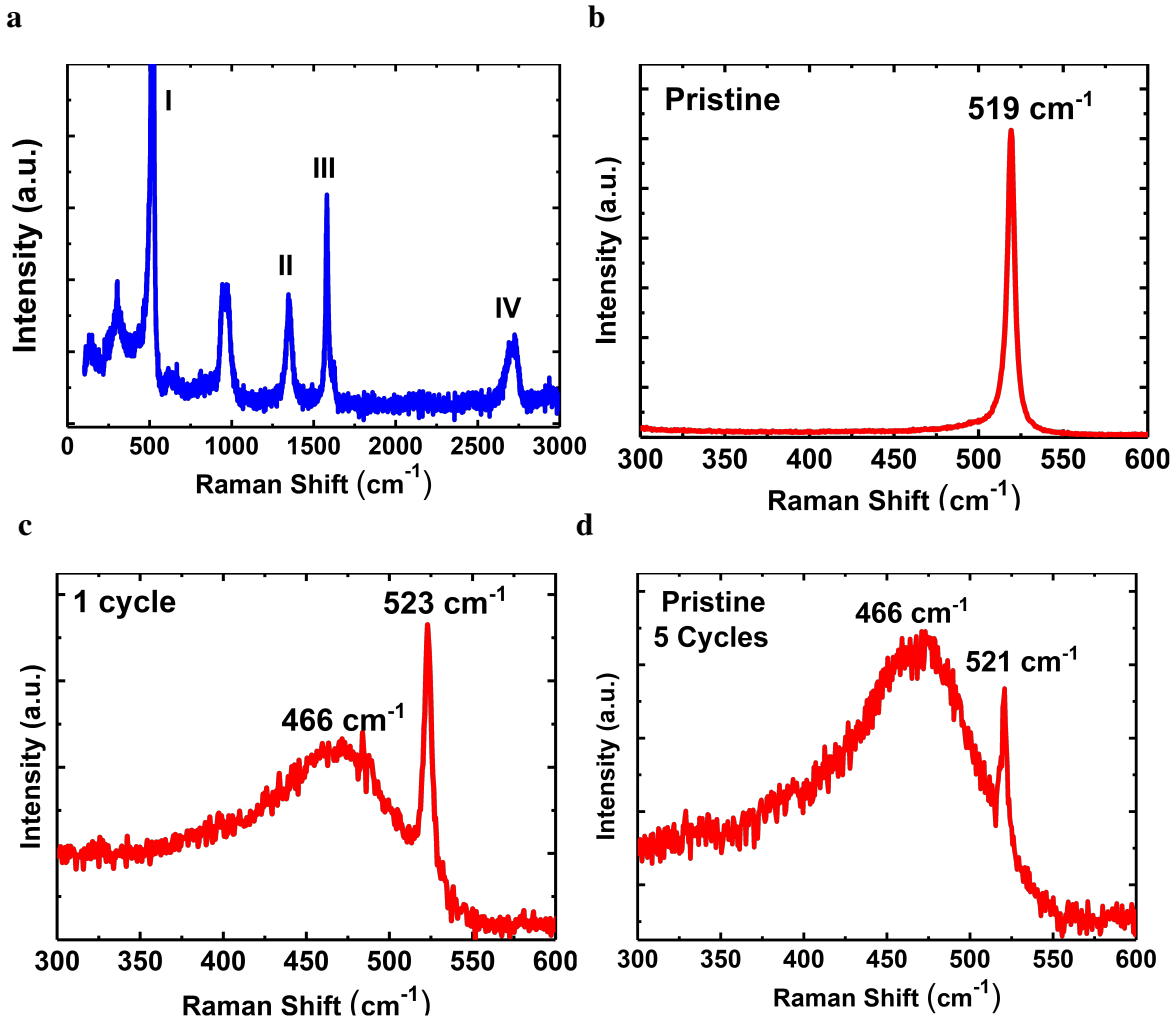

Figure. C4 a) Raman spectra of silicon-graphene anodes produced by shear mixing of 80 nm SiNPs (S80). The peak corresponding to amorphous silicon (466 cm^{-1}) and crystalline silicon (520 cm^{-1}) is also shown after a,b) 0 cycles c) 1 cycle and d) 5 cycles. The whole spectra between 100 - 3000 cm^{-1} is shown in a. The peaks labelled I, II, III and IV correspond to the crystalline Si peak and the D, G and 2D peaks of the graphene.[217]

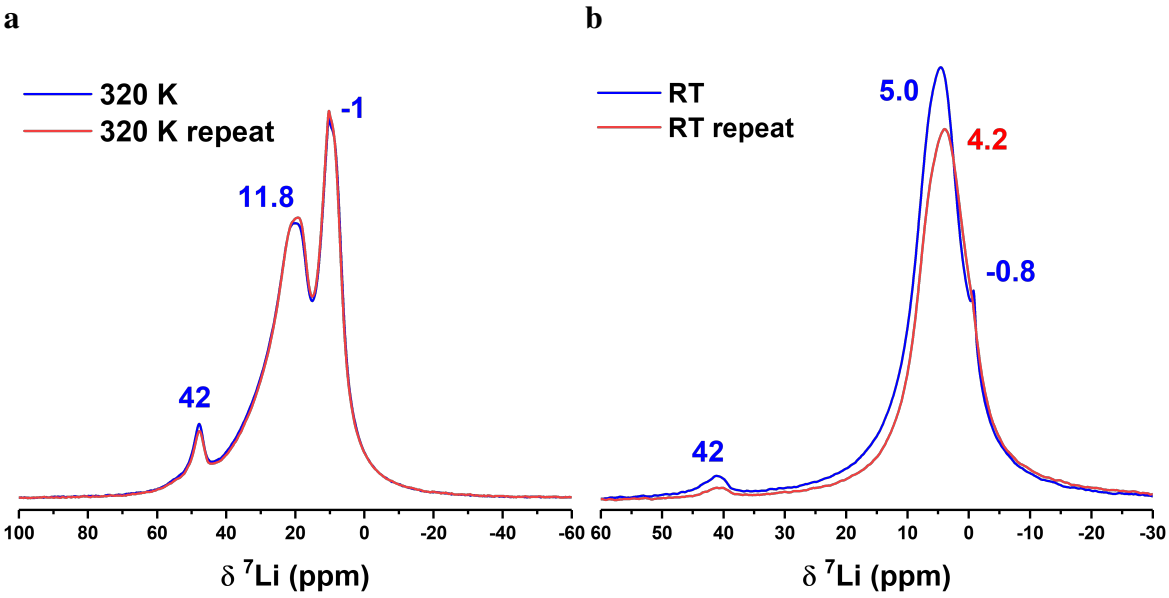

Figure. C5 *Ex-situ* ^{7}Li NMR spectra of a) electrochemically (EL) and b) chemically (CL) lithiated co-microfluidized silicon-graphene anode with 300 nm silicon (C300). Spectra are shown before and after VT NMR measurements.